The physics of the interstellar medium

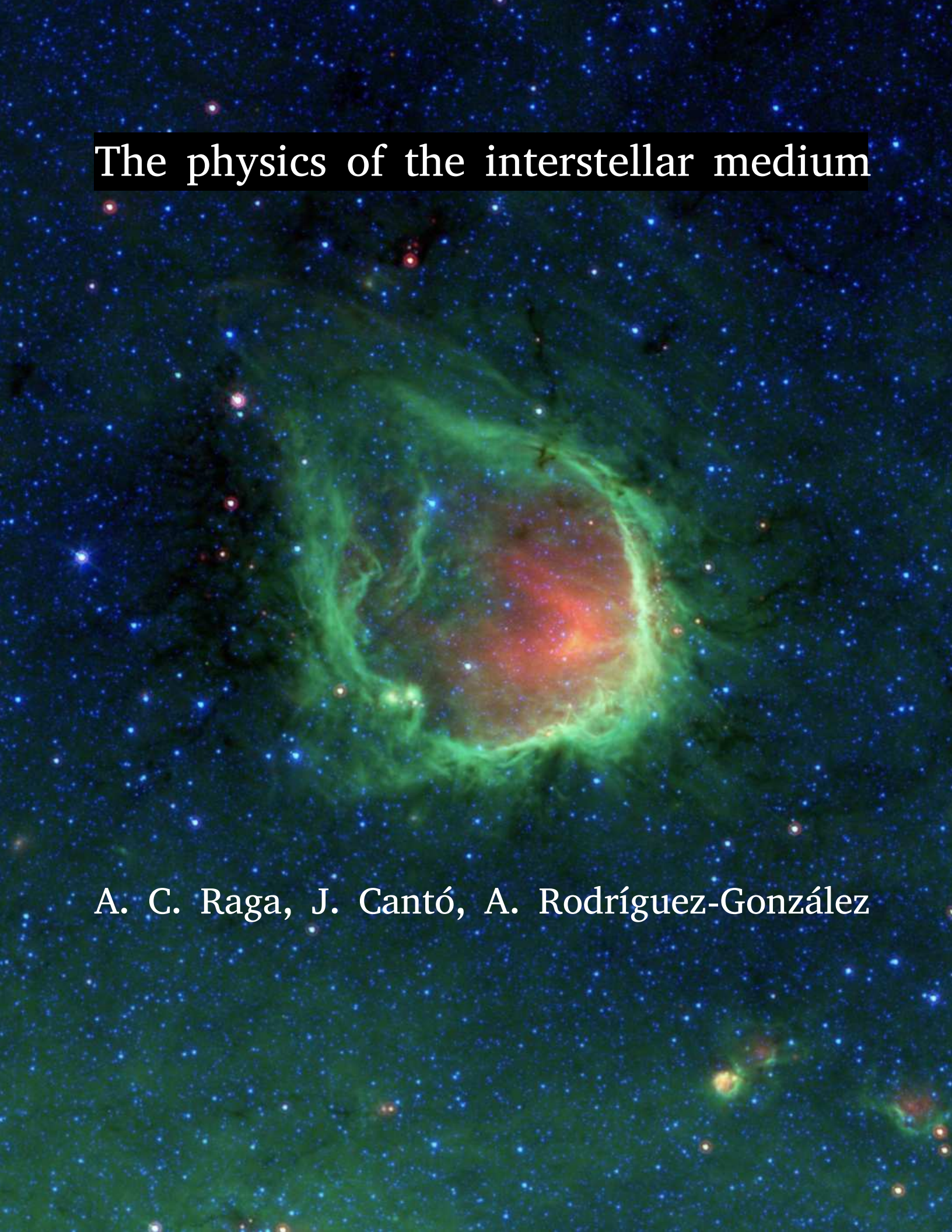

A. C. Raga, J. Cantó, A. Rodríguez-González

The physics of the interstellar medium

A. C. Raga, J. Cantó, A. Rodríguez-González

September 11, 2020

Acknowledgments: We thank our families for their long-term support and patience, and our collaborators and students for help and participation in the topics covered here. We also thank Bo Reipurth for extremely helpful comments on a first version of this book.

Contents

Part I

Introduction

Chapter 1

General comments

This book reflects the content of and is based on notes for the ISM course which has been given at the UNAM by Jorge Cantó and Alejandro Raga for over 25 years. In the more recent years, the lectures of this course are being taken over by members of the "new generation" of our group: Alejandro Esquivel, Ary Rodríguez González and Pablo Velázquez.

The course (as well as the book) is divided into three main parts:

- I. a general introduction (in which this chapter is included),
- II. the physical processes in the ionised ISM and models of static photoionised regions. This part of the course is in the style of the classical books of Aller [4] and Osterbrock[18] (the latter in its multiple editions), and includes discussions of the basic processes, the ionisation and excitation state of the gas, and the prediction of the observed line and continuum spectrum,
- III. the dynamics of the ISM. This part starts with a derivation of the gasdynamic equations and simple, general solutions of astrophysical interest (sound waves, instabilities and shock waves). This is followed by a selection of problems of ISM dynamics (e.g., expansion of HII regions, SN remnants and winds),
- IV. astrophysical jets.

The second section is in the style of the books of Dyson & Williams [13] (in its different incarnations) and Shore [31]. There is a quite extended section on jets that, though it should belong in "part III" (dynamics of the ISM), has been made into a "part IV" for organizational reasons. Stellar winds and accretion disks are missing.

Clearly also missing from this book is the chemistry of the ISM and dust (which are only given in a schematic way in our ISM course and are therefore not worthwhile to include). These topics are covered in several books which have been written by people with much more knowledge than us. Also, magnetic fields (and the modelling of magnetized flows with the magnetohydrodynamic equations) are omitted.

This book is directed to master's, PhD students or researchers interested in calculating dynamical models of the ISM. We feel that it provides more detail than previous books on how to calculate the ionisation/excitation state and how to develop dynamical ISM models than previous books. Also, the book covers a quite broad selection of different applications.

Finally, we should mention that the book is strongly focussed on theoretical issues, with only minimal descriptions of the observational characteristics of the ISM.

This book is "free access". We welcome comments from readers, and will consider them in future editions of the book. We also plan to include descriptions of more flows in a second edition of this book. Please send your comments to: raga@nucleares.unam.mx.

Chapter 2

Observational characteristics of the ISM

At the end of the XIX'th century, through spectroscopic observations Huggins [15] realized that while some of the (well known) diffuse nebulae were far away groups of stars (i.e., external galaxies), others were made of diffuse gas surrounding blue stars. This is without doubt a clear realization of the existence of material in the space between stars (the "interstellar medium").

In the western literature, the first reference to the interstellar medium apparently is the reference to the "coal sacks" in the southern Milky Way (dusty molecular clouds covering the view of the Galactic disk in the general direction of the Galactic centre). These dark clouds were of course well known for southern civilizations, some of which gave them an important role in creation/destruction myths (notably in Australia).

The interstellar medium has a mixture of gas and dust, with the gas to dust mass ratio of $\sim 10^4$ and gas to dust number ratio (of particles) $\sim 10^{12}$. The dust particles have sizes of ~ 1 μm and despite their low abundance they have important optical effects, and can also effect the thermal balance and the chemistry of the gas.

The ISM of our galaxy has abundances (by number) similar to the ones of the solar atmosphere. Typical abundances (by number, with respect to the total number of atoms/ions) of some of the elements present are: H$\rightarrow$ 0.9, He$\rightarrow$ 0.1, C$\rightarrow$ 3×10^{-4}, N$\rightarrow$ 10^{-4}, O$\rightarrow$ 5×10^{-4}, S$\rightarrow$ 2×10^{-5}, Ne$\rightarrow$ 10^{-4},

Ca$\rightarrow 2\times10^{-6}$, Fe$\rightarrow 10^{-6}$. Clearly, H and He dominate the composition of the gas (by number of particles and by mass). The heavier elements, however, have to be considered (except in the more simple models) because the energy loss due to the emission lines they emit generally dominates the thermal balance of the ISM.

Throughout this book, for the ionisation of the different elements we use the "astronomical notation": H $\rightarrow$ HI (neutral H), $H^+ \rightarrow$ HII, He $\rightarrow$ HeI, $He^+ \rightarrow$ HeII, $He^{++} \rightarrow$ HeIII, etc. In other words, the ions are denoted by the identification of the element, followed by a roman numeral corresponding to $z+1$, where z is the charge of the ion.

There are different regions of the ISM in which the gas can be mostly neutral, have a high ionisation state (with fully ionised H and He and possibly multiple ionisations of heavier elements) or be mostly molecular. Some of these regions are:

1. Molecular clouds: dense regions of the ISM in which Hydrogen forms H_2 molecules, and the heavier elements can be present in molecules of different complexity. These regions have complex, inhomogeneous structures with compact "cores" (of sizes $\sim 10^{16} \rightarrow 10^{18}$ cm) and more diffuse regions. The self-gravity of the gas is generally important. They have temperatures $T \sim 10 \rightarrow 100$ K and number densities $n \sim 10^3 \rightarrow 10^7$ cm^{-3}. There is strong evidence that dense parts of molecular clouds (dense cores) collapse to form new stars and planetary systems,

2. Photodissociation regions (PDR): regions that are generally found at the outer edges of molecular regions. Molecules, neutral atoms, and mostly singly ionised atoms are found in PDR's. Their temperatures are in the $\sim 100 \rightarrow 1000$ K range, and a wide range of densities is possible,

3. H I regions: neutral gas filling a substantial part of the Galactic disk. They have typical temperatures of $\sim 100 \rightarrow 5000$ K, and densities $\sim 1 \rightarrow 10$ cm^{-3},

4. H II regions: diffuse gas surrounding hot, massive stars, which is photoionised by the far ultraviolet radiation from the stars. They have temperatures $T \approx 10^4$ K and densities ranging from $n \sim 1$ cm^{-3} (for an H II region in a low density zone of the Galactic disk) to $\sim 10^5$ cm^{-3} (for an H II region within a high density zone of a molecular cloud),

5. Planetary nebulae: gas previously ejected from stars which are now hot, pre-white dwarf objects which photoionise material that was previously ejected by the stars. The physical processes determining their properties are similar to the ones of H II regions. Their temperatures are $T \sim 10^4$ K and densities $n \sim 100 \rightarrow 10^4$ cm^{-3}. The abundances of the heavier elements can differ appreciably from the typical ISM abundances (see above),

6. Stellar winds and jets: gas ejected from stars in the form of an approximately isotropic outflow (wind) or in the form of well collimated beams (jets). The observed stellar winds and jets have temperatures ranging from $\sim 1000 \rightarrow 10^6$ K (depending on which compact objects are ejecting them) and velocities ranging from ~ 5 km s^{-1} up to a substantial fraction of the speed of light,

7. Supernova remnants: These are expanding "bubbles" of hot gas produced by supernova explosions. These bubbles push out a shock wave that heats the gas to coronal temperatures ($\sim 10^6 \rightarrow 10^7$ K). They are found as single objects, and also (notably in some active galaxies) as groups of remnants that merge into a single "superbubble", that can eject coronal gas from the galaxy into the intergalactic medium (in what is known as a "galactic fountain").

Even though many of the theoretical aspects of the ISM have been first studied thinking about our Galaxy, the same ideas mostly apply to the ISM of external galaxies (with the caveat that other galaxies many times have different abundances of the "heavy elements" or "metals"). Also, many of the ideas about the ISM also apply to the "intergalactic medium".

Part II of the book covers the basic physics of photoionised regions (items 3 and 4 above). The same physical processes apply to all of the objects in the objects with item numbers ≥ 5. Part III discusses (mostly analytical) models for all of the objects of the above list. Part IV discusses astrophysical jets.

Part II

Physical processes in the ISM

Chapter 3

Photoionised Regions

3.1 Introduction

Starting with the paper of Huggins ([15], "On the spectrum of the great nebula in Orion..."), photoionised regions have been one of the dominant topics in research on the ISM. Photoionised regions in our galaxy fall into two main categories :

1. H II regions : these are regions of the ISM in which massive stars have formed, and the far-UV radiation from these stars photoionises the surrounding gas. The brightest and best studied region is the Orion Nebula (see Fig. 3.1).

2. Planetary nebulae : these are evolved stars which have ejected most of their material in the form of winds. The remaining, hot core of the star emits far-UV radiation which photoionises the still outflowing material which was previously ejected from the star. An example of this kind of object is the Helix Nebula (see Fig. 3.2).

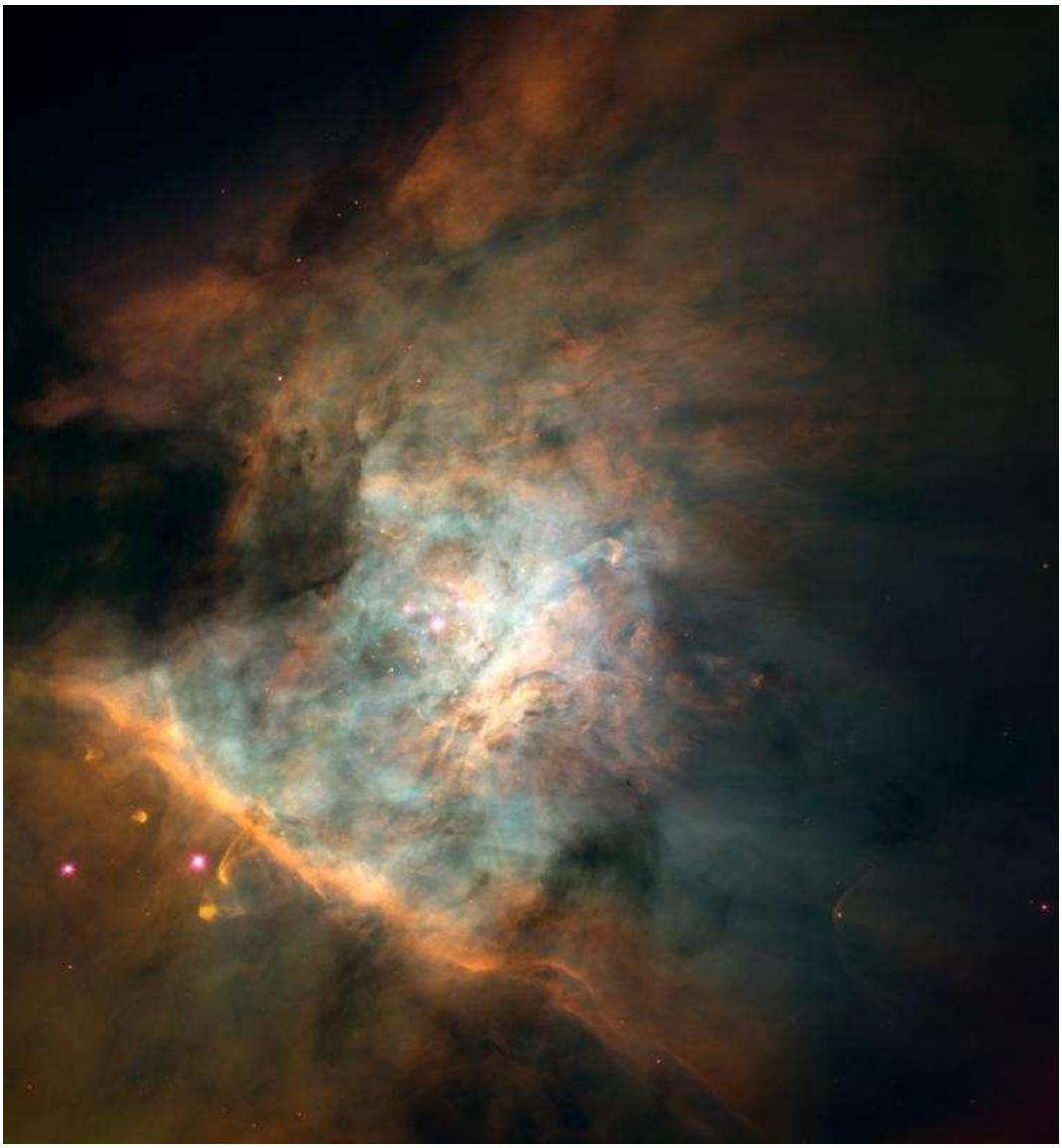

Figure 3.1: Example of an H II region: the Orion Nebula (source: George Herbig, Lick Observatory)

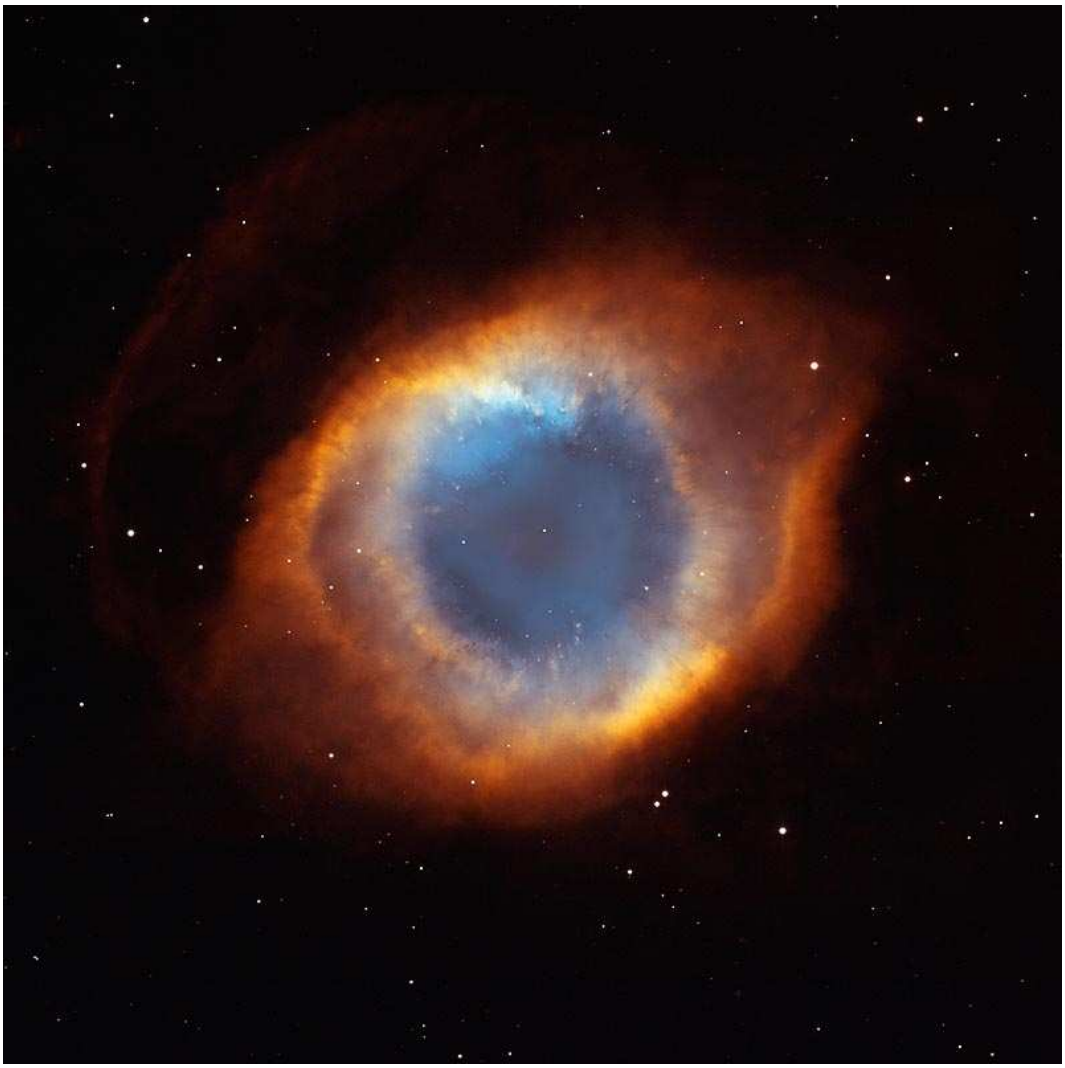

Figure 3.2: Example of a planetary nebula: the Helix [source: NASA, ESA and C. R. O'Dell (Vanderbilt University)]

3.2 The ionising photon rate produced by the central star

3.2.1 General considerations

The fundamental process giving rise to the "photoionised region" phenomenon is the production of far-UV photons by the "central source" of the nebula. This "central source" could in principle be one or several stars which produce the photoionisation.

In the ISM, the gas is mostly composed of hydrogen (H), and most of the H atoms are in the ground, $n = 1$ state. The energy difference between an electron in this state, and the lowest possible energy of a free electron is the "ionisation potential" for the $n = 1$ level of H : $\chi_H = 13.6$ eV. In order to photoionise an electron from this level, it is necessary to have photons with energies $h\nu \geq \chi_H$.

The photoionisation process is shown schematically in Fig. 3.3. A photon of energy $h\nu \geq \chi_H$ (where h is the Planck constant and ν the frequency of the photon) hits an H atom in the $n = 1$ state. The photon is absorbed, and the electron has a transition to a free state with a kinetic energy $E_k = m_e {v_e}^2/2 = h\nu - \chi_H$ (where m_e is the mass and v_e the velocity of the free electron).

Let us call L_ν the luminosity per unit frequency emitted by the central source of the nebula (the total luminosity of the star being $L = \int_0^\infty L_\nu d\nu$). The total number of ionising photons (i.e., of photons with frequencies larger than $\nu_H = \chi_H/h$) emitted per unit time is then given by :

$$S_* = \int_{\nu_H}^{\infty} \frac{L_\nu}{h\nu} d\nu \,. \tag{3.1}$$

S_* is the "ionising photon rate", and is sometimes noted as "Q" in the literature. This quantity could correspond to a single star, or to a number of hot stars present within the photoionised region.

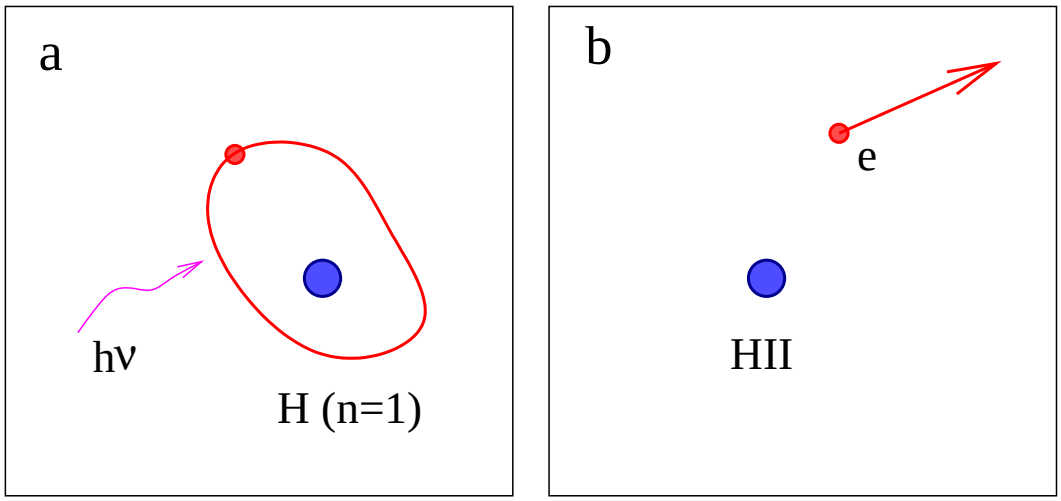

Figure 3.3: Schematic diagram showing the process of H photoionisation. **a.** in the initial state we have a photon of energy $h\nu$ hitting an H atom in the $n = 1$ state. **b.** after the interaction, we have an H nucleus (i. e., an HII ion) and a free electron with a kinetic energy $h\nu - \chi_H$ (where χ_H is the ionisation potential of hydrogen).

3.2.2 Sources emitting a black body spectrum

Let us consider that we have a star that emits a black body spectrum in the Wien limit ($h\nu/kT_* \gg 1$, where T_* is the black body temperature of the source). The luminosity per unit frequency emitted by the star then is :

$$L_\nu = 4\pi {R_*}^2 (\pi B_\nu) \approx 4\pi {R_*}^2 \frac{2\pi h\nu^3}{c^2} e^{-h\nu/kT_*} , \tag{3.2}$$

where c is the speed of light and B_ν is the Planck distribution. Using this form for the frequency-dependent luminosity L_ν, eq. (3.1) can be integrated analytically to obtain :

$$S_{*,bb} = \frac{8\pi^2 {R_*}^2}{c^2} \left(\frac{kT_*}{h}\right)^3 \left({x_0}^2 + 2x_0 + 2\right) e^{-x_0} , \tag{3.3}$$

where $x_0 \equiv h\nu_H/kT_*$. This equation gives a simple prescription for calculating the ionising photon rate S_* as a function of the radius R_* and the black body temperature T_* of the source.

3.2.3 Sources with more realistic photon distributions

In practice, the emission from a stellar atmosphere can have quite strong deviations from a black body spectrum. It is possible to integrate eq. (3.1) using the results obtained from model atmospheres. Table 3.1 gives the effective temperatures and radii for massive main sequence stars (as a function of the spectral class), and the ionising photon rates S_* computed from appropriate atmosphere models.

Table 3.1 gives the results obtained from such a computation of S_* (including also the radius R_*, the luminosity L, the mass M, the terminal wind velocity v_w and the mass loss rate $\dot{M}$) for massive stars with different effective temperatures T_{eff}, taken from [32].

In Fig. 3.4, we see the values of S_* from Table 3.1 as a function of T_{eff}, as well as the $S_{*,bb}$ obtained from eq. (3.1) for the same values of $T_* = T_{eff}$ and R_*. It is clear that for $T_{eff} > 4 \times 10^4$ K, the two values agree well, though not so for lower temperatures. This can be seen in the lower frame of Fig. 3.4, which

Table 3.1: Ionising photon rate and other parameters for massive main sequence (luminosity class V) stars (from [32])

Spectral Type	T_{eff} [K]	R_* $[R_\odot]$	$\log_{10} L$ $[L_\odot]$	M $[M_\odot]$	v_w [km s^{-1}]	$\dot{M}$ $[M_\odot \mathrm{yr}^{-1}]$	$\log_{10} S$ [s^{-1}]
O3	51230	13.2	6.04	87.6	3552	2.7E-6	49.87
O4	48670	12.3	5.88	68.9	3266	1.8E-6	49.68
O4.5	47400	11.8	5.81	62.3	3138	1.4E-6	49.59
O5	46120	11.4	5.73	56.6	3026	1.1E-6	49.49
O5.5	44840	11.0	5.65	50.4	2903	8.9E-7	49.39
O6	43560	10.7	5.57	45.2	2784	7.2E-7	49.29
O6.5	42280	10.3	5.49	41.0	2666	5.6E-7	49.18
O7	41010	10.0	5.40	37.7	2543	4.5E-7	49.06
O7.5	39730	9.6	5.32	34.1	2428	3.5E-7	48.92
O8	38450	9.3	5.24	30.8	2313	2.7E-7	48.75
O8.5	37170	9.0	5.15	28.0	2194	2.1E-7	48.61
O9	35900	8.8	5.06	25.4	2083	1.7E-7	48.47
O9.5	34620	8.5	4.97	23.3	1972	1.3E-7	48.26
B0	33340	8.3	4.88	21.2	1853	1.0E-7	48.02
B0.5	32060	8.0	4.79	19.3	1747	7.8E-8	47.71

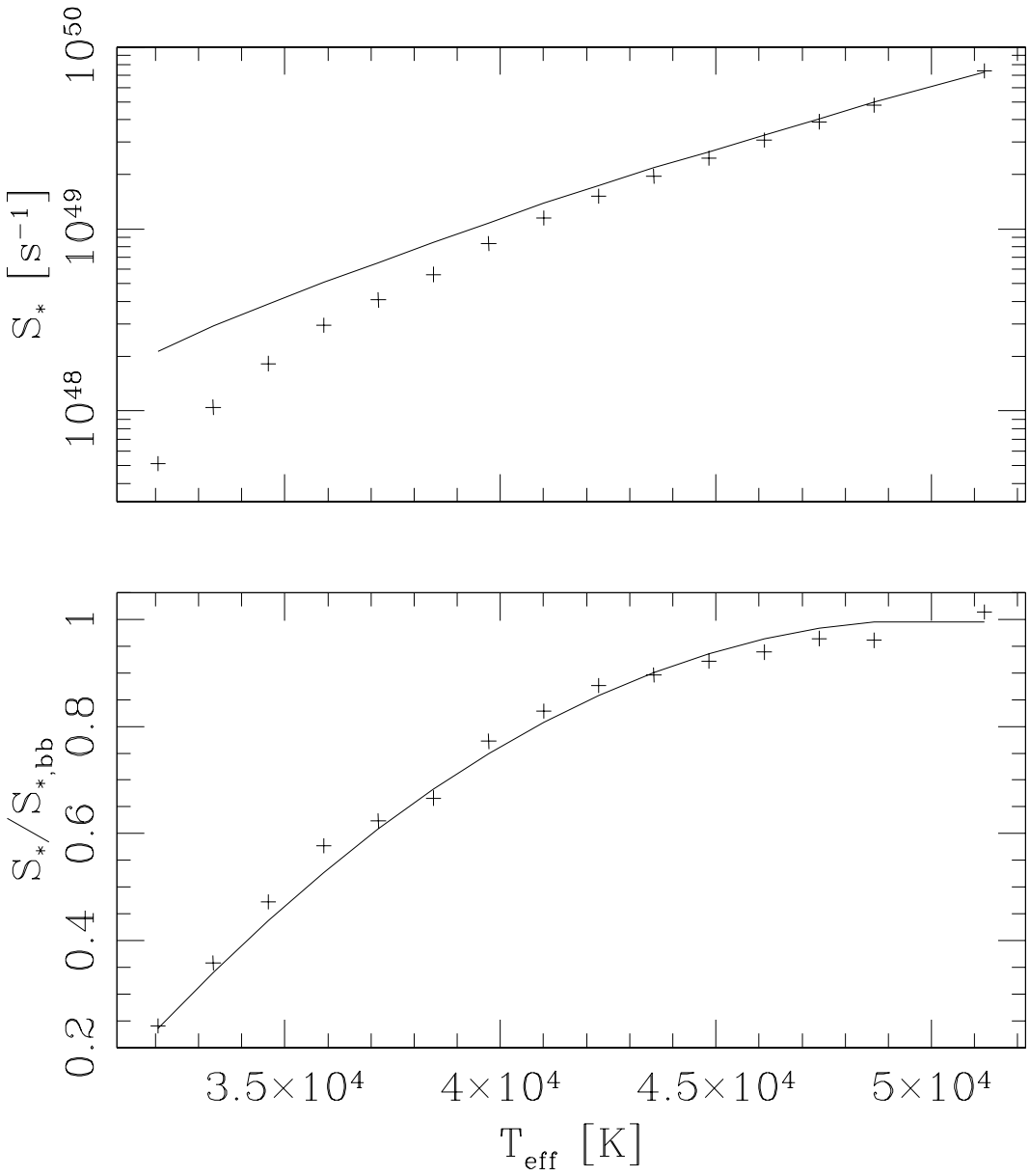

Figure 3.4: Ionising photon rate S_* as a function of T_{eff} for massive main sequence stars. Top: the crosses are the values taken from Table 3.1, and the solid line gives the $S_{*,bb}$ computed for a black-body source. Bottom: the ratio $S_*/S_{*,bb}$ as a function of T_{eff} (crosses) and the fit described in the text.

plots the $S_*/S_{*,bb}$ ratio as a function of T_{eff}. This ratio can be fitted with a quadratic polynomial of the form :

$$\frac{S_*}{S_{*,bb}}(T_{eff}) = 2.375\,t(1-t/10) - 4.938\,; \quad t = T_{eff}/10^4\mathrm{K}\,, \tag{3.4}$$

which is shown as a solid curve in Fig. 3.4. This fit has been made for temperatures in the range $30000 < T_{eff} < 50000$ K. It is then possible to use eq. (3.4) to calculate a correction factor by which one can multiply eq. (3.1) in order to obtain an ionisation photon rate closer to the one predicted from stellar atmosphere models.

In order to give a complete prescription of how to compute the ionising photon rate for luminous stars along the main sequence, we note that the values of R_* as a function of T_{eff} can be fitted by :

$$\frac{R_*}{R_\odot}(T_{eff}) = 8.225 - 1.773\,t + 0.535\,t^2\,; \quad t = T_{eff}/10^4\mathrm{K}\,. \tag{3.5}$$

Therefore, in order to obtain values of S_* that basically represent an interpolation in between the ones of Table 3.1, for a given T_{eff} one can first compute R_* from eq. (3.5), then insert the values of T_{eff} and R_* into eq. (3.3) to obtain $S_{*,bb}$, and finally multiply by the correction factor given by eq. (3.4) in order to obtain the ionising photon rate S_*.

3.3 Strömgren sphere

The simplest possible model for an H II region can be constructed as follows. We consider a star with an ionising photon rate S_* which is immersed in a homogeneous medium of temperature T and H number denisty n_H. We assume that the star photoionises the gas within a sphere of radius R_S, and that the transition between ionised interior and neutral exterior occurs over a distance $\Delta R \ll R_S$. The balance equation which determines the size of the "Strömgren sphere" is

$$S_* = \dot{N}_{rec}\,, \tag{3.6}$$

where $\dot{N}_{rec}$ is the total number of recombinations per unit time within the sphere. The number of recombinations per unit volume $\dot{n}_{rec}$ is given by

$$\dot{n}_{rec} = n_e\, n_{HII} \alpha_H(T)\,, \tag{3.7}$$

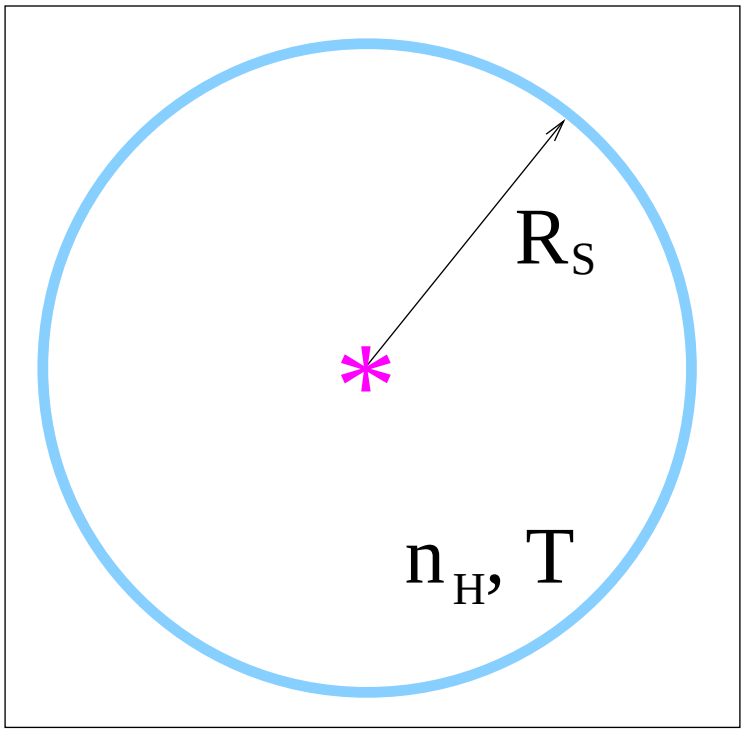

Figure 3.5: Schematic diagram showing the configuration of a Strömgren sphere produced by a star with an ionising photon rate S_* which is immersed in a homogeneous medium of temperature T and H atom+ion number density n_H. Within the ionised sphere ($R < R_S$), the gas is almost fully ionised, so that $n_e \approx n_{HII} \approx n_H$. For $R > R_S$, $n_e \approx n_{HII} \approx 0$ and $n_{HI} \approx n_H$.

where the recombination coefficient $\alpha_H(T)$ is described in detail below. Within the ionised sphere, most of the electrons come from the ionised H, so that we can set $n_e \approx n_{HII} \approx n_H$. Then, the integral of the eq. (3.7) over the volume of the sphere (obtained just by multiplying by $4\pi {R_S}^3/3$, as the medium is assumed to be homogeneous), and substituting into eq. (3.6) one obtains

$$S_* = \frac{4\pi}{3} {R_S}^3 {n_H}^2 \alpha(T) \quad \rightarrow \quad R_S = \left[\frac{3S_*}{4\pi {n_H}^2 \alpha(T)} \right]^{1/3} , \tag{3.8}$$

where the latter equation gives the "Strömgren radius" R_S of the ionised sphere.

The recombination coefficient $\alpha(T)$ is calculated as a sum over the recombination coefficients to all of the energy states of H :

$$\alpha_A(T) = \sum_{n=1}^{\infty} \alpha_n(T)\,, \tag{3.9}$$

and the recombination coefficient to state n is given by

$$\alpha_n(T) = \int_0^{\infty} \sigma_n(v)\, v f(v,T) dv\,, \tag{3.10}$$

where the integral of the product of the Maxwell-Boltzmann distribution $f(v,T)$, the effective cross section for the radiative recombination process $\sigma_n(v)$ and the velocity v is carried out over all of the possible values for the velocity of the electrons.

Actually, the electrons which recombine directly to the ground, $n = 1$ state emit a Lyman continuum photon with energy greater than 13.6 eV. Therefore, these photons contribute to the photoionisation of H atoms in other regions of the Strömgren sphere. Because of this, a better approximation is to not consider the recombinations to $n = 1$ in the recombination coefficient, as these are "inefficient recombinations" leading to a new photoionisation within the sphere. It is therefore better to put $\alpha(T) = \alpha_B(T)$ in eq. (3.8), where

$$\alpha_B(T) = \sum_{n=2}^{\infty} \alpha_n(T)\,, \tag{3.11}$$

is called the "case B" recombination coefficient of H (the "case A" recombination coefficient being given by eq. 3.9).

Tabulations of the recombination coefficients as a function of gas temperature T are given by Osterbrock (1989). It is possible to carry out simple power law fits to these tabulations, from which one obtains :

$$\alpha_A(T) = 4.15 \times 10^{-13} \mathrm{cm^3 s^{-1}} \left(\frac{10^4 \mathrm{K}}{T}\right)^{0.72}\,, \tag{3.12}$$

$$\alpha_B(T) = 2.56 \times 10^{-13} \mathrm{cm^3 s^{-1}} \left(\frac{10^4 \mathrm{K}}{T}\right)^{0.83}\,. \tag{3.13}$$

For the calculation of a Strömgren radius, one then sets $\alpha_H(T) \approx \alpha_B(10^4\mathrm{K})$ in eq. (3.8). As we shall see below, this is a reasonable value to take for the recombination coefficient because temperatures of H II regions always have values $T \sim 10^4$ K.

3.4 Strömgren regions

3.4.1 Generalization of the Strömgren sphere analysis

The simple argument of balancing the ionising photon rate S_* with the total recombination rate can be applied to more general cases than the one of a photoionised region in a homogeneous medium. In the following, three examples are presented showing how to carry out a "Strömgren region" analysis of a stratified H II region, of an H II region in which the star moves supersonically with respect to the surrounding medium, and of an expanding, constant density H II region.

3.4.2 The photoionisation of a constant velocity wind

Let us consider a stationary wind with a constant velocity v_w, independent of the spherical radius R. The mass $\dot{M}$ going through a spherical surface of radius R is

$$\dot{M} = 4\pi R^2 \rho_w v_w \,, \tag{3.14}$$

where ρ_w is the density of the wind at a radius R. For a stationary wind, $\dot{M}$ is independent of R, and is equal to the rate of mass loss from the star. Eq. (3.14) then gives the atom+ion number density

$$n_w(R) = \frac{\rho_w(R)}{m} = \frac{\dot{M}}{4\pi m v_w R^2} \,, \tag{3.15}$$

where m is the mass per atom or ion ($= m_H$ for a pure H wind, and $= 1.3 m_H$ for a wind of 90% H and 10% He).

The balance between ionising and recombination rates (see eq. 3.8 for the case

of a homogeneous medium) can be written as

$$S_* = \int_{R_*}^{R_S} n_w^2(R)\alpha_H(T)\,4\pi R^2 dR\,, \tag{3.16}$$

where $n_w(R)$ is given by eq. (3.15), R_* is the stellar radius and R_S is the outer radius of the photoionised region. We now assume that the wind is isothermal, and take $\alpha_H(T) \approx \alpha_B(10^4\mathrm{K})$ out of the integral.

Eq. (3.16) can be integrated and then inverted to obtain

$$\frac{R_S}{R_*} = \left(1 - \frac{S_*}{S_0}\right)^{-1} \;; \quad S_0 \equiv \frac{\dot{M}^2\alpha_B}{4\pi R_* {v_w}^2 m^2}\,, \tag{3.17}$$

which is plotted in Fig. 3.6. It is clear that $R_S \to \infty$ for $S_* \to S_0$. For $S_* > S_0$, the recombination rate in the full volume of the wind (out to $R \to \infty$) is smaller than the ionising photon rate S_*.

From Table 3.1, one can check numerically that $S_*/S_0 \gg 1$ for all massive main sequence stars. Therefore, these stars only use a very small fraction of their ionising photon production in order to fully photoionise their own winds.

3.4.3 Cometary H II region

Let us consider a star with an ionising photon rate S_* moving at a velocity v_* through a homogeneous medium of density n_H. We will assume that the star has no wind, and that the formation of the H II region does not lead to any modification of the initially homogeneous density of the surrounding medium. This latter assumption is valid provided that v_* is highly supersonic.

If we stand in a reference system travelling with the star, the problem corresponds to a stationary star and an environment that travels at a velocity v_* towards it. This configuration is shown in Fig. 3.7.

We place an axis directed towards the impinging flow (see Fig. 3.7) and consider the spherical radius R and cylindrical radius r of the edge of the H II region, both dependent on the angle θ between the point on the edge of the H II region and the axis (the spherical and cylindrical radii are related through $r = R\sin\theta$). The angle θ subtends a solid angle $\Delta\Omega = 2\pi(1 - \cos\theta)$.

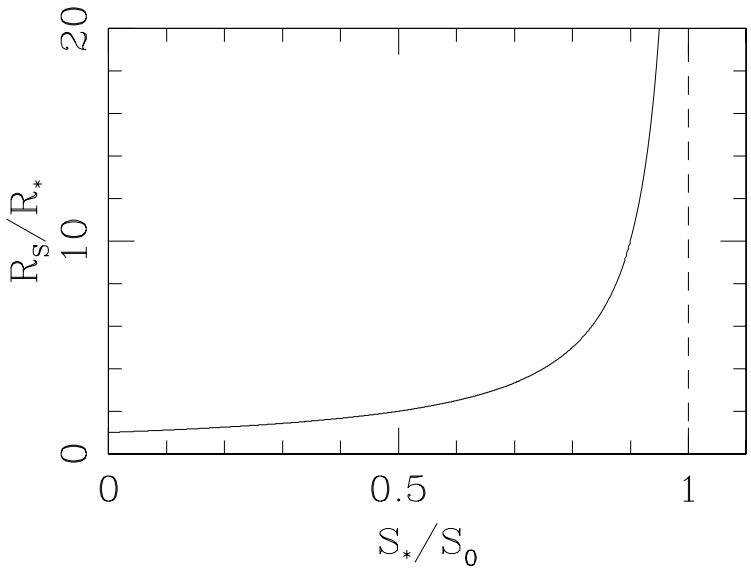

Figure 3.6: Solution for the Strömgren radius of a region with an R^{-2} density stratification. The Strömgren radius goes to infinity for $S_*/S_0 \to 1$ (see the text).

Let us now consider the ionising photons $S_*\Delta\Omega/(4\pi)$ emitted per unit time by the source into the solid angle $\Delta\Omega$. These photons have to balance the recombinations $\dot{N}_{rec}(\theta)$ in the ionised volume $V(\theta)$ subtended by the angle θ and also have to ionise the neutrals that enter from the upstream direction into the ionised region $\dot{N}_{in}(\theta)$ per unit time into this volume. In other words :

$$\frac{S_*}{4\pi}\Delta\Omega = \dot{N}_{rec}(\theta) + \dot{N}_{in}(\theta)\,, \tag{3.18}$$

where $\Delta\Omega = 2\pi(1-\cos\theta)$ is the solid angle subtended by the angle θ.

The total number of recombinations per unit time can be written as

$$\dot{N}_{rec}(\theta) = {n_H}^2\alpha_H V(\theta)\,; \quad V(\theta) = \frac{2\pi}{3}\int_0^\theta R^3 \sin\theta\, d\theta\,, \tag{3.19}$$

where $V(\theta)$ is the ionised volume limited by θ. The number of neutral atoms that enter through the boundary of the H II region per unit time is $\dot{N}_{in}(\theta) = \pi r^2 n_H v_*$.

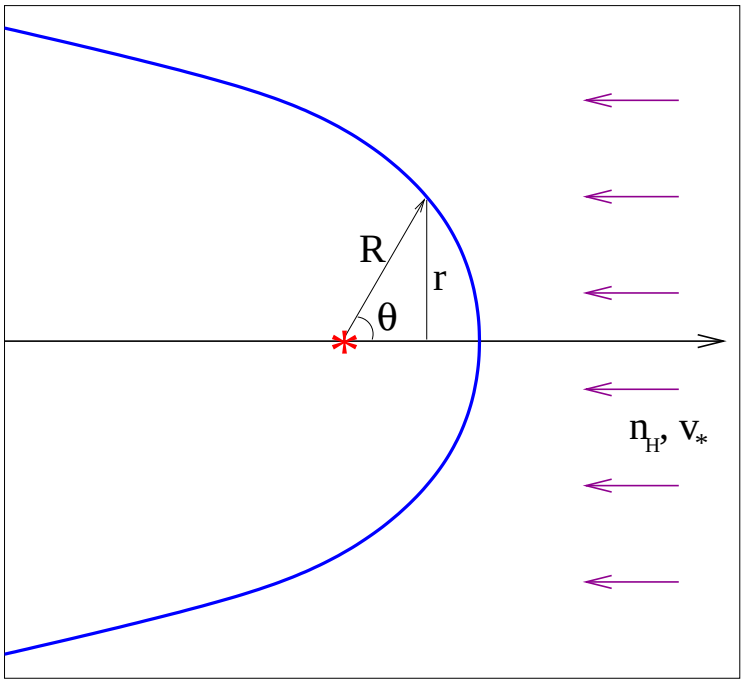

Figure 3.7: Schematic diagram showing a cometary H II region formed around a star which travels at a velocity v_* through a homogeneous ISM of density n_H.

Equation (3.18) has a general analytic solution in terms of elliptic integrals (see Rasiwala[25]). A simple, high v_* solution can be obtained noting that for larger values of v_*, $\dot{N}_{in}$ grows linearly with v_*. Instead, $\dot{N}_{rec}$ actually decreases with increasing values of v_*. Therefore for a high enough v_* we have $\dot{N}_{in} \gg \dot{N}_{rec}$, and equation (3.18) becomes

$$\frac{S_*}{4\pi}\Delta\Omega \approx \dot{N}_{in}(\theta)\,. \tag{3.20}$$

If we substitute the appropriate expressions for the solid angle and for the rate of neutrals entering the H II region, we then obtain the solution

$$r(\theta) = \sqrt{\frac{S_*}{2\pi n_H v_*}(1-\cos\theta)}\,. \tag{3.21}$$

For $\theta = 0$, this solution has an on-axis separation

$$R_0 = \lim_{\theta\to 0}\frac{r(\theta)}{\sin\theta} = \sqrt{\frac{S_*}{4\pi n_H v_*}}\,, \tag{3.22}$$

between the star and the "head" of the cometary H II region (see Fig. 3.7). For $\theta \to \pi$, the edge of the H II region reaches a maximum separation

$$r_m = \sqrt{\frac{S_*}{\pi n_H v_*}} \tag{3.23}$$

with respect to the symmetry axis. This solution was apparently first deduced by Rasiwala[25].

One can show that the approximation of neglecting the recombinations within the H II region in the balance equation (eqs. 3.18 and 3.20) is correct provided that the on-axis standoff distance R_0 (eq. 3.22) satisfies the condition $R_0 \ll R_S$, where R_S is the "standard" Strömgren radius, defined by eq. (3.8). Through some simple algebra, this condition can be rewritten as

$$v_* \gg v_S \equiv \left(\frac{\alpha_B}{3}\right)^{2/3}\left(\frac{n_H S_*}{4\pi}\right)^{1/3}\,. \tag{3.24}$$

For example, for an O5 star moving into a medium with $n_H = 1$ cm^{-3}, we have $v_S \approx 260$ km s^{-1} (where we have used the value for S_* from Table 3.1 and for α_B at 10^4 K from eq. 3.13).

By differentiating with respect to θ (see [21]), the full balance equation (eqs. 3.18-3.19) can be written as

$$\left(\frac{R}{R_S}\right)^3 + \xi \left(\frac{R}{R_S}\right) \left[\left(\frac{\dot{R}}{R_S}\right) \sin\theta + \left(\frac{R}{R_S}\right) \cos\theta \right] = 1 \,, \tag{3.25}$$

where R_S is given by eq. (3.8), $\dot{R} = dR/d\theta$ and $\xi \equiv v_*/v_S$ (see eq. 3.24). One can show that for $\xi \gg 1$ one obtains the solution described above (eq. 3.21). Also, this equation has an analytic solution for the $\xi \ll 1$ limit :

$$R(\theta) = R_S \left(1 - \xi \cos\theta\right)^{1/3} \,. \tag{3.26}$$

This solution was apparently first found by Raga et al.[21].

For calculating the shape of the cometary HII region for an arbitrary value of ξ, it is necessary to evaluate the elliptical integrals in the solution of Rasiwala[25], or, alternatively, to integrate numerically equation (3.25).

3.4.4 The initial expansion of an H II region

Let us now consider the problem of a homogeneous H II region in which the star "turns on" at $t = 0$, emitting a constant S_* ionising photon rate for $t > 0$. The outer radius R of the H II region is initially zero (actually, equal to R_* and not strictly 0), and grows monotonically with time until it reaches the value of the Strömgren radius R_S (see eq. 3.8). If we neglect the light-crossing time in which the ionising photons travel from the star to the outer radius of the nebula, we can write the balance equation

$$S_* = \frac{4\pi}{3} R^3 {n_H}^2 \alpha_B + 4\pi R^2 F \,, \tag{3.27}$$

where R is the (time-dependent) outer radius of the H II region and F is the ionising photon flux (number of ionising photons per unit area and time) reaching the outer boundary of the nebula. Each of these photons ionises a new H atom, so that

$$F = n_H \frac{dR}{dt} \,. \tag{3.28}$$

Combining eqs. (3.27-3.28), one obtains

$$\frac{dR}{dt} = \frac{S_*}{4\pi R^2 n_H} - \frac{n_H \alpha_B R}{3} \,, \tag{3.29}$$

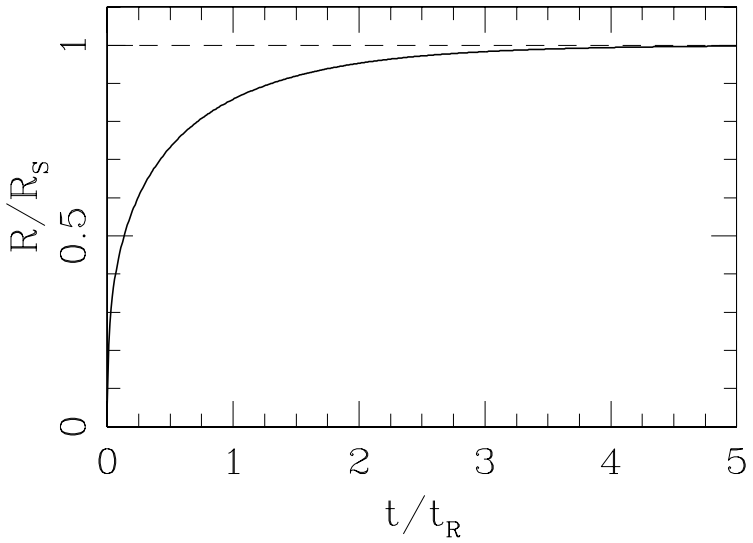

Figure 3.8: Solution for the time-dependent radius of an expanding, constant density H II region (see the text). It is clear that for $t > 3t_R$, the radius approaches R_S.

which can be integrated to obtain

$$R(t) = R_S \left(1 - e^{-t/t_R}\right)^{1/3} , \tag{3.30}$$

with

$$t_R \equiv \frac{3}{n_H \alpha_B} ; \quad R_S \equiv \left(\frac{3S_*}{4\pi {n_H}^2 \alpha_B}\right)^{1/3} . \tag{3.31}$$

Using the value of $\alpha_B(10^4\mathrm{K})$ (see eq. 3.13) and $n_H = 1$ cm^{-3}, we obtain $t_R = 1.24 \times 10^5$ yr. The solution for the expansion of the H II region is shown in Fig. 3.8.

3.5 The structure of the ionisation front

The outer boundary of an H II region is called an "ionisation front" (with H in the form of H II inside the boundary, and H as H I outside). In the treatment above we have assumed that this transition region between H II and H I has a negligible thickness $\Delta R \ll R_S$. In this section we will present

an approximate model describing this transition region, from which we can obtain an evaluation of the value of ΔR.

Let us first consider the ionisation equilibrium for H, which is dominated by the processes of photoionisation and radiative recombination :

$$n_{HI}\phi_H = n_e n_{HII}\alpha_H \,, \tag{3.32}$$

where ϕ_H is the photoionisation rate per neutral H atom :

$$\phi_H = \int_{\nu_H}^{\infty} \frac{4\pi J_\nu}{h\nu}\sigma_\nu \, d\nu \,, \tag{3.33}$$

with σ_ν the photoionisation cross section of H and

$$J_\nu = \frac{1}{4\pi}\oint I_\nu d\Omega \tag{3.34}$$

the zero-order moment of the specific intensity I_ν. If the ionising photons only come from the star (in other words, neglecting, e. g., the Lyman continuum photons emitted by the nebula), we have

$$4\pi J_\nu = \frac{L_\nu}{4\pi R^2}e^{-\tau_\nu} \,; \quad \tau_\nu = \int_0^R n_{HI}\sigma_\nu \, dR \,. \tag{3.35}$$

As we will see below, the photoionisation cross section of H has a frequency dependence $\sigma_\nu \propto \nu^{-3}$, which is very slow compared with the fast drop of the distribution $L_\nu/(h\nu)$ of the far-UV stellar photons. Therefore, the terms involving σ_ν can be taken out of the frequency integral in eq. (3.33), so that we obtain

$$\phi_H = \int_{\nu_H}^{\infty} \frac{L_\nu}{4\pi R^2 h\nu}e^{-\tau_\nu}\sigma_\nu d\nu \approx \sigma_{\nu_H} F \,, \tag{3.36}$$

with

$$F \equiv \frac{S_*}{4\pi R^2}e^{-\tau_{\nu_H}} \,. \tag{3.37}$$

Now, provided that the thickness of the ionisation front is indeed small compared to R_S (this will be shown to be indeed the case with the model that we are developing), in eq. (3.37) we can put $R = R_S$ (i. e., a constant geometrical dilution throughout the radial structure of the ionisation front). We then have

$$\frac{dF}{dl} = -F n_{HI}\sigma_{\nu_H} \,, \tag{3.38}$$

where $l = R - R_S$ is a radial coordinate measured with respect to the Strömgren radius.

We now introduce the ionisation fraction of H : $x = n_{HII}/n_H$. It is clear that $n_{HII} = x n_H$ and $n_{HI} = (1-x) n_H$. The ionisation equilibrium equation (eq. 3.32) then takes the form

$$\frac{x^2}{1-x} = \frac{\phi_H}{n_H \alpha_H} = \frac{\sigma_{\nu_H}}{n_H \alpha_H} F \,, \tag{3.39}$$

where for the second equality we have used eq. (3.36). From eq. (3.39) we can find F in terms of x, and differentiate with respect to $l = R - R_S$ to obtain

$$\frac{dF}{dl} = \frac{n_H \alpha_H}{\sigma_{\nu_H}} \frac{d}{dl}\left(\frac{x^2}{1-x}\right) = \frac{n_H \alpha_H}{\sigma_{\nu_H}} \frac{x(2-x)}{(1-x)^2} \frac{dx}{dl} \,. \tag{3.40}$$

We now combine equations (3.38) and (3.40) to obtain

$$\frac{dx}{dl} = -n_H \sigma_{\nu_H} \frac{x(1-x)^2}{2-x} \,, \tag{3.41}$$

which can be integrated to obtain

$$2 \ln\left(\frac{x}{1-x}\right) + \frac{1}{1-x} = 2 - \frac{l}{\lambda} \,, \tag{3.42}$$

where $\lambda = (n_H \sigma_{\nu_H})^{-1}$ is the photon mean free path in a neutral medium of density n_H. In order to derive this equation we have used the boundary condition $x(l=0) = 1/2$ (i. e., $x = 1/2$ at the Strömgren radius).

This solution is plotted in Fig. 3.9, from which we see that the thickness of the ionisation front is $\Delta R \approx 10\lambda$. Using the fact that $\sigma_{\nu_H} \approx 6.3 \times 10^{-18}$ cm^2, we obtain $\Delta R \approx 1.6 \times 10^{17} \mathrm{cm}\,(1\,\mathrm{cm}^{-3}/n_H)$, which can be compared with the Strömgren radii predicted for different O/B stars (see Table 3.1 and eq. 3.8) to see that we indeed have $\Delta R \ll R_S$.

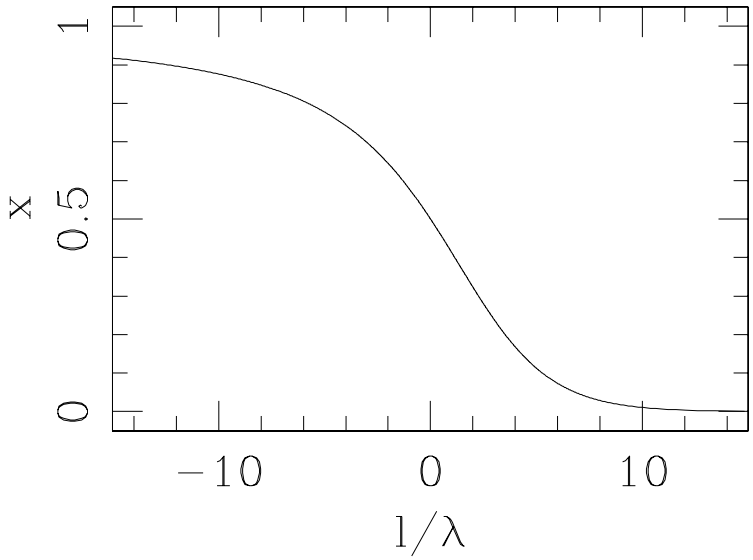

Figure 3.9: Solution for the structure of the ionisation fraction x as a function of the dimensionless distance l/λ from the Strömgren radius (see the text).

3.6 The ionisation of a nebula with many elements

3.6.1 The rate equations

For the sake of simplicity, in this section we consider the case of a constant density gas, for which the equations for an atomic/ionic network are :

$$\frac{dn_{a,z}}{dt} = {S^c}_{a,z} + {S^{ph}}_{a,z} \,, \tag{3.43}$$

with the collisional (S^c) and photoionisation (S^{ph}) source terms being given by

$${S^c}_{a,z} = n_e \left[n_{a,z-1} c_{a,z-1} + n_{a,z+1} \alpha_{a,z+1} - n_{a,z} \left(c_{a,z} + \alpha_{a,z} \right) \right] \,, \tag{3.44}$$

$${S^{ph}}_{a,z} = n_{a,z-1} \phi_{a,z-1} - n_{a,z} \phi_{a,z} \,. \tag{3.45}$$

If the $n_{a,z}$ are known, the electron density can be computed as

$$n_e = \sum_a \sum_z z \, n_{a,z} \,. \tag{3.46}$$

3.6.2 Ionisation equilibrium

The time-evolution of the ionisation rate equations leads to a final equilibrium for which $dn_{a,z}/dt = 0$ for all a and z. From eqs. (3.43-3.45) it can be shown that this condition results in the system of equations :

$$n_{a,z}\left(n_e c_{a,z} + \phi_{a,z}\right) = n_{a,z+1} n_e \alpha_{a,z+1}\,. \tag{3.47}$$

3.6.3 The collisional rate coefficients

The collisional ionisation (c) and radiative+dielectronic recombination (α) coefficients are functions of temperature T given by integrals of the form

$$\alpha(T),\ c(T)\ = \int_0^\infty f(v,T)\sigma_v\, v\, dv\,, \tag{3.48}$$

where $f(v,T)$ is the Maxwell-Boltzmann distribution for the electrons, and σ_v is the velocity-dependent collision cross section for the appropriate process.

It is common to give analytic fits to these coefficients in the "Arrhenius interpolation" form :

$$r(T) = b_1\, T^{b_2}\, e^{b_3/T}\,. \tag{3.49}$$

As an example of other formulae, Aldrovandi & Péquignot ([2], [3]) have used an interpolation

$$r(T) = b_1 \left(\frac{T}{10^4}\right)^{-b_2} + b_3 T^{-3/2} \exp\left(-b_4/T\right)\left[1 + b_5 \exp\left(-b_6/T\right)\right]\,, \tag{3.50}$$

for recombination coefficients.

Then, the b_1, b_2, ... coefficients are tabulated for all of the ionisation and recombination processes that have to be considered. An example of such a tabulation is given in Table 3.2.

Finally, we should note that for some atoms and ions, in the collision source term ${S^c}_{a,z}$ (see eq. 3.44) one also has to include "charge exchange" reactions with H. An example of important charge exchange reactions are the processes

Table 3.2: Ionisation, recombination and charge exchange coefficients

reaction	coefficients[a]
$e + HI \rightarrow 2e + HII$	1: 5.83×10^{-11}, 0.5, -157800
$e + HII \rightarrow HI$	1: 3.69×10^{-10}, -0.79, 0
$e + HeI \rightarrow 2e + HeII$	1: 2.707×10^{-11}, 0.5, -285400
$e + HeII \rightarrow HeI$	2: 4.3×10^{-13}, 0.672, 0.0019, 4.7×10^{5}, 0.3, 94000
$e + HeII \rightarrow 2e + HeIII$	1: 5.711×10^{-12}, 0.5, -631000
$e + HeIII \rightarrow HeII$	1: 2.21×10^{-9}, -0.79, 0
$e + CII \rightarrow 2e + CIII$	1: 3.93×10^{-11}, 0.5. -283000
$e + CIII \rightarrow CII$	2: 3.2×10^{-12}, 0.770, 0.038, 9.1×10^{4}, 2.0, 3.7×10^{5}
$e + CIII \rightarrow 2e + CIV$	1: 2.04×10^{-11}, 0.5, -555600
$e + CIV \rightarrow CIII$	2: 2.3×10^{-12}, 0.645, 7.03×10^{-3}, 1.5×10^{5}, 0.5, 2.3×10^{5}
$e + NI \rightarrow 2e + NII$	1: 6.18×10^{-11}, 0.5 -168200
$e + NII \rightarrow NI$	2: 1.5×10^{-12}, 0.693, 0.0031 2.9×10^{5}, 0.6, 1.7×10^{5}
$e + NII \rightarrow 2e + NIII$	1: 4.21×10^{-11}, 0.5, -343360
$e + NIII \rightarrow NII$	2: 4.4×10^{-12}, 0.675, 0.0075 2.6×10^{5}, 0.7, 4.5×10^{5}
$e + OI \rightarrow 2e + OII$	1: 1.054×10^{-10}, 0.5, -157800
$e + OII \rightarrow OI$	2: 2.0×10^{-12}, 0.646, 0.0014 1.7×10^{5}, 3.3, 5.8×10^{4}
$e + OII \rightarrow 2e + OIII$	1: 3.53×10^{-11}, 0.5, -407200
$e + OIII \rightarrow OII$	2: 3.1×10^{-13}, 0.678, 0.0014 1.7×10^{5}, 2.5, 1.3×10^{5}
$e + OIII \rightarrow 2e + OIV$	1: 1.656×10^{-11}, 0.5, -636900
$e + OIV \rightarrow OIII$	2: 5.1×10^{-12}, 0.666, 0.0028 1.8×10^{5}, 6.0, 91000
$e + SII \rightarrow 2e + SIII$	1: 7.12×10^{-11}, 0.5, -271440
$e + SIII \rightarrow SII$	2: 1.8×10^{-12}, 0.686, 0.0049 1.2×10^{5}, 2.5, 88000
$HI + NII \rightarrow HII + NI$	1: 1.1×10^{-12}, 0, 0
$HII + NI \rightarrow HI + NII$	1: 4.95×10^{-12}, 0. -10440
$HI + OII \rightarrow HII + OI$	1: 2.0×10^{-9}, 0, 0
$HII + OI \rightarrow HI + OII$	1: 1.778×10^{-9}, 0, -220

[a]The interpolation formulae are of the form "1:" Arrhenius, or "2:" Aldrovandi & Péquignot (1973), see equations (3.49) and (3.50)

HII + OI → HI + OII and HI + OII → HII + OI (see Table 3.2). These processes have rates of the form $n_{HII}n_{OI}q(T)$ and $n_{HI}n_{OII}q'(T)$, respectively, with the rate coefficients $q(T)$ and $q'(T)$ also given as tabulations or by Arrhenius interpolations (see Table 3.2).

3.6.4 The photoionisation rates

The photoionisation rates are calculated as a function of the average intensity J_ν of the radiative field through the frequency integrals

$$\phi_{a,z} = \int_{\nu_{a,z}}^{\infty} \frac{4\pi J_\nu}{h\nu} \sigma_{a,z}(\nu)\, d\nu\,, \tag{3.51}$$

where ν is the frequency, $\nu_{a,z} = \chi_{a,z}/h$ is the frequency of the ionisation edge and $\sigma_{a,z}(\nu)$ is the photoionisation cross section. Here again, one can find tabulations of coefficients of power law interpolations for the $\sigma_{a,z}(\nu)$ (see, e. g., any of the versions of the book of Osterbrock 1989).

The problem of course is that one has to solve a system of radiative transfer equations of the form

$$\frac{dI_\nu}{dl} = j_\nu - \kappa_\nu I_\nu \tag{3.52}$$

for the specific intensity I_ν (j_ν and κ_ν being the emission and absorption coefficients, respectively). This is a system of equations, since one has to solve this for many propagation directions (l being the distance element along a given direction) and frequencies. Clearly, only rays passing through the position of the central star have to be considered if one does not include the diffuse ionising photon field (i. e., the far UV radiation produced by the nebular gas itself). Models including the diffuse field (with different approximations, as well as full solutions of the radiative transfer problem) have been present in the literature since the 1970's.

After integrating these radiative transfer equations, one can then carry out the appropriate angular average

$$J_\nu = \frac{1}{4\pi} \oint I_\nu d\Omega \tag{3.53}$$

in order to obtain the average intensity of the radiative field.

3.6.5 Coronal ionisation equilibrium

If the collisional ionisation rates dominate over the photoionisation rates, eq. (3.47) takes the form :

$$n_{a,z}c_{a,z} = n_{a,z+1}\alpha_{a,z+1}\,. \tag{3.54}$$

As can be seen, this system gives ionisation fractions

$$y_{a,z} = \frac{n_{a,z}}{n_a}, \text{ with } n_a = \sum_z n_{a,z}\,, \tag{3.55}$$

which are exclusively a function of T. This result holds if charge exchange reactions are included. The resulting ionisation fractions ${y^c}_{a,z}(T)$ are called the "coronal ionisation equilibrium" state.

Clearly, if we have an ionisation fraction $y_{a,z} > {y^c}_{a,z}(T)$, then $y_{a,z}$ will evolve to a lower value with time, and the reverse is true for $y_{a,z} < {y^c}_{a,z}(T)$.

As an example, let us consider the coronal ionisation equilibrium for H. Eq. (3.54) then gives

$$n_{HI}c(T) = n_{HII}\alpha(T)\,. \tag{3.56}$$

We can combine this equation with $n_H = n_{HI} + n_{HII}$ to obtain

$$y_{HII} = \frac{n_{HII}}{n_H} = \frac{1}{1+\alpha(T)/c(T)}\,, \tag{3.57}$$

where the Arrhenius interpolations for the coefficients are $\alpha(T) = 3.69 \times 10^{-10}T^{-0.79}$ and $c(T) = 5.83 \times 10^{-11}T^{0.5}\,e^{-157800/T}$ (see equation 3.49 and the first two lines of Table 3.2). The hydrogen ionisation fraction y_{HII} as a function of temperature T obtained from eq. (3.57) is shown in Fig. 3.10.

3.6.6 Photoionisation equilibrium

If the photoionisation rates dominate over the collisional ionisation rates, eq. (3.47) takes the form :

$$n_{a,z}\phi_{a,z} = n_e n_{a,z+1}\alpha_{a,z+1}\,. \tag{3.58}$$

This is the system of equations which describe the ionisation state of a stationary H II region. An example of a simplified solution for a pure H region is given in §1.5.

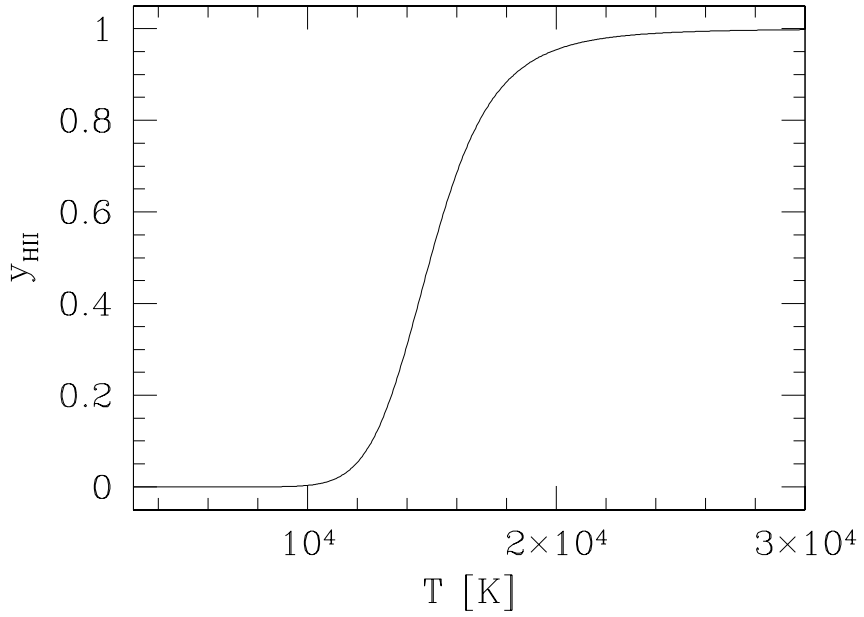

Figure 3.10: Coronal ionisation fraction of H as a function of temperature

3.7 The energy balance and the heating rate

In order to obtain the thermal structure of a photoionised region it is necessary to integrate a differential equation of the form

$$\frac{3}{2}\frac{d}{dt}(n+n_e)kT = \Gamma - L\,, \tag{3.59}$$

where n is the atom+ion number density, n_e the electron density, k Boltzmann's constant, and Γ and L the energy gain and loss (respectively) per unit volume and time of the gas. This equation is valid for a nebula in which the mass density is time-independent.

For a steady-state nebula, the time derivative in eq. (3.59) is equal to zero, and the energy balance equation is simply

$$\Gamma = L\,. \tag{3.60}$$

In photoionised regions, the energy gain is due to the process of photoionisation, which introduces "hot" electrons into the gas. The heating therefore is

a sum of terms due to the photoionisation of the different ions present in the gas, though in practice the dominant heating process is the photoionisation of HI, with smaller contributions due to the photoionisation of HeI and HeII.

The heating per unit time and volume due to the photoionisation of ion a, z is given by $\Gamma_{a,z} = n_{a,z}\psi_{a,z}$, with

$$\psi_{a,z} = \int_{\nu_{a,z}}^{\infty} \frac{4\pi J_\nu}{h\nu} h\left(\nu - \nu_{a,z}\right) \sigma_{a,z}(\nu)\, d\nu\,. \tag{3.61}$$

The integrals in the heating rate terms generally are done numerically. For the case in which the frequency dependence of the incident spectrum is given by a Planck function in the Wien limit at a temperature T_*, the integral in eq. (3.61) can be carried out analytically, if one also assumes that the $\sigma_{a,z}(\nu)$ is a slow enough function so that it can be taken out of the integral as $\sigma_{a,z}(\nu_{a,z})$. In this case, one obtains:

$$\psi_{a,z} = \phi_{a,z} kT_* \left(\frac{{x_0}^2 + 4x_0 + 6}{{x_0}^2 + 2x_0 + 2}\right)\,, \tag{3.62}$$

where $\phi_{a,z}$ is the photoionisation rate and $x_0 = h\nu_{a,z}/(kT_*)$.

3.8 The cooling function

3.8.1 Introduction

In this section, we describe in some detail how to include the more important contributions to the cooling due to different processes. Actually, the cooling is dominated by collisional excitation of emission lines. We describe the radiative recombination and free-free losses only because it is very simple to include them, though they do not make an important contribution to the cooling function (at least for a gas with solar abundances).

3.8.2 Recombination and free-free cooling

When an electron passes by an ion and recombines, the kinetic energy of the electron is lost from the thermal energy reservoir. Analogously, when an

electron loses kinetic energy in an inelastic collision (with the resulting emission of a photon), the thermal energy of the gas is reduced.

The free-free energy loss (per unit time and volume) due to the interaction of H ions and free electrons is given by :

$$L_{ff}(HII) = n_e n_{HII} \beta_{ff}(T)\,, \tag{3.63}$$

where the interpolation formula

$$\beta_{ff}(z,T) = 1.846 \times 10^{-27} z^2 T^{1/2}\,, \tag{3.64}$$

can be used (see the book of Osterbrock). In this interpolation function, one has to set a charge $z = 1$ for HII. One can use the same function (i. e., with $z = 1$) for calculating the free-free losses due to HeII ions. This is of course not correct because HeI is not a hydrogenic ion, introducing a substantial error, but this point is normally not further explored due to the fact that the H free-free cooling dominates by an order of magnitude over the He cooling. Equation (3.64) with $z = 2$ of course gives the correct cooling function for HeIII ions.

The radiative losses due to recombination of HII are given by :

$$L_{rec}(HII) = n_e n_{HII} \beta_{rec}(T)\,, \tag{3.65}$$

where the interpolation formula

$$\beta_{rec}(t) = 1.133 \times 10^{-24} t^{-1/2} \left(-0.0713 + 0.5 \ln t + 0.640 t^{-1/3}\right) \tag{3.66}$$

with $t = 157890/T$ (see Seaton 1959). The contribution of the recombination of He ions can be computed with the scaling

$$\beta_{rec}(z,T) = z \beta_{rec}(1, T/z^2)\,, \tag{3.67}$$

with $z = 1$ for HeII and $z = 2$ for HeIII.

3.8.3 Collisional ionisation

The energy loss due to collisional ionisation of the ion a, z can be written as

$$L^{ion}{}_{a,z} = n_e n_{a,z} c_{a,z}(T)\, \chi_{a,z}\,, \tag{3.68}$$

where $c_{a,z}(T)$ is the collisional ionisation coefficient and $\chi_{a,z}$ the ionisation potential of the ion a, z.

The terms that dominate the collisional ionisation cooling are the ionisation of HI, HeI and HeII. These terms dominate the cooling function for a neutral gas that is suddenly shocked to a temperature above a few times 10^4 K.

3.8.4 Collisionally excited lines

For each atom or ion that contributes substantially to the cooling function, one has to solve a system of equations giving the populations of the excited levels n_l ($l = 1, 2, ..., N$ numbering all of the relevant levels in order of increasing energy) of the ion a, z. Of course, we have the relation

$$n_{a,z} = \sum_{l=1}^{N} n_l \, . \tag{3.69}$$

Once we have computed the n_l populations, we can compute the energy loss due to the collisional excitation of all of the relevant levels of the ion a, z as

$$L_{a,z}^{col} = \sum_{l=2}^{N} n_l \sum_{m<l} A_{l,m} h\nu_{l,m} \, , \tag{3.70}$$

where $A_{l,m}$ is the Einstein A coefficient for the spontaneous transition $l \rightarrow m$ and $h\nu_{l,m}$ is the energy associated with this transition.

The non-trivial problem of finding the populations n_l of the excited levels of course still remains. Because the relaxation time for the excitation/de-excitation of the levels is generally much shorter than the cooling and/or dynamical timescales of the flow, the calculation of the n_l is usually done under a statistical equilibrium assumption. The equilibrium condition results in the set of equations :

$$\sum_{m>l} n_m A_{m,l} + n_e \sum_{m \neq l} n_m q_{m,l}(T) = n_l \left[\sum_{m<l} A_{l,m} + n_e \sum_{m \neq l} q_{l,m}(T) \right] \, , \tag{3.71}$$

where we have introduced the $q_{m,l}(T)$ which are the radiative excitation ($m < l$) or de-excitation ($m > l$) coefficients. For $m > l$, these coefficients are given

by the expression

$$q_{m,l}(T) = \frac{8.629 \times 10^{-6}}{T^{1/2}} \frac{\Omega_{ml}(T)}{g_m}\,, \tag{3.72}$$

where g_m is the statistical weight of the level at which the transition begins. The collisional excitation coefficients (i.e., $l \to m$ with $m > l$) are given by the relation

$$q_{l,m}(T) = \frac{g_m}{g_l} e^{-h\nu_{m,l}/kT} q_{m,l}(T)\,. \tag{3.73}$$

The function $\Omega_{ml}(T)$ has a value of order 1, and is only slowly dependent on T. In many calculations, these "collision strengths" are considered to be constant, and taken from tabulations such as the classical one of Mendoza (1983). However, in our modern electronic world there is the database of the Arcetri/Cambridge/NRL "CHIANTI" atomic data collaboration [1] which has tabulations of the collision strengths and the Einstein A coefficients of most of the transitions we have ever known.

We now proceed as follows. We assume that the A and q coefficients are known, as well as the temperature T (obtained, e. g., from a dynamical simulation) the electron density n_e and the ionic number density $n_{a,z}$ (both obtained from the relevant statistical equilibrium or from a solution of the non-equilibrium ionisation rate equations). We can then invert the system of linear eqs. (3.69) and (3.71) in order to find the populations n_l ($l = 1 \to N$) of the excited levels of the ion a, z.

Let us show how the equations look for a 3-level atom ($N = 3$). Eq. (3.69) takes the form

$$n_1 + n_2 + n_3 = n_{a,z}\,. \tag{3.74}$$

Now, for $l = 1$, from eq. (3.71) we obtain

$$n_1\left[-n_e(q_{12} + q_{13})\right] + n_2(A_{21} + n_e q_{21}) + n_3(A_{31} + n_e q_{31}) = 0\,, \tag{3.75}$$

and for $l = 2$, we obtain :

$$n_1 n_e q_{12} + n_2\left[-A_{21} - n_e(q_{23} + q_{21})\right] + n_3(A_{32} + n_e q_{32}) = 0\,. \tag{3.76}$$

For $l = 3$, we obtain an equation that is a linear combination of eqs. (3.75-3.76).

Now, the system of 3 linear equations (3.74-3.76) can be inverted in order to find n_1, n_2 and n_3 as a function of $n_{a,z}$, n_e and T.

[1] http://www.arcetri.astro.it/science/chianti/database/

3.8.5 The 2-level atom

Let us now consider a 2-level atom ($N = 2$). Eq. (3.69) takes the form

$$n_{a,z} = n_1 + n_2 \,, \tag{3.77}$$

and eq. (3.71) takes the form

$$n_1 n_e q_{12} = n_2 (n_e q_{21} + A_{21}) \,. \tag{3.78}$$

These two equations can be combined with eq. (3.73) to obtain :

$$n_2 = \frac{n_{a,z}}{(g_1/g_2)e^{E_{21}/kT} + 1 + n_c/n_e} \,, \tag{3.79}$$

where the critical density is defined as $n_c \equiv A_{21}/q_{12}$. Then, for $n_e \ll n_c$ (the "low density regime"), we have

$$n_2 = \frac{n_{a,z} n_e q_{12}}{A_{21}} \,, \tag{3.80}$$

and for $n_e \gg n_c$ (the "high density regime"), we have

$$n_2 = \frac{n_{a,z} g_2 e^{-E_{21}/kT}}{g_1 + g_2 e^{-E_{21}/kT}} \,, \tag{3.81}$$

which is the Boltzmann distribution (local thermodynamic equilibrium or LTE) population of level n_2.

The energy loss associated with the transition between levels 2 and 1 is :

$$L_{21} = n_2 A_{21} h\nu_{21} \,, \tag{3.82}$$

which for the low density regime then takes the form

$$L_{21} = n_{a,z} n_e q_{12} h\nu_{21} \,, \tag{3.83}$$

and for the high density regime becomes

$$L_{21} = n_2(LTE) A_{21} h\nu_{21} \,, \tag{3.84}$$

These equations illustrate the well known fact that the collisionally excited line cooling function depends quadratically on the density for the "low density regime" and linearly for the "high density regime".

3.9 The temperature of an HII region

In order to obtain an estimate of the temperature of a photoionised region, we consider the balance between the heating due to H photoionisation :

$$\Gamma \approx n_{HI}\phi_{HI}kT_* \,, \tag{3.85}$$

where T_* is the black-body temperature of the star (see equations 3.61-3.62), and the cooling due to the collisional excitation of a single line of OII :

$$L = n_e n_{OII} q_{12}(T) h\nu_{12} \,, \tag{3.86}$$

in the low density regime (see equation 3.83). This is of course an underestimate of the real cooling function, which has contributions from many collisionally excited lines.

We first use the H photoionisation equilibrium condition (see equation 3.32)

$$n_{HI}\phi_H = n_e n_{HII}\alpha_H(T) \tag{3.87}$$

and consider that inside the HII region we have $n_e \approx n_{HII} \approx n_H$ to obtain an estimate of the neutral H density :

$$n_{HI} \approx \frac{n_H^2 \alpha_H(T)}{\phi_H} \,. \tag{3.88}$$

Substituting this estimate of n_{HI} in the heating term (equation 3.85), we then obtain :

$$\Gamma \approx n_H^2 \alpha_H(T) kT_* \,, \tag{3.89}$$

where from Table 3.2 we have $\alpha_H(T) = 3.69 \times 10^{-10} T^{-0.79}$ (in c.g.s.).

For the cooling function, we assume that inside the HII region $n_{OII} \approx n_O \approx 10^{-4} n_H$, and that the transition has an energy $h\nu_{21} \sim 1$ eV (so that $h\nu_{12}/k \approx 10^4$ K). Using the temperature dependence of the collisional excitation coefficient (see equations 3.72-3.73) we then obtain

$$L \approx 10^{-4} n_H^2 \frac{8.6 \times 10^{-6} \Omega_{21}}{T^{1/2} g_1} e^{-10^4/T} \,, \tag{3.90}$$

where we can set $\Omega_{21} \sim g_1 \sim 1$.

Finally, using equations (3.89-3.90), the energy gain/loss balance condition (equation 3.60) $\Gamma = L$ gives :

$$T = \frac{10^4 \mathrm{K}}{0.29 \ln T - 0.542}\,, \tag{3.91}$$

for a $T_* = 4 \times 10^4$K stellar temperature.

Through a few iterations, it can be shown that the solution to this transcendental equation is $T \approx 5200$ K. More detailed solutions to the energy balance equation (including cooling through many lines, with the correct atomic parameters) typically give temperatures in the $5000 \rightarrow 10000$ K range.

Two interesting points should be noted:

- the temperature resulting from the energy balance is independent of the density of the gas. This result is preserved if one includes a more detailed cooling function, provided that the collisionally excited lines (which dominate the radiative cooling) are in the low density regime,
- very similar temperatures for the nebula are obtained no matter what is the value of the stellar temperature T_*. This is a result of the fact that the collisional excitation coefficients have a very strong temperature dependence at temperatures $T \sim h\nu_{ij}/k$, and that the fine structure lines of many ions have energies $\sim$ 1eV (corresponding to $\sim 10^4$ K). This high temperature dependence of the cooling function fixes the nebular temperature at $\sim 10^4$ K for a wide range of possible values for the energy gain term.

Chapter 4

The emitted spectrum

4.1 Emission lines

In the previous chapter, we have discussed how to calculate the populations of the excited levels of an atom or ion, with the objective of the calculation of the cooling due to collisionally excited lines. We now present the general statistical equilibrium equations for the populations of the excited levels of atoms/ions in the ISM :

$$\sum_{m>l} n_m A_{m,l} + n_e \sum_{m\neq l} n_m q_{m,l}(T) + n_e\, n_{a,z+1} \alpha_{z+1,l}(T) =$$

$$n_l \left[\sum_{m<l} A_{l,m} + n_e \sum_{m\neq l} q_{l,m}(T) \right] , \tag{4.1}$$

which coincides with eq. (3.71) with the exception of the second term on the left hand side of the equation, which represents the recombinations of the higher ionisation state $a, z+1$ to the excited level l of the ion a, z. The radiative+dielectronic recombination coefficient for this process is $\alpha_{z+1,l}(T)$.

Missing from eq. (3.71) are:

- collisional ionisation from the excited levels (a process that is important in higher density gas, e.g., in stellar atmospheres),

- stimulated radiative transitions (important in masers, but generally not elsewhere in the ISM).

This system of equations gives the populations of the excited levels n_l (l = 1, 2, ..., N numbering all of the relevant levels in order of increasing energy) of the ion a, z. These equations have to be supplemented with the relation

$$n_{a,z} = \sum_{l=1}^{N} n_l \, . \tag{4.2}$$

4.2 Recombination lines

In HII regions, the populations of the excited levels of HI, HeI and HeII are determined mostly by the processes of recombination (of HII, HeII and HeIII, respectively) to excited levels and spontaneous, radiative transitions to lower levels. These processes are represented by the first and third terms on the left and the first term on the right of eq. (4.1). The lines of H and He in HII regions are therefore called "recombination lines".

The lines of H (resulting from transitions from energy level N to N') are named according to the end state (N') and to the jump in energy quantum number ($\Delta N = N - N'$). For N' = 1, 2, 3, ... we have:

1. $N' = 1$: Lyman series lines,
2. $N' = 2$: Balmer series lines,
3. $N' = 3$: Paschen series lines,
4. $N' = 4$: Brackett series lines,
5. $N' = 5$: Pfund series lines,
6. $N' = 6$: Humphreys series lines.

For ΔN = 1, 2, 3, ..., the lines are denominated α, β, γ, ..., respectively.

The Lyman series lines are denoted as Lyα ($2 \rightarrow 1$ transition), Lyβ ($3 \rightarrow 1$ transition), Lyγ, ... The Balmer series are denoted as Hα ($3 \rightarrow 2$ transition),

Hβ ($4 \rightarrow 2$ transition), Hγ, ... (these are the stronger H lines observed at optical wavelengths). Prefixes "Pa", "Br" and "Pf" are used for the Paschen, Brackett and Pfund series lines, respectively.

4.2.1 The recombination cascade

Let us consider the excited levels of H. These levels are specified with two quantum numbers: N, L, with $N \geq 1$ (the energy quantum number) and $1 \leq L \leq N$ (the angular momentum quantum number). The spontaneous radiative transition rates are given by the Einstein coefficients $A_{NL,N'L'}$ which have non-zero values (for Hamiltonians in the dipole approximation) only for $L' = L \pm 1$.

The energies of the excited levels of H only depend on the energy quantum number N, and are given by

$$E_N = -\frac{\chi_H}{N^2}\,, \tag{4.3}$$

where $\chi_H = 13.6$ eV is the ionisation potential from the ground state of H.

The system of equations of statistical equilibrium for the populations n_{NL} of the excited levels of HI (see eq. 4.1) then is:

$$n_e n_{HII} \alpha_{NL}(T) + \sum_{N'=N+1}^{\infty} \sum_{L'=L\pm1} n_{N'L'} A_{N'L',NL} = n_{NL} \sum_{N'=1}^{N-1} \sum_{L'=L\pm1} A_{NL,N'L'}\,. \tag{4.4}$$

If the $A_{NL,N'L'}$ and $\alpha_{NL}(T)$ coefficients are known, this system of equations can be inverted to find the level populations n_{NL}.

The most simple way of constructing the inversion is as follows. One first defines the "branching ratio" :

$$P_{NL,N'L'} = \frac{A_{NL,N'L'}}{\sum_{N''=1}^{N-1} \sum_{L''=L\pm1} A_{NL,N''L''}}\,, \tag{4.5}$$

which gives the probability that a radiative transition out of level NL is a direct transition to $N'L'$. Clearly, $P_{NL,N'L'} \neq 0$ only if $L' = L \pm 1$.

We now calculate the "cascade matrix" $C_{NL,N'L'}$ as the probability that a transition down from NL reaches $N'L'$ either through a direct transition or

via one or more transitions through intermediate levels. For $N' = N - 1$ it is clear that we have:

$$C_{NL,N-1\,L'} = P_{NL,N-1\,L'} \,. \tag{4.6}$$

For $N' = N - 2$:

$$C_{NL,N-2\,L'} = P_{NL,N-2\,L'} + \sum_{L''=L'\pm1} C_{NL,N-1\,L''} P_{N-1\,L'',N-2\,L'} \,. \tag{4.7}$$

If we now define

$$C_{NL,NL'} = \delta_{LL'} \,, \tag{4.8}$$

we can write the general expression (for arbitrary $N' < N$) as:

$$C_{NL,N'L'} = \sum_{N''=N'+1}^{N} \sum_{L''=L'\pm1} C_{NL,N''L''} P_{N''L'',N'L'} \,. \tag{4.9}$$

Once the cascade matrix has been computed, the solutions to the equilibrium equations (4.4) can be obtained from the relation

$$n_e n_{HII} \sum_{N'=N}^{\infty} \sum_{L'=0}^{N'-1} \alpha_{N'L'}(T)\, C_{N'L',NL} = n_{NL} \sum_{N''=1}^{N-1} \sum_{L''=L\pm1} A_{NL,N''L''} \,. \tag{4.10}$$

This system of equations gives the level populations n_{NL} as a function of n_e, n_{HII} and the temperature T. Once the level populations have been computed, we can compute the emission coefficients for the $N \to N'$ transitions as :

$$j_{NN'} = \frac{h\nu_{NN'}}{4\pi} \sum_{L=0}^{N-1} \sum_{L'=L\pm1} n_{NL} A_{NL,N'L'} \equiv n_e n_{HII} \alpha^{eff}_{NN'}(T) \frac{h\nu_{NN'}}{4\pi} \,. \tag{4.11}$$

The second equality is the definition of the "effective recombination coefficient" (for the $N \to N'$ transition).

The recombination cascade is usually calculated under two possible assumptions :

- **case A:** that all of the lines are optically thin,
- **case B:** that the Lyman lines (i. e., the transitions to the 1s level) are optically thick.

The recombination cascade as derived in this section corresponds to "case A". For "case B", the same equations apply if one sets to zero the Einstein A coefficients for all Lyman lines (i. e., $A_{NL,1s} = 0$). It is also possible (in the context of a numerical model) to solve the radiative transfer in the Lyman lines, obtaining a gradual transition between cases A and B as the successive Lyman lines become optically thick.

4.2.2 Including collisions

For higher values of the energy quantum number N, collisions between protons and HI atoms producing transitions with $\Delta L = 1$ and $\Delta N = 0$ become progressively more important. Also, for temperatures > 12000 K, collisions with electrons become important for producing transitions with $\Delta N \neq 0$. Including these processes, the statistical equilibrium condition for level NL becomes:

$$n_e n_{HII} \alpha_{NL}(T) + \sum_{N'=N+1}^{\infty} \sum_{L'=L\pm1} n_{N'L'} A_{N'L',NL} +$$

$$\sum_{L'=L\pm1} n_{HII} n_{NL'} q_{NL',NL}(T) + \sum_{N'\neq N} \sum_{L'=L\pm1} n_e n_{N'L'} q_{N'L',NL}(T) =$$

$$n_{NL} \left[\sum_{N'=1}^{N-1} \sum_{L'=L\pm1} A_{NL,N'L'} + \sum_{L'=L\pm1} n_{HII} q_{NL,NL'}(T) + \sum_{N'\neq N} \sum_{L'=L\pm1} n_e q_{NL,N'L'}(T) \right] . \tag{4.12}$$

The collisional rates can be calculated as a function of the collision strengths as:

$$q_{NL,N'L'}(T) = \frac{8.629 \times 10^{-6}}{T^{1/2}} \frac{\Omega_{NL,N'L'}(T)}{2(2L+1)} , \tag{4.13}$$

which can be obtained from eq. (3.72) by setting $g_{NL} = 2(2L + 1)$.

The Einstein A coefficients, and interpolations for the recombination coefficients and the collision strengths for the $N = 1 \rightarrow 5$ levels of H are given in Tables 4.1-4.5. The recombination coefficient fits were carried out with the data in the rrc98##_h1.dat file of the Open-ADAS database. The electron collision strengths are fits to data in the copha#h_hal96h.dat and hlike_aek89h.dat files

Table 4.1: Energies and α's for the $N = 1 \rightarrow 5$ levels of H

level	E_N [cm^{-1}]	$\log_{10}(\alpha) = b_0 + b_1 t + b_2 t^2 + b_3 t^3\,;\;\; t = \log_{10}(T)$
1 : 1s	0	-9.9506 -1.2751 0.2385 -0.0244
2 : 2s	82259	-10.938 -1.1858 0.2235 -0.0238
3 : 2p	82259	-12.712 0.3821 -0.1176 -0.0032
4 : 3s	97492	-11.622 -1.0353 0.1896 -0.0215
5 : 3p	97492	-13.256 0.4629 -0.1347 -0.0020
6 : 3d	97492	-14.931 1.8421 -0.4766 0.0223
7 : 4s	102824	-12.087 -0.9310 0.1639 -0.0197
8 : 4p	102824	-13.651 0.5184 -0.1481 -0.0011
9 : 4d	102824	-15.173 1.8650 -0.4814 0.0226
10 : 4f	102824	-15.659 2.3114 -0.6300 0.0348
11 : 5s	105292	-12.442 -0.8533 0.1442 -0.0183
12 : 5p	105292	-13.939 0.5469 -0.1560 -0.0005
13 : 5d	105292	-15.398 1.8720 -0.4835 0.0227
14 : 5f	105292	-15.724 2.3138 -0.6301 0.0348
15 : 5g	105292	-15.455 2.1117 -0.6324 0.0369

of this database. The proton collision strengths are fits to the results of Seaton (1955) for the 2s-2p transition and Pengelly & Seaton (1964) and Brocklehurst (1971) for all of the other transitions.

Actually, though He II/H I collisions are not important for the angular momentum redistribution in H I, the He III/H I collisions are indeed important. Therefore, if He III has a substantial ionisation fraction, it is necessary to include terms $\propto n_{HeIII} n_{nL}$ in eq. (4.12). The rate coefficient can be calculated from eq. (4.13) using a value for the collision strength of $\Omega_{HeIII} = Z^2 \sqrt{C_{He}} \Omega_{HII}(T/Z^2 C_{He})$ where Ω_{HII} is the strength of the proton/HI collisions (see Table 4.5), $Z = 2$ is the charge of the He III ion, and

$$C_{He} \equiv \frac{\mu_{(He-p)}}{\mu_{(p-p)}} = \frac{8}{5}\,, \tag{4.14}$$

where $\mu_{(He-p)}$ is the reduced mass of the He/H system, and $\mu_{(p-p)}$ is the reduced mass of the H/H system.

Table 4.2: A_{ij} and Ω_{ij} for the $N = 1 \rightarrow 5$ levels of H

transition[a,b]		A_{ij} [s^{-1}]	$\Omega_{ij}(T) = b_0 + b_1 T + b_2 T^2$
2s→1s[a]	2 1	8.23	0.230701989 1.98505873E-06 -1.17145274E-11
2p→1s[a]	3 1	627000000.	0.370130298 9.41438027E-06 1.51916572E-11
3s→1s[a]	4 1	...	0.0555455253 1.09205141E-06 -7.22330208E-12
3p→1s[a]	5 1	167000000.	0.098599152 2.85713646E-06 -9.07527461E-12
3d→1s[a]	6 1	...	0.0471315582 1.49942413E-06 -6.83592715E-12
4s→1s[a]	7 1	...	0.0235801449 9.82577622E-07 -6.29846528E-12
4p→1s[a]	8 1	68200000.	0.0459912361 1.91578268E-06 -6.68320426E-12
4d→1s[a]	9 1	...	0.0247052783 4.82612921E-07 -1.93361593E-12
4f→1s[a]	10 1	...	0.0090413543 2.0730546E-08 -2.3834257E-13
5s→1s[a]	11 1	...	0.0118558411 5.12325143E-07 -3.26312452E-12
5p→1s[a]	12 1	34400000.	0.023435627 9.81865036E-07 -3.5210708E-12
5d→1s[a]	13 1	...	0.0127150878 2.43235821E-07 -9.73250094E-13
5f→1s[a]	14 1	...	0.00470449272 1.10018321E-08 -1.29156399E-13
5g→1s[a]	15 1	...	0.00062369044 -7.61068457E-09 3.66057556E-14
2p→2s[b]	3 2	...	378.724659 -0.000613531164 1.75879255E-09
3s→2s[a]	4 2	...	1.17686218 3.96001554E-05 -7.52731563E-11
3p→2s[a]	5 2	22500000.	1.81152248 9.2099616E-05 1.5241836E-10
3d→2s[a]	6 2	...	1.10043841 0.000191744768 -5.29052966E-10
4s→2s[a]	7 2	...	0.341652766 1.58109749E-05 -4.06526299E-11
4p→2s[a]	8 2	9670000.	0.647024189 5.23380315E-05 -1.70490774E-10
4d→2s[a]	9 2	...	0.552293565 5.52457995E-05 -2.56306745E-10
4f→2s[a]	10 2	...	0.399588795 4.43059453E-05 -2.09877084E-10
5s→2s[a]	11 2	...	0.520122966 8.2949122E-06 -3.48249174E-11
5p→2s[a]	12 2	4950000.	0.867017494 4.03942982E-05 -2.03482662E-10
5d→2s[a]	13 2	...	0.7094405 3.14156261E-05 -2.0075731E-10
5f→2s[a]	14 2	...	0.585537946 2.42882913E-05 -1.42870771E-10
5g→2s[a]	15 2	...	0.235978314 3.61284928E-06 -2.77494818E-11
3s→2p[a]	4 3	6310000.	1.94752427 1.92358023E-05 -7.79667781E-11
3p→2p[a]	5 3	...	6.51940845 0.000167401531 -6.12473933E-10
3d→2p[a]	6 3	64700000.	9.38290597 0.000714844201 5.37590056E-11
4s→2p[a]	7 3	2580000.	0.681844753 1.63355835E-05 -1.05496624E-10
4p→2p[a]	8 3	...	1.99947241 9.24779953E-05 -4.1253316E-10
4d→2p[a]	9 3	20600000.	2.58156827 0.000352482476 -1.28581419E-09

[a]coll. strengths from the copha#h_hal96h.dat file, data produced by H. Anderson

[b]coll. strengths from the hlike_aek89h.dat file, with apparently as yet unpublished calculations by Berrington et al. (1988)

Table 4.3: A_{ij} and Ω_{ij} for the $N = 1 \rightarrow 5$ levels of H, continued

transition		A_{ij} [s^{-1}]	$\Omega_{ij}(T) = b_0 + b_1 T + b_2 T^2$
4f→2p[a]	10 3	...	2.39511694 0.000125033557 -5.78553883E-10
5s→2p[a]	11 3	1290000.	0.776657809 1.74219443E-05 -1.32396161E-10
5p→2p[a]	12 3	...	2.43249038 6.02215821E-05 -3.78765622E-10
5d→2p[a]	13 3	9430000.	3.62224098 0.000196222456 -9.9819329E-10
5f→2p[a]	14 3	...	3.26614961 6.91791533E-05 -4.25243164E-10
5g→2p[a]	15 3	...	0.99771057 3.75655605E-06 -4.17823612E-11
3p→3s[b]	5 4	...	1450.93085 -0.00325160827 1.40768513E-08
3d→3s[b]	6 4	...	159.126917 -0.000840487719 3.48162807E-09
4s→3s[a]	7 4	...	1.08111582 0.000380437576 -1.15295628E-09
4p→3s[a]	8 4	3070000.	2.54886314 0.00040309013 5.56322488E-10
4d→3s[a]	9 4	...	3.14373004 0.000745642053 -2.42690635E-09
4f→3s[a]	10 4	...	3.7462125 0.000781879325 -3.57428797E-09
5s→3s[a]	11 4	...	1.54637257 0.000149080149 -6.63657887E-10
5p→3s[a]	12 4	1640000.	4.08813628 0.000169921842 -5.02562755E-10
5d→3s[a]	13 4	...	5.01383832 0.000247476134 -1.33289923E-09
5f→3s[a]	14 4	...	4.10691834 0.000127133679 -8.58848203E-10
5g→3s[a]	15 4	...	4.88714716 0.000244329779 -1.47617099E-09
3d→3p[b]	6 5	...	2146.0592 -0.00593632728 2.11624071E-08
4s→3p[a]	7 5	1840000.	3.40339559 0.000203061141 -6.75501874E-10
4p→3p[a]	8 5	...	8.60902539 0.00151186995 -4.7539148E-09
4d→3p[a]	9 5	7040000.	8.27640654 0.0025566506 -1.11232159E-09
4f→3p[a]	10 5	...	11.9669457 0.00323828319 -1.23422432E-08
5s→3p[a]	11 5	905000.	3.74173931 8.69809273E-05 -5.06385819E-10
5p→3p[a]	12 5	...	13.2467032 0.000539548421 -2.6260229E-09
5d→3p[a]	13 5	3390000.	15.2917815 0.00109804005 -4.70346691E-09
5f→3p[a]	14 5	...	16.2298902 0.000576218201 -3.63526886E-09
5g→3p[a]	15 5	...	18.1883828 0.000832453286 -4.85370914E-09
4s→3d[a]	7 6	...	4.21900483 4.84256639E-05 -2.15917333E-10
4p→3d[a]	8 6	348000.	13.4777083 0.000441890063 -2.29071345E-09
4d→3d[a]	9 6	...	24.9062683 0.00272229022 -1.01404508E-08
4f→3d[a]	10 6	13800000.	9.82447156 0.0119510675 -3.02823382E-08
5s→3d[a]	11 6	...	3.97162814 3.51386987E-05 -3.27759745E-10
5p→3d[a]	12 6	150000.	16.1334958 0.000110362663 -9.71870659E-10
5d→3d[a]	13 6	...	28.3632617 0.000957519873 -5.33191712E-09
5f→3d[a]	14 6	4540000.	49.7607587 0.00325075814 -1.53230468E-08
5g→3d[a]	15 6	...	38.330885 0.0015114171 -7.86878077E-09

Table 4.4: A_{ij} and Ω_{ij} for the $N = 1 \rightarrow 5$ levels of H, continued

transition		A_{ij} [s^{-1}]	$\Omega_{ij}(T) = b_0 + b_1 T + b_2 T^2$
4p→4s[b]	8 7	...	2964.29958 -0.00909288594 4.12297852E-08
4d→4s[b]	9 7	...	619.32623 -0.00430283349 2.8734997E-08
4f→4s[b]	10 7	...	124.174361 -0.00123347544 8.48440058E-09
5s→4s[a]	11 7	...	1.53806207 0.00173503526 -6.68625477E-09
5p→4s[a]	12 7	737000.	6.98282747 0.00152554702 -4.1843167E-09
5d→4s[a]	13 7	...	8.73782844 0.00225377148 -8.18431429E-09
5f→4s[a]	14 7	...	25.3224504 0.00222572566 -1.23041554E-08
5g→4s[a]	15 7	...	32.4265974 0.00129765509 -8.23655146E-09
4d→4p[b]	9 8	...	5549.92453 -0.0223901556 1.16294866E-07
4f→4p[b]	10 8	...	813.908792 -0.00744222541 4.90894342E-08
5s→4p[a]	11 8	645000.	13.3059416 0.00114087942 -6.17355099E-09
5p→4p[a]	12 8	...	22.7873231 0.00728109837 -2.4723519E-08
5d→4p[a]	13 8	1490000.	18.8738115 0.00699294439 -1.36005205E-08
5f→4p[a]	14 8	...	62.7008007 0.00875749509 -4.05388707E-08
5g→4p[a]	15 8	...	106.846064 0.00572769064 -3.40406121E-08
4f→4d[b]	10 9	...	6073.98362 -0.0339745489 1.90841831E-07
5s→4d[a]	11 9	...	15.6264397 0.000478850892 -2.67628835E-09
5p→4d[a]	12 9	188000.	53.7360076 0.00270059254 -1.56288932E-08
5d→4d[a]	13 9	...	84.0809099 0.0136172636 -5.41143791E-08
5f→4d[a]	14 9	2580000.	19.6994986 0.0223537455 -5.43237367E-08
5g→4d[a]	15 9	...	203.182691 0.0186641991 -9.35579156E-08
5s→4f[a]	11 10	...	12.3197499 2.74000635E-05 -3.51956415E-10
5p→4f[a]	12 10	...	47.7768773 0.000422602729 -3.52908665E-09
5d→4f[a]	13 10	50500.	105.135303 0.00307257987 -2.04380745E-08
5g→4f[a]	14 10	...	214.905676 0.018876845 -8.97469485E-08
5g→4f[a]	15 10	4250000.	144.086649 0.0760463582 -2.17769691E-07
5p→5s[b]	12 11	...	3924.60946 -0.00580398959 1.26210156E-08
5d→5s[b]	13 11	...	1442.42044 -0.00109774214 -3.32855828E-09
5f→5s[b]	14 11	...	447.109793 -0.00126487521 7.13987753E-09
5g→5s[b]	15 11	...	177.821648 -0.00169342267 1.00377598E-08
5d→5p[b]	13 12	...	8334.24411 -0.0118233038 2.21988618E-08
5f→5p[b]	14 12	...	2535.51791 -0.00757608021 3.9359465E-08
5g→5p[b]	15 12	...	652.74903 -0.00368088927 1.87021691E-08
5f→5d[b]	14 13	...	11531.0448 -0.023057997 8.77424046E-08
5g→5d[b]	15 13	...	2608.36252 -0.0157262948 8.37538465E-08
5g→5f[b]	15 14	...	12351.5748 -0.0429626285 1.81619962E-07

Table 4.5: Ω_{ij} for the proton collision, $\Delta N = 0$, $\Delta l = \pm 1$ transitions of H

transition		$\Omega_{ij}(T) = b_0 + b_1 \log_{10}(T)$
2p→2s	3 2	-29010.0 9999.0
3p→3s	5 4	-19765.4 20134.4
3d→3s	6 4	-66225.3 45302.3
4p→4s	8 7	-41439.6 67114.5
4d→4p	9 8	-294061.2 193289.8
4f→4d	10 9	80263.0 201343.6
5p→5s	12 11	-145593.4 167786.3
5d→5p	13 12	-650479.8 528526.8
5f→5d	14 13	-18963.3 719084.1
5g→5f	15 14	-247476.4 587252.1

4.3 Collisionally excited lines

4.3.1 General formalism

The lines of most of the atoms or ions observed in the ISM (except for the lines of H and He) are populated by collisional excitations up from the ground electronic state. This is because multi-electron atoms/ions do not have the large energy gap between the ground state and the first excited state characteristic of HI and HeI/II. Because of this, collisions with free electrons in a $\sim 10^4$ K ($\sim$ 1 eV) gas can easily excite the first few levels in these atoms/ions. The contribution from the recombination cascade then becomes only a small perturbation on the level populations, which are mainly determined only by (upwards and downwards) collisional transitions and by (downwards) radiative transitions. The transitions among the low lying levels of multi-electron atoms/ions are normally "magnetic dipole" or "electric quadrupole" transitions (having non-zero A coefficients only when higher order perturbation Hamiltonians are considered), and are usually called "forbidden lines" (and are denoted as, e. g., [O II] lines, in between square brackets). Some of the collisionally excited lines in multi-electron atoms/ions (particularly, the UV lines) are "permitted" lines (i. e., "electric dipole" transitions).

For these atoms/ions, the statistical equilibrium equation (4.1) reduces to the more simple form given in the previous chapter (see eq. 3.71), which we repeat

here:

$$\sum_{m>l} n_m A_{m,l} + n_e \sum_{m\neq l} n_m q_{m,l}(T) = n_l \left[\sum_{m<l} A_{l,m} + n_e \sum_{m\neq l} q_{l,m}(T) \right] , \qquad (4.15)$$

where $q_{m,l}(T)$ are the radiative excitation ($m < l$) or de-excitation ($m > l$) coefficients. For $m > l$, these coefficients are given by the expression

$$q_{m,l}(T) = \frac{8.629 \times 10^{-6}}{T^{1/2}} \frac{\Omega_{ml}(T)}{g_m} , \qquad (4.16)$$

where g_m is the statistical weight of the level at which the transition begins. The collisional excitation coefficients (i. e., $l \rightarrow m$ with $m > l$) are given by the relation

$$q_{l,m}(T) = \frac{g_m}{g_l} e^{-h\nu_{m,l}/kT} q_{m,l}(T) . \qquad (4.17)$$

In eq. (4.15), the indexes m and l refer to a numbering system in which increasing values correspond to higher energy levels. The low lying levels in multi-electron atoms or ions generally correspond to the ground state configuration of the energy quantum number. Therefore, the energy quantum number is not given, and the levels are denoted by their angular momentum configuration in the form

$$^{2s+1}L_j \qquad (4.18)$$

where s is the spin, L the orbital angular momentum (denoted S, P, D, ... for $L = 0$, 1, 2, ..., respectively) and j the total angular momentum quantum numbers. Two things should be noted:

- the statistical weight of the level is $g = 2j + 1$,
- the levels with the same s and L but different j form groups of $2s + 1$ levels with closely lying energies. These are called "singlet", "doublet" or "triplet" levels for $2s + 1 = 1$, 2 and 3, respectively.

Examples of the possible energy configurations are given in the "Grotrian diagrams" shown in Figures 4.1-4.5. A good source for obtaining the A coefficients and the collision strengths Ω is the material in the book of Pradhan & Nahar [20].

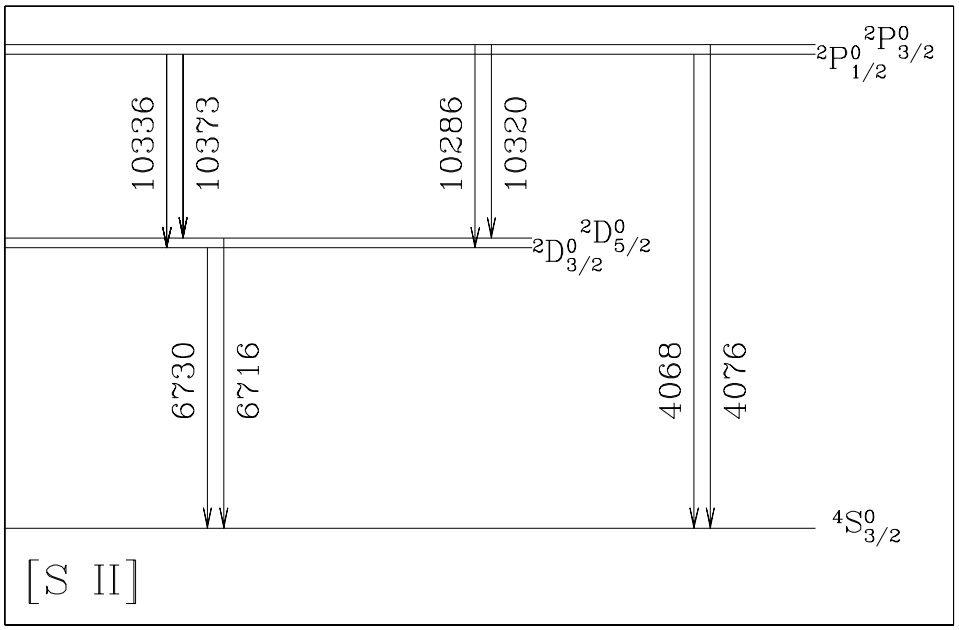

Figure 4.1: Energy level diagram showing the optical and IR forbidden transitions of S II. The wavelengths of the transitions are given in Å. For historical reasons, the $^2D - ^4S$ transitions are called the "nebular", the $^2P - ^4S$ the "auroral" and the $^2P - ^2D$ the "transauroral" lines.

In using the parameters from such tabulations, one has to sometimes divide collision strengths given for a term with several levels into collision strengths for the individual levels. For example, if a collision strength $\omega(SLJ, S'L')$ is tabulated (for a transition originating in level SLJ and ending in a multiplet $S'L'$), the collision strengths for the transitions between levels SLJ and the individual levels $S'L'J'$ of the $S'L'$ multiplet are given by :

$$\Omega(SLJ, S'L'J') = \frac{2J'+1}{(2S'+1)(2L'+1)}\Omega(SLJ, S'L')\,, \tag{4.19}$$

where $2J'+1$ is the statistical weight of the $S'L'J'$ level and $(2S'+1)(2L'+1)$ is the statistical weight of the $S'L'$ term.

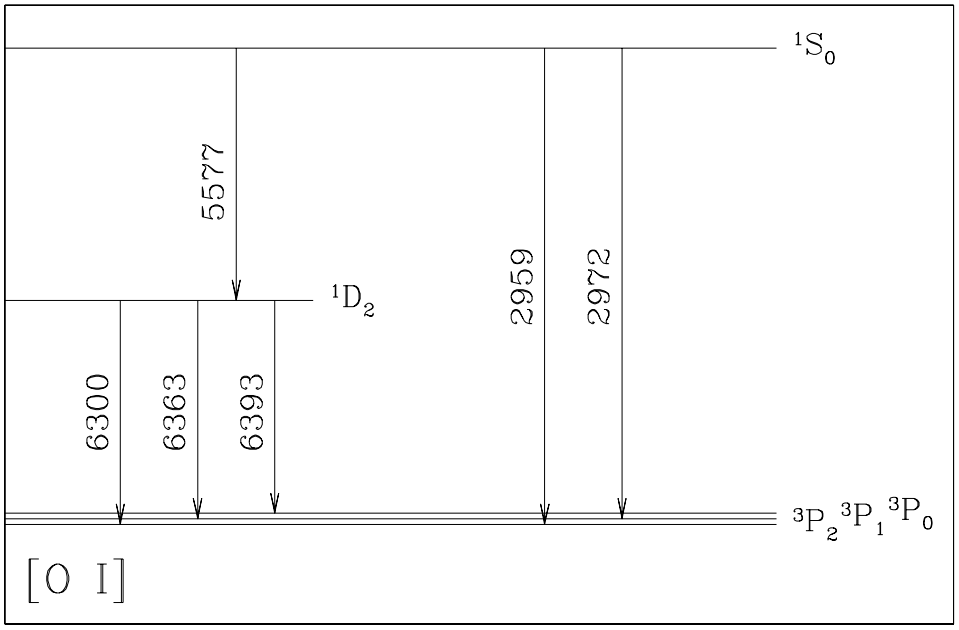

Figure 4.2: Energy level diagram showing the UV, optical and IR forbidden transitions of O I. The wavelengths of the transitions are given in Å.

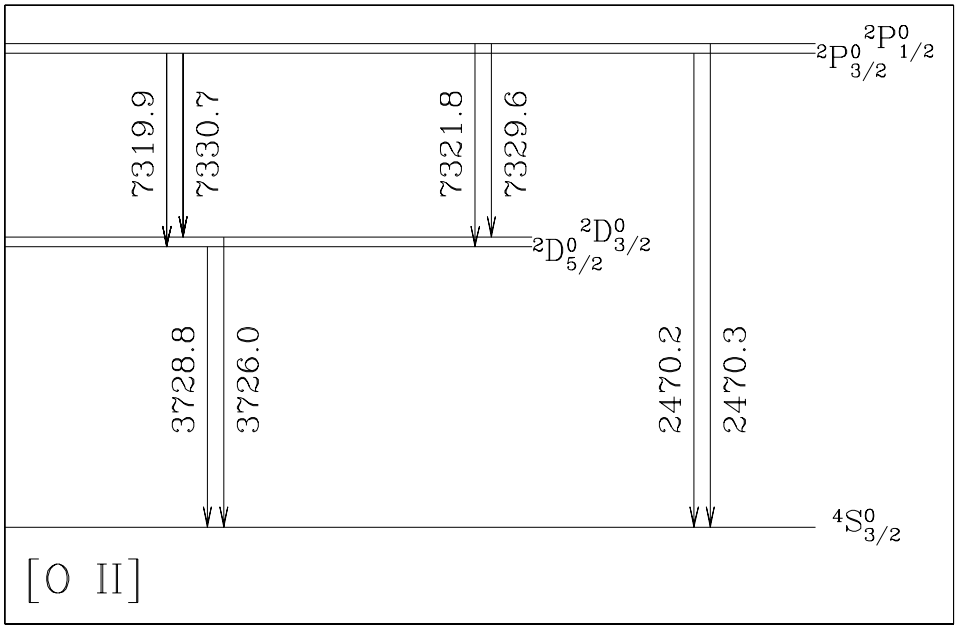

Figure 4.3: Energy level diagram showing the UV, optical and IR forbidden transitions of O II. The wavelengths of the transitions are given in Å.

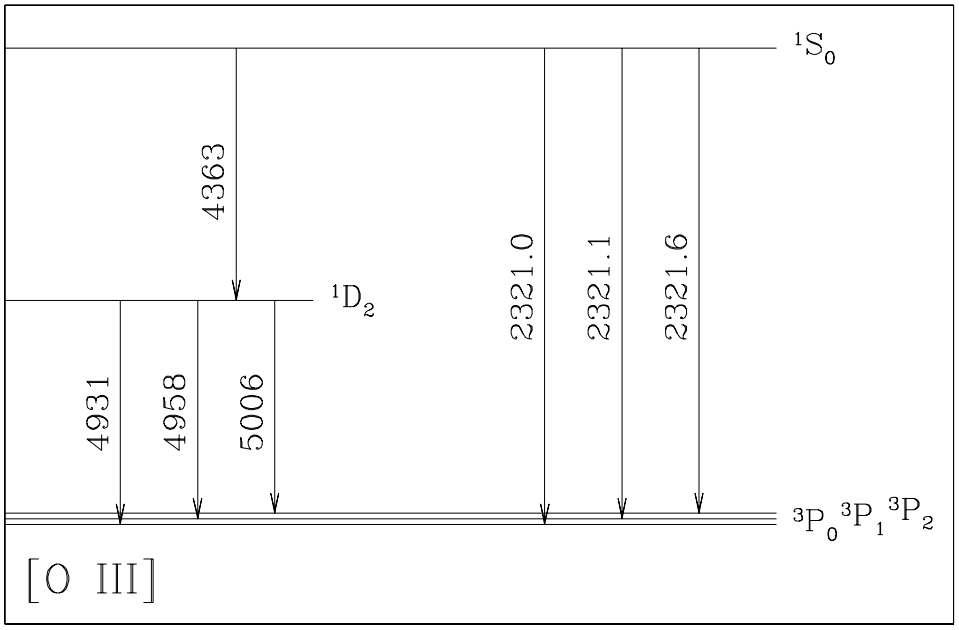

Figure 4.4: Energy level diagram showing the UV, optical and IR forbidden transitions of O III. The wavelengths of the transitions are given in Å.

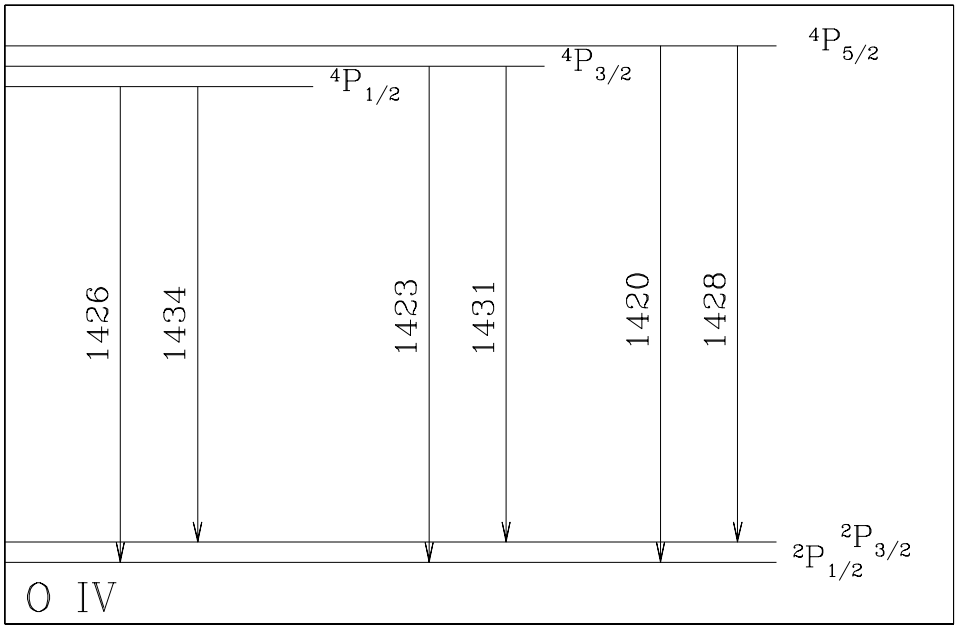

Figure 4.5: Energy level diagram showing the UV permitted/forbidden transitions of O IV. The wavelengths of the transitions are given in Å.

4.3.2 The 3-level atom

For an atom/ion with three levels, the equilibrium equations are :

$$n_3 \left[A_{31} + A_{32} + n_e(q_{31} + q_{32})\right] = n_e(n_1 q_{13} + n_2 q_{23}) \,, \tag{4.20}$$

$$n_2 \left[A_{21} + n_e(q_{21} + q_{23})\right] = n_3 A_{32} + n_e(n_1 q_{12} + n_2 q_{32}) \,, \tag{4.21}$$

$$n_e n_1 (q_{12} + q_{13}) = n_3 A_{31} + n_2 A_{21} + n_e(n_2 q_{21} + n_3 q_{31}) \,. \tag{4.22}$$

Actually, only two out of these three equations are linearly independent, so that one has to choose two of them, and solve them together with the conservation equation :

$$n_1 + n_2 + n_3 = n \,, \tag{4.23}$$

where n is the total number density of the atom/ion that is being considered. The resulting system of 3 equations (with n_1, n_2 and n_3 as unknowns, and n_e, n and T as given parameters) can be solved.

Let us consider the case in which $A_{32} = 0$ and also $q_{23} = q_{32} = 0$. Equations (4.20-4.21) then take the form :

$$n_3(A_{31} + n_e q_{31}) = n_e n_1 q_{13} \,, \tag{4.24}$$

$$n_2(A_{21} + n_e q_{21}) = n_e n_1 q_{12} \,. \tag{4.25}$$

Dividing these two equations, we have

$$\frac{n_3}{n_2} = \left[\frac{A_{21} g_2 T^{1/2}/(n_e C \Omega_{12}) + 1}{A_{31} g_3 T^{1/2}/(n_e C \Omega_{13}) + 1}\right] \frac{g_3}{g_2} e^{-E_{23}/kT} \,, \tag{4.26}$$

where we have also used eq. (4.16) and the fact that $E_{13} = E_{12} + E_{23}$. In this equation, $C = 8.629 \times 10^{-6}$ (in c.g.s.).

We now consider the emission from an optically thin, homogeneous slab. The ratio of the intensities of the lines corresponding to the transitions $3 \to 1$ and $2 \to 1$ is then given by :

$$\frac{I_3}{I_2} = \frac{n_3 A_{31} E_{31}}{n_2 A_{21} E_{21}} = \left[\frac{A_{21} g_2 T^{1/2}/(n_e C \Omega_{12}) + 1}{A_{31} g_3 T^{1/2}/(n_e C \Omega_{13}) + 1}\right] \frac{g_3}{g_2} e^{-E_{23}/kT} \frac{A_{31} E_{31}}{A_{21} E_{21}} \,, \tag{4.27}$$

where for the second equality we have used eq. (4.26).

In the low electron density regime, this ratio takes the form :

$$\frac{I_3}{I_2} = \frac{\Omega_{13}}{\Omega_{12}} e^{-E_{23}/kT} \frac{E_{31}}{E_{21}} \,, \tag{4.28}$$

In the high electron regime, the line ratio takes the form :

$$\frac{I_3}{I_2} = \frac{g_3}{g_2} e^{-E_{23}/kT} \frac{A_{31} E_{31}}{A_{21} E_{21}} \,. \tag{4.29}$$

coinciding with the line ratio predicted from levels populated with a thermodynamic equilibrium Boltzmann distribution.

Therefore, both in the high and in the low density regime the line ratio is only a function of the temperature T of the gas. From a line ratio in one of these regimes, we can take an observed value for I_3/I_2 and use eqs. (4.28) or (4.29) to obtain a direct determination of the temperature of the emitting region. If the line ratio is not in the high or low density regime, the observed line ratio can be used to derive a relation between n_e and T (from eq. 4.27) that has to be obeyed by the electron density and temperature of the emitting region.

An interesting case is provided by ions (such as S II, see Fig. 4.1) which have two close-spaced levels 2 and 3 (i. e., with $E_{23} \ll kT$). For such levels, eq. (4.27) simplifies to

$$\frac{I_3}{I_2} \approx \left[\frac{A_{21} g_2 T^{1/2}/(n_e C \Omega_{12}) + 1}{A_{31} g_3 T^{1/2}/(n_e C \Omega_{13}) + 1} \right] \frac{\Omega_{13}}{\Omega_{12}} \frac{A_{31} E_{31}}{A_{21} E_{21}} \,. \tag{4.30}$$

Therefore, the line ratio only has the $T^{1/2}$ temperature dependence explicitly shown in eq. (4.30) and the slow dependence on T of the collision strengths. Because of this slow dependence on T, one can use "density indicators" (i. e., line ratios with $E_{23} \ll kT$) to directly obtain the electron density of the emitting gas as a function of the observed line ratio. This can be done by, e. g., setting $T \approx 10^4$ K in eq. (4.30) and inverting it to find n_e as a function of I_3/I_2.

4.3.3 Diagnostic diagrams

In general, one can determine the fraction of atoms (or ions) in each of the excited levels by inverting the statistical equilibrium conditions given by eq.

Table 4.6: A_{ij} and Ω_{ij} for the 5-level O I ion

transition		λ [Å]	$A_{i,j}$ [s^{-1}]	$\Omega = b_0 + b_1 t\,;\ t = \log_{10}(T/10^4\mathrm{K})$
$^3P_1 - ^3P_2$	2 1	6.32E5	8.92E-5	-0.00675 0.1067
$^3P_0 - ^3P_2$	3 1	4.41E5	1.0E-10	0.0026 0.0257
$^3P_0 - ^3P_2$	3 2	1.46E6	1.74E-5	-0.0102 0.0393
$^1D_2 - ^3P_2$	4 1	6300.3	0.0634	0.00365 0.1383
$^1D_2 - ^3P_1$	4 2	6363.8	0.0211	0.00215 0.0820
$^1D_2 - ^3P_0$	4 3	6393.5	7.23E-6	0.00075 0.0277
$^1S_0 - ^3P_2$	5 1	2959.2	2.88E-4	0.00065 0.0166
$^1S_0 - ^3P_1$	5 2	2972.3	0.0732	0.00035 0.0100
$^1S_0 - ^3P_2$	5 3	2979.2	0.0	0.00015 0.0033
$^1S_0 - ^1D_2$	5 4	5577.4	1.22	0.0517 0.0489

(4.15). These populations can be used to calculate the line ratios that would be produced by a homogeneous, optically thin slab :

$$\frac{I_{kl}}{I_{mn}} = \frac{n_k A_{kl} E_{kl}}{n_m A_{mn} E_{km}}\,. \tag{4.31}$$

Line ratios involving sums of lines (in the numerator and/or the denominator) are sometimes also used.

As the n_k/n_m ratio only depends on n_e and T, each of the observed line ratios determines an allowed locus in the (n_e, T) plane. Therefore, if one observes several line ratios (of transitions that do not start in the same excited level), each of them should give an allowed locus in the (n_e, T) plane, all of which intersect at the n_e and T values of the gas that is emitting the observed lines.

In practice, the allowed loci for three or more line ratios do not intersect exactly at the same point. This can be due to the errors in the observed line ratios and/or to the fact that the emitting region is not homogeneous.

Tables 4.7 and 4.10 give the A coefficients and polynomial fits to the collision strengths Ω from the tabulation found in the book of Pradhan & Nahar [20].

4.3.4 Example: plasma diagnostics with the [S II] lines

With the coefficients given in Table 4.10 one can solve a 5-level atom problem (for the levels shown in fig. 4.1), and obtain predictions for all of the ratios

Table 4.7: A_{ij} and Ω_{ij} for the 5-level O II ion

transition		λ [Å]	$A_{i,j}$ [s^{-1}]	$\Omega = b_0 + b_1 t + b_2 t^2\,;\ t = \log_{10}(T/10^4\mathrm{K})$
$^2D^0_{5/2} - ^4S^0_{3/2}$	2 1	3728.8	3.50E-5	0.7890 0.0106 0.0020
$^2D^0_{3/2} - ^4S^0_{3/2}$	3 1	3726.0	1.79E-4	0.5245 0.0104 0.0000
$^2D^0_{3/2} - ^4D^0_{5/2}$	3 2	4.97E6	1.30E-7	1.2750 -0.122 0.020
$^2P^0_{3/2} - ^4S^0_{3/2}$	4 1	2470.3	0.0057	0.2600 0.010 0.000
$^2P^0_{3/2} - ^4D^0_{5/2}$	4 2	7319.9	0.107	0.7080 0.0194 0.002
$^2P^0_{3/2} - ^4D^0_{3/2}$	4 3	7330.7	0.0578	0.3953 0.0113 0.001
$^2P^0_{1/2} - ^4S^0_{3/2}$	5 1	2470.2	0.0234	0.1318 0.0021 0.001
$^2P^0_{1/2} - ^4D^0_{5/2}$	5 2	7321.8	0.0615	0.2850 0.010 0.000
$^2P^0_{1/2} - ^4D^0_{3/2}$	5 3	7329.6	0.102	0.2630 0.0146 -0.002
$^2P^0_{3/2} - ^4P^0_{1/2}$	5 4	5.00E7	2.08E-11	0.2735 0.0132 0.000

Table 4.8: A_{ij} and Ω_{ij} for the 6-level O III ion

transition		λ [Å]	$A_{i,j}$ [s^{-1}]	$\Omega = b_0 + b_1 t + b_2 t^2\,;\ t = \log_{10}(T/10^4\mathrm{K})$
$^3P_1 - ^3P_0$	2 1	883562.	2.62E-05	0.5462 0.0666 -0.0266
$^3P_2 - ^3P_0$	3 1	326611.	3.02E-11	0.2718 0.0527 0.0209
$^3P_2 - ^3P_1$	3 2	518145.	9.76E-05	1.2959 0.2080 -0.0481
$^1D_2 - ^3P_0$	4 1	4932.6	2.74E-06	0.2555 0.0737 0.0371
$^1D_2 - ^3P_1$	4 2	4958.9	0.00674	0.7677 0.2229 0.0941
$^1D_2 - ^3P_2$	4 3	5006.7	0.0196	1.2795 0.3715 0.1543
$^1S_0 - ^3P_0$	5 1	2314.9	...	0.0328 0.0109 0.0074
$^1S_0 - ^3P_1$	5 2	2321.0	0.223	0.0983 0.0325 0.0225
$^1S_0 - ^3P_2$	5 3	2332.1	7.85E-4	0.1639 0.0545 0.0368
$^1S_0 - ^1D_2$	5 4	4363.2	1.78	0.5837 0.1952 -0.3451
$^5S^0_2 - ^3P_0$	6 1	1657.7	...	0.1342 0.0351 -0.0509
$^5S^0_2 - ^3P_1$	6 2	1660.8	212.	0.4032 0.1050 -0.1617
$^5S^0_2 - ^3P_2$	6 3	1666.1	522.	0.6718 0.1758 -0.2744

Table 4.9: A_{ij} and Ω_{ij} for the 5-level O IV ion

transition		λ [Å]	$A_{i,j}$ [s^{-1}]	$\Omega = b_0 + b_1 t + b_2 t^2\,;\ t = \log_{10}(T/10^4\mathrm{K})$
$^2P^0_{3/2} - ^2P^0_{1/2}$	2 1	2.587E5	5.18E-4	2.4020 0.9164 -1.1751
$^4P_{1/2} - ^2P^0_{1/2}$	3 1	1426.46	1.81E3	0.1332 0.0452 0.0146
$^4P_{1/2} - ^2P^0_{3/2}$	3 2	1434.07	1.77E3	0.1024 0.0625 0.0339
$^4P_{3/2} - ^2P^0_{1/2}$	4 1	1423.84	2.28E1	0.2002 0.0801 0.0422
$^4P_{3/2} - ^2P^0_{3/2}$	4 2	1431.42	3.28E2	0.2692 0.1379 0.0898
$^4P_{3/2} - ^4P_{1/2}$	4 3	1.680E6	...	1.0906 0.2002 0.1056
$^4P_{5/2} - ^2P^0_{1/2}$	5 1	1420.19	...	0.1365 0.0904 0.0625
$^4P_{5/2} - ^2P^0_{3/2}$	5 2	1427.78	1.04E3	0.5683 0.2345 0.1108
$^4P_{5/2} - ^4P_{1/2}$	5 3	3.260E5	...	0.6876 0.0359 0.4118
$^4P_{5/2} - ^4P_{3/2}$	5 4	5.620E5	1.02E-4	2.0497 0.2653 0.7749

Table 4.10: A_{ij} and Ω_{ij} for the 5-level S II ion

transition		λ [Å]	$A_{i,j}$ [s^{-1}]	$\Omega = b_0 + b_1 t + b_2 t^2\,;\ t = \log_{10}(T/10^4\mathrm{K})$
$^2D^0_{3/2} - ^4S^0_{3/2}$	2 1	6730.8	0.000882	3.112 -0.712 -0.622
$^2D^0_{5/2} - ^4S^0_{3/2}$	3 1	6716.5	0.00026	4.658 -1.066 -0.865
$^2D^0_{5/2} - ^4D^0_{3/2}$	3 2	3145000.	3.35E-07	7.124 0.750 11.734
$^2P^0_{1/2} - ^4S^0_{3/2}$	4 1	4076.4	0.0906	0.905 0.342 0.304
$^2P^0_{1/2} - ^4D^0_{3/2}$	4 2	10336.3	0.163	1.787 -0.741 2.045
$^2P^0_{1/2} - ^4D^0_{5/2}$	4 3	10373.3	0.0779	2.017 -0.791 2.320
$^2P^0_{3/2} - ^4S^0_{3/2}$	5 1	4068.6	0.225	2.015 0.583 -1.759
$^2P^0_{3/2} - ^4D^0_{3/2}$	5 2	10286.7	0.133	2.778 -1.107 3.224
$^2P^0_{3/2} - ^4D^0_{5/2}$	5 3	10320.4	0.179	4.834 -1.981 5.379
$^2P^0_{3/2} - ^4P^0_{1/2}$	5 4	2140000.	1.03E-06	2.411 0.142 -3.585

between the [S II] emission lines.

Fig. 4.6 gives a few selected line ratios as a function of electron density, for three chosen temperatures ($T = 5000$, 10000 and 15000 K). It is clear that the line ratios between lines arising from close-lying upper levels (i.e., the 6730/16 and the 4076/68 ratios, see Fig. 4.1) are good "electron density indicators" (i.e., they have a large n_e dependence and shallow T dependence). The (6030+ 16) / (4076 + 68) line ratio (calculated with lines from well separated upper levels, see Fig. 4.1) show strong n_e and T dependence (see Fig. 4.6).

Now, let us assume that observationally we determine the ratios : $I(6730)$ / $I(6716) = 1.63 \pm 0.03$, $I(4076)$ / $I(4068) = 0.305 \pm 0.015$ and $I(6730 + 16)$ / $I(4076 + 68) = 3.4 \pm 0.1$. For each of these line ratios, the solution to the 5-level atom can be used to constrain a region in the (n_e, T)-plane.

The result of this exercise is shown in Fig. 4.7. Actually, for each observed line ratio we show two curves : one for the upper boundary and one for the lower boundary of the line ratio range permitted by the observational errors. An analysis of Fig. 4.7 shows that a point with $n_e = 3720$ cm^{-3} and $T = 16000$ K is consistent with all of the observed line ratios.

It is also clear that the 4076/4068 line ratio does not provide a lot of information. This is a direct result of the fact that the observed 4076/4068 ratio lies in the "low density regime" (see Fig. 4.6).

4.4 Continuum emission

4.4.1 General considerations

The continuum of photoionised regions has three main contributions: the recombination, free-free and two-photon continua of H. In regions in which He is in the form of He II, the He III/II recombination continuum can also have an important contribution.

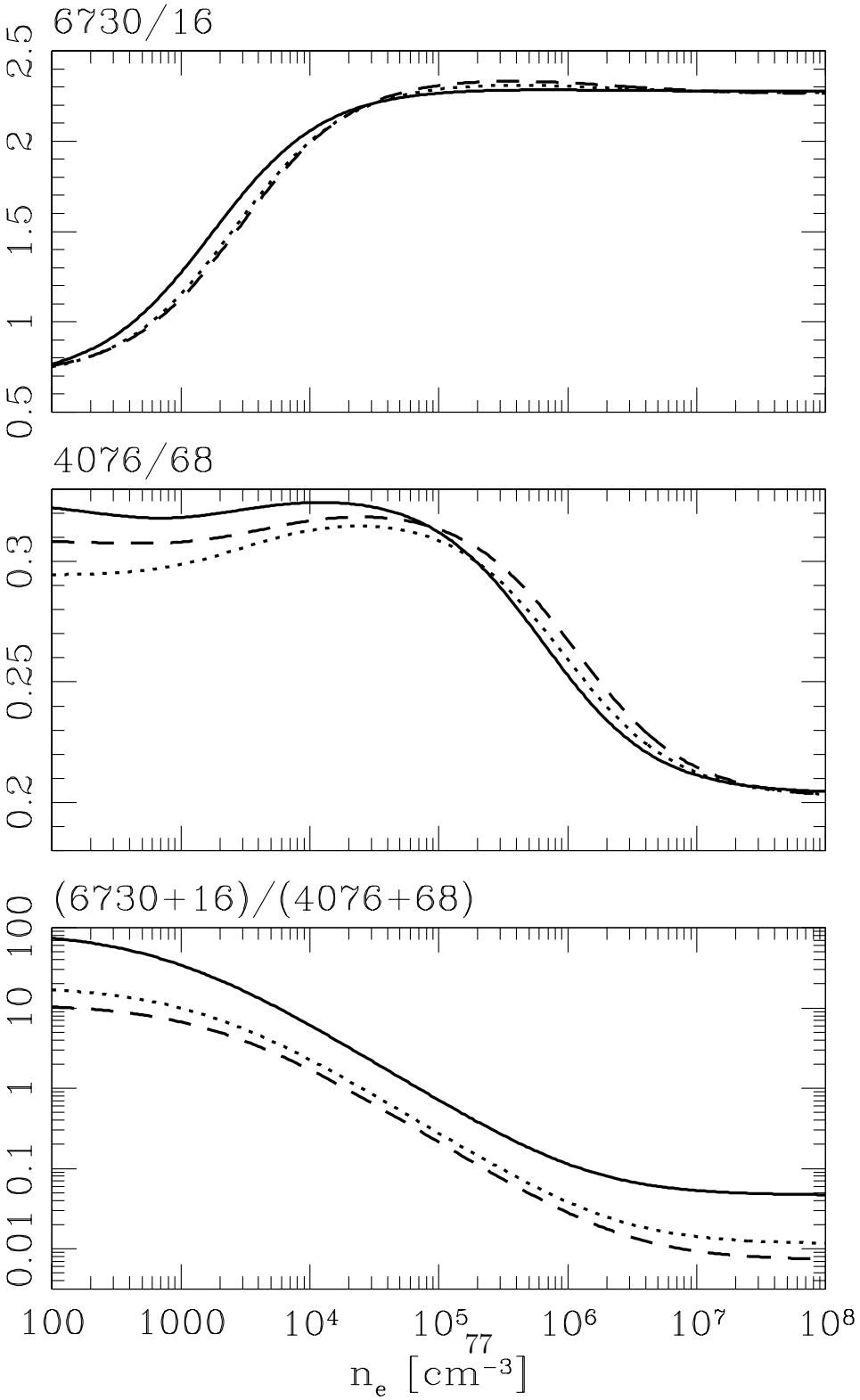

Figure 4.6: Selected [S II] line ratios given as a function of the electron density. Curves calculated for three temperatures are shown : $T = 5000$ K (solid lines), $T = 10000$ K (dotted lines) and $T = 15000$ K (dashed lines).

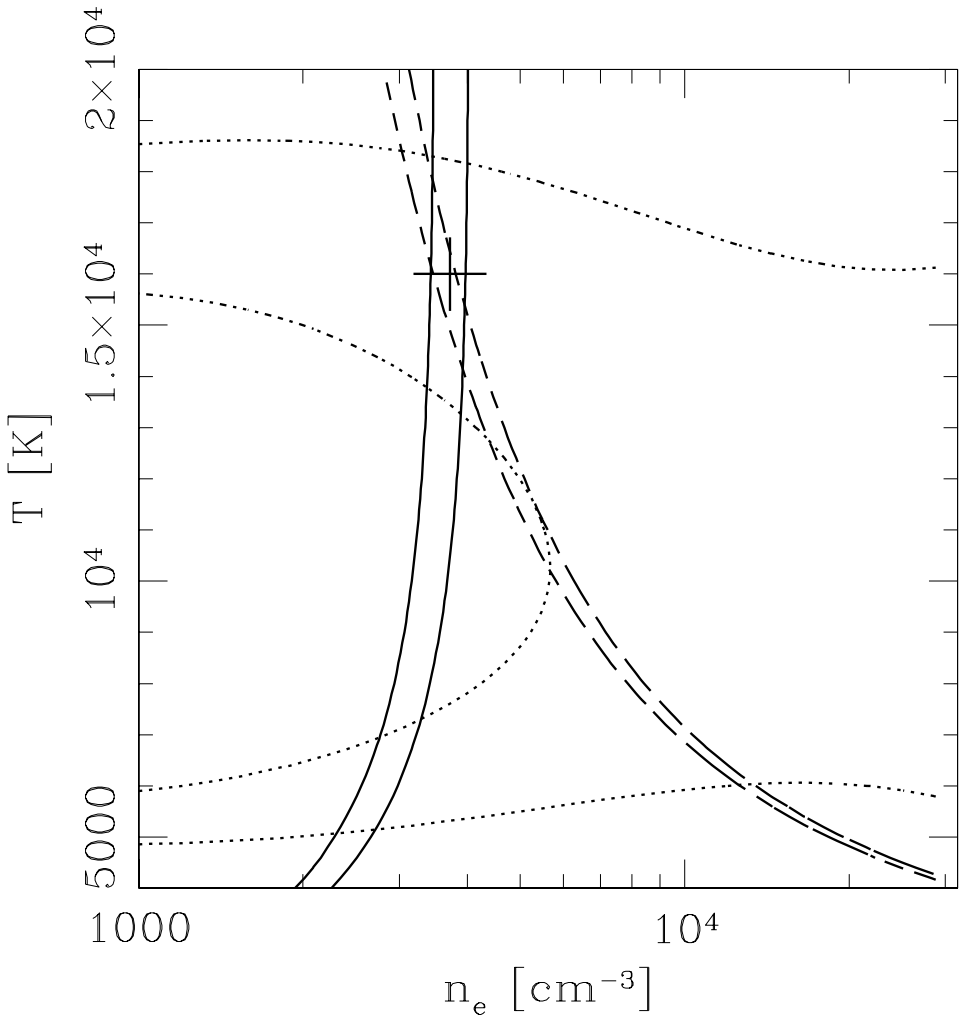

Figure 4.7: [S II] diagnostic diagram showing the regions allowed by an $I(6730)/I(6716) = 1.63 \pm 0.03$ line ratio (solid lines), an $I(4076)/I(4068) = 0.305 \pm 0.015$ ratio (dotted lines) and an $I(6730+16)/I(4076+68) = 3.4 \pm 0.1$ ratio (dashed lines). These ratios determine an electron density $n_e = 3720$ cm^{-3} and a temperature $T = 16000$ K (this point is shown with a cross).

4.4.2 The recombination continua

Recombinations of free electrons to an excited level N of a hydrogenic ion of charge Z (with energy $\chi_N = Z^2\chi_H/N^2$, where χ_H is the ionisation potential from the ground state of H) produce photons with energies

$$h\nu = \frac{1}{2}m_e v^2 + \chi_N \,, \tag{4.32}$$

where m_e is the mass and v the velocity of the free electron.

The recombination continuum can then be calculated as a sum of the continua due to recombinations to all excited levels, which are given by

$$j_\nu^{(N)} = \frac{n_{ion}n_e}{4\pi} v\sigma_N(\nu) f(v,T) h\nu \frac{dv}{d\nu} \,, \tag{4.33}$$

where $\sigma_N(\nu)$ is the cross section for recombination to level N and

$$f(v,T) = \frac{4}{\sqrt{\pi}} \left(\frac{m_e}{2kT}\right)^{3/2} v^2 e^{-m_e v^2/(2kT)} \,, \tag{4.34}$$

is the Maxwell-Boltzmann distribution of the electrons, and $dv/d\nu = h/(m_e v)$ [obtained from the relation $d(m_e v^2/2) = d(h\nu)$, see eq. 4.32].

From the principle of detailed balancing, it is possible to derive a Milne relation of the form:

$$\sigma_N(v) = \frac{w_{HI}}{w_{HII}} \frac{h^2\nu^2}{m_e^2 c^2 v^2} a_N(\nu) \,, \tag{4.35}$$

where $a_N(\nu)$ is the photoionisation cross section from level N and $w_{HI} \approx 2$ and $w_{HII} = 1$ are the HI and HII partition functions, respectively. This relation is derived in Appendix 1 of the book of Osterbrock [18].

Combining eqs. (4.32-4.35), we obtain:

$$j_\nu^{(N)} = \frac{n_{HII}n_e}{4\pi} \gamma_N(\nu) \,, \tag{4.36}$$

with

$$\gamma_N(\nu) = \left(\frac{2}{\pi}\right)^{1/2} \frac{2N^2h^4\nu^3}{c^2(m_e kT)^{3/2}} a_N(\nu)\, e^{(\chi_N - h\nu)/kT} \,. \tag{4.37}$$

Given the photoionisation cross section $a_N(\nu)$, eqs. (4.36-4.37) then give us the continua to all levels N of a hydrogenic ion.

For a hydrogenic ion of charge Z, the photoionisation cross section $a_N(\nu)$ is given by

$$a_N(Z,\epsilon) = 7.907 \times 10^{-18}\mathrm{cm}^2 \frac{N}{Z^2}\left(1+N^2\epsilon\right)^{-3} g_{bf}(N,\epsilon)\,, \tag{4.38}$$

for $\epsilon \geq 0$ and $a_N(Z,\epsilon) = 0$ for $\epsilon < 0$. The photon energy is

$$h\nu = Z^2\chi_H\left(\frac{1}{N^2}+\epsilon\right)\,, \tag{4.39}$$

with $\chi_H = 13.6$ eV, and the g_{II} Gaunt's factor is approximately given by

$$g_{bf}(N,\epsilon) = 1{+}0.1728N^{-2/3}(u{+}1)^{-2/3}(u{-}1){-}0.0496N^{-4/3}(u{+}1)^{-4/3}(u^2{+}4u/3{+}1)\,, \tag{4.40}$$

with $u = N^2\epsilon$ (see Seaton [29]). The precision of this expansion for the Gaunt factor has been evaluated by Brown & Mathews [7].

Finally, the total bound-free emission of the hydrogenic ion can be written as :

$$j_\nu = \frac{n_Z n_e}{4\pi}\gamma(\nu)\,, \tag{4.41}$$

with

$$\gamma(\nu) = \sum_{N\geq 1}\gamma_N(\nu)\,. \tag{4.42}$$

The $\gamma(\nu)$ coefficient obtained for H (i. e., setting $Z = 1$) is plotted in Fig. 4.8 for three chosen values of the temperature T. It is clear that the slopes of the continua as well as the "jumps" at the frequencies corresponding to the ionisation energies of the levels of H depend quite strongly on the temperature. Therefore, observed values for these parameters can be used as a temperature diagnostic of the emitting plasma.

The formalism used above can of course be used to derive the HeII recombination continuum (by setting $Z = 2$ in all of the expressions). The intensity of this continuum can be comparable to the H recombination continuum in regions where He is twice ionised. The recombination continuum of HeI has γ values (see eq. 4.41, setting $n_Z = n_{HeII}$) which are similar to the ones of HI (see Brown & Mathews [7]). The HeI recombination emission coefficient is therefore of order 10% of the HI emission coefficient (for an He/H$\sim$ 0.1 abundance).

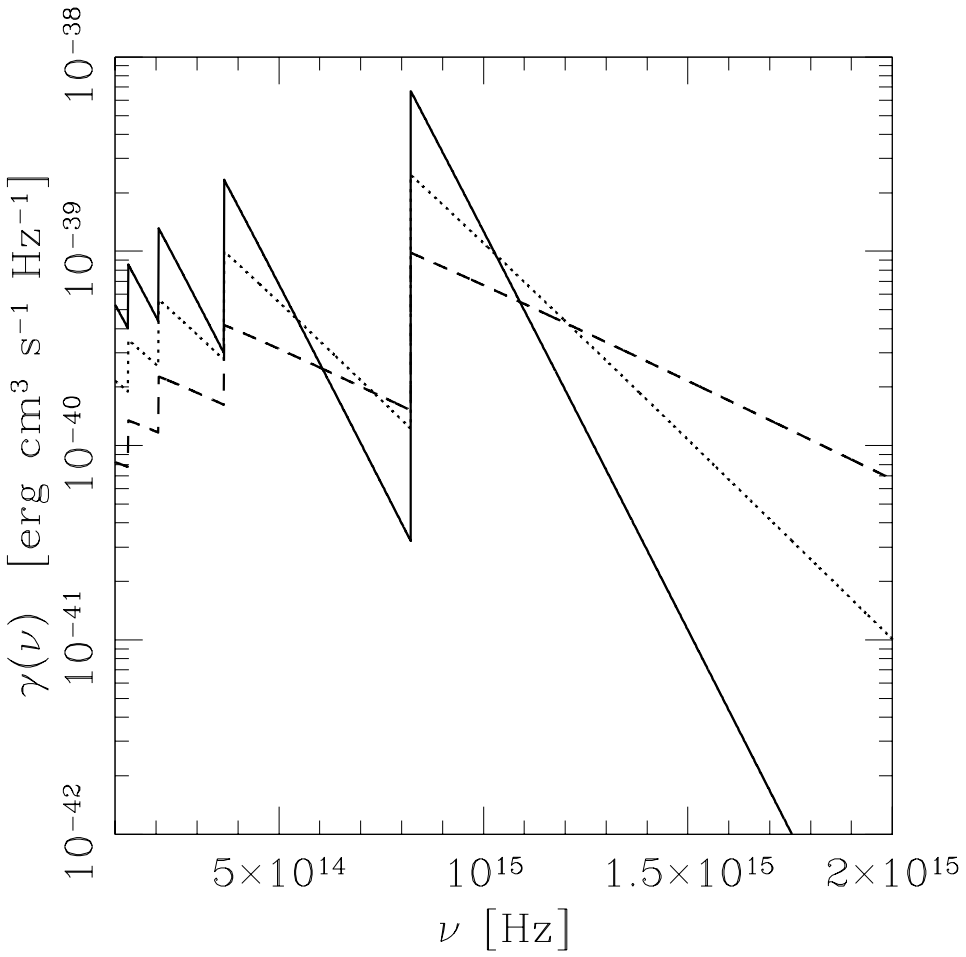

Figure 4.8: Recombination continuum of H. Curves calculated for three temperatures are shown : $T = 5000$ K (solid line), $T = 10000$ K (dotted line) and $T = 20000$ K (dashed line).

4.4.3 The free-free continua

The free-free continuum emission coefficient due to electron transitions in the electric field of an ion of charge Z is given by:

$$j_\nu = \frac{n_e n_Z}{4\pi} \frac{32 Z^2 e^4 h}{3 m_e^2 c^3} \left(\frac{\pi \chi_{Z-1}}{3kT} \right)^{1/2} e^{-h\nu/kT} \, g_{ff}(T, Z, \nu) \,, \tag{4.43}$$

where χ_{Z-1} is the ionisation potential of the ion with charge $Z-1$. For a hydrogenic ion $\chi_{Z-1} = Z^2 \chi_H$, and the Gaunt factor g_{ff} is given by :

$$g_{ff}(T, Z, \nu) = 1 + 0.1728 \left(\frac{h\nu}{Z^2 \chi_H} \right)^{1/3} (1 + 2\mu) -$$

$$0.0496 \left(\frac{h\nu}{Z^2 \chi_H} \right)^{2/3} \left(1 + 2\mu/3 + 4\mu^2/3 \right) \tag{4.44}$$

with $\mu = kT/h\nu$ (see Seaton [29]). This expression leads to $g_{ff} \approx 1$ for the optical region of the spectrum.

The free-free continuum dominates the radio spectrum. For radio frequencies, an appropriate expression for the Gaunt factor is:

$$g_{ff}(T, Z, \nu) = \frac{\sqrt{3}}{\pi} \left[\ln \left(\frac{8 k^3 T^3}{\pi^2 Z^2 e^4 m_e \nu^2} \right)^{1/2} - 1.4425 \right] . \tag{4.45}$$

With eqs. (4.43-4.45) we can compute the free-free continua of HII and HeIII (setting $n_Z = n_{HII}$, $Z = 1$ and $n_Z = n_{HeIII}$, $Z = 2$, respectively). It is usual practice to include the HeII free-free continuum as well as the HeI recombination continuum in an approximate way by assuming that they have the same temperature and frequency dependence as the corresponding H emission coefficients. As the HeI recombination and HeII free-free continua are down by an order of magnitude with respect to the H continua, this assumption does not introduce a large error in the computed continuum spectrum.

4.4.4 The two-photon continuum

Electrons in the 2s state of H decay to the 1s level through a 2-photon transition with Einstein coefficient $A_{2s,1s} = 8.23$ s^{-1} (see Table 4.2).

The emission coefficient is given by :

$$j_\nu^{(2q)} = \frac{n_{2s} A_{2s,1s}}{4\pi} g(\nu)\,, \tag{4.46}$$

where $g(\nu)$ is given in Table 4.11 (the values are taken from Brown & Mathews [7]). An analytic fit to these values is :

$$g_a(y) = 9.23 \exp\left\{ -\left[\eta/0.3\right]^{(1.3+1.6\eta)} \right\} - 0.61\,, \tag{4.47}$$

in units of 10^{-27} erg Hz^{-1}, with $\eta = 0.5 - y$ and $y = \nu/\nu_{21}$ ($\nu_{21} = 3\chi_H/4h$ being the frequency of the $2 \rightarrow 1$ transition of H). The analytic fit in eq. (4.47) is valid for $y \leq 0.5$. For $y > 0.5$, the relation

$$g(1-y) = \frac{(1-y)\ g(y)}{y}\,, \tag{4.48}$$

should be used in order to compute the $g(y)$ function from the analytic fit (eq. 4.47). This equation represents the fact that the photon distribution (i. e., of the number of emitted photons) is symmetric with respect to $\nu_{21}/2$. The errors of the analytic fit obtained from eqs. (4.47-4.48) can be appreciated in Fig. 4.9. We should note that the function $g_a(y)$ (eq. 4.47) becomes negative for $0 \leq y < 0.015$ and should therefore be set to zero. Because of this feature, the cutoff at high energies of the 2-photon continuum computed with eq. (4.47) is shifted by 1.5 % with respect to ν_{21}.

The simplest possible way of calculating the population of n_{2s} of the $2s$ level is to assume a balance of the form :

$$n_{2s}\left(A_{2s,1s} + n_e q_{1s,2s}^{(e)} + n_{HII} q_{1s,2s}^{(p)}\right) = n_e n_{HII} \alpha_{2s}(T)\,, \tag{4.49}$$

where the collisional rates $q^{(e)}$ and $q^{(p)}$ can be calculated with the corresponding collision strengths given in Tables 4.2 and 4.5. The effective recombination coefficient to the $2s$ level $\alpha_{2s}(T)$ has been tabulated by Brown & Mathews [7], and can be obtained from the interpolation formula:

$$\log_{10}\left[\alpha_{2s}(T)\right] = -13.077 - 0.696t - 0.0987t^2\,;\ \ t = \log_{10}(T/10^4\mathrm{K})\,, \tag{4.50}$$

in erg cm^3 s^{-1}. Eq. (4.49) represents the balance between the recombination cascade electrons that end in level $2s$ (right hand term) and the electrons that

Table 4.11: Frequency dependence of the H 2-photon emission

$y = \nu/\nu_{21}$	$g(y)$ [10^{-27}erg Hz^{-1}]	$y = \nu/\nu_{21}$	$g(y)$ [10^{-27}erg Hz^{-1}]
0.00	0.0	0.55	9.46
0.05	0.303	0.60	10.17
0.10	0.978	0.65	10.77
0.15	1.836	0.70	11.12
0.20	2.78	0.75	11.34
0.25	3.78	0.80	11.12
0.30	4.80	0.85	10.40
0.35	5.80	0.90	8.80
0.40	6.78	0.95	5.76
0.45	7.74	1.00	0.0
0.50	8.62		

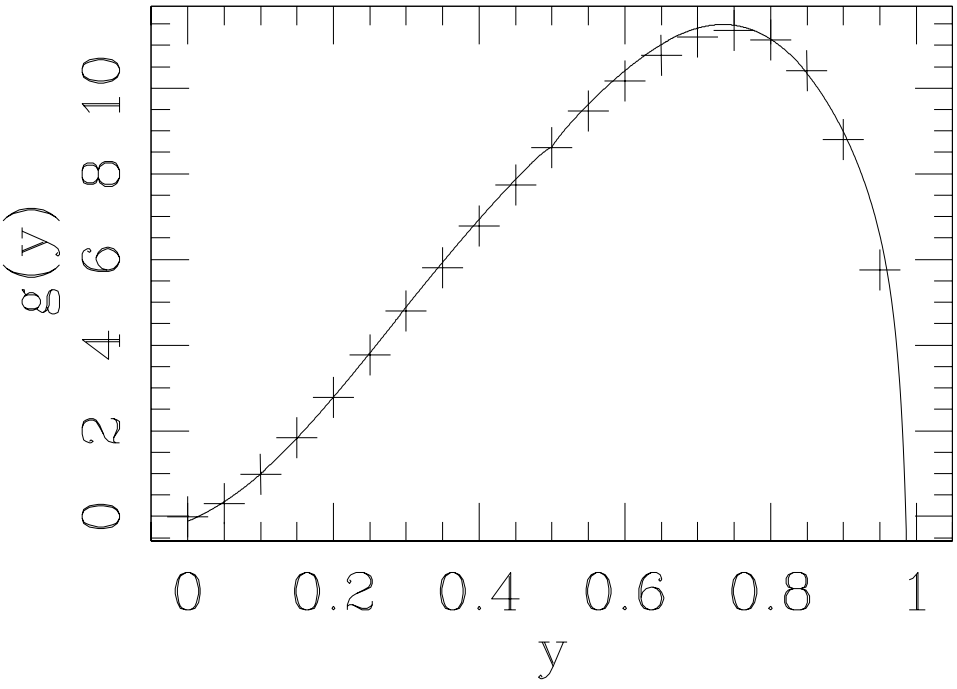

Figure 4.9: Frequency dependence of the 2-photon continuum of H : $g(y)$ (in 10^{-27}erg Hz^{-1}) as a function of $y = \nu/\nu_{21}$. The crosses are the values of Brown & Mathews [7] and the solid line the analytic fit described in the text.

leave $2s$ through 2-photon transitions to $1s$ or through collisional transitions to the $2p$ level. At high enough optical depths of the Lyα line, the population of level $2p$ can be high enough for $2p \rightarrow 1s$ collisional transitions to become important. This effect is discussed by Brown & Mathews [7]. Another possibly important effect is found in a partially neutral gas of temperatures $T \geq 12000$ K, in which $1s \rightarrow 2s$ collisional transitions can be important. This effect can lead to a hugely increased intensity of the 2-photon continuum.

Combining eqs. (4.46) and (4.49) we then obtain :

$$j_\nu^{(2q)} = \frac{n_e n_{HII} \alpha_{2s}(T) g(\nu)}{4\pi \left[1 + \left(n_e q_{1s,2s}^{(e)} + n_{HII} q_{1s,2s}^{(p)}\right) / A_{2s,1s}\right]} \,. \tag{4.51}$$

A more detailed model for the intensity of the 2-photon continuum would involve a solution of the recombination cascade with collisions in order to obtain a better estimate of n_{2s}.

Part III

Dynamics of the ISM

Chapter 5

The equations of gasdynamics

5.1 General considerations

It is in principle possible to derive the gasdynamic equations as velocity moments of Vlasov's equation (for a single particle distribution function). In its turn, Vlasov's equation can be derived from Liouville's theorem (i. e., the fundamental equation of statistical mechanics) through methods such as the "BBGKY" hierarchy. These derivations can be found in most standard plasma physics or particle kinetics books. In this chapter, we will describe the mathematically simple and physically more inspiring "macroscopic derivation" of the gasdynamic equations (described in different forms in most books on gasdynamics or hydrodynamics).

In order to be able to describe a gas (a system of many interacting particles) as a fluid, the following conditions must be satisfied :

- the mean free path λ of the particles must be much smaller than the characteristic distance L of the spatial variations of the macroscopic variables of the gas (such as the density),
- the mean time between collisions t_{coll} must be much smaller than the characteristic timescale t_{flow} of changes in the flow,
- the mean distance $l \sim n^{-1/3}$ (where n is the number density) between neighbouring particles must also be much smaller than L.

The $\lambda \ll L$ condition implies that the gas particles effectively see an infinite, homogeneous environment, and therefore (provided that the $t_{coll} \ll t_{flow}$ condition is also satisfied) attain a local thermodynamic equilibrium. This means that in a reference system moving with the flow the particles have a TE, Maxwell-Boltzmann velocity distribution (with a well defined local temperature T). Therefore, the thermal energy and the pressure/density/temperature law are given by the relations obtained for a (real or ideal) gas in TE.

The $n^{-1/3} \ll L$ condition implies that one can have small volumes in which the flow variables are approximately constant, but which still have very large numbers of particles within them, so that a fluid description is still meaningful within these volumes. As we will see in the following sections, this is a fundamental assumption necessary for deriving the gasdynamic equations.

5.2 Macroscopic derivation

Let us consider a control volume element V, surrounded by a surface S, which has a fixed position and shape as a function of time. Such a fixed volume element (surrounded by an immaterial surface) is called an "Eulerian" control volume. The gas freely flows through this control volume (see Fig. 5.1).

5.3 Fluxes

Let us consider a fixed surface element ΔS, through which the gas flows at a velocity $\underline{u}$. From the diagram shown in Figure 5.2, it is clear that all of the material within the volume

$$\Delta V = u_n \, \Delta t \, \Delta S \tag{5.1}$$

(where u_n is the flow velocity normal to the surface element) goes through ΔS in a time Δt.

Therefore, if we have any volumetric quantity A of the flow (for example, we could have $A = \rho$, the mass density of the gas), the flux of this quantity through a unit surface is :

$$F_A = \frac{A \Delta V}{\Delta t \, \Delta S} = A u_n \, . \tag{5.2}$$

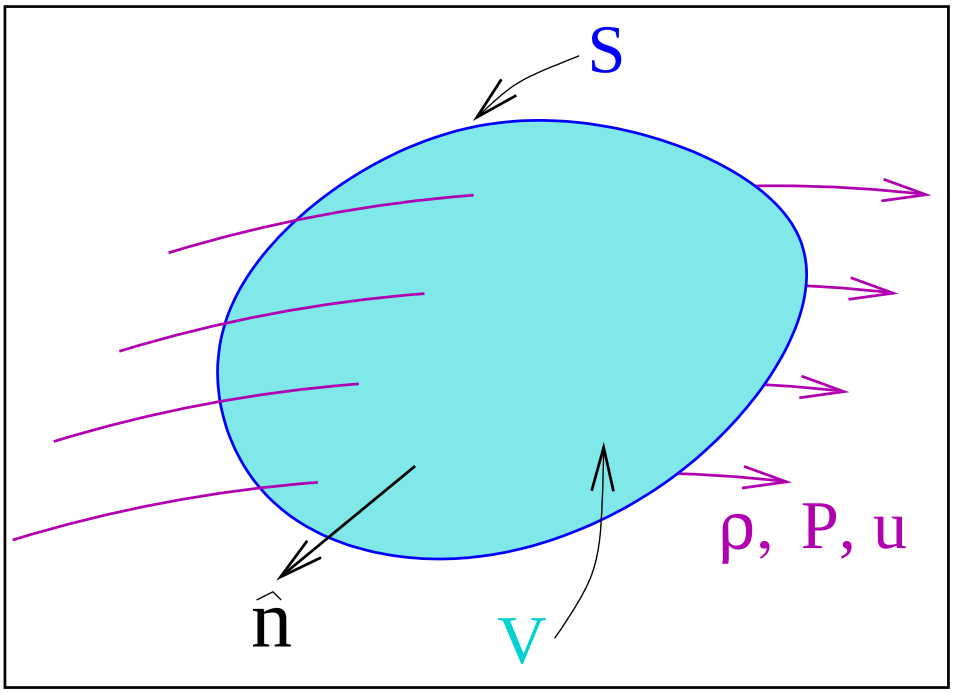

Figure 5.1: An imaginary, fixed ("Eulerian") control volume through which flows a continuous medium of density ρ, pressure P and flow velocity $\underline{u}$. The volume V is surrounded by the surface S. The surface has an outward pointing normal unit vector $\hat{n}$.

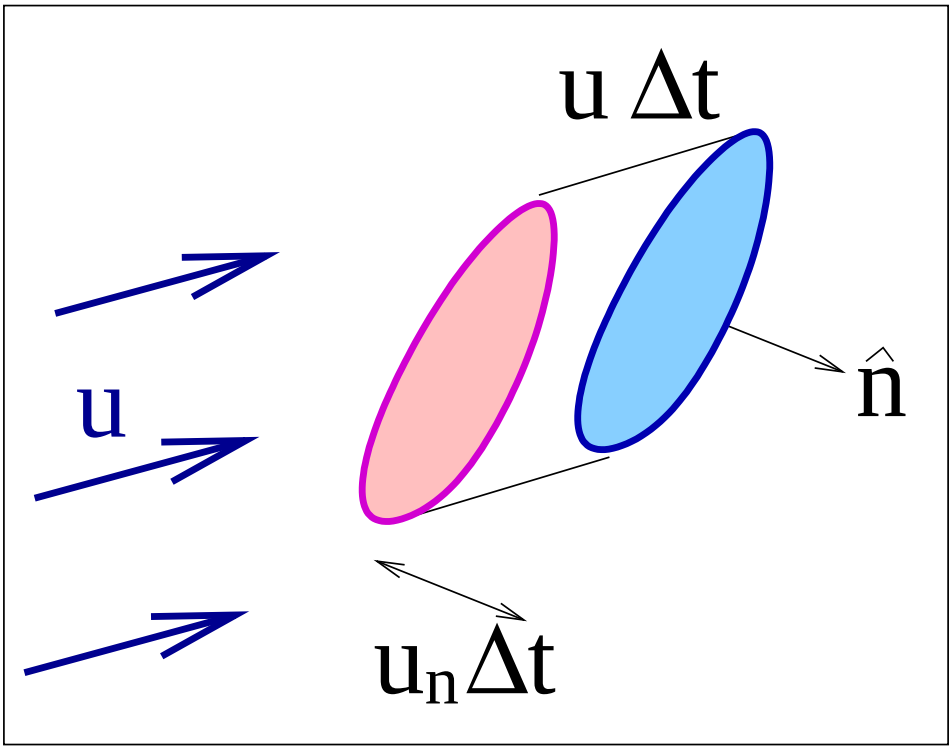

Figure 5.2: The gas (with velocity $\underline{u}$) flows through a fixed surface element (in blue) ΔS, with normal vector $\hat{n}$.

For example, for the $A = \rho$ case, F_A corresponds to the mass per unit area and time going through a surface oriented such that u_n is the normal velocity.

One can then define a vector flux

$$\underline{F_A} = A\underline{u}\,, \tag{5.3}$$

and the mass going through a surface with normal unit vector $\hat{n}$ (per unit area and time) is then given by

$$F_A = \underline{F_A} \cdot \hat{n}\,. \tag{5.4}$$

5.4 The continuity equation

Let us now consider the mass

$$M = \iiint_V \rho\, d^3x \tag{5.5}$$

within the control volume V shown in Figure 5.1, where ρ is the mass density of the gas. In the absence of mass sources or sinks, M will change only as the result of the net mass going in/out through the surface S :

$$\frac{\partial M}{\partial t} = -\oiint_S \rho\underline{u} \cdot \hat{n}\, dS\,, \tag{5.6}$$

where $\rho\underline{u}$ is the mass flux (see §3.3), the "$-$" sign accounts for the fact that $\hat{n}$ points outwards. Combining equations (5.5-5.6), using Gauss's theorem for converting the surface integral into a volume integral and commuting the time derivative with the volume integral, we then obtain :

$$\iiint_V \left[\frac{\partial \rho}{\partial t} + \nabla \cdot (\rho\underline{u})\right] d^3x = 0\,. \tag{5.7}$$

The final step is obtained by noting that for a volume $V \ll L^3$ (where L is the characteristic length of variations along the flow), the integral in eq. (5.7) will have a value $= [\,]\,V$, where the integrand "$[\,]$" is evaluated in any point within the volume V. We should note that for a fluid approximation to be valid, a

volume satisfying the $V \ll L^3$ condition can still have a very large number of particles within it (see §3.1). Therefore, eq. (5.7) implies that

$$\frac{\partial \rho}{\partial t} + \nabla \cdot (\rho \underline{u}) = 0 \,, \tag{5.8}$$

for all times and positions. This differential equation is called the "continuity equation" of gasdynamics.

5.5 The momentum equation

Let us now consider the momentum along the i-th direction

$$\Pi_i = \iiint_V \rho u_i \, d^3x \tag{5.9}$$

within the control volume V shown in Figure 5.1, where u_i ($i = 1, 2, 3$) is the i-th component of the flow velocity.

The momentum conservation equation can then be written as :

$$\frac{\partial \Pi_i}{\partial t} = - \oiint_S \rho u_i \underline{u} \cdot \hat{n} \, dS - \oiint_S P \hat{e}_i \cdot \hat{n} \, dS \,, + \iiint_V f_i \, d^3x \tag{5.10}$$

where the first term on the right represents the net amount of i-th momentum going in or out through the surface of the volume element (see Fig. 5.1), the second term is the i-th component of the force of the gas pressure on the volume element, and the third term represents the force on the volume due to an external force (per unit volume) f_i acting on the flow along the i-th direction (this could be, e. g., the force due to gravity). The $\hat{e}_i$ are the unit vectors along the coordinate axes.

Following the method of §3.4, from eq. (5.10) we derive :

$$\frac{\partial \rho u_i}{\partial t} + \nabla \cdot (\rho u_i \underline{u}) + \frac{\partial P}{\partial x_i} = f_i \,. \tag{5.11}$$

For the case of a gravitational force, we would have $f_i = \rho g_i$ (with g_i the i-th component of the gravitational acceleration).

5.6 The energy equation

We now consider the equation for the kinetic+thermal energy per unit volume

$$E = \frac{1}{2}\rho u^2 + \frac{P}{\gamma - 1}\,, \tag{5.12}$$

where u is the modulus of the flow velocity and $\gamma = C_p/C_v$ is the specific heat ratio ($= 5/3$ for a monoatomic gas, and $= 7/5$ for diatomic molecules with thermalized rotation states).

For deriving the equation we consider the energy flux $E\underline{u}$, the work $P\underline{u}$ of the pressure force on the surface of the control volume, the work $\underline{f} \cdot \underline{u}$ of possible external forces $\underline{f}$ (per unit volume), and the net energy gain/loss per unit volume $G - L$ due to emission/absorption of radiation. Following the method of §3.4, one obtains the energy equation :

$$\frac{\partial E}{\partial t} + \nabla \cdot [\underline{u}\,(E + P)] = G - L + \underline{f} \cdot \underline{u}\,. \tag{5.13}$$

The "gasdynamic" or "Euler" equations (eqs. 5.8, 5.11 and 5.13) are a closed set of differential equations from which one can in principle derive ρ, $\underline{u}$ and P as a function of position and time, for any given set of initial and boundary conditions. In the following sections, we present the Euler equations in different notations and for different coordinate systems.

5.7 Different forms of the Euler equations

5.7.1 Using Einstein's notation

Continuity equation :

$$\frac{\partial \rho}{\partial t} + \frac{\partial}{\partial x_i}\,(\rho u_i) = 0\,, \tag{5.14}$$

Momentum equation :

$$\frac{\partial \rho u_j}{\partial t} + \frac{\partial}{\partial x_i}\,(\rho u_i u_j + P\delta_{ij}) = f_i\,, \tag{5.15}$$

Energy equation :

$$\frac{\partial E}{\partial t} + \frac{\partial}{\partial x_i}\left[u_i\left(E+P\right)\right] = G - L + f_i u_i\,, \tag{5.16}$$

where $E = u_i u_i/2 + P/(\gamma - 1)$.

In these equations, i, j =1, 2, 3 represent the three coordinates of a Cartesian reference system. If one of these indexes appears twice in one term, a sum from 1 to 3 is implied. For example,

$$u_i u_i = \sum_{i=1}^{3} u_i u_i\,, \tag{5.17}$$

$$\frac{\partial}{\partial x_i}\left(\rho u_i u_j\right) = \sum_{i=1}^{3} \frac{\partial}{\partial x_i}\left(\rho u_i u_j\right)\,. \tag{5.18}$$

5.7.2 In vector/tensor notation

Continuity equation :

$$\frac{\partial \rho}{\partial t} + \nabla \cdot \left(\rho \underline{u}\right) = 0\,, \tag{5.19}$$

Momentum equation :

$$\frac{\partial \rho \underline{u}}{\partial t} + \nabla \cdot \left(\rho \underline{u}\underline{u} + P\underline{\underline{I}}\right) = \underline{f}\,, \tag{5.20}$$

Energy equation :

$$\frac{\partial E}{\partial t} + \nabla \cdot \left[\underline{u}\left(E+P\right)\right] = G - L + \underline{f} \cdot \underline{u}\,. \tag{5.21}$$

In the momentum equation, $\underline{\underline{I}} = \delta_{ij}$ is the unit second rank tensor. A Cartesian coordinate system is assumed.

5.7.3 Cartesian equations, all terms written explicitly

Following the normal notation used in gasdynamics, we name (u, v, w) the three components of the flow velocity $\underline{u}$, along the axes of an (x, y, z), Cartesian reference system.

Continuity equation :

$$\frac{\partial \rho}{\partial t} + \frac{\partial}{\partial x}\rho u + \frac{\partial}{\partial y}\rho v + \frac{\partial}{\partial z}\rho w = 0\,, \tag{5.22}$$

Momentum equation(s) :

$$\frac{\partial}{\partial t}\rho u + \frac{\partial}{\partial x}\rho u^2 + \frac{\partial}{\partial y}\rho uv + \frac{\partial}{\partial z}\rho uw + \frac{\partial P}{\partial x} = f_x\,, \tag{5.23}$$

$$\frac{\partial}{\partial t}\rho v + \frac{\partial}{\partial x}\rho uv + \frac{\partial}{\partial y}\rho v^2 + \frac{\partial}{\partial z}\rho vw + \frac{\partial P}{\partial y} = f_y\,, \tag{5.24}$$

$$\frac{\partial}{\partial t}\rho w + \frac{\partial}{\partial x}\rho uw + \frac{\partial}{\partial y}\rho vw + \frac{\partial}{\partial z}\rho w^2 + \frac{\partial P}{\partial z} = f_z\,, \tag{5.25}$$

Energy equation :

$$\begin{aligned}\frac{\partial E}{\partial t} + \frac{\partial}{\partial x}u(E+P) + \frac{\partial}{\partial y}v(E+P) + \frac{\partial}{\partial z}w(E+P)& \\ = G - L + uf_x + vf_y + wf_z\,,& \end{aligned}\tag{5.26}$$

where $E = \rho(u^2 + v^2 + w^2)/2 + P/(\gamma - 1)$.

5.7.4 2D Cartesian equations, all terms written explicitly

We name (u, v) the two components of the flow velocity $\underline{u}$, along the axes of an (x, y), Cartesian reference system.

Continuity equation :

$$\frac{\partial \rho}{\partial t} + \frac{\partial}{\partial x}\rho u + \frac{\partial}{\partial y}\rho v = 0\,, \tag{5.27}$$

Momentum equation(s) :

$$\frac{\partial}{\partial t}\rho u + \frac{\partial}{\partial x}\rho u^2 + \frac{\partial}{\partial y}\rho uv + \frac{\partial P}{\partial x} = f_x\,, \tag{5.28}$$

$$\frac{\partial}{\partial t}\rho v + \frac{\partial}{\partial x}\rho uv + \frac{\partial}{\partial y}\rho v^2 + \frac{\partial P}{\partial y} = f_y\,, \tag{5.29}$$

Energy equation :

$$\frac{\partial E}{\partial t} + \frac{\partial}{\partial x}u(E+P) + \frac{\partial}{\partial y}v(E+P) = G - L + uf_x + vf_y\,, \tag{5.30}$$

where $E = \rho(u^2+v^2)/2 + P/(\gamma-1)$.

5.7.5 2D cylindrical equations, all terms written explicitly

We name (u, v) the two components of the flow velocity $\underline{u}$, along the axes of an (z, r), cylindrical reference system.

Continuity equation :

$$\frac{\partial \rho}{\partial t} + \frac{\partial}{\partial z}\rho u + \frac{\partial}{\partial r}\rho v + \frac{\rho v}{r} = 0\,, \tag{5.31}$$

Momentum equation(s) :

$$\frac{\partial}{\partial t}\rho u + \frac{\partial}{\partial z}\rho u^2 + \frac{\partial}{\partial r}\rho uv + \frac{\partial P}{\partial z} + \frac{\rho uv}{r} = f_z\,, \tag{5.32}$$

$$\frac{\partial}{\partial t}\rho v + \frac{\partial}{\partial z}\rho uv + \frac{\partial}{\partial r}\rho v^2 + \frac{\partial P}{\partial r} + \frac{\rho v^2}{r} = f_r\,, \tag{5.33}$$

Energy equation :

$$\frac{\partial E}{\partial t} + \frac{\partial}{\partial x}u(E+P) + \frac{\partial}{\partial r}v(E+P) + \frac{v(E+P)}{r} = G - L + uf_z + vf_r\,, \quad (5.34)$$

where $E = \rho(u^2+v^2)/2 + P/(\gamma-1)$.

5.7.6 1D equations

Continuity equation :

$$\frac{\partial \rho}{\partial t} + \frac{\partial}{\partial x}\rho u + \frac{\eta \rho u}{x} = 0\,, \quad (5.35)$$

Momentum equation :

$$\frac{\partial}{\partial t}\rho u + \frac{\partial}{\partial x}(\rho u^2 + P) + \frac{\eta \rho u^2}{x} = f\,, \quad (5.36)$$

Energy equation :

$$\frac{\partial E}{\partial t} + \frac{\partial}{\partial x}u(E+P) + \frac{\eta u(E+P)}{x} = G - L + uf\,, \quad (5.37)$$

where $E = \rho u^2/2 + P/(\gamma-1)$. For $\eta = 0$, 1 and 2, we have the 1D Cartesian, cylindrical (with $x = r$, the cylindrical radius) and spherical (with $x = R$, the spherical radius) Euler equations, respectively.

5.8 Gasdynamic equations in Lagrangean form

5.8.1 General form

The "Lagrangean" description of a flow is based on considering a "Lagrangean" fluid parcel, which moves and changes shape following the motion and distortion of the fluid. The free variables in such a description are the initial coordinates $\underline{x}_0$ of all fluid parcels, and the time t. The position of the parcels $\underline{x}$ is obtained as a function of $\underline{x}_0$ and t through the solution to the gasdynamic equations.

Using the chain rule, it is evident that

$$\frac{d}{dt}[\,] = \frac{\partial}{\partial t}[\,] + \underline{u} \cdot \nabla[\,]\,, \tag{5.38}$$

where the total time-derivative is the Lagrangean derivative (i. e., following a fluid parcel) and the partial time-derivative is the Eulerian one (i. e., at a fixed spatial position).

One can then take the Euler equations (in the form given by eqs. 5.19-5.21) and combine them with eq. (5.38) to obtain the Lagrangean gasdynamic equations :

Continuity equation :

$$\frac{d\rho}{dt} + \rho \nabla \cdot \underline{u} = 0\,, \tag{5.39}$$

Momentum equation (in the form of Newton's second law) :

$$\rho \frac{d\underline{u}}{dt} + \nabla P = \underline{f}\,, \tag{5.40}$$

Energy equation :

$$\frac{d\epsilon}{dt} + P \frac{d}{dt}\left(\frac{1}{\rho}\right) = \frac{G - L}{\rho}\,, \tag{5.41}$$

where $\epsilon = P/(\gamma - 1)\rho$ is the thermal energy per unit mass of the gas.

It is also possible to combine the terms of Eq. (5.41) to derive the "entropy equation" :

$$\frac{d}{dt}\left(P\rho^{-\gamma}\right) = \frac{(\gamma - 1)}{\rho^{\gamma}}\left(G - L\right)\,, \tag{5.42}$$

with $S = \ln\left(P\rho^{-\gamma}\right)$ being the specific entropy of the gas.

5.8.2 1D equations

In the 1D case, it is possible to use a mass coordinate:

$$m = \int \rho r^{p} dr\,, \tag{5.43}$$

(where $p = 0$ for the plane-parallel, $p = 1$ for the cylindrical and $p = 2$ for the spherically symmetric case) instead of a spatial coordinate.

The Euler equations then take the form:

$$\frac{\partial}{\partial t}\left(\frac{1}{\rho}\right) - \frac{\partial}{\partial m}\left(r^p u\right) = 0\,, \tag{5.44}$$

$$\frac{\partial u}{\partial t} + r^p \frac{\partial P}{\partial m} = 0\,, \tag{5.45}$$

$$\frac{\partial}{\partial t}\left[\frac{P}{(\gamma-1)\rho} + \frac{u^2}{2}\right] + \frac{\partial}{\partial m}\left(r^p P u\right) = 0\,, \tag{5.46}$$

where ρ is the density, u the flow velocity and P the pressure. The external forces and energy gains/losses have been set to zero.

Chapter 6

Sound waves and linear stability analysis

6.1 General considerations

In this chapter we discuss how to linearize the gasdynamic equations, and use this method to derive a few simple solutions. These are plane sound waves, and plane Kelvin-Helmholtz and Rayleigh-Taylor instabilities.

6.2 Sound waves

Let us consider the propagation of a 1D (plane) sound wave. A sound wave is defined as a small perturbation (in density, velocity and pressure) which travels through a gas. We will consider the most simple case of a medium which is initially homogeneous (with constant density ρ_0 and pressure P_0) and at rest (zero velocity). We then write the perturbed density, pressure and velocity as

$$P + P_0\,, \quad \rho + \rho_0\,, \quad u\,, \tag{6.1}$$

with $P \ll P_0$, $\rho \ll \rho_0$ and u "with small values" (we will discuss later what this actually means).

If we insert these variables into the 1D, plane gasdynamic equations (eqs.

5.35-5.37), we obtain

$$\frac{\partial}{\partial t}\left[\rho+\rho_0\right]+\frac{\partial}{\partial x}\left[\left(\rho+\rho_0\right)u\right]=0\,, \tag{6.2}$$

$$\frac{\partial}{\partial t}\left[\left(\rho+\rho_0\right)u\right]+\frac{\partial}{\partial x}\left[\left(\rho+\rho_0\right)u^2+P+P_0\right]=0\,, \tag{6.3}$$

$$\frac{\partial}{\partial t}\left[E\right]+\frac{\partial}{\partial x}\left[u\left(E+P+P_0\right)\right]=0\,, \tag{6.4}$$

with $E=(\rho+\rho_0)u^2/2+(P+P_0)/(\gamma-1)$.

We now consider that ρ_0 and P_0 are constant, and we neglect all terms with quadratic or cubic dependence on the perturbations (and their spatial or time derivatives). In practice we eliminate all terms involving the terms ρu, u^2 or uP. In this way, we obtain the linearized, plane gasdynamic equations :

$$\frac{\partial\rho}{\partial t}+\rho_0\frac{\partial u}{\partial x}=0\,, \tag{6.5}$$

$$\rho_0\frac{\partial u}{\partial t}+\frac{\partial P}{\partial x}=0\,, \tag{6.6}$$

$$\frac{\partial P}{\partial t}+\gamma P_0\frac{\partial u}{\partial x}=0\,. \tag{6.7}$$

We now play at combining these equations to obtain differential equations for each of the perturbed variables (ρ, P and u). For example, if we take the time derivative of eq. (6.6), and subtract from this the spatial derivative of eq. (6.7), we obtain

$$\frac{\partial^2 u}{\partial t^2}-\frac{\gamma P_0}{\rho_0}\frac{\partial^2 u}{\partial x^2}=0\,. \tag{6.8}$$

Through combinations of eqs. (6.5-6.7) we find that the other two perturbed quantities (ρ and P) follow the same differential equation. Therefore, all three variables f satisfy the differential equation

$$\frac{\partial^2 f}{\partial t^2}-c_s^2\frac{\partial^2 f}{\partial x^2}=0\,, \tag{6.9}$$

with

$$c_s\equiv\sqrt{\frac{\gamma P_0}{\rho_0}}\,. \tag{6.10}$$

Eq. (6.9) allows any solution of the form $f(x - c_s t)$ or $f(x + c_s t)$ (or linear combinations of these two forms), corresponding to waves travelling in the $-x$ or $+x$ directions (respectively). These waves travel at the sound speed c_s, defined by eq. (6.10). The linear waves correspond to small velocity perturbations with $u \ll c_s$.

6.3 Isothermal sound waves

In ISM flows, it is common to assume that the flow is approximately isothermal. This is a reasonable approximation, e. g., for flows within H II regions in which the rapid heating/cooling processes tend to fix the temperature at a value $T_0 \approx 10^4$ K. In order to model sound waves in such an environment, one uses the linearized continuity and momentum equations (eqs. 6.5-6.6), and replaces the energy equation with the condition

$$P = \rho \frac{RT_0}{\mu}\,, \tag{6.11}$$

where R is the gas constant and μ the molecular weight. The molecular weight is $\mu = m/m_H$, where m is the average mass of the gas particles and m_H is the mass of Hydrogen.

The solution of this system of equations corresponds to waves that travel at a velocity

$$c_{is} = \sqrt{\frac{RT_0}{\mu}} = \sqrt{\frac{P_0}{\rho_0}}\,. \tag{6.12}$$

This is called the "isothermal sound speed", which coincides with the "adiabatic" sound speed (see eq. 6.10) evaluated for a $\gamma = 1$ specific heat ratio.

6.4 Kelvin-Helmholtz instability

We consider the interface between two parallel flows with different velocities U_a (for $y > 0$) and U_b (for $y < 0$), with corresponding densities ρ_a and ρ_b. We write the Euler equations in a reference frame with x parallel to the flow velocity,

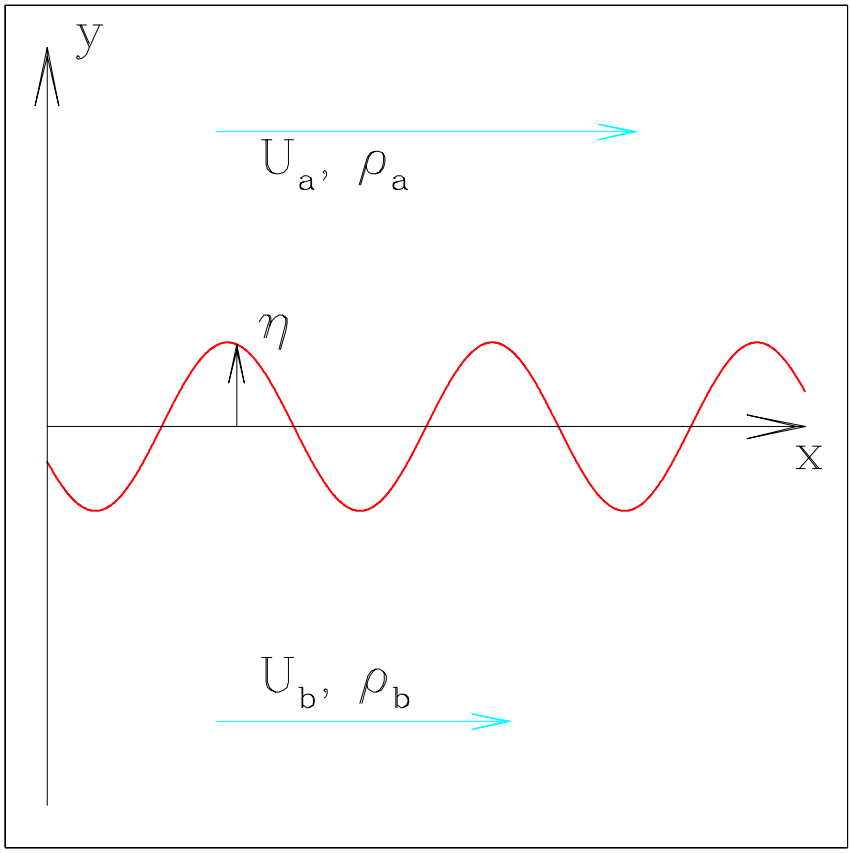

Figure 6.1: Schematic diagram of the interface between two parallel flows of velocities U_a and U_b and densities ρ_a and ρ_b. The interface initially lies on the $y = 0$ axis, but is perturbed at later times, following the $\eta(x, t)$ curve.

and y perpendicular to the interface, as shown in the schematic diagram of Figure (6.1).

We consider the 2D flow equations, the incompressible (!) continuity equation:

$$\frac{\partial u}{\partial x} + \frac{\partial v}{\partial y} = 0\,, \tag{6.13}$$

the x-component of the momentum equation in the form of Newton's law:

$$\frac{\partial u}{\partial t} + u\frac{\partial u}{\partial x} + v\frac{\partial u}{\partial y} = -\frac{1}{\rho}\frac{\partial P}{\partial x}\,, \tag{6.14}$$

and the y-component:

$$\frac{\partial v}{\partial t} + u\frac{\partial v}{\partial x} + v\frac{\partial v}{\partial y} = -\frac{1}{\rho}\frac{\partial P}{\partial y}\,, \tag{6.15}$$

where u and v are the flow velocities along the x- and y-axes (respectively), and P is the gas pressure. The density ρ has a value ρ_a for the top flow, and ρ_b for the bottom flow (see Figure 6.1). These two flows are initially separated by the $y = 0$ axis, but at larger times the boundary is perturbed, and has a shape $y = \eta(x, t)$ (see Figure 6.1) with an associated vertical velocity v_η given by:

$$v_\eta = \frac{\partial \eta}{\partial t} + u\frac{\partial \eta}{\partial x}\,. \tag{6.16}$$

We now propose small perturbations on the flow variables, so that $u \to U + u$ (where U has a value U_a for the top flow and U_b for the bottom flow) with $u \ll U$, and $P \to \overline{P} + P$, (with constant P_0) with $P \ll \overline{P}$. Also, we assume thast v is small.

We then re-write equations (6.13-6.16) keeping only linear terms in u, v, P and their derivatives, obtaining:

$$\frac{\partial u}{\partial x} + \frac{\partial v}{\partial y} = 0\,, \tag{6.17}$$

unchanged with respect to the full equation (6.13),

$$\frac{\partial u}{\partial t} + U\frac{\partial u}{\partial x} = -\frac{1}{\rho}\frac{\partial P}{\partial x}\,, \tag{6.18}$$

$$\frac{\partial v}{\partial t} + U\frac{\partial v}{\partial x} = -\frac{1}{\rho}\frac{\partial P}{\partial y}\,, \tag{6.19}$$

and

$$v_\eta = \frac{\partial \eta}{\partial t} + U\frac{\partial \eta}{\partial x}\,. \tag{6.20}$$

In these equations. $U = U_a$ and $\rho = \rho_a$ for the top flow, and $U = U_b$. $\rho = \rho_b$ for the bottom flow.

We now propose a solution of the form:

$$u = e^{-i(kx-nt)}u_0(y)\,, \tag{6.21}$$

$$v = e^{-i(kx-nt)}v_0(y)\,, \tag{6.22}$$

$$P = e^{-i(kx-nt)}P_0(y)\,, \tag{6.23}$$

and

$$\eta = e^{-i(kx-nt)}\eta_0\,, \tag{6.24}$$

with constant n, k and η_0. We suppose that the x-dependence is a sine/cosine, so that k is real. On the other hand, n is complex. with an imaginary part which is the "growth rate" giving an exponential rise/decay of the solution.

Now, substituting these equations into equations (6.17-6.20) we obtain:

$$\frac{\partial v}{\partial y} = iku\,, \tag{6.25}$$

$$\frac{kP}{\rho} = (n - kU)u\,, \tag{6.26}$$

$$\frac{1}{\rho}\frac{\partial P}{\partial y} = i(n - kU)v\,, \tag{6.27}$$

and

$$v_\eta = i(n - kU)\eta\,. \tag{6.28}$$

Equations (6.25-6.28) are the result of substituting the proposed solution (equations 6.21-6.24) into the linearized equations (6.17-6.20).

We now take the y-derivative of equation (6.27), and combine it with equations (6.25-6.26) to obtain:

$$\frac{\partial^2 P}{\partial y^2} = k^2 P\,, \tag{6.29}$$

which can be integrated to obtain:

$$P_0(y) = p_0 e^{-ky}\,,\;\; y > 0\;;\quad P_0(y)) = p_0 e^{ky}\,,\;\; y < 0\,, \tag{6.30}$$

where we have chosen the non-divergent exponentials for the top and bottom flows. We should note that the boundary between the two flows lies on $y = 0$ only for $t = 0$, and here (consistent with the linearity of the equations) we are not considering the perturbation of the boundary for $t > 0$.

Now, substituting equations (6.30) and (6.28) into equation (6.27), for $y \to \eta^+$ we have:

$$\frac{kP_a}{\rho_a} = -(n - kU_a)^2\eta\,, \tag{6.31}$$

and for $y \to \eta^-$:

$$\frac{kP_b}{\rho_b} = -(n - kU_b)^2\eta\,, \tag{6.32}$$

where P_a and P_b are the pressures on both sides of the interface. The $P_a = P_b$ condition then gives:

$$(n - kU_a)^2\rho_a = -(n - kU_b)^3\rho_b\,, \tag{6.33}$$

with solution

$$n = k\left[\frac{\rho_a U_a + \rho_b U_b}{\rho_a + \rho_b} \pm i\sqrt{\rho_a\rho_b}\left(\frac{|U_a - U_b|}{\rho_a + \rho_b}\right)\right]\,. \tag{6.34}$$

Therefore, n has a non-zero imaginary part (with both signs) that gives an exponential growth for perturbations of all spatial wavenumbers k.

This "Kelvin-Helmholtz instability" gives rise to turbulence at the boundary between two flows of different velocities (e.g., at the outer boundary of a jet beam). There is an extended literature of the application of this instability, including the effect of having a compressible flow, as well as the incorporation of different geometries, to astrophysical flows.

6.5 Rayleigh-Taylor instability

It is possible to carry out the analysis of the previous section also including the presence of an external gravitational acceleration g in the $-y$ direction.

Following a similar derivation, one obtains a dispersion relation of the form:

$$n = k\left[\frac{\rho_a U_a + \rho_b U_b}{\rho_a + \rho_b} \pm \sqrt{\frac{g}{k}\frac{\rho_b - \rho_a}{\rho_a + \rho_b} - \rho_a\rho_b\left(\frac{U_a - U_b}{\rho_a + \rho_b}\right)^2}\right], \tag{6.35}$$

This dispersion relation shows that in the $\rho_b > \rho_a$ case ("heavy fluid on the bottom"), n is real if

$$k \leq \frac{g}{\rho_a\rho_b}\frac{\rho_a^2 - \rho_b^2}{(U_a - U_b)^2}, \tag{6.36}$$

corresponding to stable solutions. The interface becomes unstable only if this condition is not met. It has been written in the astrophysical literature that this "stability limit" provides an explanation of the appearance of waves for a strong enough wind blowing over a surface of water. However, checking the geophysical literature one rapidly sees that the formation of waves requires a considerably more complex analysis.

If one sets $U_a = U_b$, for $\rho_a > \rho_b$ ("heavy fluid on top") one still has an imaginary part of n (with both positive and negative values), leading to an unstable growth of perturbations. This is called the "Rayleigh-Taylor instability", and also has extensive astrophysical applications.

Chapter 7

Shock waves

7.1 General considerations

As in general astrophysical flows range from transonic to hypersonic conditions, an understanding of shock waves is essential. Shock waves are generally produced in supersonic flows.

For example, in Fig. 7.1 we show a numerical simulation of the steady flow pressure stratification produced by a blunt bullet moving at a $M = 30$ Mach number within a uniform, $\gamma = 7/5$ medium. It is clear that the pressure shows two surfaces with discontinuous pressure increases. These two shock waves are called the "bow shock" and the "tail shock".

Many astrophysical flows produce directly observable shock waves. Notable examples are jets (from stars or from massive compact objects) and supernovae.

7.2 Plane-parallel shock waves

Let us now consider the simplest possible shock wave problem : a plane shock wave moving along the direction normal to the shock surface. If we consider a coordinate system moving with the shock wave, with the x-axis pointing towards the post-shock direction, we have the situation shown in Fig. 7.2.

The transition from the pre-shock flow variables (ρ_0, u_0 and P_0, see Fig. 7.2)

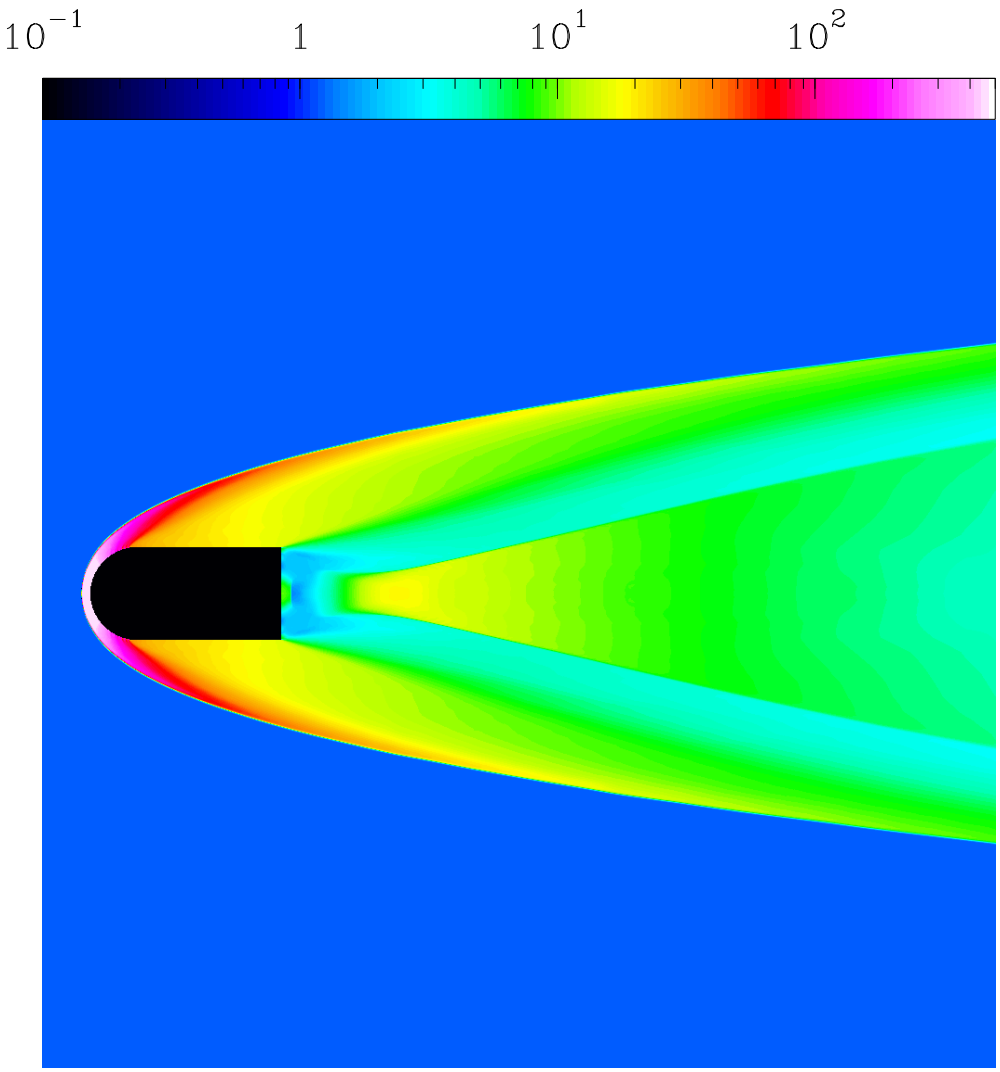

Figure 7.1: Pressure stratification in a blunt bullet flow moving at $M = 30$ in a $\gamma = 7/5$ gas, well into the hypersonic regime.

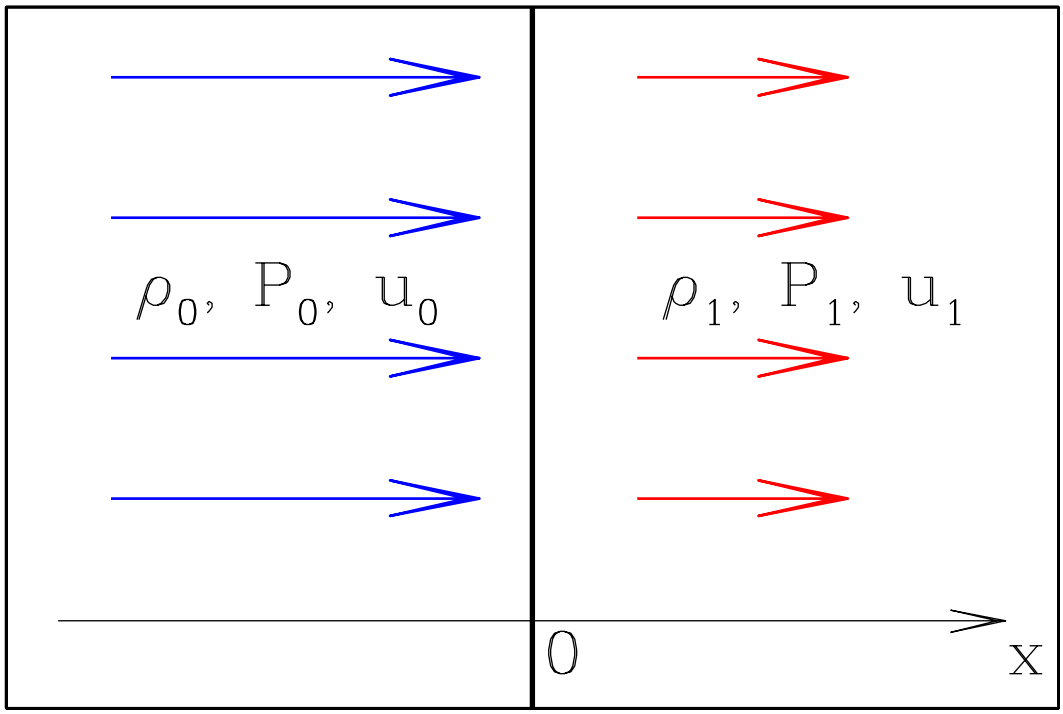

Figure 7.2: Schematic diagram of a plane-parallel shock, seen in a coordinate system which travels with the shock, which at all times is then located at $x = 0$.

to the post-shock variables (ρ_1, u_1 and P_1) occurs over distances comparable to the mean free path λ of the particles in the gas. Therefore, the transition is generally not appropriately described by the gasdynamic equations, and a kinetic approach has to be used.

Because shock waves correspond to discontinuous solutions of the gasdynamic equations, the mass, momentum and energy gasdynamic equations (eqs. 5.35-5.37) do give the appropriate relations between the pre- and post-shock variables. However, a description of the details of the transition lie beyond a gasdynamic description.

In the reference system moving with the shock wave (see Fig. 7.2) the problem has no time-dependence. Hence, the 1D gasdynamic equations simplify to : $\rho u = const.$, $\rho u^2 + P = const.$, $u(E+P) = const.$ (with $E = \rho u^2/2 + P/(\gamma-1)$), where we have assumed that the energy loss/gain within the shock transition is negligible. Therefore, the pre- and post-shock variables follow the relations :

$$\rho_0 u_0 = \rho_1 u_1 \,, \tag{7.1}$$

$$\rho_0 u_0^2 + P_0 = \rho_1 u_1^2 + P_1 \,, \tag{7.2}$$

$$u_0 \left(\frac{\rho_0 u_0^2}{2} + \frac{\gamma P_0}{\gamma - 1} \right) = u_1 \left(\frac{\rho_1 u_1^2}{2} + \frac{\gamma P_1}{\gamma - 1} \right) . \tag{7.3}$$

From these equations, we can find the postshock variables (ρ_1, u_1 and P_1) as a function of the preshock variables (ρ_0, u_0 and P_0)

In order to do this, we first combine eqs. (7.1-7.2) to obtain :

$$P_1 = P_0 + \rho_0 u_0^2 \left(1 - \frac{\rho_0}{\rho_1} \right) . \tag{7.4}$$

Substituting u_1 (from eq. 7.1) and P_1 (from eq. 7.4) into eq. (7.3), we obtain a quadratic equation for ρ_1/ρ_0 :

$$\left(\frac{\rho_1}{\rho_0} \right)^2 \left[\frac{(\gamma-1)M_0^2}{2} + 1 \right] - \left(\frac{\rho_1}{\rho_0} \right) \left(\gamma M_0^2 + 1 \right) + \frac{(\gamma+1)M_0^2}{2} = 0 \,, \tag{7.5}$$

where $M_0 = u_0/c_0$, with $c_0 = \sqrt{\gamma P_0/\rho_0}$. This equation has solutions

$$\frac{\rho_1}{\rho_0} = \frac{\gamma M_0^2 + 1 \pm \sqrt{(M_0^2-1)^2}}{(\gamma-1)M_0^2 + 2} \,, \tag{7.6}$$

giving $\rho_1/\rho_0 = 1$ for the "$-$" sign, and giving the compression at a shock wave for the "+" sign :

$$\frac{\rho_1}{\rho_0} = \frac{(\gamma+1)M_0^2}{(\gamma-1)M_0^2+2}\,. \tag{7.7}$$

Combining eqs. (7.7) and (7.1) we then obtain

$$\frac{u_1}{u_0} = \frac{(\gamma-1)M_0^2+2}{(\gamma+1)M_0^2} \quad \left(= \frac{\rho_0}{\rho_1}\right)\,, \tag{7.8}$$

and using eq. (7.4) we finally obtain :

$$P_1 = P_0 + \frac{2(M_0^2-1)}{(\gamma+1)M_0^2}\rho_0 u_0^2\,. \tag{7.9}$$

Eqs. (7.7-7.9) are called the "shock jump relations" (alternatively, the "Rankine-Hugoniot" or just "Hugoniot" relations).

For $M_0 = u_0/c_0 \gg 1$, we obtain the so-called "strong shock" jump relations :

$$\frac{\rho_1}{\rho_0} = \frac{u_0}{u_1} = \frac{\gamma+1}{\gamma-1}\,, \tag{7.10}$$

$$P_1 = \frac{2}{\gamma+1}\rho_0 u_0^2\,. \tag{7.11}$$

As in most cases ISM shocks are indeed hypersonic (i. e., with $M_0 \gg 1$), these strong shock relations are applicable in most of the problems that will be covered in this book.

7.3 Comments on the gasdynamic derivation of the shock jump relations

In the previous section, we have obtained the correct relation between the pre- and post-shock variables of an energy conserving flow. One might question why for this derivation we have chosen to use the energy equation (apart from the mass and momentum equations) rather than the entropy equation (5.42), which for a plane-parallel,time-independent flow is $P\rho^{-\gamma}$=const. .

Our choice of the energy equation is due to the fact that the thermal+kinetic energy (per unit mass) of the flow is conserved when going through a shock, but the entropy is not conserved. The lack of entropy conservation can be verified by calculating the pre- and post-shock entropies with the corresponding sets of flow variables.

In order to produce the shock transition it is necessary to have a dissipative process that converts kinetic energy of the flow into thermal energy (while keeping a constant thermal+kinetic energy per unit mass). In weak shocks (with $M_0 \sim 1$), the dissipative process can be described in terms of a "viscocity" of the flow, and the shock transition can in principle be described in terms of the viscous gasdynamic (or "Navier-Stokes") equations.

For strong shocks (with $M_0 \gg 1$), a viscous description is not appropriate (because the width of the shock transition is of the same order as the mean free path of the particles), and the full transport equation for the gas particles (the so-called "Boltzmann equation") has to be solved in order to calculate the shock transition. This problem is not addressed in this book, but has some astrophysical applications (basically, in the description of "non-radiative shocks" in supernovae remnants, in which the shock transition is directly observed).

Another astrophysical application of models of the shock transition are the so-called "C-shocks" (the C signifying "continuous"), in which the shock transition in a weakly ionised gas is the result of the drag between ions and neutrals (in particular, through the charge exchange process). The transition between pre- and post-shock variables in these shocks can be fully described with the gasdynamic equations (with two sets of equations describing the neutral and ionised components of the gas, and including appropriate coupling terms). This problem is also not discussed in this book.

7.4 Shock with radiative cooling

From the strong shock jump conditions (eqs. 7.10-7.11), we see that the post-shock temperature T_1 is given by :

$$T_1 = \frac{P_1 \mu m_H}{k \rho_1} = \frac{2(\gamma-1)}{(\gamma+1)^2} \frac{\mu m_H u_0^2}{k} = 1.13 \times 10^5 \, \mathrm{K} \left(\frac{u_0}{100 \, \mathrm{km \, s^{-1}}} \right)^2 , \qquad (7.12)$$

where k is Boltzmann's constant, μ is the molecular weight of the gas and m_H is the mass of H. The third term of the equation was calculated assuming $\gamma = 5/3$ and $\mu = 1/2$ (appropriate for a fully ionised, H gas). We have normalized the relation to a typical $u_0 = 100$ km s^{-1} velocity for a shock in a SNR or in a stellar jet.

This hot gas cools, emitting radiation at IR, optical and UV wavelengths to a temperature of a few thousand K. So, we assume that the cooling region ends when the gas has attained a temperature $T_2 \sim 10^3$ K. At this point, the gas has recombined, and has an isothermal sound speed $c_2 = \sqrt{kT_2/\mu m_H} \sim 3$ km s^{-1}.

We can then use the mass and momentum conservation equations (eqs. 7.1-7.2) to determine the value of ρ_2 after the cooling region. Combining these two equations, we obtain the quadratic equation

$$\rho_2 c_2^2 - \rho_2 \left(u_0^2 + P_0\right) + \rho_0^2 u_0^2 = 0\,, \tag{7.13}$$

which has the shock solution :

$$\frac{\rho_2}{\rho_0} = \frac{c_0^2}{2c_2^2}\left[M_0^2 + 1 + \sqrt{M_0^4 + 2M_0^2(1-2\alpha) + 1}\right]\,, \tag{7.14}$$

where $M_0 = u_0/c_0$ and $\alpha = (c_2/c_0)^2$, with c_0 and c_2 being the pre-shock and post-cooling region isothermal sound speeds (respectively).

The strong shock relation (obtained for $M_0 \gg 1$) then is :

$$\frac{\rho_2}{\rho_0} = \left(\frac{u_0}{c_2}\right)^2\,. \tag{7.15}$$

In other words, the compression is equal to the square of the Mach number $M_{0,2} = u_0/c_2$ computed with the pre-shock velocity and the post-cooling region sound speed.

For the case in which $c_2 = c_0$, we obtain :

$$\frac{\rho_2}{\rho_0} = M_0^2\,. \tag{7.16}$$

This is called the "isothermal shock" jump relation, and is valid for all Mach numbers.

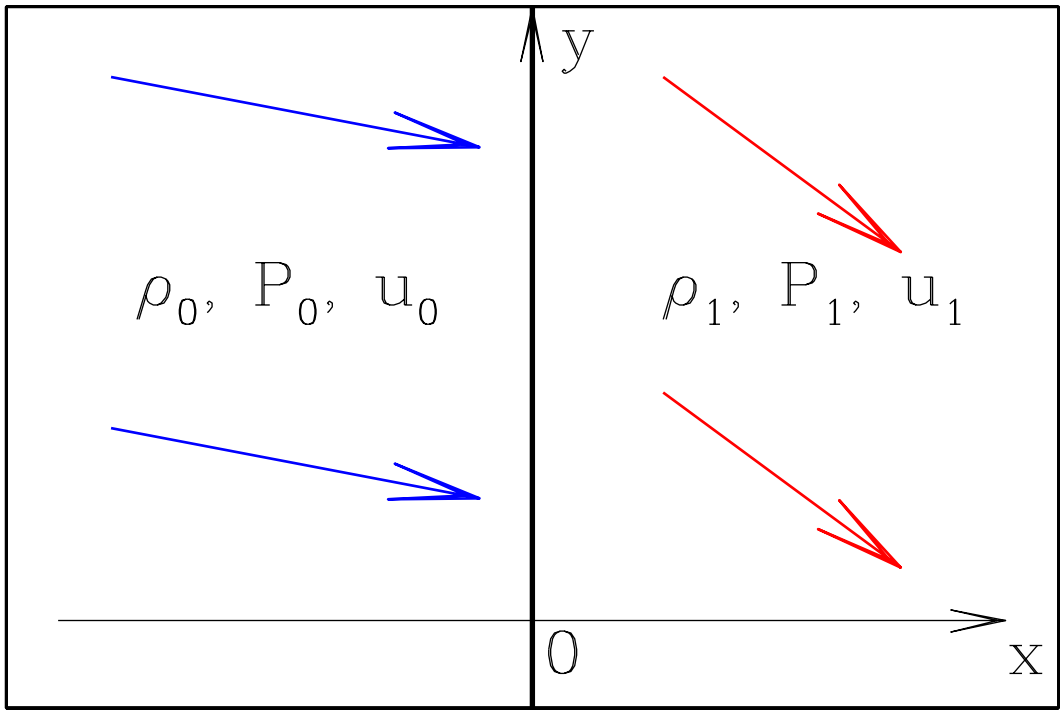

Figure 7.3: Schematic diagram of a plane, oblique shock.

7.5 Oblique shock jump relations

Let us now consider a plane, oblique shock. In such a shock, the flow enters the shock at an angle (with respect to the shock front) different from $\pi/2$, and is refracted at its passage through the shock. This is shown schematically in Fig. 7.3.

Let us consider a Cartesian coordinate system at rest with the shock, with its x-axis pointing along the normal to the plane shock (towards the post-shock region) and its y-axis in the plane that contains the normal to the shock and the pre-shock velocity $\underline{u}_0$. From simple symmetry arguments it is clear that the post-shock velocity $\underline{u}_1$ will also lie on the xy-plane.

We then write the steady, 2D Euler equations (see eqs. 5.27-5.30) with no y-dependence :

$$\frac{\partial}{\partial x}\left(\rho u_n\right) = 0\,, \tag{7.17}$$

$$\frac{\partial}{\partial x}\left(\rho u_n^2 + P\right) = 0\,, \tag{7.18}$$

$$\frac{\partial}{\partial x}\left(\rho u_n u_t\right) = 0\,, \tag{7.19}$$

$$\frac{\partial}{\partial x}\left\{u_n\left[\frac{\rho}{2}\left(u_n^2 + u_t^2\right) + \frac{\gamma P}{\gamma - 1}\right]\right\} = 0\,, \tag{7.20}$$

where u_n and u_t are the components of the flow velocity parallel to the x- and y-axes, respectively (see Fig. 7.3).

From these equations, we can obtain the relations that have to be satisfied between the pre-shock variables (ρ_0, $u_{n,0}$, $u_{t,0}$ and P_0), and the post-shock variables (ρ_1, $u_{n,1}$, $u_{t,1}$ and P_1) :

$$\rho_0 u_{n,0} = \rho_1 u_{n,1}\,, \tag{7.21}$$

$$\rho_0 u_{n,0}^2 + P_0 = \rho_1 u_{n,1}^2 + P_1\,, \tag{7.22}$$

$$\rho_0 u_{n,0} u_{t,0} = \rho_1 u_{n,1} u_{t,1}\,, \tag{7.23}$$

$$u_{n,0}\left[\frac{\rho_0}{2}\left(u_{n,0}^2 + u_{t,0}^2\right) + \frac{\gamma P_0}{\gamma - 1}\right] = u_{n,1}\left[\frac{\rho_1}{2}\left(u_{1,0}^2 + u_{t,1}^2\right) + \frac{\gamma P_1}{\gamma - 1}\right]. \tag{7.24}$$

Eqs. (7.21) and (7.23) can be combined to give the jump condition for the tangential velocity :

$$u_{t,1} = u_{t,0}\,, \tag{7.25}$$

in other words, the component of the velocity parallel to the shock wave is preserved when going through the shock.

Now, combining eqs. (7.21), (7.24) and (7.25), we obtain an energy equation involving only the normal component of the flow velocity :

$$\frac{u_{n,0}^2}{2} + \frac{\gamma}{\gamma - 1}\frac{P_0}{\rho_0} = \frac{u_{n,1}^2}{2} + \frac{\gamma}{\gamma - 1}\frac{P_1}{\rho_1}\,. \tag{7.26}$$

It is clear that eqs. (7.21), (7.22) and (7.23) are the same equation system as the one for a plane-parallel shock (eqs. 7.1-7.3, with eq. 7.26 actually being the ratio between eqs. 7.1 and 7.3). Therefore, the compression and the post-shock pressure are given by eqs. (7.7) and (7.9) :

$$\frac{\rho_1}{\rho_0} = \frac{u_{n,0}}{u_{n,1}} = \frac{(\gamma + 1)M_{n,0}^2}{(\gamma - 1)M_{n,0}^2 + 2}\,, \tag{7.27}$$

$$P_1 = P_0 + \frac{2(M_{n,0}^2 - 1)}{(\gamma + 1)M_{n,0}^2}\rho_0 u_{n,0}^2 \,, \tag{7.28}$$

but with $u_{n,0}$ instead of u_0, and the pre-shock Mach number being replaced with the Mach number $M_{n,0} = u_{n,0}/c_0$ associated with the normal component of the pre-shock velocity.

In the case of a radiative shock, eqs. (7.27-7.28) would have to be replaced with the appropriate jump conditions, obtained by replacing the pre-shock flow velocity u_0 by $u_{n,0}$.

We should note that in most circumstances the oblique shock relations can be applied to arbitrary shocks in a supersonic gas. For example, they can locally be applied to curved shocks, provided that the radius of curvature of the shock is much larger than the thickness of the shock transition. They can also be applied to shocks in time-dependent flows, provided that the evolutionary timescale of the flow is much larger than the time-scale for passage of the gas through the shock transition. These conditions are generally contained by the conditions required for a fluid description to be appropriate (see the beginning of chapter 5).

7.6 Examples of flows with plane shock fronts

7.6.1 Flow colliding normally with a rigid wall

Let us consider the problem of a plane, supersonic wind (of density ρ_w, pressure P_w and velocty v_w) hitting a rigid wall (oriented perpendicular to the direction of the wind velocity). The physical situation is shown in Fig. 7.4.

A shock is formed initially against the wall, and this shock then travels (at a velocity v_s, see Fig. 7.4) in the upstream direction, forming a post-shock region in which the gas is at rest with respect to the wall. In a reference frame moving with the shock, we have a medium with pre-shock flow parameters $\rho_0 = \rho_w$, $P_0 = P_w$ and $u_0 = v_w + v_s$. The fact that the post-shock flow is at rest with respect to the wall implies that $u_1 = v_s$.

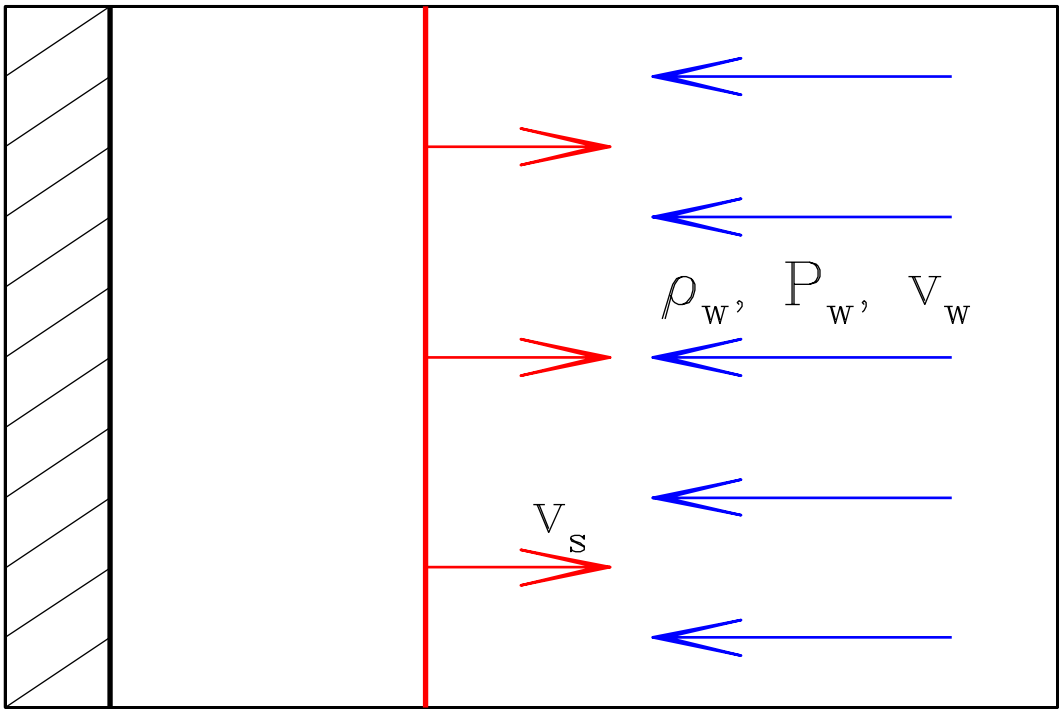

Figure 7.4: Schematic diagram of a flow constituted by a supersonic wind which collides with a solid wall (perpendicular to the direction of the flow).

Using eq. (7.8), we have that

$$\frac{v_w + v_s}{v_s} = \frac{\gamma + 1}{\gamma - 1 + \frac{2c_0^2}{(v_w+v_s)^2}}\,, \tag{7.29}$$

where $c_0 = \sqrt{\gamma P_0/\rho_0}$ is the pre-shock sound speed. From this equation, we can derive a quadratic equation for v_s :

$$2v_s^2 + v_s v_w(3-\gamma) - 2c_0^2 - (\gamma-1)v_w^2 = 0\,, \tag{7.30}$$

which has the solution

$$\frac{v_s}{v_w} = \frac{1}{4}\left[\gamma - 3 + \sqrt{(\gamma+1)^2 + 16(c_0/v_w)^2}\right]\,, \tag{7.31}$$

which in the hypersonic regime ($v_w \gg c_0$) gives

$$\frac{v_s}{v_w} = \frac{\gamma-1}{2}\,. \tag{7.32}$$

7.6.2 Flow hitting a wedge

Let us consider the problem of a supersonic flow which hits the leading edge of a rigid wedge. If the wedge has a small enough half-opening angle ϕ, a "regular shock reflection" occurs. In this configuration, two plane shocks (which are attached to the leading edge) redirect the incoming flow to directions parallel to the two plane surfaces of the wedge (see the top frame of Fig. 7.5). For large enough values of ϕ, instead of a regular shock reflection, a detached bow shock is formed (right frame of Fig. 7.5).

The regular reflection regime has a simple analytic solution. For deriving this solution, we consider one of the two sides of the flow/wedge interaction, as shown in Fig. 7.6. We have a flow which hits the surface of a plane "shelf" (at an angle ϕ to the surface), and an oblique shock (at an angle α to the surface) redirects the incoming flow to a direction parallel to the shelf.

From Fig. 7.6 it is clear that the pre-shock flow (of velocity u_0) has components $u_{n,0}$ and $u_{t,0}$ normal and parallel (respectively) to the shock given by :

$$u_{n,0} = u_0 \sin(\phi+\alpha)\,; \quad u_{t,0} = u_0 \cos(\phi+\alpha)\,. \tag{7.33}$$

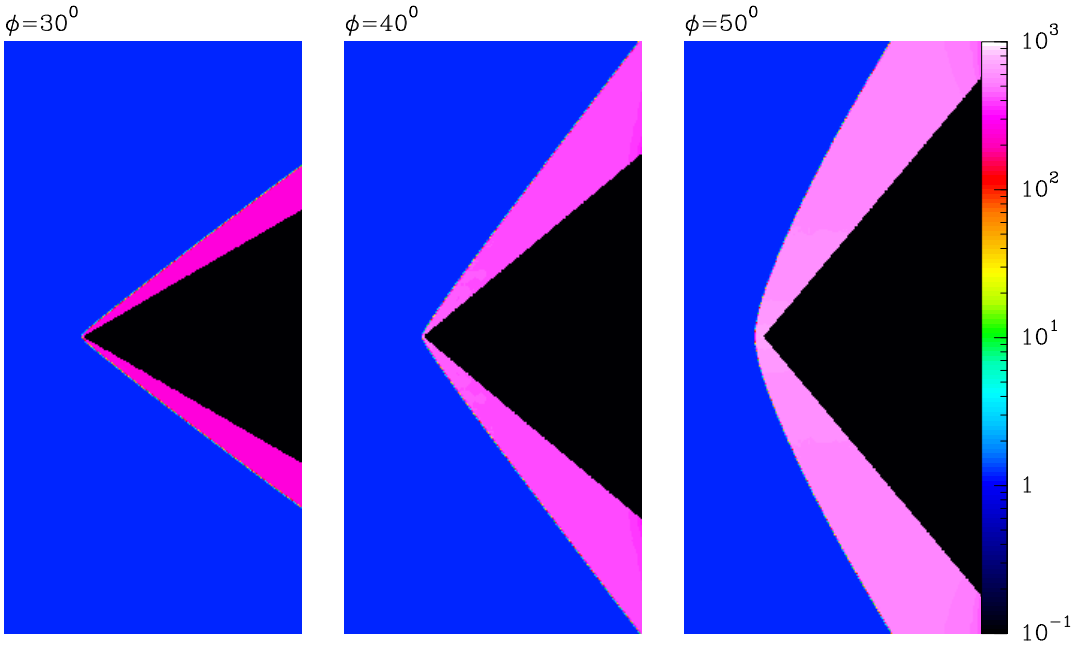

Figure 7.5: Pressure stratifications resulting from the interaction of a $M = 30$, $\gamma = 7/5$ flow (propagating to the right, along the abscissa) with a rigid wedge. The three plots are labeled with the half-opening angle of the wedges. The $\phi = 30°$ and $\phi = 40°$ flows are stationary. The flow obtained for the $\phi = 50°$ wedge (right frame) is non-stationary, and the displayed stratification corresponds to a time evolution equal to 3 times the flow crossing time scale of the abscissa of the displayed domain. The displayed pressure stratifications have been obtained with numerical simulations using the 2D Euler equations.

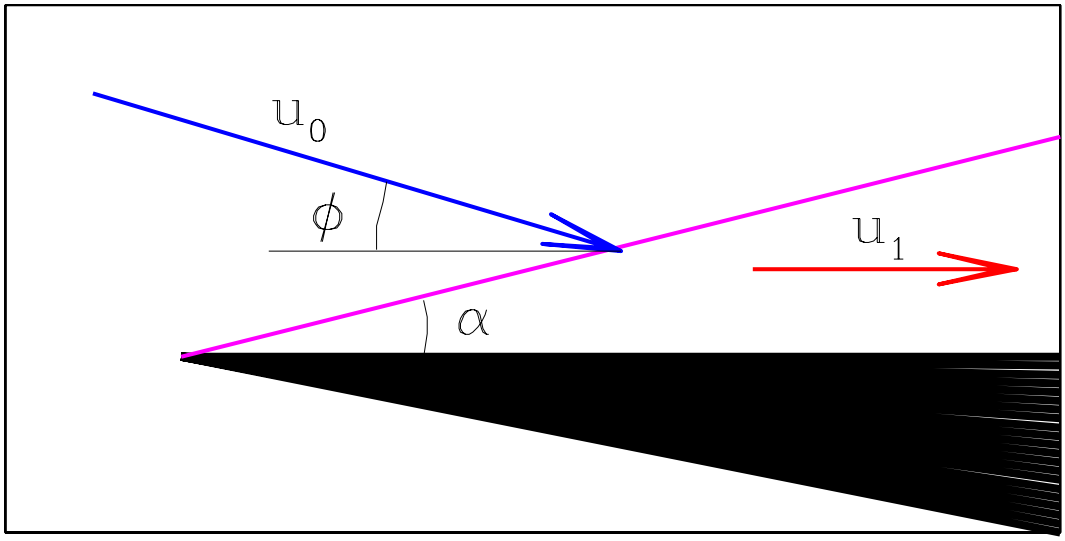

Figure 7.6: Schematic diagram showing the interaction of a flow that hits a plane, solid shelf (in black) at an angle ϕ to its surface. A regular reflection is produced, with an oblique shock (at an angle α) that redirects the flow to a direction parallel to the surface of the shelf.

From the oblique shock jump conditions, the post-shock flow velocity then has the normal and tangential components :

$$u_{n,1} = \frac{u_{n,0}}{\xi}\,; \quad u_{t,1} = u_{t,0}\,, \tag{7.34}$$

where ξ is the compression at the shock. If the shock is strong, we have

$$\xi = \frac{\gamma+1}{\gamma-1}\,. \tag{7.35}$$

The post-shock flow is parallel to the surface of the shelf. Therefore, the component v_{surf} normal to the shelf of the post-shock flow has to be zero :

$$v_{surf} = u_{t,1}\sin\alpha - u_{n,1}\cos\alpha = 0\,. \tag{7.36}$$

Combining eqs. (7.33), (7.34) and (7.36) we then obtain :

$$\tan(\alpha+\phi) = \xi\tan\alpha\,. \tag{7.37}$$

This is the equation that determines the angle α (between the shock and the shelf) as a function of the incidence angle ϕ (see Fig. 7.6) and the compression ξ at the shock.

Using the identity

$$\tan(\alpha+\phi) = \frac{\tan\alpha+\tan\phi}{1-\tan\alpha\tan\phi}\,, \tag{7.38}$$

we can rewrite eq. (7.37) in the form

$$\xi\tan^2\alpha + \frac{1-\xi}{\tan\phi}\tan\alpha + 1 = 0\,. \tag{7.39}$$

This quadratic equation has solutions

$$\tan\alpha = \frac{\xi-1}{2\xi\tan\phi}\left[1 \pm \sqrt{1 - \frac{4\xi\tan^2\phi}{(\xi-1)^2}}\right]\,. \tag{7.40}$$

The α vs. ϕ relations obtained (from eq. 7.40) for strong shocks with $\gamma = 5/3$ ($\rightarrow \xi = 4$) and $\gamma = 7/5$ ($\rightarrow \xi = 6$) are shown in Fig. 7.7.

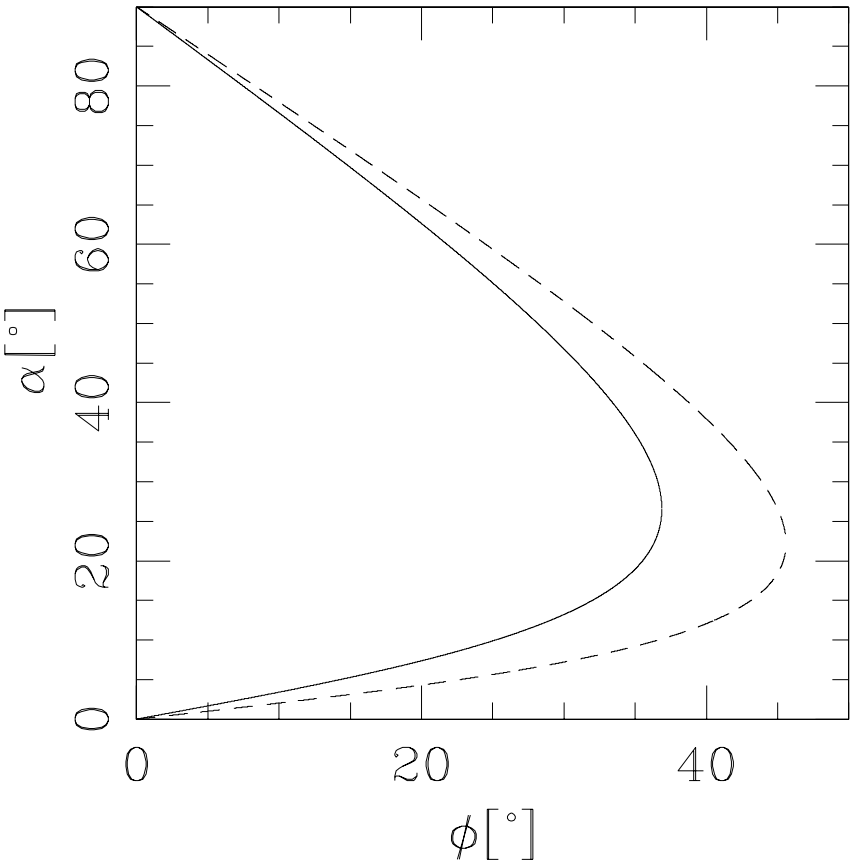

Figure 7.7: Angle α between the shock and the plane surface (in the regular shock reflection problem) as a function of the incidence angle ϕ for a hypersonic flow with $\gamma = 5/3$ (solid line) and $\gamma = 7/5$ (dashed line).

In this Figure, we see that for a given ϕ there are two possible values of α (obtained from the $+/-$ signs of eq. 7.40). These are called the "strong" (larger α value) and the "weak" solutions. It is an experimental fact that regular reflections invariably adopt the weak solution. Numerical solutions of this problem (see Fig. 7.5) also adopt the weak solution.

From Fig. 7.7 it is clear that there is a maximum possible value ϕ_{max} beyond which there are no solutions to the regular shock reflection problem. The value of ϕ_{max} is obtained by setting the square root term of eq. (7.40) to zero, which gives

$$\tan \phi_{max} = \frac{\xi - 1}{2\sqrt{\xi}} \,. \tag{7.41}$$

Combining this equation with the strong shock jump condition (eq. 7.35), we obtain $\phi_{max} = 36°.87$ for $\gamma = 5/3$ and $\phi_{max} = 45°.58$ for $\gamma = 7/5$.

For incidence angles of the flow $\phi > \phi_{max}$ a regular shock reflection is not possible, and the "flow on wedge" problem then adopts a solution with a curved bow shock (see the right frame of Fig. 7.5). There is no analytic solution for this flow configuration.

Chapter 8

1D, stationary, radiative shocks

8.1 General considerations

After the passage of an astrophysical shock wave, the hot, post-shock gas emits radiation and cools again. Provided that the shock velocity is high enough, the post-shock gas becomes rapidly ionised, and then emits a rich emission line spectrum. This radiative energy loss cools the gas, and the ions recombine to lower ionisation states.

The most simple possible model for this post-shock relaxation region is to consider a stationary, plane-parallel flow. The plane-parallel approximation is valid provided that the size of the relaxation region is small compared to the radius of curvature of the shock wave (a condition not necessarily met in ISM shock waves). The assumption that the flow is stationary is also dubious at best, since many objects have evolutionary timescales which are comparable to the post-shock cooling timescale. Also, it has been found that the relaxation regions behind shock waves of high enough velocities (> 100 km s^{-1}) are thermally unstable, so that the stationary solutions are probably never attained by a real shock.

Regardless of these problems, the plane-parallel, stationary radiative shock is the most simple possible problem with direct application to ISM shocks from which a concrete prediction of the emitted spectrum can be made. It serves as an illustration of the elements that have to be considered when trying to model more complex flows with shock waves in the ISM.

8.2 The equations for the recombination region

From the 1D Euler equations (eqs. 5.35-5.37), we see that a radiative plane-parallel, stationary, $\gamma = 5/3$ flow (in the absence of external forces) satisfies the equations

$$\rho u = \rho_0 u_0 \,, \tag{8.1}$$

$$\rho u^2 + P = \rho_0 u_0^2 + P_0 \,, \tag{8.2}$$

$$\frac{dh}{dx} = \frac{G - L}{\rho u} \,; \quad h = \frac{u^2}{2} + \frac{5}{2}\frac{P}{\rho} \,, \tag{8.3}$$

where ρ_0, P_0 and u_0 are the flow variables at some point in which they are known (in our case, these would be the pre-shock conditions), and G, L are the energy gain and loss (respectively) per unit volume and time.

The procedure for calculating the structure of the recombination region is to integrate numerically eq. (8.3) over a finite distance step Δx, going from $h(x)$ to $h(x + \Delta x)$, and then to use the relations

$$\rho = \frac{(5/2)(P_0 + \rho_0 u_0^2) + \sqrt{(5/2)^2 (P_0 + \rho_0 u_0^2)^2 - 8h\rho_0^2 u_0^2}}{2h} \,, \tag{8.4}$$

$$P = P_0 + \rho_0 u_0^2 \left(1 - \frac{\rho_0}{\rho}\right) \,, \tag{8.5}$$

$$u = \frac{\rho_0 u_0}{\rho} \,, \tag{8.6}$$

(which can be deduced from eqs. 8.1-8.3) to calculate the flow variables ρ, P and u as a function of the "advanced position" specific enthalpy $h(x + \Delta x)$ and the pre-shock variables ρ_0, P_0 and u_0. From the flow variables one can then calculate

$$n = \frac{\rho}{\overline{m}} \,; \quad T = \frac{P}{k(n + n_e)} \,, \tag{8.7}$$

where n is the ion+atom number density, n_e the electron density, and $\overline{m}$ is the average mass per atom or ion ($\overline{m} = m_H$ for a pure H gas, and $\overline{m} = 1.3 m_H$ for a 90% H and 10% He gas).

Before being able to integrate eq. (8.3) one has to calculate what is the ionisation state of the gas. This is necessary in order to calculate n_e (see eq. 8.7) and to calculate the heating and cooling functions (G and L, respectively).

8.3 The ionisation state of the gas

If the gas were in coronal ionisation equilibrium, we could compute the ionisation state of the gas as a function of the local temperature. Unfortunately, in the cooling region behind a shock wave the cooling and recombination timescales are comparable, so that the gas is actually not in ionisation equilibrium. Because of this, it is necessary to integrate the rate equations

$$u\frac{dy_{a,z}}{dx} = n_e \left\{ y_{a,z+1}\alpha_{a,z+1}(T) + y_{a,z-1}c_{a,z-1}(T) - y_{a.z}\left[\alpha_{a,z}(T) + c_{a,z}(T)\right]\right\} +$$

$$y_{a,z-1}\phi_{a,z-1} - y_{a,z}\phi_{a,z}\,, \tag{8.8}$$

where $y_{a,z} = n_{a,z}/n_a$ is the fractional ionisation state of the ion of charge z of element a, and the α, c and ϕ coefficients are the recombination, collisional ionisation and photoionisation rates (respectively). We also have the auxilliary relations :

$$\sum_z y_{a,z} = 1\,, \tag{8.9}$$

$$\sum_a \left[n_a \sum_z y_{a,z} \right] = n\,, \tag{8.10}$$

$$\sum_a \left[n_a \sum_z z y_{a,z} \right] = n_e\,, \tag{8.11}$$

$$\frac{1}{n}\sum_a n_a m_a = \overline{m}\,, \tag{8.12}$$

$$n_a = f_a\, n\,, \tag{8.13}$$

where m_a is the mass and f_a the abundance (by number) of element a.

This then represents the main difficulty in computing the structure of the relaxation region behind an astrophysical shock wave. In order to compute the ionisation state of the gas (necessary for computing the electron density n_e and the heating and cooling functions) it is necessary to integrate a set of rate equations (see eq. 8.8) including all of the relevant ions together with the equation for the specific enthalpy (eq. 8.3).

8.4 The photoionisation rates

The main difficulty in computing the ionisation rate equations (eqs. 8.8) is naturally related to the photoionisation rates

$$\phi_{a,z} = \int_{\nu_{a,z}}^{\infty} \frac{4\pi J_\nu}{h\nu} a_\nu^{a,z} d\nu \,, \tag{8.14}$$

where $\nu_{a,z}$ is the frequency associated with the ground state ionisation edge and $a_\nu^{a,z}$ the photionisation cross section of ion a, z.

The intensity I_ν is obtained through an integration of the plane-parallel radiative transfer equation :

$$\mu \frac{dI_\nu}{dx} = j_\nu - \kappa_\nu I_\nu \,, \tag{8.15}$$

where the emission coefficient j_ν is dominated by the contribution from the H Lyman continuum, but also has contributions from the He II and He III recombination continua, and from resonance lines of a limited set of ions (see, e. g., the paper of Shull and McKee [30]). In eq. (8.15), $\mu = \cos\theta$ where θ is the angle between the propagation direction of the ray and the x-axis.

The radiative transfer equation (eq. 8.15) has the integral form (for $\mu > 0$) :

$$I_\nu(x, \mu) = \frac{1}{\mu} \int_{-\infty}^{x} j_\nu(x') e^{-\tau_\nu(x', x)/\mu} dx' \,, \tag{8.16}$$

where

$$\tau_\nu(x', x) = \int_{x'}^{x} \kappa_\nu(x'') dx'' \,. \tag{8.17}$$

A similar expression (but with integration limits from $+\infty$ to x) is obtained for directions with $\mu < 0$. The average intensity J_ν can then be computed as :

$$J_\nu(x) = \frac{1}{4\pi} \oint I_\nu \, d\omega = \frac{1}{2} \int_{-1}^{1} I_\nu(x, \mu) d\mu \,. \tag{8.18}$$

Combining eqs. (8.16-8.18) and commuting the position and angular integrals, we finally obtain :

$$J_\nu(x) = \frac{1}{2} \int_0^{\infty} j_\nu(x') E_1 \left[|\tau_\nu(x', x)| \right] \, dx' \,, \tag{8.19}$$

where the first order exponential integral $E_1(\tau)$ is defined by

$$E_1(\tau) \equiv \int_\tau^\infty \frac{e^{-t}}{t} dt = \int_0^1 \frac{e^{-\tau/\mu}}{\mu} d\mu \,. \tag{8.20}$$

Tabulations and rational/exponential approximations to $E_1(\tau)$ can be found in the book of Abramowitz & Stegun [1].

Therefore, in order to calculate the photoionisation rates it is necessary to compute the average intensity J_ν at all positions x along the flow (eqs. 8.17, 8.19 and 8.20) at least for a limited number of frequency values. For example, one finds in the literature numerical models that use a set of frequencies coinciding with the ionisation edges of all of the ions considered in the calculation.

In numerical integrations of the plane-parallel, radiative shock problem it is found that in general the photoionisation rates do not play a dominant role. Therefore, approximate solutions of the post-shock region can be obtained neglecting the photoionisation rates in the ionisation rate equations eqs. 8.8). Including the photoionisation rates forces one to do a more complex numerical solution, involving an iterative procedure.

8.5 The minimal relaxation region model

Let us now consider a very simple model for the post-shock relaxation region. In our model, we consider eqs. (8.3-8.7), and write a single equation for the ionisation fraction $y = n_{HII}/n_H$ of Hydrogen :

$$\frac{dy}{dx} = \frac{ny}{u} \left[(1-y)c(T) - y\alpha(T) \right] , \tag{8.21}$$

with the interpolation functions given after eq. (3.57) for the $\alpha(T)$ and $c(T)$ coefficients. In this equation we have set $n_e = yn$, $n_{HII} = yn$ and $n_{HI} = (1-y)n$, with $n = \rho/\overline{m}$ (where $\overline{m} \approx m_H$).

We now set $G = 0$ (neglecting the energy gain due to photoionisation, consistently with the fact that we have neglected the photoionistion rates in eq. 8.21) and compute L as :

$$L = n^2 y(1-y)c(T)\chi_H + n^2 y T^{0.63} \left(6.1 \times 10^{-19}\right) \left[1 - e^{-(T/10^5)^{1.63}}\right] , \tag{8.22}$$

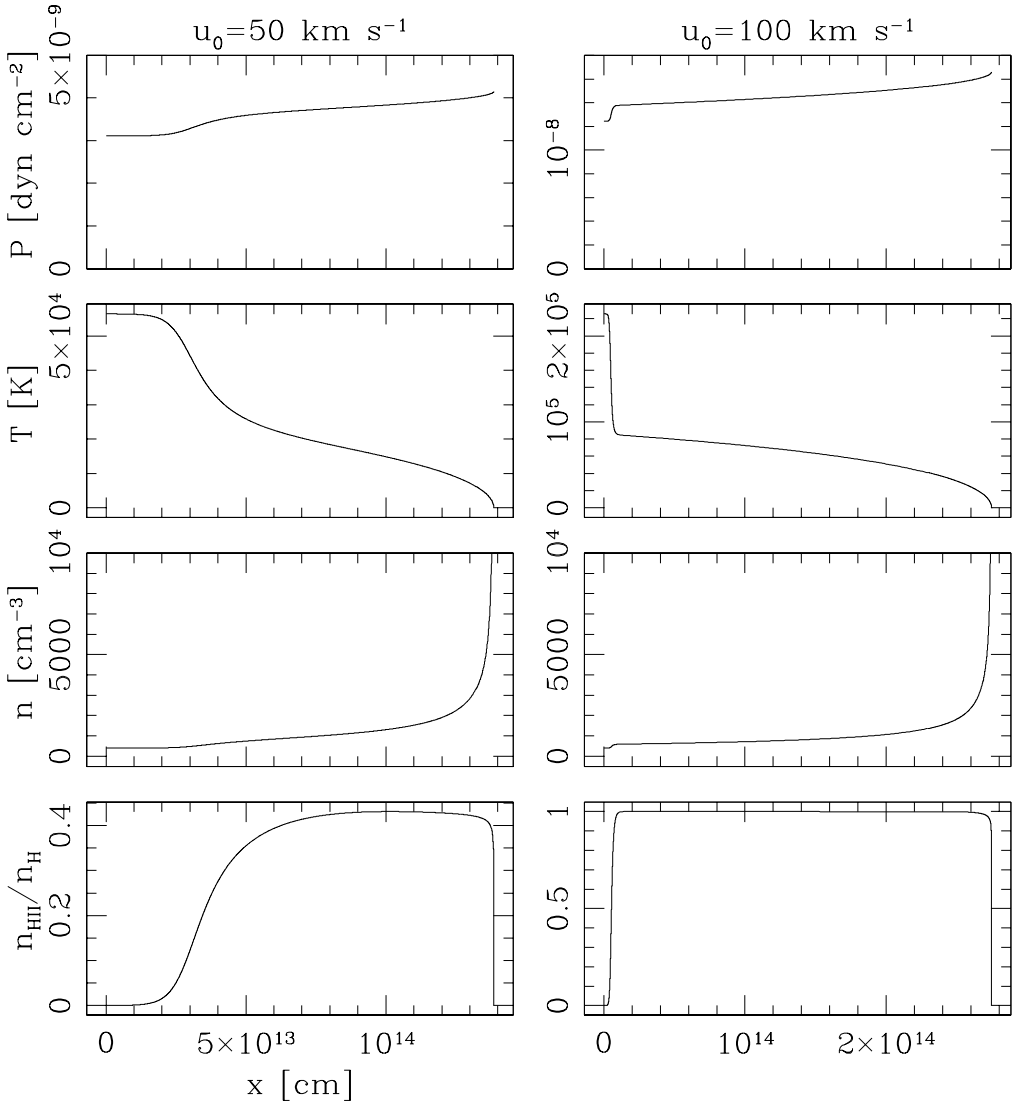

Figure 8.1: Structures of the relaxation region behind a shock wave computed from the "minimal model" described in the text.

where the first term on the right is the cooling due to collisional ionisation of H (with $\chi_H = 13.6$ eV) and the second term is an analytic approximation to the temperature behaviour of the coronal ionisation cooling function (all variables are in cgs units).

We now choose a set of pre-shock parameters : u_0, T_0, n_0 and y_0, and numerically integrate eqs. (8.3) and (8.21) until the gas recombines and reaches low temperatures. Results of this exercise obtained for $T_0 = 100$ K, $n_0 = 100$ cm^{-3}, $y_0 = 10^{-4}$ and $u_0 = 50$, 100 km s^{-1} are shown in Fig. 8.1.

These solutions show the typical stratification of the post-shock relaxation region : a region close to the shock wave in which the gas gets collisionally ionised, followed by a more extended, cooler region in which H eventually recombines again. This latter region is called the "recombination" or "cooling" region. There is an abundant literature on solutions of this type, of which Hartigan et al. [14] is a standard reference.

8.6 The cooling distance

From models of the relaxation region behind a plane-parallel shock it is possible to calculate a "cooling distance" d_c. We define d_c as the distance from the shock to the point where the temperature has dropped to a value of 10^4 K. It is also possible to choose another value for this temperature (e. g., 10^3 K), but it is clear from Fig. 8.1 that for a range of shock velocities similar values for d_c are obtained regardless of the precise temperature value that has been chosen.

Fig. 8.2 shows the cooling distance (to 10^4 K) as a function of shock velocity u_0, for a pre-shock number density $n_0 = 100$ km s^{-1}, obtained from the shock model tabulation of Hartigan et al. [14]. In order to obtain the scaling of the cooling distance with pre-shock density, we consider the following scaling argument. The cooling distance d_c can be estimated as :

$$d_c \sim \frac{E_{T,1}}{L_1} u_1 \propto \frac{n_1 k T_1 u_1}{n_1^2 \Lambda(T_1)} \propto \frac{f(u_0)}{n_0} \,. \tag{8.23}$$

In other words, the cooling distance is given by the ratio between the post-shock thermal energy ($E_{T,1}$) and cooling function ($L_1 = n_1^2 \Lambda(T_1)$, assuming low density regime cooling) multiplied by the post-shock velocity u_1. In the

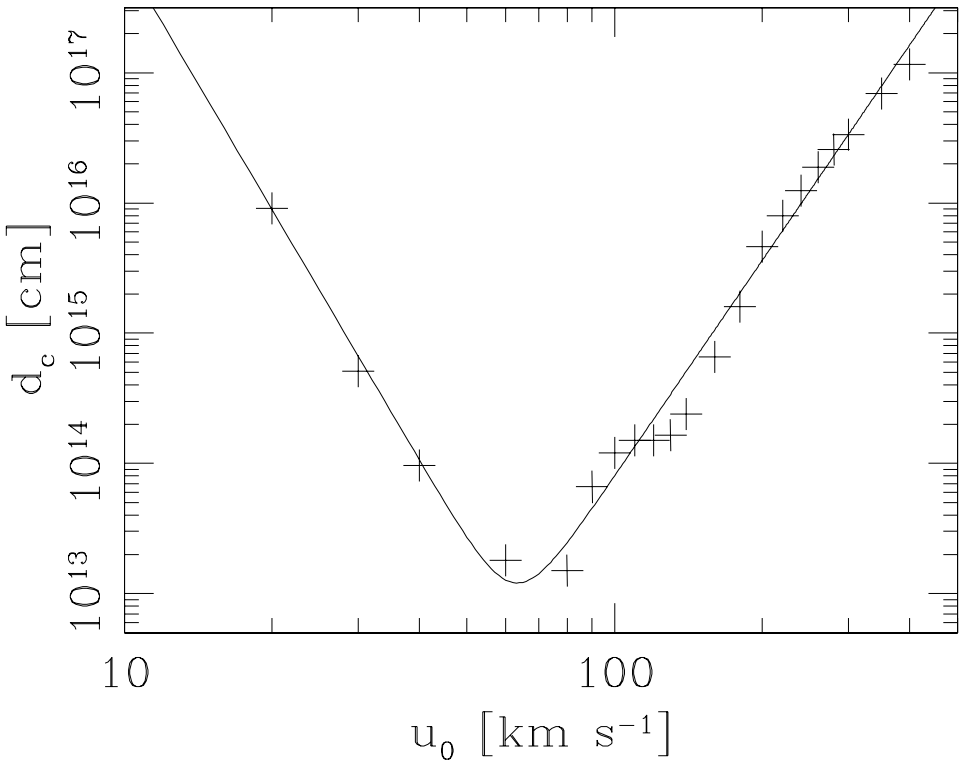

Figure 8.2: Cooling distance (to 10^4 K) as a function of shock velocity u_0 for shocks with a pre-shock number density $n_0 = 100$ cm^{-3} (values from Hartigan et al. [14]).

last proportionality of eq. (8.23, we have used the fact that for a strong shock, the post-shock velocity is $u_1 = u_0/4$, the post-shock density is $n_1 = 4n_0$ (eqs. 7.6 and 7.8), and the post-shock temperature T_1 is a function of the pre-shock velocity u_0 (eq. 7.12).

Therefore, provided that the cooling function is in the low density regime (i. e., $L = n^2\Lambda(T)$), the cooling distance is proportional to the ratio of a function of the shock velocity ($f(u_0)$, see eq. 8.23) and the pre-shock density n_0. If one looks at the predictions of the radiative shock models of Hartigan et al. [14], it is clear that the $d_c \propto n_0^{-1}$ scaling is indeed satisfied. The dependence of d_c on the shock velocity u_0 is shown in Fig. 8.2.

Different analytic fits to this d_c vs. u_0 dependence have been suggested in the literature. A possible fit (incorporating both the n_0 and the u_0 dependencies) is :

$$d_c = \left(\frac{100\,\mathrm{cm}^{-3}}{n_0}\right) \times$$

$$\left\{ \left[3 \times 10^{11}\mathrm{cm}\right] \left(\frac{u_0}{100\,\mathrm{km\,s}^{-1}}\right)^{-6.4} + \left[8 \times 10^{13}\mathrm{cm}\right] \left(\frac{u_0}{100\,\mathrm{km\,s}^{-1}}\right)^{5.5} \right\} . \quad (8.24)$$

This fit is shown (together with the d_c values of Hartigan et al. [14]) in Fig. 8.2.

8.7 Preionisation

Shocks of velocity higher than ~ 100 km s^{-1} have a "radiative precursor". This is a region ahead of the shock wave in which ionising photons produced by the post-shock region photoionise the gas, producing a leading photoionised region (see Fig. 8.3). This region can be computed by solving the gasdynamic (8.1-8.3) and rate (8.8) equations, including the photoionisation rate and heating terms.

In this section, we present a simple, analytic model for this region (following Shull and McKee [30]). We first take the results from the shock models of Raymond et al. [26], who give predictions of the flux F of ionising photons emitted into the pre-shock region as a function of the shock velocity u_0 and the pre-shock density n_0. The resulting $F/(n_0 u_0)$ ratio (which is only a function of u_0) predicted from these models is plotted in Fig. 8.4. This function can be

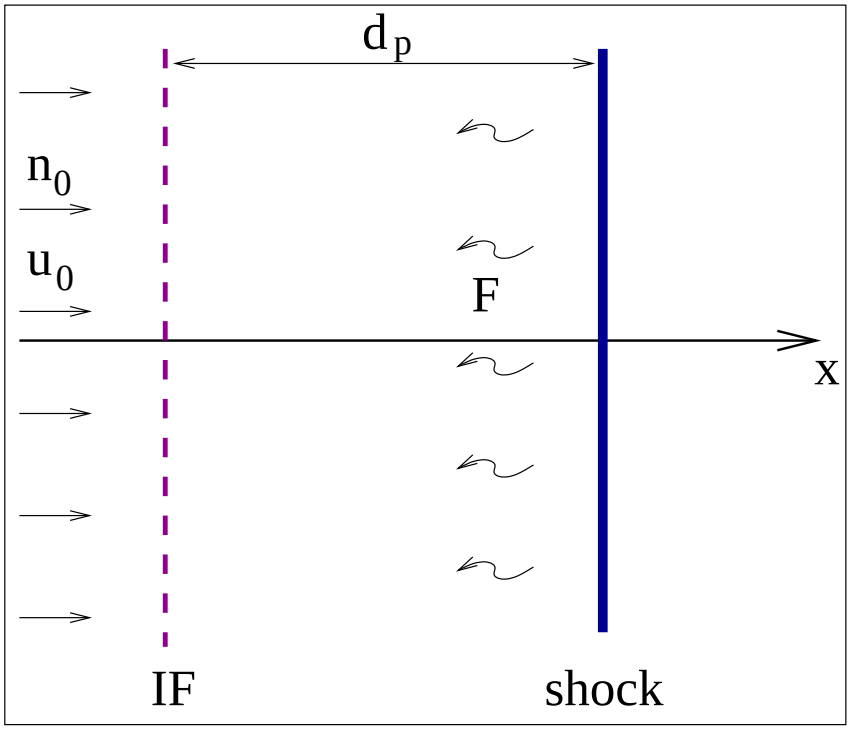

Figure 8.3: Schematic diagram showing the photoionisation region ahead of a shock wave. This region is preceded by an ionisation front (IF).

fitted with the interpolation :

$$\frac{F}{n_0 u_0} = v_0^{2.8-0.6v_0}\,; \quad v_0 = \frac{u_0}{110\,\mathrm{km\,s^{-1}}} < 2.458\,,$$

$$= 3.293\,; \quad v_0 \geq 2.458\,. \tag{8.25}$$

A simple, Strömgren region argument gives the relation :

$$F = n_0 u_0 + n_0^2 \alpha_H d_p\,, \tag{8.26}$$

where d_p is the x-extent of the preionisation region (see Fig. 8.3), $\alpha_H \approx 2.56 \times 10^{-13}$ cm^{3}s^{-1} (see eq. 3.13) is the H recombination coefficient, and $n_0 u_0$

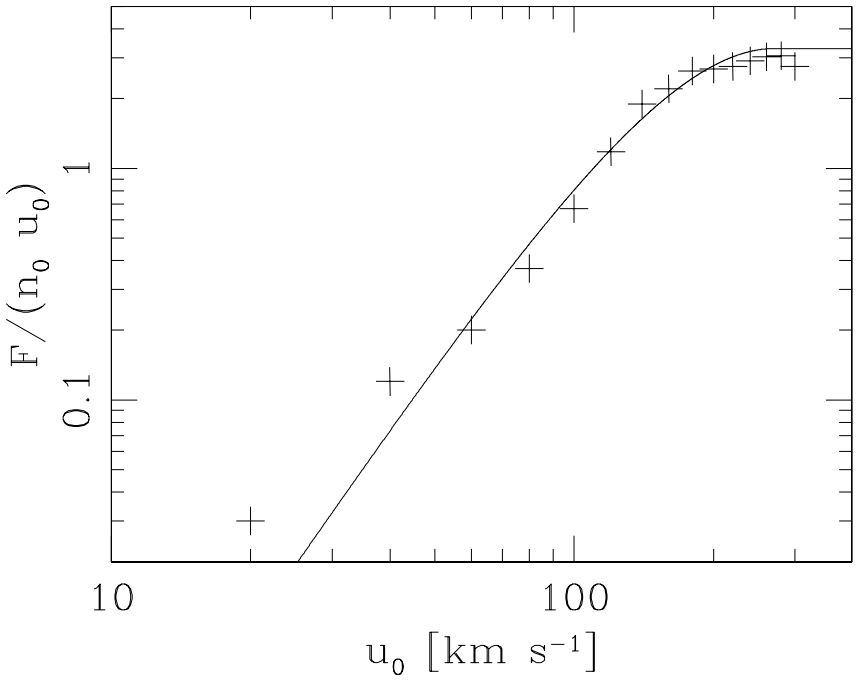

Figure 8.4: The $F/(n_0 u_0)$ ratio between the emitted flux F of ionising photons and the incident flux $n_0 u_0$ of neutrals (entering the shock wave) is shown as a function of the shock velocity u_0.

is the flux of incoming neutrals. From this equation, we obtain :

$$d_p = \left[4.30 \times 10^{17}\mathrm{cm}\right] \left(\frac{100\,\mathrm{cm}^{-3}}{n_0}\right) v_0 \left(v_0^{2.8-0.6v_0} - 1\right) \; ; \quad v_0 = \frac{u_0}{110\,\mathrm{km\,s}^{-1}} \, . \tag{8.27}$$

The resulting d_p vs. u_0 relation is shown in Fig. 8.5. It is clear that $d_p = 0$ for $u_0 \leq 100$ km s^{-1}. In this shock velocity regime, the material entering the shock wave is only partially ionised, with the pre-shock H ionisation fraction given in an approximate way by

$$y_0 = \frac{F}{n_0 u_0} \, , \tag{8.28}$$

where the right hand side is given as a function of u_0 by eq. (8.25). This ionisation fraction is shown (as a function of u_0) in Fig. 8.5.

8.8 The emission line spectra of shocks compared to photoionised regions

The optical emission line spectra of evolved supernova remnants and of Herbig-Haro objects (both of which arise in shock waves with velocities of ~ 100 km s^{-1}) show lines of a wide range of ionisation energies. For example, collisionally excited lines of [O III], [O II] and [O I], lines of [C III], [C II] and [C I], and lines of [S III] and [S II]. Recombination lines of H and He are also seen. All of the collisionally excited lines cited above are strong (i. e., of intensities comparable to the ones of the H recombination lines), with the higher ionisation lines absent in some objects.

Photoionised regions have qualitatively different spectra, with recombination lines of H and He and collisionally excited lines of ionised species, but with very faint lines of neutral (e. g., [C I] and [O I]) or low ionisation energy species (e. g., [S II]). The explanation for this is that C and O are at least singly ionised (and S twice ionised) within the Strömgren radius, and that outside the ionised region (where we do have C I and O I) the electron density is too small to produce an appreciable collisional excitation of the levels giving rise to the emission lines. Therefore, in photoionised regions the emission of lines from neutrals only comes from the transition region around the Strömgren radius,

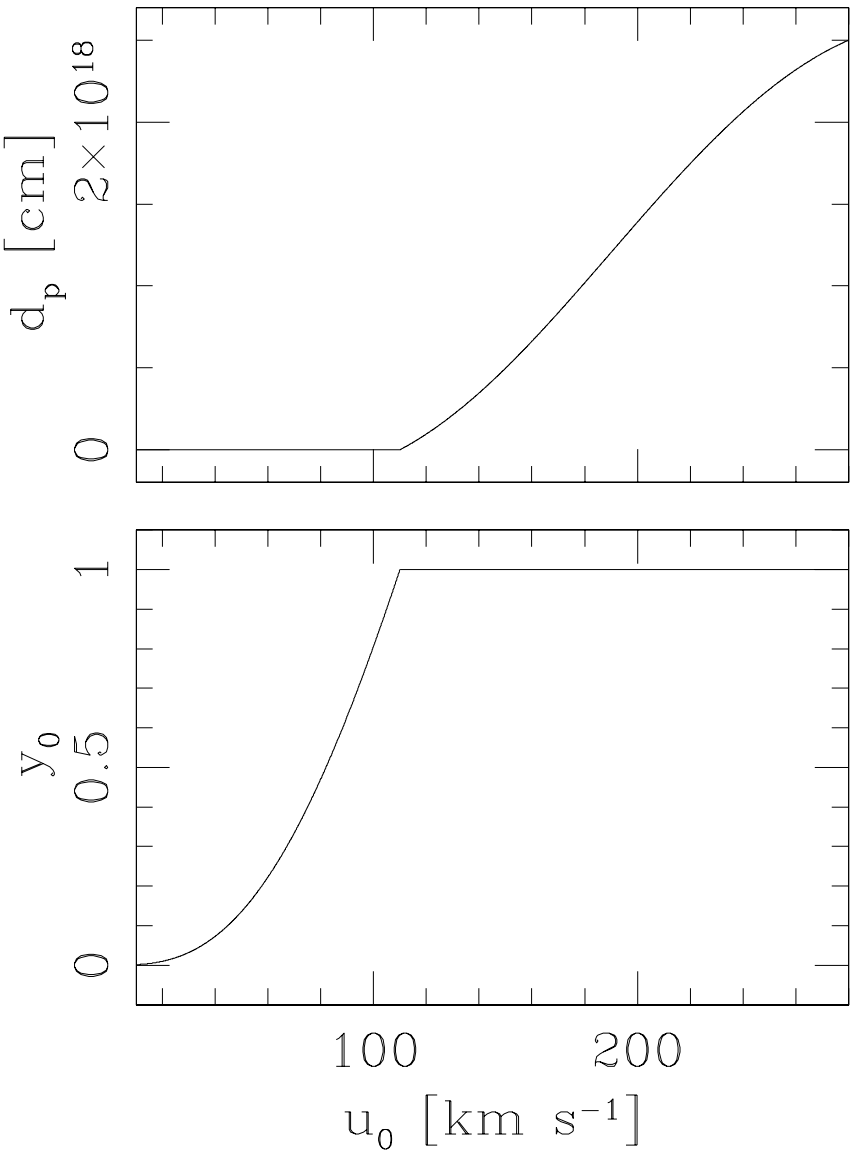

Figure 8.5: "Strömgren size" of the preionisation region d_p (top) and pre-shock H ionisation fraction y_0 (bottom) as a function of shock velocity u_0 for shocks with $n_0 = 100$ cm^{-3}.

where the gas is partially neutral (so that both neutrals and an appreciable electron density are present). Because this transition region is very narrow compared to the size of the photoionised region, the lines that exclusively come from the transition region are very faint compared to the lines produced within the bulk of the photoionised region.

On the other hand, the transition region between ionised and neutral gas is by far the densest part of a post-shock cooling region, so that its emission dominates the emission spectrum produced by the shock. The spectrum of a shock therefore corresponds to a transition region in which all ionisation states present (including neutrals) contribute strong emission lines.

Chapter 9

The hydrodynamic expansion of an HII region

9.1 The final, pressure equilibrium configuration

Following the expansion to the initial Strömgren radius (see section 3.4.4), the hot, high pressure ionised region pushes away the cold, neutral surrounding gas. This expansion of the HII region stops when the photoionised gas has lowered its density enough so as to reach pressure equilibrium with the surrounding, undisturbed neutral gas. This chapter describes the model derived in [23] for the hydrodynamical expansion of an H II region.

Let us consider a star with an ionising photon rate S_* in a uniform, neutral medium of density n_0 and isothermal sound speed c_0 ($c_0 \approx 1$ km s^{-1} for a 100 K environmental temperature). The initial, constant density expansion phase (section 3.4.4) leads to the formation of an ionised region of radius

$$R_S = \left(\frac{3S_*}{4\pi n_0^2 \alpha} \right)^{1/3} , \tag{9.1}$$

where $\alpha = 2.59 \times 10^{-13}\mathrm{cm}^3\mathrm{s}^{-1}$ is the case B recombination coefficient of H at 10^4 K (see equation 3.8). The ionised region has a temperature $\sim 10^4$ K, so that its isothermal sound speed is $c_i \approx 10$ km s^{-1}.

The HII region will then expand until its number density (of atoms+ions) reaches a value n_f, determined by the condition of pressure equilibrium with the surrounding environment :

$$n_f c_i^2 = n_0 c_0^2 \rightarrow n_f = n_0 \left(\frac{c_0}{c_i}\right)^2 . \tag{9.2}$$

The Strömgren radius of the pressure equilibrium configuration is then:

$$R_f = \left(\frac{3S_*}{4\pi n_f^2 \alpha}\right)^{1/3} = \left(\frac{c_i}{c_0}\right)^{4/3} R_S \, . \tag{9.3}$$

In other words, given that $c_i/c_0 \approx 10$ (see above), the final radius of the HII region (corresponding to the pressure equilibrium configuration) is ~ 20 times the initial Strömgren radius.

The mass of the final HII region then is :

$$M_f = \frac{4\pi R_f^3}{3} n_f 1.3 m_H = \left(\frac{c_i}{c_0}\right)^4 M_i \, , \tag{9.4}$$

where M_i is the mass within the initial Strömgren radius (before the hydrodynamic expansion), and $1.3m_H$ is the mass per atom/ion of a gas with a H fractional abundance (by number) of 0.9 and an He abundance of 0.1 . Therefore the mass of the HII region grows by a factor of $\sim 10^4$ as it evolves from the initial Strömgren radius to the final, pressure equilibrium configuration.

Interestingly, the expanding HII region pushes out an environmental mass

$$M_{env} \approx \frac{4\pi R_f^3}{3} n_0 1.3 m_H = \left(\frac{c_i}{c_0}\right)^2 M_f \, . \tag{9.5}$$

Therefore, the expanding HII region pushes out a mass M_{env} which is ~ 100 times larger than the mass $M_{ion} = M_f - M_i$. M_{ion} ($\approx M_f$) is the mass that was initially part of the neutral environment, which was photoionised (and therefore incorporated into the HII region) during the hydrodynamic expansion phase.

In this way we see that, from the point of view of the neutral environment, the HII region acts as a piston, pushing out a mass $\sim M_{env}$ (see equation 9.5), and incorporating into the HII region only $\sim 1\%$ of this mass.

9.2 An analytic model for the expansion

We consider the problem of an HII region in its "hydrodynamic expansion phase", following the initial, constant density expansion to the "initial Strömgren radius", given by equation (9.1). Once the ionisation front has reached a radius R_S, the high temperature gas (of isothermal sound speed c_i and initial density n_0) starts to expand, pushing a shock into the surrounding environment (of sound speed c_0 and density n_0). If we assume that this shock is isothermal, and that it has a shock velocity v_s, the compression in the shock is $= M_0^2$, where $M_0 = v_s/c_0$. The velocity of the post-shock material relative to the shock therefore is

$$v_1 = v_s/M_0^2 \,. \tag{9.6}$$

If the ionisation front moves at a velocity dR/dt (where R is the time-dependent radius of the photoionised region), the velocity v_s (with which the shock travels away from the source) is

$$v_s = \frac{dR}{dt} + v_1 = \frac{dR}{dt} + c_0^2/v_s \,, \tag{9.7}$$

where for the second equality we have used equation (9.6). Let us note that Dyson & Williams ([13]) assumed that $v_s = dR/dt$. From this equation, it is possible to find v_s as a function of dR/dt:

$$v_s = \frac{1}{2}\left[\frac{dR}{dt} + \sqrt{\left(\frac{dR}{dt}\right)^2 + 4c_0^2}\right] \tag{9.8}$$

and dR/dt as a function of v_s:

$$\frac{dR}{dt} = v_s - \frac{c_0}{v_s} \,. \tag{9.9}$$

We now assume that the expanding HII region is approximately homogeneous (of density n), and that it is in pressure balance with the shocked, neutral material:

$$nc_i^2 = n_0 v_s^2 \,, \tag{9.10}$$

and that it is in global photoionisation equilibrium:

$$S_* = \frac{4\pi}{3} R^3 n^2 \alpha \rightarrow \left(\frac{n}{n_0}\right)^2 = \left(\frac{R_S}{R}\right)^3 \,, \tag{9.11}$$

where for deriving the second equality we have used the definition of the initial Strömgren radius (equation 3.8).

We now combine equations (9.9-9.11) to obtain :

$$\frac{1}{c_i}\frac{dR}{dt} = \left(\frac{R_S}{R}\right)^{3/4} - \sigma\left(\frac{R}{R_S}\right)^{3/4} , \tag{9.12}$$

where $\sigma = c_0^2/c_i^2$ is equal to 1/2 times the environment-to-ionised medium temperature ratio. If we set $\sigma = 0$ we regain the differential equation derived by Dyson & Williams ([13]).

With the boundary condition $R(t=0) = R_S$, this equation can be integrated analytically to obtain :

$$t' = \frac{1}{3\sigma^{7/6}}\left[f(r) - f(1)\right] , \tag{9.13}$$

with

$$f(r) = -12\sigma^{1/6}r^{1/4} + 2\sqrt{3}\tan^{-1}\left(\frac{\sqrt{3}\sigma^{1/6}r^{1/4}}{1-\sigma^{1/3}r^{1/2}}\right)$$
$$+ \ln\left[\frac{(\sigma^{1/3}r^{1/2} + \sigma^{1/6}r^{1/4} + 1)(\sigma^{1/6}r^{1/4}+1)^2}{(\sigma^{1/3}r^{1/2} - \sigma^{1/6}r^{1/4} + 1)(\sigma^{1/6}r^{1/4}-1)^2}\right] , \tag{9.14}$$

where $r = R/R_S$ and $t' = tc_i/R_S$.

It can be shown that for $\sigma = 0$ equation (9.13) coincides with the solution of the book of Dyson & Williams ([13]) :

$$t'_{DW} = \frac{4}{7}\left(r^{7/4} - 1\right) . \tag{9.15}$$

Figure 9.1 shows a comparison between the solution given (for different values of $\sigma = c_0^2/c_i^2$) by equation (9.13) and "Dyson's solution" (equation 9.15).

It is also possible to use the implicit $R(t)$ solution that we have derived (equation 9.13) to derive an equation of motion for the shock wave driven into the neutral medium. This is done by substituting the $R(t)$ solution into equation (9.12), and then inserting the derived $dR/dt(t)$ into equation (9.8). In this way, we obtain v_s as a function of t, and one can in principle integrate this equation numerically in order to obtain the radius of the shock wave as a function of time. This is done in the following section in order to compare the resulting prediction with the results of a gasdynamical simulation.

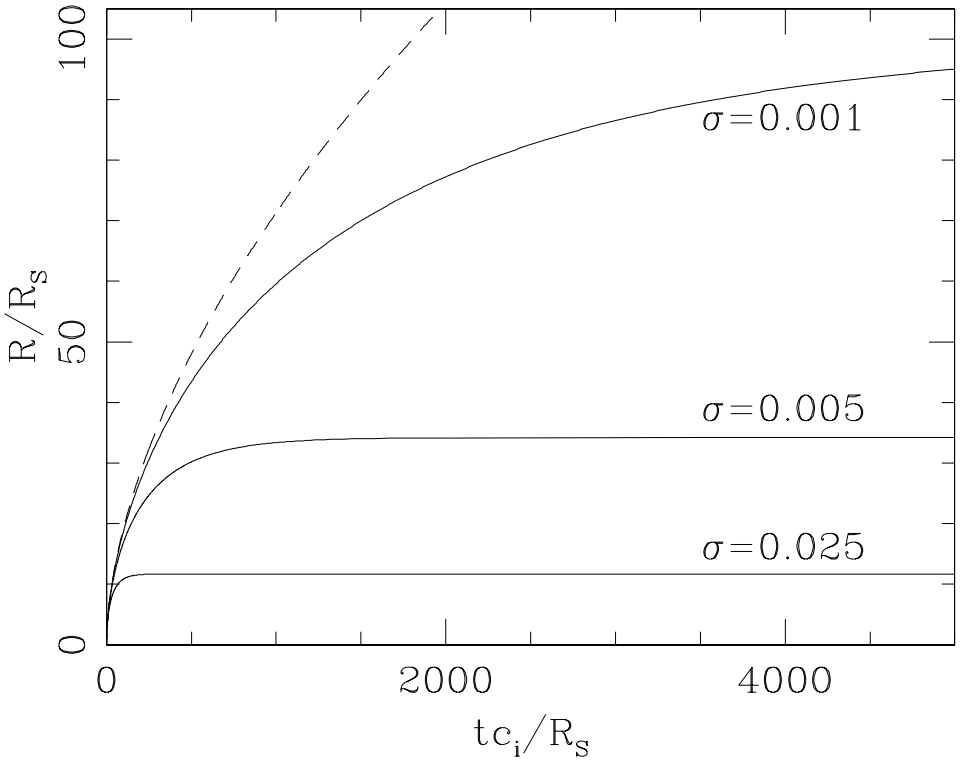

Figure 9.1: The solution for an expanding HII region into a pressureless, $\sigma = 0$ environment (Dyson's solution) is shown with a dashed line. The solid lines correspond to solutions with the σ values given by the corresponding labels.

9.3 Gasdynamic simulation

Let us now consider the gasdynamic equations for a spherically symmetric, two-temperature photoionised region:

$$\frac{\partial n}{\partial t} + \frac{\partial nu}{\partial R} + \frac{2nu}{R} = 0\,, \tag{9.16}$$

$$\frac{\partial nu}{\partial t} + \frac{\partial}{\partial R}\left[n(u^2 + c^2)\right] + \frac{2nu^2}{R} = 0\,, \tag{9.17}$$

$$\frac{\partial n_{HI}}{\partial t} + \frac{\partial n_{HI}u}{\partial R} + \frac{2n_{HI}u}{R} = (n - n_{HI})^2\alpha - n_{HI}\phi\,, \tag{9.18}$$

$$\phi = \frac{S_*\sigma_{\nu_0}}{4\pi R^2}e^{-\tau_{\nu_0}}\,; \quad \tau_{\nu_0} = \sigma_{\nu_0}\int_0^R n_{HI}\,dR'\,, \tag{9.19}$$

where R is the spherical radius, u the (radial) fluid velocity, n is the number density of the (pure H) gas, n_{HI} is the neutral H number density, $n - n_{HI}$ is the ionised H density (equal to the electron density) and $\alpha = 2.59\times10^{-13}$erg cm^{3}s^{-1} is the case B recombination coefficient of H at 10^4 K. The photoionisation rate ϕ is computed in the standard "grey HII region" approximation (in which the frequency dependence of the photoionisation cross section σ_ν is not considered), so that it is given (as a function of the ionising photon rate S_* and the Lyman limit HI photoionisation cross section $\sigma_{\nu_0} = 6.3\times10^{-18}$cm^2) by equation 9.19). Finally, the sound speed is computed as a function of the neutral fraction of the gas as :

$$c = \left(\frac{n_{HI}}{n_H}\right)c_0 + \left(1 - \frac{n_{HI}}{n_H}\right)c_i\,, \tag{9.20}$$

with $c_i = 10$ km s^{-1} (the isothermal sound speed of the ionised gas) and $c_0 = 1$ km s^{-1} (the sound speed of the external, neutral gas).

We compute a model with $S_* = 10^{49}$ s^{-1} (the ionising photon rate of an O7 main sequence star). We initialize the spherical computational domain with a uniform, $n = 10^7$cm^{-3} number density. Initially, we set $n_{HI} = 0$ for $R \leq R_S$ and $n_{HI} = n$ for $R > R_S$, where $R_S = 4.52\times10^{15}$cm is the Strömgren radius obtained with the chosen values of S_* and n.

With these initial conditions, equations (9.16-9.19) are integrated in a spherical computational grid of 2000, equally spaced grid points extending from $R = 0$

to an outer radius $R_{out} = 10^{18}$cm. This outer radius is large enough to contain all perturbations within the computational domain.

Figure 9.2 shows the (R, t)-plane density stratification obtained from this simulation. The flow develops a low density, ionised region with a decreasing expansion velocity. The ionised region reaches its maximum outer radius at $t \approx 5.5 \times 10^4$ yr, and then its radius decreases slowly with time, and finally stabilizes at a constant value for $t > 1.3 \times 10^5$ yr.

Also shown in Figure 9.2 are the analytic solution for the radius of the ionised region (equation 9.13) and the corresponding radius of the shock propagating into the neutral gas (obtained by integrating numerically equation 9.8). It is clear that the analytic solution (equation 9.13) reproduces well both the initial expansion and the final radius of the photoionised region. The analytic solution, however, fails to reproduce the "overshoot" (i.e., the HII region with radius larger than the final radius) obtained in the numerical simulation for $t \sim 5 \times 10^4$ yr. Finally, in Figure 9.2 we also show Dyson's solution (see equation 9.15).

9.4 The timescale for convergence to the pressure equilibrium configuration

The analytic model presented above allows us to make a simple prediction of the timescale for the expansion to attain the final, pressure equilibrium configuration. Equation (9.12) can be written in the form :

$$t = \frac{R_f}{c_0} I \,, \tag{9.21}$$

with

$$I = \int_{\sigma^{2/3}}^{R/R_f} \left(\frac{1}{x^{3/4}} - x^{3/4} \right) dx \,, \tag{9.22}$$

where $R_f = R_S/\sigma^{2/3}$ is the final, pressure equilibrium radius of the HII region expansion (with R_S given by equation 3.8) and $x = R/R_f$ is the spherical radius in units of R_f.

In order to obtain a simple prediction of the relaxation timescale of the HII region expansion, we now assume that $\sigma = (c_0/c_i)^2 \ll 1$ (which is generally

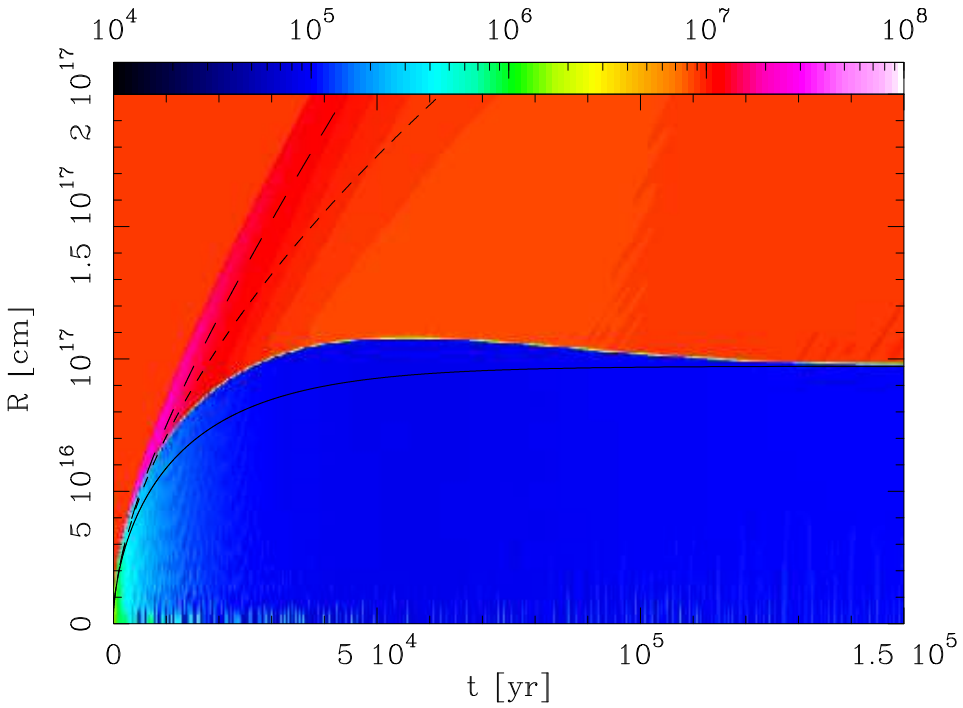

Figure 9.2: Density stratification in the (t, R)-plane of the numerical simulation described in the text. The low density region corresponds to the photoionised gas which first expands, and then reaches a final radius (determined by the pressure equilibrium of the ionised and neutral regions). The solid line is the prediction from the analytic model (equation 9.13) for the motion of the ionisation front, and the long-dash line the corresponding prediction for the motion of the shock wave. The short-dash line is Dyson's solution (equation 9.15). The density stratification is shown with the logarithmic scale given (in cm^{-3}) by the top bar.

true for a $\sim 10^4$ K HII region expanding into a ~ 100 K neutral/molecular environment), and therefore set the lower limit of the I integral (equation 9.22) to zero. We can then evaluate the time t in which a given fraction R/R_f of the final radius is attained from equations (9.21-9.22).

For example, if we evaluate the I integral (equation 9.22, which has an analytic solution similar to the one given in equation 9.13), for $R/R_f = 0.8$ we obtain $I = I_8 = 0.7085$ and for $R/R_f = 0.9$ we obtain $I = I_9 = 1.1353$. Therefore, for obtaining an estimate of the timescale t_f in which the HII region attains $\sim$ 80-90% of its final radius R_f, we can set $I \approx 1$ in equation (9.21), which gives

$$t_f \approx 10^5 \,\mathrm{yr} \left(\frac{R_f}{0.1\,\mathrm{pc}}\right) \left(\frac{1\,\mathrm{km\,s^{-1}}}{c_0}\right)$$

$$\approx 3 \times 10^4 \,\mathrm{yr} \left(\frac{S_*}{10^{49}\mathrm{s^{-1}}}\right) \left(\frac{10^7 \mathrm{cm^{-3}}}{n_0}\right)^{2/3} \left(\frac{1\,\mathrm{km\,s^{-1}}}{c_0}\right)^{7/3} , \qquad (9.23)$$

where in the second equality we have set $c_i = 10$ km s^{-1}. Therefore, ultra compact HII regions (with radii of ~ 0.1 pc) have reached the final, pressure equilibrium configuration in a $t_f \sim 10^5$ yr timescale. Normal HII regions, with environmental densities $n_0 \sim 100$ cm^{-3} would reach the pressure equilibrium configuration in $\sim 6.5 \times 10^7$ yr, which is close to 2 orders of magnitude larger than the main sequence lifetimes of the central O stars. Therefore, such regions will still be in the expansion phase when the central stars end their life in a SN explosion.

Chapter 10

Wind-driven HII regions

10.1 The general problem

HII regions are produced by the photoionisation of the ISM due to the radiation of one or more massive O/B stars. These stars also eject a stellar wind (see Table 3.1), which pushes the surrounding ISM into a higher pressure, shell structure. In order to have a more realistic model for the expansion of an HII region, it is necessary to consider the effect of this wind (together with the photoionisation process).

This problem has been described in some detail in the review paper of Capriotti & Kozminski [9], as well as in the book of Dyson & Williams [13]. The more detailed model of [24] is presented in the following sections.

10.2 The flow configuration

We assume that we have the flow configuration shown in Figure 10.1:

1. a star has an isotropic wind (of mass loss rate $\dot{M}$ and terminal velocity v_w) which is turned on at $t = 0$. At a time $t > 0$ the undisturbed wind fills the inner, spherical region labeled "I" in the schematic diagram. The star also emits S_* ionising photons per unit time (starting at $t = 0$). The outer boundary of this region is a spherical shock, which has a radius

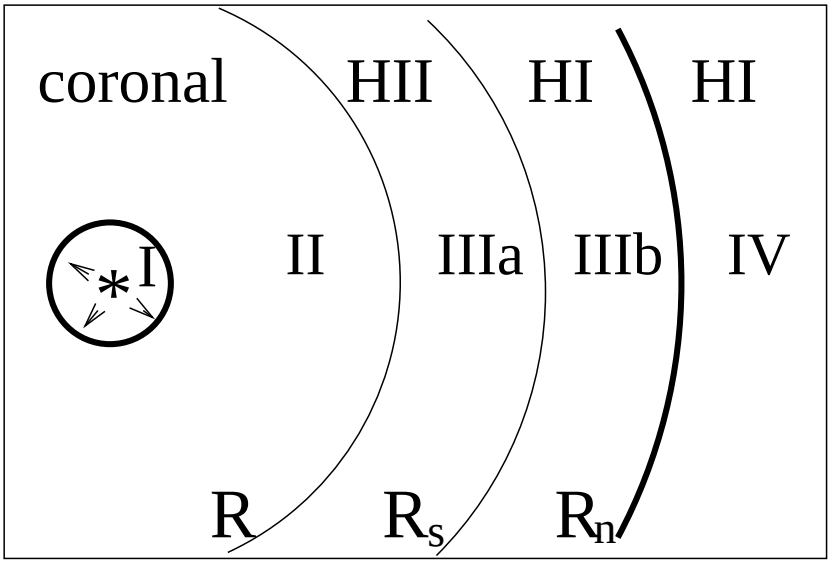

Figure 10.1: Schematic diagram of a wind-driven HII region. The asterisk indicates the position of the ionising photon+stellar wind source. Region I is filled with the expanding stellar wind, ending at an outer shock (thick, inner circle). Region II is filled with the hot, shocked wind, and ends in a contact discontinuity (at a radius R). Region IIIa is the photoionised environment region (of outer radius R_S). Region IIIb is the perturbed, neutral environment region, pushed out by the outer shock (of radius R_n), which travels into the unperturbed environment (region IV).

much smaller than the ones of all of the other regions of the flow,

2. the shocked stellar wind produces a hot bubble of coronal gas (region II, which is non-radiative for the case of an O/B central star) limited on the outside by a contact discontinuity which separates the stellar wind from disturbed environmental material,

3. the hot bubble pushes out a shock wave (the outer boundary of region III in the schematic diagram) into the surrounding, neutral environment (region IV). The shell of displaced environmental material has an inner region (region IIIa) which is photoionised by the S_* ionising photon rate of the central star, and a neutral outer region (region IIIb).

We first assume that region IIIa (the HII region) is much thinner than region IIIb (the region filled with shocked, neutral material, see Figure 10.1). For this "thin HII region" case, one can derive a model resulting in a first order differential equation with an approximate analytic solution. This model is described in section 10.3.

We then remove this assumption, and derive a "thick HII region" model, which results in a differential equation which we integrate numerically. This model is described in section 10.4.

10.3 Thin HII region model

10.3.1 Derivation of the model equation

As described in section 10.2, we assume that the stellar wind goes through a shock, and fills in a large bubble of hot, coronal gas. The kinetic energy of the wind feeds the thermal energy of the bubble and the kinetic energy of the swept-up material. The resulting energy equation is:

$$\frac{\dot{M} v_w^2}{2} t = \frac{3}{2} PV + \frac{1}{2} M_s v_s^2 \,, \tag{10.1}$$

where $\dot{M}$ is the mass loss rate and v_w the terminal velocity of the wind, P and V are the pressure and volume (respectively) of the stellar wind bubble and M_s and v_s are the mass and velocity (respectively) of the swept-up shell.

Following the classical derivation (see [13]), we use the estimates

$$P \approx \rho_0 \dot{R}^2 \,, \;\; M_s \approx \frac{4\pi}{3} R^3 \rho_0 \,, \;\; v_s \approx \dot{R} \,, \tag{10.2}$$

where R is the outer radius of the hot bubble (so that $V = 4\pi R^3/3$).

Combining equations (10.1-10.2), we obtain an energy conservation equation of the form:

$$\frac{\dot{M} v_w^2}{2} t = \frac{8\pi}{3} R^3 P \;\; \rightarrow \;\; P = \frac{3 \dot{M} v_w^2 t}{16 \pi R^3} \,, \tag{10.3}$$

for a bubble of uniform pressure P and radius R at an evolutionary time t.

The relations in equation (10.2) are strictly valid for the case in which the swept-up material (regions IIIa and IIIb in Figure 10.1) forms a thin shell. However, we will apply equation (10.3) for the case in which region IIIb (of neutral swept-up gas, see Figure 10.1) is not thin. This is not likely to result in large errors because the thermal energy of the shell dominates over the kinetic energy of the shell by a factor of ≈ 3. Therefore, an incorrect estimate of the kinetic energy of the (no longer thin) shell does not introduce large errors in the energy equation.

We now follow the derivation of Chapter 7, and assume that the outer shock (driven by the swept-up shell into the undisturbed environment) is isothermal, so that the postshock velocity v_{ps} and pressure P_{ps} are given by the isothermal Rankine-Hugoniot relations:

$$v_{ps} = \frac{c_0^2}{v_n}\,, \quad P_{ps} = \rho_0 v_n^2\,, \tag{10.4}$$

where v_n is the shock velocity and ρ_0 the ambient density. In the following, we set $P_{ps} = P$ (where P_{ps} is the post-shock pressure, see equation 10.4 and P the pressure of the hot bubble, see equation 10.3).

Also, from the standard "shock pushed by a piston" problem, we have the relation

$$v_n = v_{ps} + \dot{R}\,, \tag{10.5}$$

where $\dot{R}$ is the velocity of the outer edge of the hot bubble.

Now, combining equations (10.3-10.5), we obtain the differential equation:

$$\frac{dr}{d\tau} = \left(\frac{\tau}{r^3}\right)^{1/2} - \left(\frac{r^3}{\tau}\right)^{1/2}\,, \tag{10.6}$$

where $r = R/R_0$ (the dimensionless radius of the bubble) and $\tau = t/t_0$ (dimensionless time) with:

$$R_0 \equiv \sqrt{\frac{3\dot{M}v_w^2}{16\pi\rho_0 c_0^3}}\,, \quad t_0 \equiv \frac{R_0}{c_0}\,, \tag{10.7}$$

where c_0 is the isothermal sound speed of the undisturbed environment.

Once a solution $r(\tau)$ to equation (10.6) has been found, the outer radius R_n of the perturbed, neutral environment (region IV of Figure 10.1) can be found

by combining equations (10.4-10.5) to obtain

$$\frac{dr_n}{d\tau} = \left(\frac{\tau}{r^3}\right)^{1/2}, \tag{10.8}$$

where $r_n = R_n/R_0$ and r comes from the previously obtained solution (of equation 10.6). Equation (10.8) can then be integrated to obtain the (dimensional) radius $R_n = R_0 r_n$ of the spherical shock travelling into the neutral environment.

For parameters appropriate for a high density, ultracompact HII region powered by a main sequence O7 star we have

$$R_0 = 0.76\,\mathrm{pc}\left(\frac{\dot{M}}{5\times10^{-7}\mathrm{M}_\odot\mathrm{yr}^{-1}}\right)^{1/2}$$
$$\left(\frac{v_w}{2500\,\mathrm{km\,s}^{-1}}\right)\left(\frac{10^7\,\mathrm{cm}^{-3}}{n_0}\right)^{1/2}\left(\frac{1\,\mathrm{km\,s}^{-1}}{c_0}\right)^{3/2}, \tag{10.9}$$

where n_0 is the number density of atomic nuclei. From this value of R_0 we can calculate the characteristic time $t_0 = R_0/c_0 \approx 7\times10^5$ yr. Therefore, ultracompact HII regions (with sizes of ~ 0.1 pc and evolutionary times $\sim 10^5$ yr) are in a regime with a dimensionless radius $r = R/R_0 \sim 0.1$-1 and a dimensionless time $\tau = t/t_0 \sim 0.1$-1.

10.3.2 Numerical and analytic solutions

Equation (10.6) can be integrated numerically with the initial condition $r(0) = 0$ to obtain the radius R of the hot bubble as a function of time, and an integration of equation (10.8) gives the radius R_n of the outer shock vs. t. The results of such integrations are shown in Figure 10.2.

It is possible to find a series of approximate analytic solutions to equation (10.6). For $\tau \ll 1$ the first term on the right hand side of equation (10.6) dominates over the second term, and (neglecting the second term) one then obtains the integral

$$r(\tau) = \left(\frac{5}{3}\right)^{2/5}\tau^{3/5}, \tag{10.10}$$

which is the classical solution for an expanding, wind-driven bubble (see [13]).

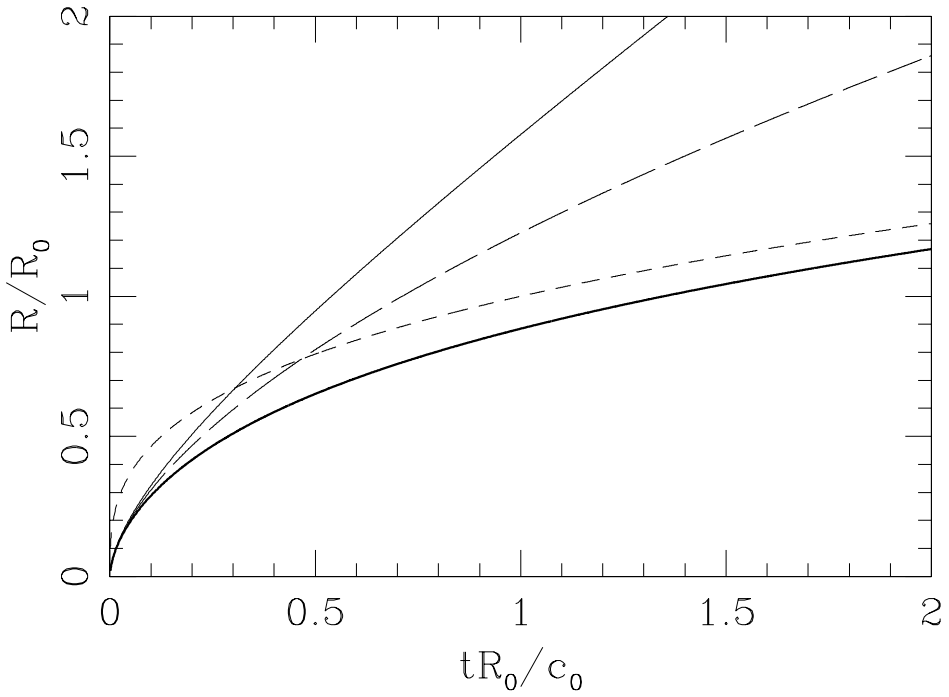

Figure 10.2: Radius R of the thick shell (thick, solid line) and R_n of the outer shock (thin, solid line) resulting from a numerical integration of equations (10.6) and (10.8). The radii are given in units of R_0 (see equation 10.9) and the time in units of R_0/c_0 (where c_0 is the isothermal sound speed of the surrounding, neutral environment). The long-dash line shows the inner analytic solution (equation 10.10, valid for $R \ll R_0$) and the short-dash line the outer analytic solution (equation 10.11, valid for $R \gg R_0$).

For $\tau \gg 1$, the two terms on the right hand side of equation (10.6) become very large, reaching an approximate balance. Setting these two terms equal to each other, one obtains the solution

$$r(\tau) = \tau^{1/3}\,. \tag{10.11}$$

It can be straightforwardly shown that this solution corresponds to a bubble in pressure equilibrium with the surrounding environment, expanding quasi-statically as more material is progressively injected by the stellar wind.

In Figure 10.2 we see that (as expected) the numerical integration of equation (10.6) gives a radius that approaches the low τ (equation 10.10) and high τ

(equation 10.11) solutions in the appropriate limits. It is possible, however, to obtain approximate analytic solutions that reproduce the numerical solution for all values of τ.

To find these approximate solutions, we first rewrite equation (10.6) in the form:

$$\frac{dy}{dx} = \frac{3\,(x^2 - y^2)}{y^{2/3}}\,, \tag{10.12}$$

with $x = \tau^{1/2}$ and $y = r^{3/2}$. This equation can be straightforwardly solved to obtain x as a function of dx/dy and y, and the resulting relation can then be used to do successive iterations of the form:

$$x_{n+1} = \sqrt{y^2 + \frac{y^{2/3}}{3(dx_n/dy)}}\,, \tag{10.13}$$

to obtain increasingly more accurate approximations to the $y(x)$ solution of equation (10.12).

Let us call $x_0(y)$ the first approximation to the solution of (10.12). One possibility is to set $x_0(y)$ equal to the large τ solution (equation 10.11), which in terms of the x, y variables takes the form

$$x_0(y) = y\,. \tag{10.14}$$

Inserting this relation in equation (10.13), we obtain the first iteration:

$$x_1(y) = \sqrt{y^2 + \frac{1}{3}y^{2/3}}\,. \tag{10.15}$$

Reinserting $x_1(y)$ in (10.13) we then obtain the second iteration:

$$x_2(y) = \sqrt{y^2 + \frac{3y\sqrt{y^2 + \frac{1}{3}y^{2/3}}}{1 + 9y^{4/3}}}\,. \tag{10.16}$$

It is possible to proceed with further iterations, but the resulting $x(y)$ relations are very extended.

A second possibility is to use the small τ solution (equation 10.10) as the first guess. The iterations then proceed as follows:

$$x_0(y) = \left(\frac{3}{5}\right)^{1/3} y^{5/9}\,, \tag{10.17}$$

$$x_1(y) = \sqrt{y^2 + \left(\frac{3}{5}\right)^{2/3} y^{10/9}}\,, \tag{10.18}$$

$$x_2(y) = \sqrt{y^2 + \frac{y^{2/3}\sqrt{y^2 + \left(\frac{3}{5}\right)^{2/3} y^{10/9}}}{3\left[y + \frac{1}{3}\left(\frac{5}{3}\right)^{1/3} y^{1/9}\right]}}\,. \tag{10.19}$$

The two "second iteration" solutions (equations 10.16 and 10.19) are shown (together with the results from a numerical integration of equation 10.6) in the top panel of Figure 10.3.

In order to evaluate the accuracy of our two "second iteration" solutions (equations 10.16 and 10.19), we first calculate the corresponding τ vs. r relations, and then calculate the relative error in the radius

$$\epsilon(\tau) = \left|\frac{r_e(\tau) - r_2(\tau)}{r_e(\tau)}\right|\,, \tag{10.20}$$

where $r_e(\tau)$ is the "exact" solution (obtained from a an accurate numerical integration of equation 10.6) and $r_2(\tau)$ is one of the two "second iteration" approximate solutions (equations 10.16 and 10.19).

The two corresponding relative errors are plotted as a function of time in the bottom panel of Figure 10.3. From this graph we see that the approximate solution given by equation (10.16) has a maximum deviation from the exact solution of $\sim 10\%$, and that the more complex approximate solution given by equation (10.19) has a maximum deviation of $\sim 5\%$.

10.4 Thick HII region model

10.4.1 Derivation of the model equation

We now develop a similar model to the one of section 10.3.1, but relaxing the condition that the photoionised region (region IIIa in Figure 10.1) is narrow. If we assume photoionisation equilibrium (correct for all HII regions, see [22]), the outer radius R_S of the photoionised region obeys the relation:

$$S_* = \frac{4\pi}{3} n_i^2 \alpha_H \left(R_S^3 - R^3\right)\,, \tag{10.21}$$

where R is the radius of the hot bubble (region II of Figure 10.1), n_i is the ion number density of region IIIa (assumed to be homogeneous within the region), S_* is the rate of photoionising photons (emitted by the central star), $\alpha_H \approx 2.6 \times 10^{-13}\mathrm{cm}^3\mathrm{s}^{-1}$ is the case B hydrogen recombination coefficient at 10^4K.

The conditon of pressure equilibrium between the photoionised region and the hot bubble is

$$P = \overline{m} n_i c_i^2 \,, \tag{10.22}$$

where P is the pressure of the stellar wind bubble (see equation 10.3), c_i (≈ 10 km s^{-1}) is the isothermal sound speed of the photoionised gas and $\overline{m}$ is the average mass per ion ($= 1.3\mathrm{m}_H$ for a 90% H, 10% He gas, by number).

Also, the condition of pressure equilibrium between regions IIIa (the photoionised region) and IIIb (the shocked, neutral region) implies that

$$P = \rho_0 v_n^2 \,, \tag{10.23}$$

where we have used the isothermal shock jump conditions (equation 10.4). As described in section 10.3.1, v_n is the velocity of the outer shock driven into the undisturbed environment.

Finally, the "shock pushed by a piston" relation (equation 10.5) now takes the form:

$$v_n = v_{ps} + \dot{R}_S = \frac{c_0^2}{v_n} + \dot{R}_S \,, \tag{10.24}$$

where $\dot{R}_S$ is the velocity of the outer edge of the photoionised region, and for obtaining the second equality we have used equation (10.4).

Combining equations (10.3) and (10.21-10.24), we obtain a differential equation for R_S of the form:

$$\frac{1}{c_0}\frac{dR_S}{dt} = \sqrt{\frac{P}{\rho_0 c_0^2}} - \sqrt{\frac{\rho_0 c_0^2}{P}} \,, \tag{10.25}$$

where

$$\frac{P}{\rho_0 c_0^2} = \lambda \left(\frac{c_0}{R_f} t\right) \left(\frac{R_f}{R_S}\right)^3 + \sqrt{\left(\frac{c_0}{R_f}\lambda t\right)^2 \left(\frac{R_f}{R_S}\right)^6 + \left(\frac{R_f}{R_S}\right)^3} \,. \tag{10.26}$$

The solutions of equations (10.25-10.26) depend on the value of the dimensionless parameter

$$\lambda \equiv \frac{1}{2}\left(\frac{R_0}{R_f}\right)^2 , \tag{10.27}$$

where R_0 is given by equations (10.7,10.9) and

$$R_f = \left(\frac{3S_*}{4\pi n_0^2 \alpha_H}\right)^{1/3} \left(\frac{c_i}{c_0}\right)^{4/3} . \tag{10.28}$$

R_f is the final radius obtained by a "wind-less" HII region which has reached pressure equilibrium with a surrounding, homogeneous neutral environment (see, e. g., the book of Dyson & Williams [13]). For parameters appropriate for an ultracompact HII region powered by an O7 star, we have

$$\lambda = 290 \left(\frac{\dot{M}}{5\times 10^{-7}\mathrm{M}_\odot \mathrm{yr}^{-1}}\right)^{1/2} \left(\frac{v_w}{2500\,\mathrm{km\,s^{-1}}}\right)^2 \left(\frac{10^7\,\mathrm{cm^{-3}}}{n_0}\right)^{1/3} \left(\frac{10^{49}\,\mathrm{s^{-1}}}{S_*}\right)^{2/3} \left(\frac{1\,\mathrm{km\,s^{-1}}}{c_0}\right)^{1/3} \left(\frac{10\,\mathrm{km\,s^{-1}}}{c_i}\right)^{8/3} . \tag{10.29}$$

It is straightforward to see that equations (10.25-10.26) have the following two limits:

1. for $\lambda \gg 1$, these equations become equation (10.6) of section 10.3.1, i.e., the model for a wind-driven shell with a negligibly thin HII region,

2. for $\lambda = 0$, these equations are identical to the ones derived in chapter 9 for the expansion of an HII region in the absence of a stellar wind.

Therefore, by spanning all positive values of the dimensionless parameter λ, we have models ranging from a "wind-less" to a "wind dominated" expanding HII region.

In the following section we present numerical solutions (of equations 10.25-10.26) giving the radius R_S of the expanding HII region as a function of time.

We also integrate equation (10.8) (setting $r = R_S/c_0$ in the right hand term) to obtain the radius R_n of the outer shock driven into the undisturbed environment, and combine equations (10.21-10.22) to obtain the radius of the hot bubble (region II of Figure 10.1):

$$\left(\frac{R}{R_f}\right)^3 = \left(\frac{R_S}{R_f}\right)^3 - \left(\frac{\rho_0 c_0^2}{P}\right)^2 , \tag{10.30}$$

where the second term on the right is given by equation (10.26).

10.4.2 Numerical solutions

In Figure 10.4, we show the numerical results obtained from numerical integrations of the "thick HII region" model (described in section 10.4.1) for different values of the dimensionless parameter λ (see equations 10.27, 10.29). The $\lambda = 0$ solution (top left panel) is identical to the "wind-less expanding HII region" model of chapter 9. The $\lambda = 100$ solution is most similar to the "thin HII region" model described in section 10.3 (i.e., the solution shown in Figure 10.2).

As can be seen in Figure 10.4, for progressively larger values of λ, a larger, inner hot wind bubble and a narrower HII region are obtained. In order to evaluate the relative thickness of the HII region, we have computed the value of

$$\frac{\Delta R}{R_S} = \frac{R_S - R}{R_S} , \tag{10.31}$$

(where R_S and R are the outer radii of the HII region and of the hot bubble, respectively) as a function of t. The results are shown in Figure 10.5, in which we see that for $\lambda = 10$, the HII region has become a shell with a thickness of $\sim 1\%$ of the radius of the ionised nebula. For the $\lambda \sim 100$ value expected for ultracompact HII regions driven by a main sequence O star (see equation 10.29), the photoionised gas is confined to an extremely narrow shell (see Figure 10.5).

10.5 Summary

In this chapter, we have applied the "thick shell" formalism to the case of a source producing both a photoionising radiation field and a stellar wind. For the case in which the HII region is thin (compared to the width of the swept-up ambient medium shell), the problem can be solved analytically with an iterative method. This method gives solutions which approximate the exact solution with accuracies of better than $\sim$ 5% (see section 10.3). Our new solution to the wind-driven bubble expansion problem has a transition from a $R \propto t^{3/5}$ law (i.e., the "classical" solution, see [13]) for $R \ll R_0$ (see equation 10.9) to a $R \propto t^{1/3}$ law for $R \gg R_0$. Ultracompact HII regions lie close to the transition between these two regimes.

The problem in which the HII region is not thin leads to a more complex differential equation, which we have integrated numerically. Different solutions are found for different values of the dimensionless parameter $\lambda \equiv R_0/(2R_f)$ (where R_0 is given by equation 10.9 and R_f is the final, pressure equilibrium radius of an HII region from a wind-less source). For increasing values of λ, we obtain solutions ranging from the wind-less case ($\lambda = 0$) to solutions in which the HII region becomes a very thin shell (approaching the "thin HII region" analytic solution.

The transition to the thin HII region regime (for increasing λ values) is shown in Figures 10.4 and 10.5. Interestingly, for the nominal parameters that we have chosen for an ultracompact HII region, we obtain $\lambda \approx 300$ (see equation 10.29), so that they are clearly in the "thin HII region" regime.

In order to illustrate the effect of a stellar wind on the characteristics of an HII region, in Figure 10.6 we show the HII region radius R_S and the expansion velocity (dR_S/dt) obtained for $\lambda = 0$ (i.e., a wind-less HII region), $\lambda = 290$ (the value obtained for our chosen ultracompact HII region parameters, see equation 10.29) and for $\lambda = 10$ (an arbitrary, intermediate λ value). From this figure we see that while for $\lambda = 0$ the expansion velocity falls below ≈ 1 km s^{-1} in ~ 500 yr, for $\lambda = 10$ the expansion velocity remains above ≈ 1 km s^{-1} for an evolutionary time $\sim 1.5 \times 10^5$ yr. For $\lambda = 290$, the expansion velocity remains above ~ 3 km s^{-1} for $\sim 2 \times 10^4$ yr and above ~ 2 km s^{-1} for $\sim 1.5 \times 10^5$ yr.

Interferometric observations show that some ultracompact HII regions have a "thick shell" morphology, with shell widths of $\sim$ 10-20% of the nebular

radius (see [10]). Comparing this result with our predictions of the thickness of the HII region, we would conclude that these "thick shell" objects have a dimensionless parameter $\lambda < 1$ (see Figure 10.5).

However, from equation (10.29) and the Table of main sequence O/B stellar parameters of Sternberg et al. [32], we see that HII regions (expanding into a $n_0 = 10^7 \mathrm{cm}^{-3}$, uniform environment) have $\lambda = 150 \rightarrow 670$, the lower limit corresponding to a B0 star, and the upper limit to an O3 star. If we lower the environmental density to $n_0 = 10^4 \mathrm{cm}^{-3}$, we would obtain a $\lambda = 15 \rightarrow 70$ range (see equation 10.29), still an order of magnitude higher than the λ values necessary for producing a "thick HII shell" morphology (see above and Figure 10.5).

Interestingly, the more recent paper of Marcolino et al. [17] calculates mass loss rates for O8 and O9 main sequence which are two orders of magnitude below previously obtained rates (such as the ones of Sternberg et al. [32], given in Table 3.1, see above). These new mass loss rates would imply that $\lambda \sim 1$ for late OV stars.

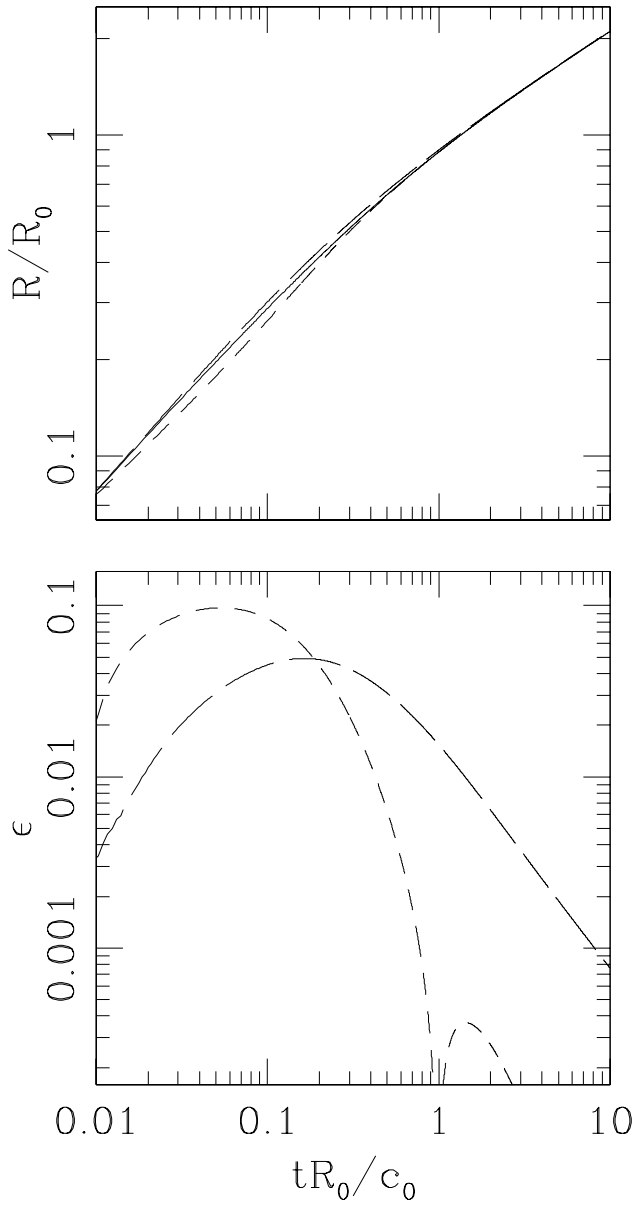

Figure 10.3: Top panel: radius of the hot bubble as a function of time obtained from the "exact" (i.e., numerical) solution of equation 10.6 (solid line) and the radii obtained from the two approximate analytic solutions (short dash: equation 10.16; long dash: equation 10.19). Lower panel: relative deviations (see equation 10.20) of equation 10.16 (short dash) and equation 10.19 (long dash) from the "exact" solution.

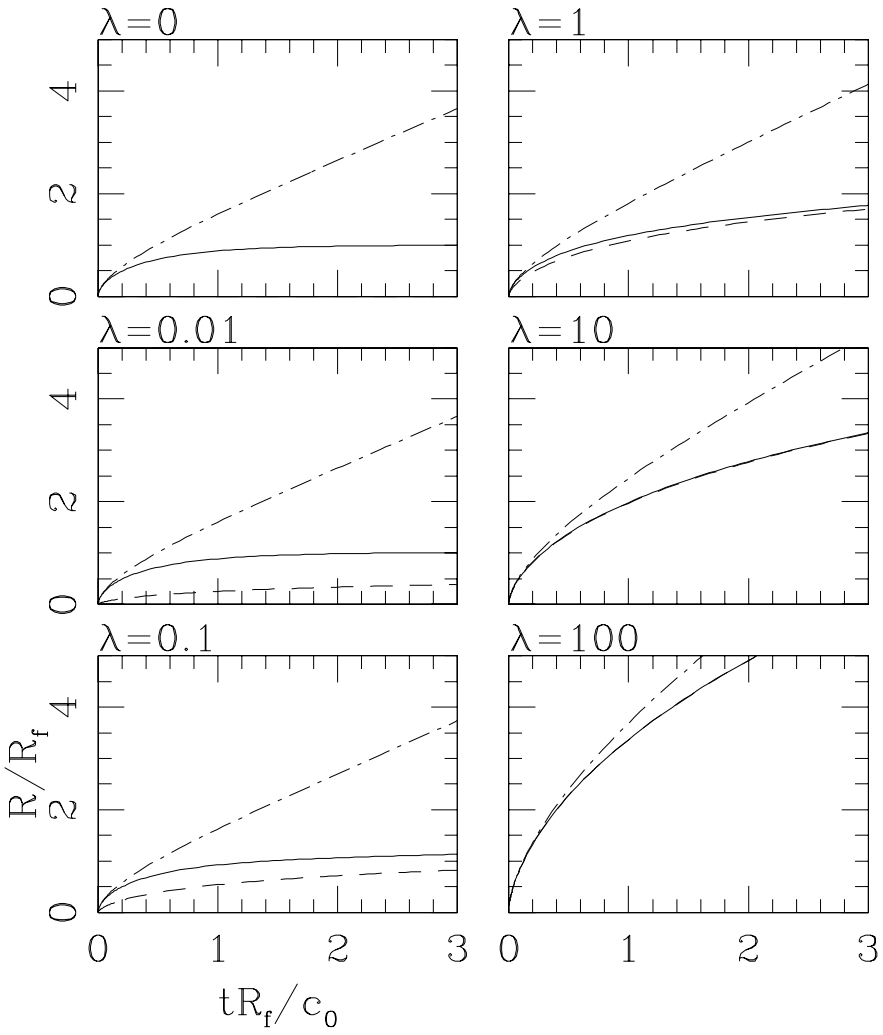

Figure 10.4: Hot bubble radius (dashed line), outer radius of the HII region (solid line) and radius of the shock driven into the surrounding environment (dash-dot line) as a function of time, obtained from numerical solutions of the "thick HII region model" of section 10.4. The six panels are labeled with the values of the dimensionless parameter λ (see equations 10.27, 10.29) used for each solution.

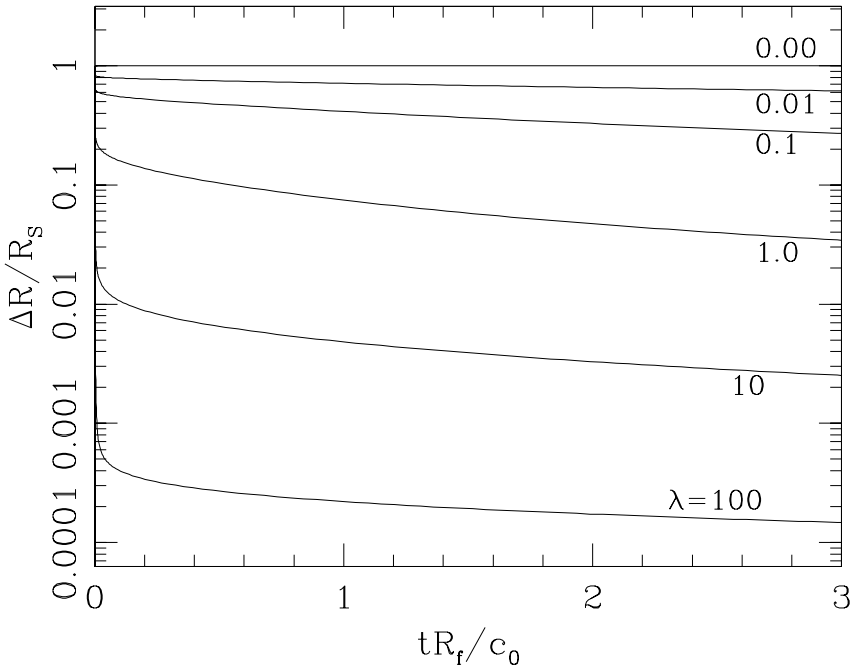

Figure 10.5: Relative width of the HII region (see equation 10.31) as a function of time obtained for different values of the dimensionless parameter λ (see equation 10.27).

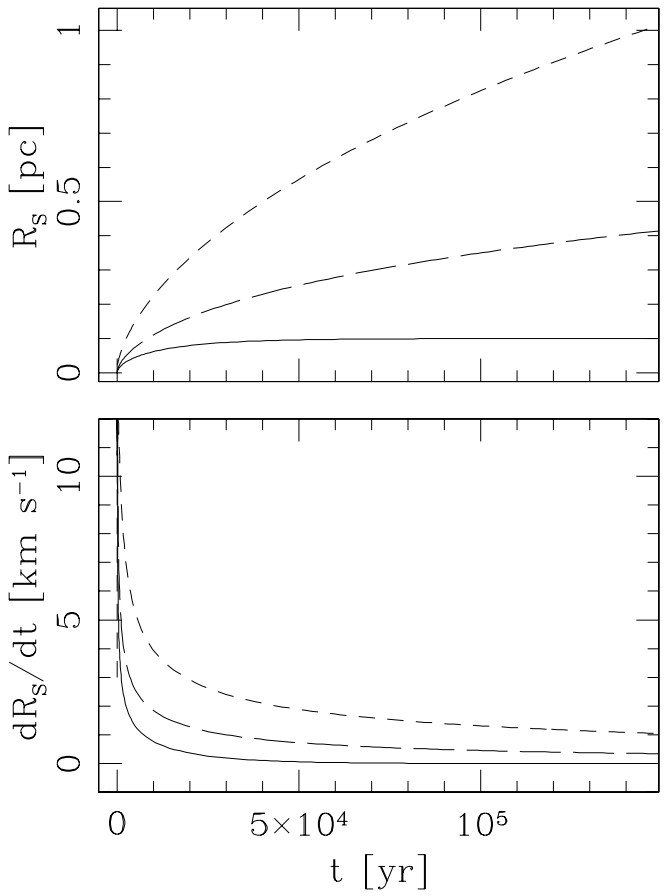

Figure 10.6: Outer radius of the HII region (top panel) and expansion velocity (lower panel) for an ultracompact HII region (of isothermal sound speed c_i = 10 km s^{-1}) driven by a source with $S_* = 10^{49}$s^{-1} into a uniform environment of density $n_0 = 10^7$cm^{-3} (and isothermal sound speed c_0 = 1 km s^{-1}). Three solutions are shown, corresponding to stellar winds such that the dimensionless parameter λ (see equations 10.27, 10.29) has values of 290 (short dash line), 10 (long dash line) and 0 (solid line).

Chapter 11

Supernova remnants

11.1 Introduction

The evolution of supernovae (SN) explosions typically has three distinct phases: an initial "ejectum dominated" phase, which is followed by the Taylor-Sedov phase (in which the expansion has lost the memory of the initial explosion), and by a later, radiative phase (in which the outer shock becomes radiative).

The hot material ejected by the supernova (with an energy typically of $10^{49} \rightarrow 10^{50}$ erg) initially expands freely, at a velocity which depends on the details of the explosion itself. As the material expands, it incorporates more and more ambient material. When this latter component starts to dominate the dynamics of the expansion, the explosion enters the so-called "Taylor-Sedov", energy conserving phase. At later stages of the evolution of a supernova remnant the outer shock becomes radiative, and the expansion enters a final, "momentum conserving" regime.

In this chapter, we first describe the problem of a non-radiative blast wave generated by a point explosion. This problem was studied theoretically by Taylor and by Sedov (who found the full, self-similar analytic solution). The self-similar solution explored by these authors applies to a blast wave in the "strong shock" regime (in which the shock wave moves outwards at a highly supersonic velocity).

A simplified model, in which it is assumed that the swept-up environmental

material is piled up into a "thin shell" (pushed out by an inner, low mass, hot bubble), is described in detail in the book of Zel'dovich & Raizer [34], and leads to an expansion law which is very similar to the one of Sedov. In this "thin shell model", it is also assumed that the expansion drives a strong shock.

In the following, we present a more general derivation of this "thin shell model", allowing the outer shock to have a transition from a strong shock (in the early evolution of the expansion) to a weak shock regime (in the later evolution).

11.2 Dimensional arguments

From a simple, dimensional argument it is possible to derive the general form of the expansion of a spherical blast wave. If we have an explosion of energy E in a uniform medium of density ρ_0, driving a strong, spherical blast wave of radius $R(t)$, it is clear that the parameters E, ρ_0, R and t can be combined into a single, dimensionless parameter:

$$\Pi = \frac{Et^2}{\rho_0 R^5} \,. \tag{11.1}$$

From "Buckingham's Π theorem", because we have a single, independent dimensionless number, this dimensionless number has to be constant. Therefore, the radius of the blast wave as a function of time is:

$$R = C \left(\frac{E}{\rho} \right)^{1/5} t^{2/5} \,, \tag{11.2}$$

where C is an unknown constant (in principle of order 1). If the shock wave becomes weak, this solution is no longer valid, since the sound speed c_0 (or, alternatively, the pressure P_0) of the environment also plays a role in the solution, resulting in the creation of a second dimensionless parameter.

In the following, we present a model from which one recovers equation (11.2, but with known C) for the strong shock limit, and which also describes the regime in which the blast wave is no longer strong.

11.3 The model equation

In order to derive an analytic model for an explosion in an environment with a non-negligible pressure, we use the "expanding shell" model described in the book of Zel'dovich & Raizer [34] and, in the astrophysical context, in the book of Dyson & Williams [13].

In this model, one assumes that a hot, low mass bubble pushes out the surrounding, uniform environment into an outwardly moving shell. The initial energy E of the explosion is divided between thermal energy of the hot bubble and kinetic energy of the shell, so that at any time in the expansion we have:

$$E = \frac{PV}{\gamma - 1} + \frac{1}{2} M_s v_s^2 \,, \tag{11.3}$$

where γ is the specific heat ratio, P and V are the pressure and volume (respectively) of the bubble (at an arbitrary time) and M_s and v_s are the mass and velocity (respectively) of the swept-up shell.

Following the classical derivation, we use the estimates

$$P \approx \frac{2}{\gamma + 1} \rho_0 v_c^2 \,, \tag{11.4}$$

$$v_c \approx \frac{\gamma + 1}{2} v_s \,, \tag{11.5}$$

$$M_s \approx V \rho_0 \,, \tag{11.6}$$

where R is the outer radius of the hot bubble (so that the volume of the bubble is $V = 4\pi R^3/3$), M_S is the shell mass, $v_s = \dot{R}$ the shell velocity, γ the specific heat ratio and ρ_0 is the density of the uniform, undisturbed environment. In principle the specific heat ratio γ for the swept-up environment (equations 11.4-11.5) could be different from the specific heat ratio of the gas within the hot bubble (equation 11.3). Equation (11.4) is the strong shock jump relation, and equation (11.5) gives the velocity v_c of a strong shock pushed out by a plane piston of velocity v_s. Equation (11.6) gives the shell mass assuming that the shell is thin, and that it incorporates all of the environmental material swept up by the expansion of the hot bubble.

Combining equations (11.3-11.6), we obtain an energy conservation equation of the form:

$$E = \Gamma \, R^3 P \,, \tag{11.7}$$

with

$$\Gamma \equiv \frac{8\pi}{3}\frac{\gamma}{\gamma^2-1}\,, \tag{11.8}$$

for a bubble of uniform pressure P and radius R. Equation (11.7) indicates that a constant fraction $(\gamma+1)/2\gamma$ of the initial energy E remains as thermal energy of the hot bubble at all evolutionary times (also, a constant fraction $(\gamma-1)/2\gamma$ of this energy is in the form of shell kinetic energy, see equation 11.3).

We will now assume that this energy distribution also holds for the regime in which the outer shock is no longer strong. This is of course not correct, but as Γ (see equation 11.8) appears only to a power of 1/3 in the final solution, the assumption of a constant value for Γ is not likely to introduce large errors.

We now consider the general (i.e., no longer "strong") shock jump relations:

$$P_1 = \frac{2}{\gamma+1}\rho_0 v_c^2 - \frac{\gamma-1}{\gamma+1}P_0\,, \tag{11.9}$$

$$v_1 = \frac{\gamma-1}{\gamma+1}v_c + \frac{2}{\gamma+1}\frac{c_0^2}{v_c}\,, \tag{11.10}$$

where c_0 is the adiabatic sound speed and P_0 $(= \rho_0 c_0^2/\gamma)$ the pressure of the undisturbed environment, P_1 is the post-shock pressure and v_1 the post-shock velocity (in the shock reference system).

If we assume that the hot bubble acts like a plane piston (i.e., that the shell is not very thick), the relation between the shell velocity v_s $(= \dot{R}$, where R is the radius of the hot bubble, see above) and the shock velocity v_c is: $v_c = v_s + v_1$. Combining this relation with equation (11.10), we obtain the "piston relation":

$$\frac{\dot{R}}{c_0} = \frac{2}{\gamma+1}\left(\frac{v_c}{c_0} - \frac{c_0}{v_c}\right)\,. \tag{11.11}$$

If we now assume that the post-shock pressure P_1 is equal to the pressure P of the hot bubble, combining equations (11.7) and (11.9) we obtain:

$$\left(\frac{v_c}{c_0}\right)^2 = \frac{1}{c_0}^2\dot{R}_c^2 = \frac{1}{2\gamma}\left[(\gamma+1)\left(\frac{R_f}{R}\right)^3 + \gamma - 1\right]\,, \tag{11.12}$$

with

$$R_f \equiv \left(\frac{\gamma E}{\Gamma \rho_0 c_0^2} \right)^{1/3} . \tag{11.13}$$

In equation (11.12), R_c is the (time-dependent) radius of the outer shock. It is clear that if we set $R = R_f$ (where R is the radius of the hot bubble, see above), from equation (11.12) we obtain $v_c = c_0$, and inserting this result in (11.11) we obtain $\dot{R} = 0$. This is the regime of large evolutionary times, in which the hot bubble attains a final radius R_f, and the (weak) outer shock travels sonically into the surrounding environment.

11.4 Solutions for the bubble radius

Equations (11.11) and (11.12) can be straightforwardly combined to obtain a differential equation for the radius R of the hot bubble:

$$\frac{1}{c_0}\frac{dR}{dt} = \frac{2}{\gamma+1}\left[\sqrt{\frac{\gamma+1}{2\gamma}\left(\frac{R_f}{R}\right)^3 + \frac{\gamma-1}{2\gamma}} - \frac{1}{\sqrt{\frac{\gamma+1}{2\gamma}\left(\frac{R_f}{R}\right)^3 + \frac{\gamma-1}{2\gamma}}} \right] . \tag{11.14}$$

Using the boundary condition $R(t=0) = 0$, the solution to this equation is:

$$\frac{c_0 \gamma^{1/3}}{R_f}\left(\frac{2}{\gamma+1}\right)^{4/3} t = \frac{2}{5} r^{5/2} F_1 \left[\frac{5}{6}, -\frac{1}{2}, 1, \frac{11}{6}, -ar^3, (1-a)r^3 \right] , \tag{11.15}$$

where F_1 is the Appell hypergeometric function of two variables,

$$r \equiv \left(\frac{2\gamma}{\gamma+1} \right)^{1/3} \frac{R}{R_f} , \tag{11.16}$$

with R_f given by equation (11.13), and

$$a = \frac{\gamma-1}{2\gamma} . \tag{11.17}$$

For the $\gamma = 1$ case, equation (11.14) has the simpler integral:

$$\frac{c_0}{R_f} t_1 = \frac{1}{6} \Bigg\{ 2\sqrt{3} \tan^{-1} \left(\frac{\sqrt{3r}}{r-1} \right)$$

$$+ \ln \left[\frac{(\sqrt{r}+1)^2 (1+\sqrt{r}+r)}{(\sqrt{r}-1)^2 (1-\sqrt{r}+r)} \right] \Bigg\} , \tag{11.18}$$

with r given by equation (11.16).

The radius R of the hot bubble as a function of time t (actually computed as t vs. R from equations 11.15, 11.18) is shown for $\gamma = 5/3$, $7/5$ and 1 in Figure 11.1. It is clear from this figure that (if plotted in the correct dimensionless form) the solutions for the different values of γ differ by at most a few percent. Therefore, for an arbitrary γ (within the $5/3 \rightarrow 1$ range shown in Figure 11.1), it is a good approximation to compute the time-evolution of the hot bubble through:

$$t \approx \frac{\gamma + 1}{2} t_1(r) , \tag{11.19}$$

with r given as a function of the dimensional radius R of the bubble by equation (11.16), and $t_1(r)$ obtained through equation (11.18). With this approximation, the more complex evaluation of the Appel hypergeometric function of two variables (equation 11.15) is avoided.

We end by pointing out that if one takes the $R \ll R_f$ limit in equation (11.14), the resulting differential equation can be straightforwardly integrated to obtain:

$$\frac{R_{TS}}{R_f} = \left[\frac{25}{2\gamma(\gamma+1)} \right]^{1/5} \left(\frac{c_0 t}{R_f} \right)^{2/5} , \tag{11.20}$$

which corresponds to the "strong shock" Taylor-Sedov solution in which the hot bubble expands as time to the 2/5 power. It can be shown that equations (11.15) and (11.18) coincide with equation (11.20) for $R \ll R_f$.

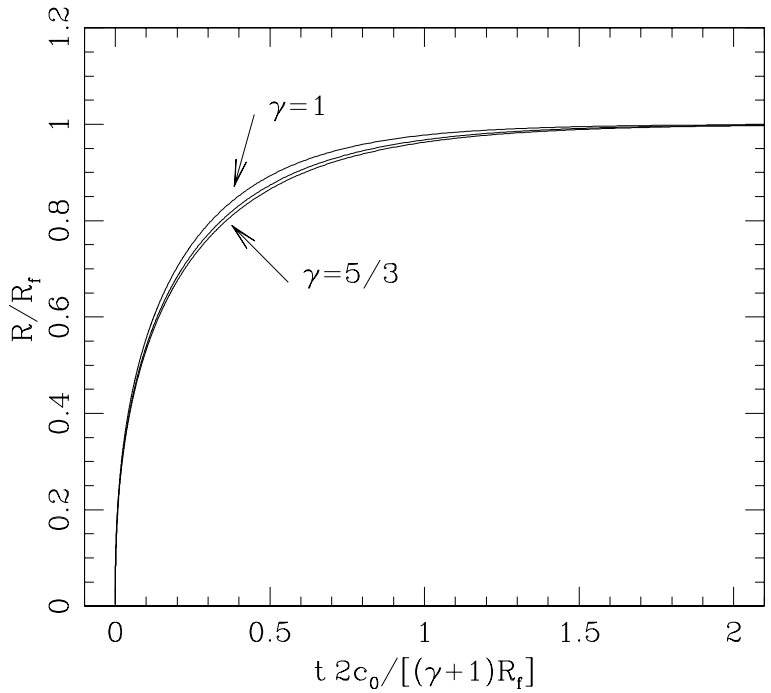

Figure 11.1: Radius R of the hot bubble (in units of R_f, see equation (11.13) as a function of time t [in units of $(\gamma+1)R_f/(2c_0)$] for three different values of the specific heat ratio γ. The curves corresponding to $\gamma = 5/3$ and $\gamma = 1$ are labeled, and the middle curve corresponds to $\gamma = 7/5$.

11.5 Solution for the shock radius

In order to find the radius R_c of the outer shock as a function of time, we combine equations (11.11) and (11.12) to obtain:

$$\frac{dR_c}{dR} = \frac{1 + \alpha(R/R_f)^3}{(1-\alpha)\left[1-(R/R_f)^3\right]}\,, \tag{11.21}$$

where R is the radius of the hot bubble (given as a function of time by equations 11.15-11.19), R_f is given by equation (11.13) and

$$\alpha = \frac{\gamma - 1}{\gamma + 1}\,. \tag{11.22}$$

This equation can be directly integrated to obtain:

$$\frac{R_c}{R_f} = -\frac{(\gamma-1)}{2}\left(\frac{R}{R_f}\right) + \frac{\gamma}{\sqrt{3}}\tan^{-1}\left(\frac{\sqrt{3}R/R_f}{2+R/R_f}\right)$$

$$+\frac{\gamma}{6}\ln\left[\frac{1+R/R_f+(R/R_f)^2}{(1-R/R_f)^2}\right]\,. \tag{11.23}$$

We have taken the $\gamma = 7/5$, $5/3$ and 1 $R(t)$ solutions of equation (11.15) shown in Figure 11.1, and used equation (11.23) to compute the corresponding $R_c(t)$ shock radii. The obtained results are shown in Figure 11.2.

Finally, we note that in the strong shock, $R \ll R_f$ limit, both equations (11.21) and (11.23) give

$$R_c = \frac{(\gamma+1)}{2}R\,. \tag{11.24}$$

Therefore, using equation (11.20) we recover the Taylor-Sedov solution in which the shock wave radius grows as $t^{2/5}$.

Figure 11.3 shows the pressure and density stratifications in a time-radius plane obtained from a numerical integration of the spherically symmetric gas-dynamic equations. Also shown are the analytic solutions obtained for the shock wave (black, solid line in the top frame) and for the outer radius of the hot bubble (black, dashed line in the bottom frame). Finally, the strong shock solutions (white solid and dashed lines) of equations (11.20) and (11.24)

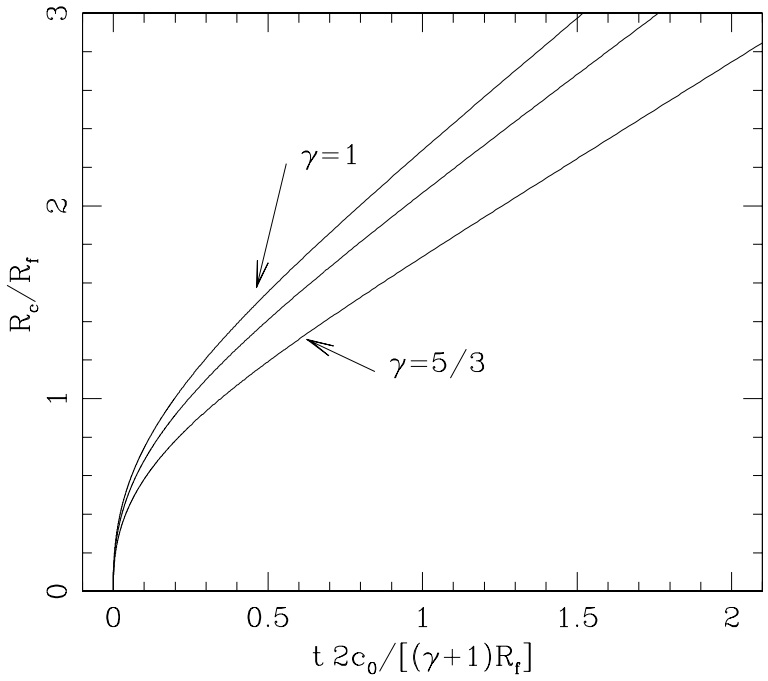

Figure 11.2: Radius R_c of the outer shock (in units of R_f, see equation (11.13) as a function of time t [in units of $(\gamma+1)R_f/(2c_0)$] for three different values of the specific heat ratio γ. The curves corresponding to $\gamma = 5/3$ and $\gamma = 1$ are labeled, and the middle curve corresponds to $\gamma = 7/5$.

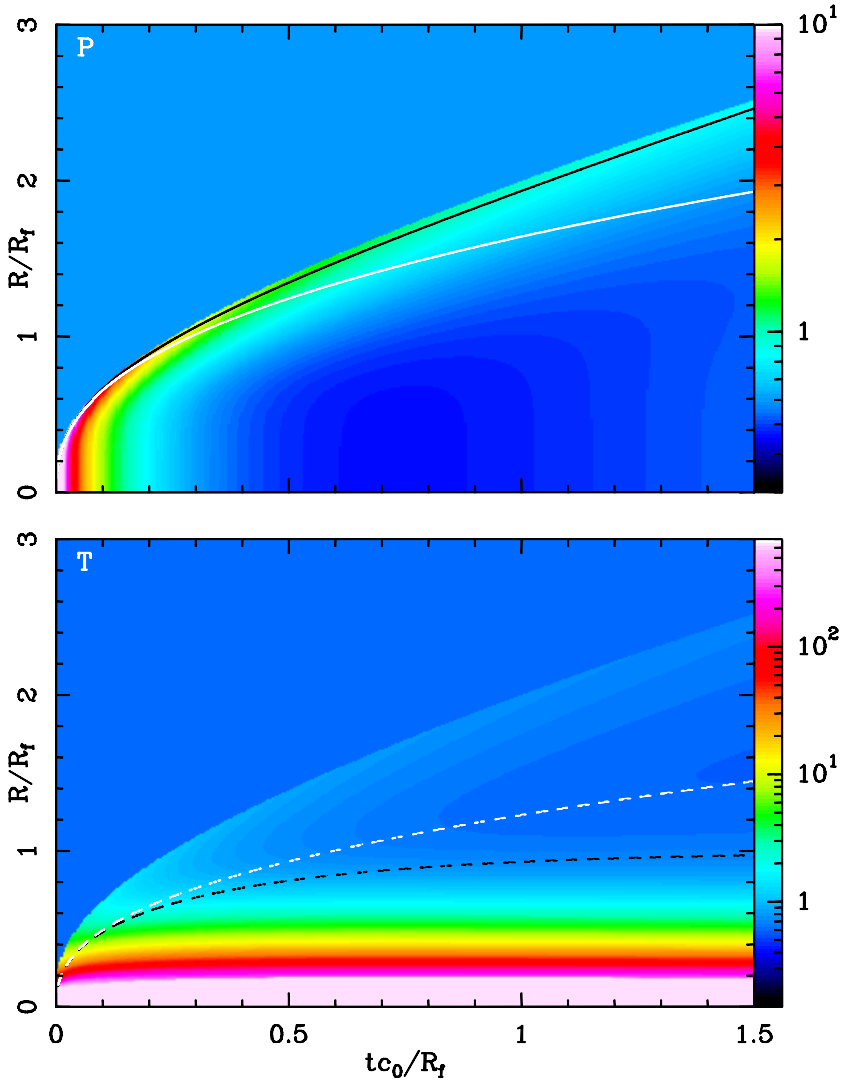

Figure 11.3: Pressure (top) and temperature (bottom frame) stratifications in the (t, R)-plane obtained from the numerical simulation described in the text. The dimensionless pressure and temperature are plotted with the logarithmic scales given by the bars on the right. The positions of the outer shock (black, solid line in the top frame) and the outer radius of the hot bubble (black, dashed line in the bottom frame) predicted from the strong/weak shock analytic model are also shown. Finally, the white curves show the predictions from the "strong shock' solutions (solid line $\rightarrow$ outer shock; dashed line $\rightarrow$ outer boundary of hot bubble).

are also included. From the top frame of Figure 11.3, it is clear that while the strong shock solution (white, solid line) shows strong deviations from the numerical simulation for $t > R_f/c_0$, the new "strong/weak shock" solution (equations 11.15 and 11.23) agrees to within $\sim 5\%$ with the simulated shock position for all of the displayed times.

It is less clear what is the feature in the numerical simulation that corresponds to the outer radius of the "hot bubble". In the bottom frame, we see that the radius R of the hot bubble (obtained from equation 11.15) encloses a hot region with a strongly stratified temperature. For larger radii, the temperature has values similar to the temperature of the undisturbed environment (except for a narrow, hotter region just behind the outer shock).

The radius of the "hot bubble" of the analytic model does not correspond to the position of the outer edge of the initial bubble imposed in the numerical simulation. At a time $t = 1.5\, c_0/R_f$, the initial bubble has expanded to a radius of $\approx 0.17 R_f$ (seen as the saturated, high temperature region in the bottom frame of Figure 11.3). The "hot bubble" of the analytic model has approximately 5 times this radius, and its mass is dominated by environmental material heated by the blast wave at early evolutionary times.

11.6 Astrophysical application of the weak shock solution

This chapter presents an extension of the analytic "hot bubble/swept-up shell" model for non-radiative, spherical blast waves described in the book of Zel'dovich & Raizer [34] to the case in which the outer shock has a strong/weak shock transition. The resulting model has a full analytic solution, which gives the radii of the hot bubble and of the outer shock as a function of time.

The analytic model has an initial behaviour which is similar to the "strong shock", Taylor-Sedov solution. For radii of the hot bubble $R \sim R_f$ and times $t \sim R_f/c_0$ (where R_f is given by equation 11.13), the analytic solution has a transition to a "weak shock" regime, in which the hot bubble stops growing (the bubble remaining in approximate pressure equilibrium with the undisturbed environment) and the outer shock velocity approaches c_0 (the environmental sound speed).

While the application of the present model to "ground based" explosions is evident, it also has astrophysical applications. Tang & Wang [33] showed that SN explosions within pre-existing hot bubbles can reach the "weak shock" regime. In the context of our analytic model, this can be seen by setting $n_0 \sim 1$ cm^{-3}, $c_0 \sim 1000$ km s^{-1} (the environmental number density and sound speed, respectively) and $E \sim 10^{50}$ erg in equation (11.13), to obtain $R_f \sim 2.3$ pc. As can be seen from Figure 11.1, the bubble reaches a radius R_f at a time $t_f \sim R_f/c_0 \sim 2200$ yr. At a time $\sim t_f$, the outer shock also becomes weak (see Figure 11.1).

Therefore, if we have a pre-existing, hot bubble of radius $R_0 > R_f$, the explosion will generate an inner, higher temperature core (of radius $\sim R_f$), and the outer shock will perturb only weakly the remaining, outer region of the initial bubble. This hot core will eventually be dissipated as a result of thermal conduction. If the initial hot bubble is stratified, the hot core generated by the SN explosion would migrate, "floating" towards the direction of maximum (negative) pressure gradient. This discussion of SN explosions in pre-existing hot bubbles does not differ substantially from the one of Tang & Wang [33].

A second possible astrophysical application of our model is for SN explosions within molecular clouds. This situation has been explored theoretically by Chevalier [11]. In order to evaluate whether a SN explosion will reach the weak shock regime within a molecular cloud, we set $n_0 \sim 10^6$ cm^{-3}, $c_0 \sim 1$ km s^{-1} and $E \sim 10^{50}$ erg in equation (11.13), obtaining $R_f \sim 2.3$ pc. The evolution of the remnant to the weak shock regime will take place in $t_f \sim R_f/c_0 \sim 2.2 \times 10^6$ yr. Therefore, if we have a SN explosion within a molecular cloud of radius larger than ~ 2.3 pc, it will contain the hot bubble generated by the explosion. This contained bubble will generate convective instabilities through which it will eventually mix with the outer regions of the molecular cloud.

We should note that though the present model is strictly non-radiative, it is still possible to apply it to the case in which the outer shock is highly radiative. This can be done by considering $\gamma = 5/3$ for the non-radiative, hot bubble (i.e., setting $\gamma = 5/3$ in equation 11.8) and $\gamma = 1$ in the equations resulting from the shock relations (i.e., in equations 11.15-11.18 and 11.21-11.22). In this way, the model can be applied to the case of a SN within a molecular cloud, in which the transition from a non-radiative to a radiative outer shock takes place in the early stages of the evolution of the remnant.

However (at least in its present form), the model cannot be applied to a "normal" SN remnant, in which substantial parts of the evolution are both in the non-radiative and radiative outer shock regimes.

11.7 The radiative phase

In a normal SN remnant, the outer shock reaches velocities of ~ 300 km s^{-1} while still being strong. At lower shock velocities, the post-shock cooling time and cooling distance rapidly become very short (compared to the evolutionary timescale of the remnant), so that the outer shell becomes radiative.

From then on, the outer shell coasts along, conserving momentum, and slowing down as this momentum is shared with newly swept-up environmental material. The simplest model for the motion of such a shell is as follows (see the book of Dyson & Williams 1980 [13]).

Let us consider that at $t = t_0$ we have a shell of radius R_0, velocity v_0, mass M_0 and momentum $\Pi_0 = M_0 v_0$. At all times, the mass of the shell is:

$$M = \frac{4\pi}{3} R^3 \rho_0 \,. \tag{11.25}$$

For a momentum conserving shell (i.e., with $\Pi = Mv = \Pi_0$ for all times), we then have

$$\frac{dR}{dt} = \frac{\Pi_0}{M} = \left(\frac{R_0}{R}\right)^3 v_0 \,, \tag{11.26}$$

which can be integrated to obtain:

$$R(t) = R_0 \left[1 + \frac{4 v_0 (t - t_0)}{R_0}\right]^{1/4} \,. \tag{11.27}$$

Therefore, at large evolutionary times the shell follows a $R \propto t^{1/4}$ ($\rightarrow v \propto t^{-3/4}$) law, with a faster slowing down than the Taylor-Sedov phase.

Clearly, the model discussed here could be elaborated. The two clear improvements are:

1. including the force due to the inner, hot bubble,

2. including the strong/weak shock transition in the outer shock.

While the first of these items has already been explored in the literature, as far as we are aware the second item has not yet been attempted.

Chapter 12

Gravitational collapse

12.1 General considerations

In the "nebular hypothesis" proposed by Laplace towards the end of the XVII-Ith century, the solar system is supposed to condense out of a diffuse, rotating cloud of gas. This idea is preserved in more modern astrophysics for the formation of stars in general, as there is now very substantial evidence of the existence of recently formed stars associated with dense regions of the ISM.

Let us describe a semi-qualitative model for the collapse of a gas cloud in the ISM due to its own self-gravity. If one has a spherical, self-gravitating cloud with an outer pressure P, the balance between the pressure force and the gravitational force of the cloud can be written in an approximate way as:

$$4\pi R^2 P \approx \frac{GM^2}{R^2}\,, \tag{12.1}$$

where R is a characteristic radius of the cloud, P the external pressure, $M = 4\pi\rho R^3/3$ the mass of the cloud (with ρ representing an average density) and G the gravitational constant.

We now assume that the pressure and density follow an adiabat:

$$P = P_0 \left(\frac{\rho}{\rho_0}\right)^{\gamma}\,, \tag{12.2}$$

where γ is the specific heat ratio. Equations (12.1) and (12.2) can be combined

to obtain:

$$M_J = \xi \left(\frac{P_0}{G\rho_0^\gamma} \right)^{1/(2-\gamma)} R^{(4-3\gamma)/(2-\gamma)} \,. \tag{12.3}$$

In this equation, ξ is a constant of order unity (a calculation of its value involves a considerably more complex model, see the following section). M_J is the so-called "Jeans mass", for which a cloud of external radius R is in the hydrostatic equilibrium resulting from the balance between the pressure force and the self-gravity of the cloud.

Clearly, there are two possible behaviours, depending on whether the exponent $\alpha = (4-3\gamma)/(2-\gamma)$ is positive or negative:

a. $\alpha > 0$ ($\gamma < 4/3$ or $\gamma > 2$): if we compress a cloud in initial hydrostatic equilibrium (i.e., with mass $M = M_J$ at the initial cloud radius), the Jeans mass of the compressed configuration is smaller than the initial mass of the cloud. Therefore, the cloud has an imbalance between the (now insufficient) pressure force and the self-gravity, and the cloud continues to collapse,

b. $\alpha < 0$ ($4/3 < \gamma < 2$): a compression of an initially hydrostatic cloud results in an increase of the Jeans mass. Therefore, the mass of the compressed cloud will be lower than the Jeans mass, so that the cloud will re-expand under the effect of the positive imbalance between the internal pressure and the self-gravity.

For a self-gravitating molecular cloud core, the balance between the heating (by absorption of UV and X-ray photons by dust) and the cooling (by emission of lines of CO and other molecules) results in an approximately isothermal behaviour. Therefore, a relation $P = \rho c_0^2$ (where c_0 is the approximately constant isothermal sound speed) is satisfied, so that $\gamma \approx 1$ (see equation 12.2). Then, the Jeans mass is given by:

$$M_J = \frac{\xi c_0^2 R}{G} \,, \tag{12.4}$$

and the cloud is in the unstable, $\alpha > 0$ regime described above.

This derivation is only an approximation to the real problem, since it is based only on an approximate pressure/gravity balance condition (see equation 12.1). A more thorough derivation of the stability condition for a spherical, isothermal cloud core is derived in the following sections.

12.2 The isothermal, self-gravitating sphere

12.2.1 The Lane-Emden equation

A self-gravitating, hydrostatic cloud has a radially stratified density. The balance between the pressure gradient and the gravitational force can be written as:

$$\frac{dP}{dR} = -\frac{\rho G M_R}{R^2}\,, \tag{12.5}$$

where P and ρ are the gas pressure and density (respectively), R is the spherical radius and

$$M_R = 4\pi \int_0^R \rho R'^2 dR'\,, \tag{12.6}$$

is the mass within a radius R.

Now, for the isothermal case, we have $P = \rho c_0^2$ (where c_0 is the isothermal sound speed). Grouping terms and taking a derivative with respect to R of equation (12.5) one obtains the so-called "isothermal, Lane-Emden equation":

$$\frac{d}{dR}\left(R^2 \frac{d\ln\rho}{dR}\right) = -\frac{4\pi G}{c_0^2}\rho R^2\,. \tag{12.7}$$

An exact solution to this equation is the "singular, isothermal sphere":

$$\rho_S(R) = \frac{c_0^2}{2\pi G}\frac{1}{R^2}\,. \tag{12.8}$$

As we will see in the following section, there is also a more general, non-singular solution of the Lane-Emden equation.

12.2.2 The non-singular solution

The non-singular isothermal sphere (which also satisfies equation 12.7) does not have a full, analytic solution. It is possible to propose a Taylor series of the solution, and substituting it into (12.7) to obtain the coefficients of this series by matching terms with the same power of R. To second order in R, one obtains the well known solution:

$$\rho_2(R) = \rho_c\left[1 - \left(\frac{R}{R_c}\right)^2\right]\,, \tag{12.9}$$

where ρ_c is the central density and

$$R_c \equiv \sqrt{\frac{3c_0^2}{2\pi G\rho_c}} \tag{12.10}$$

is the so-called "core radius" of the non-singular sphere.

If one defines dimensionless variables $r = R/R_c$ and $\rho' = \rho/\rho_c$, the isothermal, Lane-Emden equation becomes:

$$\frac{d}{dr}\left(r^2 \frac{d\ln\rho'}{dr}\right) = -6\rho' r^2 \,. \tag{12.11}$$

The dimensionless, singular solution then is:

$$\rho'_S(r) = \frac{1}{3r^2} \,, \tag{12.12}$$

and the second order, $r \ll 1$ solution is:

$$\rho'_2(r) = 1 - r^2 \,. \tag{12.13}$$

It is a well-known result that the non-singular solution (obtained, e.g., by integrating numerically equation 12.11 with the boundary conditions $\rho' = 1$ and $d\rho'/dr = 0$ at $r = 0$) asymptotically approaches the singular solution (equation 12.12) for $r \gg 1$. A certain amount of effort has been made to design interpolation formulae that match the Taylor series expansion (equation 12.13) for small r and the singular solution (equation 12.12) for large r, and reproduce the non-singular solution (for all r) with a certain degree of accuracy.

The simplest of the proposed interpolations is:

$$\rho'_a(r) = \frac{1}{1+r^2} \,. \tag{12.14}$$

This interpolation has the virtue of coinciding (to second order in r) with the Taylor series solution (equation 12.13), and having a $\rho \propto r^{-2}$ dependence for $r \gg 1$. However, the proportionality constant ($= 1$) of the large r dependence of equation (12.14) is larger by a factor 3 than the constant of the singular solution (see equation 12.12).

In order to have a better analytic approximation to the non-singular isothermal sphere, it is necessary to divide the solution into a "far field" and a "near field" regime. This is described in the following two sections.

12.2.3 The $R \gg R_c$, "far field" solution

For $R \gg R_c$ (i.e., for $r \gg 1$), the non-singular solution of the isothermal, Lane-Emden equation (equation 12.11) asymptotically approaches the singular solution (equation 12.12). In order to study the characteristics of this approach, we propose a function $q(r)$ such that:

$$\rho'(r) = [1 + q(r)]\, \rho'_s(r)\,, \tag{12.15}$$

where $\rho'_s(r) = 1/(3r^2)$ (see equation 12.12). Substituting equation (12.15) into equation (12.11) we obtain a differential equation for q of the form:

$$2q + \frac{2rq'}{1+q} - \frac{r^2 q'^2}{(1+q)^2} + \frac{r^2 q''}{1+q} = 0\,, \tag{12.16}$$

where $q' = dq/dr$ and $q'' = d^2q/dr^2$. We now assume that q, q', $q'' \ll 1$, and therefore only keep in equation (12.16) the terms with linear dependencies on these functions. We then obtain:

$$2q + 2rq' + r^2 q'' = 0\,. \tag{12.17}$$

Proposing a solution of the form $q = Cr^p$ (with constant C and p) and substituting into (12.17), one straigthforwardly obtains that $p = 1/2 + i\sqrt{7}/2$. Therefore, the real (as opposed to complex) solution has the form:

$$q_l(r) = \frac{A}{r^{1/2}} \cos\left(\frac{\sqrt{7}}{2} \ln r + \phi\right)\,, \tag{12.18}$$

in which A and ϕ are the two integration constants. This solution is derived in a more elaborate way in the book of Chandrasekhar (1967, first published in 1939).

From equation (12.18), we see that indeed $q_l(r) \to 0$ (in other words, $\rho' \to \rho'_s$, see equation 12.15) for $r \gg 1$, but that it changes sign periodically as a function of $\ln r$. Therefore, the non-singular solution crosses the singular solution repeatedly, with intervening excursions of decreasing amplitude for larger values of r (see equation 12.18).

We now take the "exact" solution $\rho_{ex}(r)$ of the isothermal, Lane-Emden equation (obtained by integrating equation 12.11 with a second-order, variable step

Table 12.1: Coefficients for interpolation (12.21)

j	A_j	a_j^2
1	24.941621	9.229485
2	−22.890004	13.490639
3	−0.602714	106.575159
4	0.551098	5172.242487

method), and use it to compute the corresponding deviation q_{ex} from the singular solution:

$$q_{ex}(r) = \frac{\rho_{ex}(r)}{\rho_s(r)} - 1\,, \tag{12.19}$$

as follows from equation (12.15). We then obtain the values $A_0 = 0.735$ and $\phi_0 = 5.396$ from a least squares fit of $q_l(r)$ (equation 12.18) to the exact solution (equation 12.19) in the $r = 10 \to 10^4$ radial range.

Finally, from equation (12.15) we obtain:

$$\rho(r) = \rho_s(r) f_{near}(r)\,; \quad f_{near}(r) = 1 + q_l(r)\,, \tag{12.20}$$

with $q_l(r)$ given by equation (12.18).

12.2.4 The $R \sim R_c$, "near field" solution

For $R \sim R_c$ we take the interpolation formula proposed by Hunter ([16]):

$$\rho_H(r) = \sum_{j=1}^{4} \frac{A_j}{a_j^2 + 6r^2}\,, \tag{12.21}$$

where the A_j and a_j^2 coefficients are given in Table 12.1. This interpolation has a good behaviour out to $\log_{10} r \approx 1.5$.

The natural choice for a switch between the near and far field solutions is at a dimensionless radius $r_1 = 27.643$, at which the "near field" and the "far field" approximations coincide.

12.2.5 The full solution

The full density stratification can then be written in the form:

$$\rho(R) = \frac{c_0^2}{2\pi G R^2} f\left(\frac{R}{R_c}\right) , \tag{12.22}$$

where R is the spherical radius, G the gravitational constant, c_0 the isothermal sound speed, R_c is the core radius (see equation 12.10) and ρ_c the central density.

The $f(r)$ function (with $r = R/R_c$) is approximated by a "near" and a "far field" interpolation (f_{near} and f_{far}, respectively), with a switch at a radius $r_1 = 27.643$:

$$f(r) = f_{near}(r)\,, r \leq r_1\,; \quad f(r) = f_{far}(r)\,, r > r_1\,, \tag{12.23}$$

with

$$f_{near}(r) = \sum_{j=1}^{4} \frac{A_j}{2 + a_j^2/(3r^2)}\,, \tag{12.24}$$

and

$$f_{far}(r) = 1 + \frac{A}{r^{1/2}} \cos\left(\frac{\sqrt{7}}{2}\ln r + \phi\right) , \tag{12.25}$$

where $A = 0.735$, $\phi = 5.396$ and the values of A_j and a_j given in Table 12.1.

With these forms for $f_{near}(r)$ and $f_{far}(r)$ it is straightforward to calculate the derivative $f'(r)$ of f with respect to r:

$$f'(r) = f'_{near}(r)\,, r \leq r_1\,;$$

$$f'(r) = f'_{far}(r)\,, r > r_1\,, \tag{12.26}$$

with

$$f'_{near}(r) = \frac{2}{3}\sum_{j=1}^{4} \frac{a_j^2 A_j r}{(2r^2 + a_j^2/3)^2}\,, \tag{12.27}$$

and

$$f'_{far}(r) = -\frac{A}{2r^{3/2}}\left[\sqrt{7}\sin\left(\frac{\sqrt{7}}{2}\ln r + \phi\right) + \cos\left(\frac{\sqrt{7}}{2}\ln r + \phi\right)\right]. \tag{12.28}$$

We can also calculate the integral

$$F(r) = \int_0^r f(r')dr' \tag{12.29}$$

as

$$F(r) = I_1(r)\,, r \leq r_1\,;$$
$$F(r) = I_1(r_1) + I_2(r) - I_2(r_1)\,, r > r_1\,, \tag{12.30}$$

where

$$I_1(r) = \sum_{j=1}^{4} \frac{A_j}{2}\left[r - \frac{a_j}{\sqrt{6}}\tan^{-1}\left(\frac{\sqrt{6}r}{a_j}\right)\right]\,, \tag{12.31}$$

$$I_2(r) = r + \frac{Ar^{1/2}}{4}\left[\sqrt{7}\sin\left(\frac{\sqrt{7}}{2}\ln r + \phi\right) + \cos\left(\frac{\sqrt{7}}{2}\ln r + \phi\right)\right]\,. \tag{12.32}$$

12.2.6 General properties of the isothermal sphere

Let us consider a self-gravitating sphere of isothermal sound speed c_0 embedded in an environment of pressure $\rho_e c_0^2$ (so that the outer density of the sphere has a value ρ_e). From equation (12.22) we can then obtain the outer radius R_e of the sphere:

$$R_e = \sqrt{\frac{c_0^2}{2\pi G\rho_e}f(r_e)}\,, \tag{12.33}$$

and also the total mass:

$$M = 4\pi\int_0^{R_e}\rho(R')R'^2dR' = \frac{2c_0^2R_c}{G}F\left(\frac{R_e}{R_c}\right)\,, \tag{12.34}$$

Combining equations (12.33), (12.34) and (12.10) we then obtain the total mass

$$M = \frac{2c_0^3}{\sqrt{2\pi\rho_e G^3}}\frac{f^{1/2}(r_e)F(r_e)}{r_e}\,, \tag{12.35}$$

as a function of the ratio $r_e = R_e/R_c$ between the external radius and the core radius of the sphere.

The outer radius and total mass of the sphere (equations 12.33 and 12.35) are plotted as a function of R_e/R_c in Figure 12.1. In this figure, we see that for a

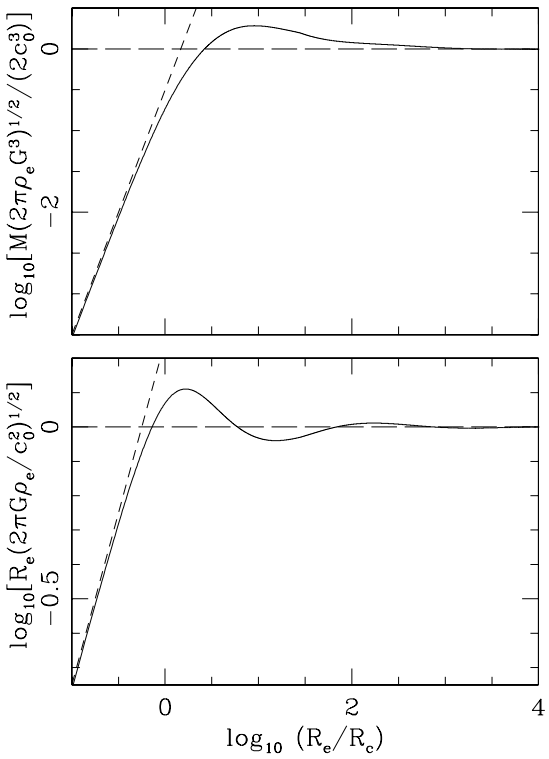

Figure 12.1: Dimensionless mass (top) and outer radius (bottom) of a non-singular isothermal sphere as a function of the outer to core radius ratio R_e/R_c (solid lines). The long dash, horizontal lines represent the values obtained for the singular sphere. The short dash lines represent a $M \propto (R_e/R_c)^3$ (top graph) and a $R_e \propto R_e/R_c$ dependence (bottom).

sphere with weak gravity (i.e., with $R_c \gg R_e$) we naturally obtain $R_e \propto R_e/R_c$ and $M \propto (R_e/R_c)^3$, as would be expected for a sphere with an approximately uniform density (with a value $\approx \rho_e$).

From Figure 12.1 we also see that for $R_e/R_c \gg 1$, the outer radius and the total mass reach asymptotic values R_a and M_a (respectively), with values

$$R_a = \sqrt{\frac{c_0^2}{2\pi G \rho_e}}\,, \tag{12.36}$$

$$M_a = \frac{2c_0^3}{\sqrt{2\pi\rho_e G^3}}\,, \tag{12.37}$$

corresponding to the radius and mass of the singular isothermal sphere solution (equation 12.8). These values can be obtained from equations (12.33) and (12.35) by setting $f(r_e) = 1$ and $F(r_e) = r_e$.

12.3 Stability of the isothermal sphere

12.3.1 Bonnor's stability criterion

Finally, we are at the point of being able to determine the stability properties of an isothermal, self-gravitating sphere. Bonnor [5] suggested the following stability criterion for radial perturbations. If we have a sphere of total mass M and external radius R_e, it is gravitationally stable provided that

$$\left(\frac{dP_e}{dR_e}\right)_{M=const.} = c_0^2 \left(\frac{d\rho_e}{dR_e}\right)_{M=const.} < 0\,, \tag{12.38}$$

where P_e is the outer pressure of the sphere and ρ_e its outer density (obtained by setting $R = R_e$ in equation 12.22). In other words, the self-gravitating sphere is stable if it can react to an increase in the pressure of the surrounding environment by generating a new hydrostatic structure with a smaller external radius. With the approximate, analytic non-singular solution described above, we evaluate this criterion in the following way.

First, differentiating equation (12.35) we obtain:

$$\frac{G}{2c_0^2} dM = \left[F(r_e) + R_c \frac{dF}{dr_e}(r_e)\frac{\partial r_e}{\partial R_c}\right] dR_c + R_c \frac{dF}{dr_e}(r_e)\frac{\partial r_e}{\partial R_e} dR_e\,, \tag{12.39}$$

where $r_e = R_e/R_c$. In this equation, $\partial F/\partial r_e = f(r_e)$, $\partial r_e/\partial R_c = -R_e/R_c^2$ and $\partial r_e/\partial R_e = 1/R_c$. Setting $dM = 0$ in equation (12.39) we then have:

$$\frac{dR_c}{dR_e} = \frac{1}{r_e - F(r_e)/f(r_e)}\,, \tag{12.40}$$

for a variation at constant M.

We now evaluate equation (12.22) at the external radius R_e and differentiate to obtain:

$$\frac{2\pi G}{c_0^2}\frac{d\rho}{dR_e} = \frac{1}{R_e^2}\left[-\frac{2}{R_e} f(r_e) + \frac{df}{dr_e}\frac{dr_e}{dR_e}\right]\,, \tag{12.41}$$

where

$$\frac{dr_e}{dR_e} = \frac{1}{R_c} - \frac{R_e}{R_c^2}\frac{dR_c}{dR_e}\,. \tag{12.42}$$

Finally, combining equations (12.40-12.42) we obtain

$$\frac{2\pi G}{c_0^2}\frac{d\rho}{dR_e} = \frac{1}{R_e^3}\left[\frac{r_e f'(r_e)}{1 - r_e f(r_e)/F(r_e)} - 2f(r_e)\right]\,, \tag{12.43}$$

where $f(r_e)$ (see equation 12.22), $F(r_e)$ (equation 12.25) and $f' = df(r_e)/dr_e$ are obtained from the approximate analytic solution described above.

Figure 12.2 shows the fractional deviation q between the non-singular and singular solutions (equation 12.15), and the dimensionless values of $|d\rho/dR_e|$ and $R_e^3\, d\rho/dR_e$ obtained from equation (12.43) and from the exact (i.e., numerical) non-singular solution. The results obtained from the approximate, analytic and the exact (numerical) isothermal sphere solutions are basically indistinguishable.

From the two lower plots of Figure 12.2, we see that $d\rho/dR < 0$ for small radii, and that $d\rho/dR = 0$ for a radius $R_s = 2.633\, R_c$. For $R_s < R < 3.672\, R_c$ we have $d\rho/dR > 0$ (and, hence, an unstable behaviour, see equation 12.38), and at larger radii we have an approximately logarithmically periodical repetition of radial bands of stable (i.e., negative $d\rho/dR$) and unstable (positive $d\rho/dR$) behaviour, following the periodical crossings in $\ln R$ between the non-singular and singular solutions of the asymptotic, large R regime (seen in the top graph of Figure 12.2 and in equation 12.25).

Bonnor [5] argued that all of the isothermal spheres with $R > R_s$ are unstable (regardless of whether their outer radius R is within one of the stable or unstable outer bands), as perturbations at the outer radius of the cloud will propagate inwards into unstable regions. This result is confirmed by later numerical simulations with the full gasdynamic equations.

12.3.2 The Jeans mass of an isothermal sphere

We are then in a position of being able to obtain the Jeans Mass of a self-gravitating isothermal sphere embedded in an environment of pressure P_e. The density at the outer boundary of the sphere then is $\rho_e = P_e/c_0^2$.

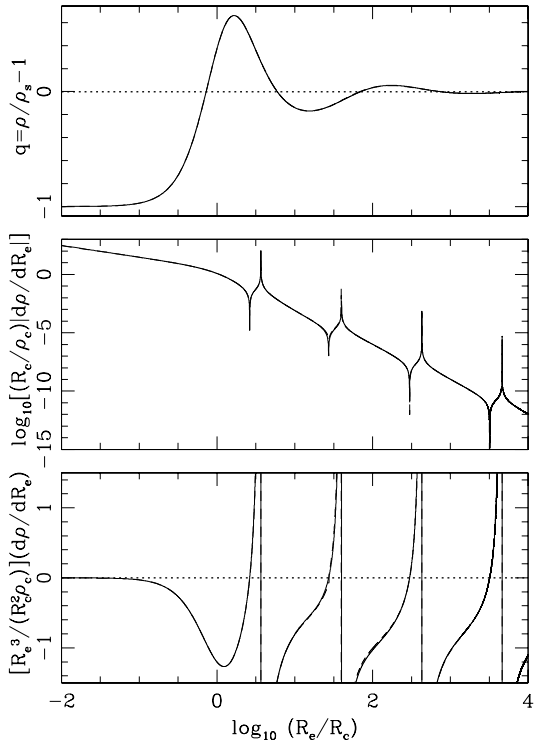

Figure 12.2: Fractional deviation q between the non-singular and the singular solutions (top), and dimensionless forms of $|d\rho/dR_e|$ (centre) and $R_e^3 d\rho/dR_e$ (bottom) as a function of R_e/R_c. The values derived from the approximate analytic solution (shown with solid lines), and the values obtained from the exact (numerical) non-singular solution (shown with dashed lines) are basically indistinguishable.

The maximum possible mass for stability is obtained setting $R_e = R_s = 2.633\, R_c$ in equation (12.34), obtaining

$$M_s = \frac{2c_0^2 R_c}{G} F(2.633) = 1.634 \frac{c_0^2 R_e}{G}\,, \tag{12.44}$$

where for the second equality we have used the fact that $F(2.633) = 2.151$ (see equation 12.30). This equation should be compared with the mass obtained with the semi-qualitative arguments, which resulted in equation (12.4).

Using equation (12.22), we can write M_s in terms of the density ρ_e at the edge

of the sphere:

$$M_s = 2\pi R_e^3 \rho_e \frac{F(2.633)}{f(2.633)} = 9.120\, R_e^3 \rho_e\,. \tag{12.45}$$

In other words, the maximum mass for radial stability of the isothermal sphere is only 2.18 times the mass of a uniform sphere of density ρ_e with the same outer radius.

Part IV

Jets

Chapter 13

Astrophysical and laboratory jets

13.1 General description

Since the beginning of the XX-th century, there has been a substantial amount of literature on experiments of subsonic and supersonic jets. Subsonic jets become fully turbulent within a length scale similar to the jet diameter, as they leave the nozzle that produces them. Supersonic jets have an outer, turbulent boundary layer, and an inner "laminar core". This laminar core is more extended axially for higher Mach number jets.

Within the laminar core and even extending into the fully turbulent region, in laboratory (or in "aeronautical") jets one typically sees a series of "crossing shock cells" or "recollimation shocks" at fixed distances along the jet axis, with the shocks becoming weaker farther away from the outflow source. Early on in the astrophysical literature of jet-like flows there was the notion that the chains of knots that were observed to extend outwards from the sources were something similar to the recollimation shocks in laboratory jets.

Also, in the astrophysical literature there is an extended study of instabilities at the outer wall of the jet beam. These are Kelvin-Helmholtz instabilities which give rise to the formation of shocks that can travel into the jet beam. In laboratory jets, these instabilities give rise to the turbulent boundary layer at

the edge of the jet beam, and at large enough distances from the source produce a fully turbulent jet. In a rather long term, the astrophysical literature has apparently reached a similar conclusion (though we are possibly being unjust with this oversimplification).

The older literature of laboratory jets dealt with "developed jets", which are turned on, and then analysed and photographed once the initial, highly time-dependent transient has ended. In the more recent literature, we see many experiments of the so-called "starting jets", in which the initial states of the jet flow are analyzed. This is particularly easy to do with laser-generated jets, in which the time-delays between the laser which powers the jet and the laser used to "photograph" the flow can be quite precisely adjusted (to microseconds or even nanoseconds).

The discovery that most of the observed emitting knots in astrophysical jets move at highly supersonic velocities away from the source (in extragalactic as well as in stellar jets) implies that the structures of these jets are not the steady, recollimation shocks of laboratory jets. Also, the fact that many times the astrophysical jets are "bipolar" (i.e., have oppositely directed "jets" and "counterjets") and have surprisingly symmetric knot-to-knot correspondences between the jet and the counterjet implies that the knots are produced as a result of a variability of the outflow very close to the position of the source.

Our description of astrophysical jets (Part IV of the present book) we will therefore be biased to describing the effects of a time-variability of the ejection. We will first address the effects of a time-dependence in the (modulus of) the ejection velocity and the density. Then we will discuss the effects of a variable ejection direction, produced by a precession of the outflow axis and/or an orbital motion of the outflow source.

Our discussion will be directed to jets from young stars, in which it is observationally seen that the Mach number of the flow is very high (in the range of $10 \rightarrow 100$). Even though the observational constraints are not as strong, it is thought that while some extragalactic jets have high Mach numbers, others have $M \sim 1$, and are therefore fully turbulent jets. Therefore, caution should be used when applying the theoretical ideas of this part of the book to extragalactic jets.

13.2 Herbig-Haro objects

The best understood astrophysical jets are the ones ejected from young stellar objects or from recently formed stars. There is a wealth of observational data about these so-called Herbig-Haro (HH) objects:

- they show a rich emission-line and continuum spectrum, which has been observed from radio wavelengths to X-rays,
- the HH jets in our Galaxy are many times well resolved in ground based and/or in space based observations,
- their evolutionary timescale is short enough that proper motions and general time evolution of the flows is seen within a human lifetime.

An example of a HH jet is shown in Figures 13.1 and 13.2. Some of these characteristics make them different from extragalactic jets (which are mostly observed only through their continuum emission) or jets from symbiotic stars or jets associated with γ-ray bursts, which are not spatially resolved.

Due to the availability of plasma diagnostics (based on emission line ratios) and observations of spatially resolved, time-evolving structures, the physical parameters and the processes relevant for HH jets are relatively well constrained. Because of this, in presenting jet models this book generally makes comparisons with HH jets, though the models in principle are applicable to other hypersonic astrophysical and laboratory jets.

From the point of view of numerical simulations, HH jets are relatively complex, because they are strongly radiative flows, with post-shock cooling distances that are very small compared to the characteristic sizes (e.g., the jet width) of the flows. Also, the ionisation state of the gas is generally out of equilibrium, so that the photoionisation or the coronal equilibrium relations do not apply, and the non-equilibrium state of the multi-element gas has to be explicitly treated.

From the point of view of analytic models, the situation is not so dire. The strong radiative cooling guarantees that the Mach number remains extremely high throughout the flow, so that the inter-shock regions can be treated with good approximation as free-streaming. For some flows one can use an isothermal approximation, also greatly simplifying the problem.

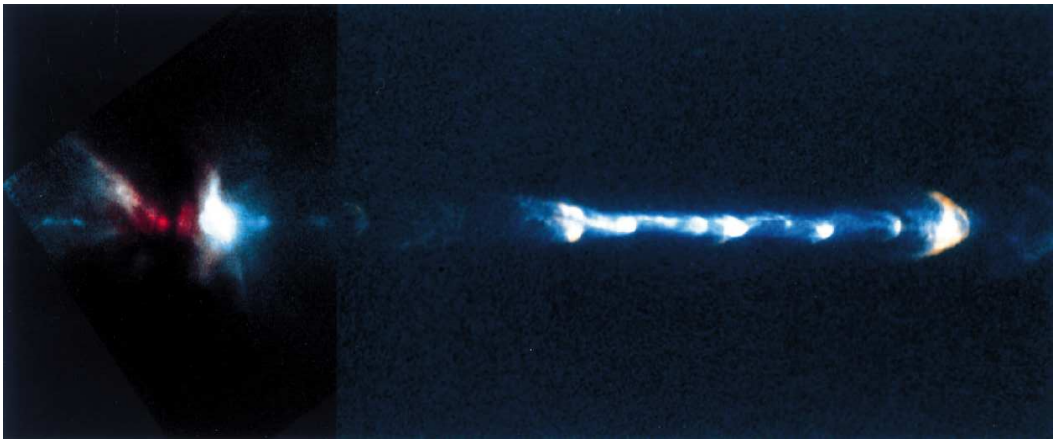

Figure 13.1: Example of a Herbig-Haro jet: the region around the source of the HH 111 outflow observed with the Hubble Space Telescope. The outflow source is located in the left region of the image (source: Bo Reipurth)

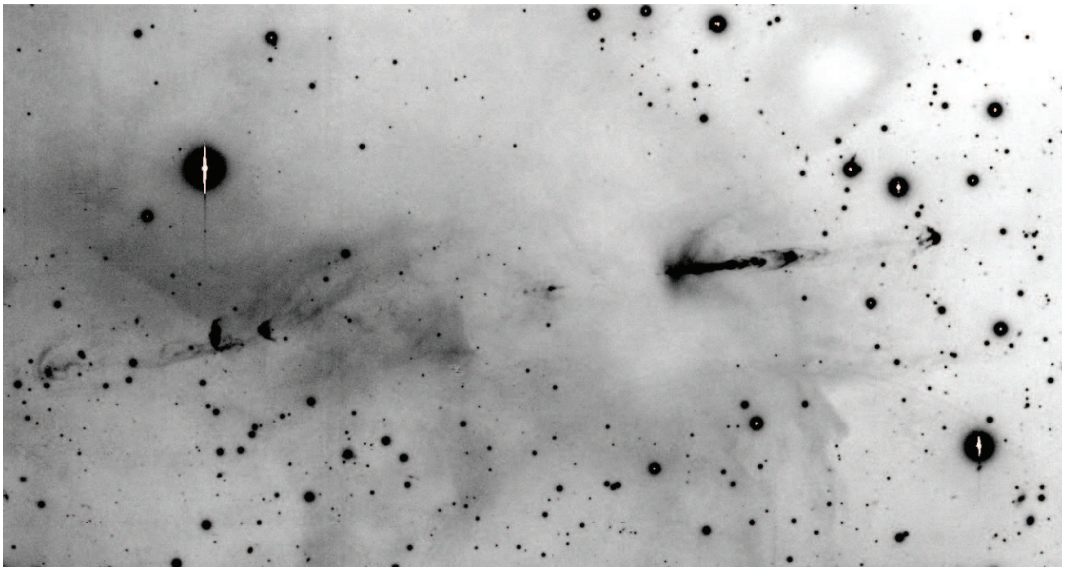

Figure 13.2: A wider view of the HH 111 outflow, observed with the Subaru telescope. The bright jet segment on the right side of the image corresponds to the region shown in Figure 13.1 (source: Bo Reipurth)

In the early 1990's, it was realized that simulations with an arbitrarily imposed ejection velocity variability lead to the formation of chains of two-shock "internal working surfaces" travelling down the jet beam. Many possible choices of parameters for such a variability give simulated jets which strikingly resemble HH jets, with a chain of aligned knots close to the outflow source, and a large "head" (resulting from the "turning on" of the jet flow) at larger distances. Also, a two-mode ejection velocity variability leads to the formation of chains of "short period knots", which catch up each other to form "long period knots".

If one chooses a random time-variability (e.g., a variability with a time-interval between ejection velocity peaks which has a uniform distribution between 0 and a maximum value τ_m), one obtains a series of knots which initially have a maximum ejection time-separation τ_m between successive knots. At larger distances from the source, these knots have mergers that eventually lead to more massive knots with larger separations.

Such has been the success of these "variable ejection models" for modelling HH jets, that they nowadays dominate the literature on the theory of astrophysical jets (which is not a necessarily healthy situation for the field). Because of this, our discussion of the theory of jets is centred on variable ejection flows (chapters 14, 15, 16, 17 and 19).

Chapter 14

Hypersonic, variable velocity jets

14.1 The head of a jet

Let us consider the propagation of the head of a jet into an environment which is stationary with respect to the outflow source (this is called the "starting jet" problem in the non-astrophysical literature). For the case of a hypersonic jet, the head of the jet has a two-shock structure (called a "working surface"), with a "jet shock" (or Mach disk) which slows down the jet material and a "bow shock" which accelerates the environmental gas. This shock structure is schematically shown in Figure 14.1.

If the jet is instantaneously "turned on", the two shocks in the working surface will initially be spatially coincident, and they separate until an approximately steady configuration is formed (in which the material entering the working surface from the jet and from the environment is balanced by a sideways ejection). In this steady configuration, the bow shock and the jet shock travel away from the outflow source with the same velocity v_{ws}.

We can then make a Galilean transformation to a reference system moving away from the source with a velocity v_{ws}, and the working surface flow takes the configuration shown in the bottom frame of Figure 14.1. From this figure, we see that if the two shocks are strong, the post-shock pressure behind the

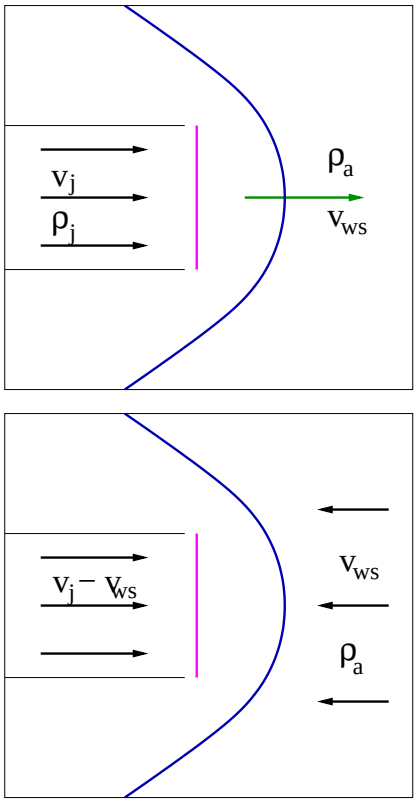

Figure 14.1: Working surface at the head of a jet in a reference frame at rest with respect to the outflow source (top) and in a reference frame moving with the working surface (bottom). The bow shock is in blue and the jet shock (or Mach disk) in purple.

bow shock is

$$P_{bs} = \frac{2}{\gamma + 1} \rho_a v_{ws}^2 \,, \tag{14.1}$$

and the pressure behind the jet shock is

$$P_{js} = \frac{2}{\gamma + 1} \rho_j \left(v_j - v_{ws} \right)^2 \,, \,, \tag{14.2}$$

where we have assumed that a single value γ of the specific heat ratio applies to all the flow.

Now, if the working surface is moving at a constant velocity, the condition

$$P_{bs} = P_{js} \quad \rightarrow \quad \rho_a v_{ws}^2 = \rho_j \left(v_j - v_{ws}\right)^2 \tag{14.3}$$

has to be satisfied (otherwise, the material within the working surface would be accelerating or decelerating). The second equation in (14.3) is the so-called "ram-pressure balance" condition. The ram-pressure balance condition is also valid for a working surface with a variable velocity, but in which the inertia of the material in between the two shocks is negligible

From equation (14.3) we obtain

$$v_{ws} = \frac{\beta v_j}{1+\beta}\,; \quad \text{with } \beta = \sqrt{\frac{\rho_j}{\rho_a}}\,. \tag{14.4}$$

The shock velocity of the bow shock is $v_{bs} = v_{ws}$, and the shock velocity of the jet shock (see Figure 14.1) is

$$v_{js} = v_j - v_{ws} = \frac{v_j}{1+\beta}\,. \tag{14.5}$$

Therefore, for low values of $\beta = \sqrt{\rho_j/\rho_a}$ we have a jet shock with a shock velocity $v_{js} \approx v_j$, and a slow moving working surface (with $v_{ws} \ll v_j$). For high values of β, we have a fast moving working surface with $v_{ws} \approx v_j$. In astrophysical jets, the low β case appears to be applicable for extragalactic jets, and the high β case is appropriate for stellar jets.

For a working surface with radiative shocks, one can take the predictions of the emission from plane-parallel shock models and obtain interpolation formulae of the form:

$$\frac{L_{line}}{\sigma} = C \rho_{pre} v_{shock}^{\alpha}\,, \tag{14.6}$$

where L_{line}/σ is the luminosity in a given line per unit area of the plane shock, ρ_{pre} is the pre-shock density, v_{shock} the shock velocity, and C and α are two constants derived from a fit to the line emission (in a specified shock velocity range). Let us note that the Hα emission can be fitted with $\alpha \approx 3$.

Then, if we assume that the jet and bow shocks have the same surface area σ, the bow shock to jet shock line intensity ratio is:

$$r = \frac{L_{line}^{bs}}{L_{line}^{js}} = \frac{\rho_j v_{js}^{\alpha}}{\rho_a v_{bs}^{\alpha}} = \beta^{\alpha-2}\,, \tag{14.7}$$

where for the second equality we have used equation (14.6) and for the third equality we have also used equations (14.4) and (14.5).

For example, if we take the predictions from the plane-parallel shock models of Hartigan et al. [14], for the Hα emission of shocks with velocities $v_s \sim 100$ km s^{-1}, we find that a reasonable fit is obtained with equation (14.6) for $\alpha \approx 3$. Therefore, we would conclude that the bow to jet shock Hα intensity ratio is $r = \beta = \sqrt{\rho_j/\rho_a}$. Therefore, for the case of a "heavy jet" (i.e., with $\rho_j > \rho_a$) the bow shock emission dominates.

14.2 An internal working surface

Let us assume that we have a working surface formed by the interaction between a slower outflow (of density ρ_1 and velocity u_1) interacting with faster material (of density ρ_2 and velocity u_2) ejected at later times by the same source. The resulting "internal working surface" is shown in Figure 14.2.

Standing in a reference system moving with the working surface (bottom frame of Figure 14.2), we see that the ram-pressure balance condition is:

$$\rho_1 \left(v_{ws} - u_1\right)^2 = \rho_2 \left(u_2 - v_{ws}\right)^2 \,, \tag{14.8}$$

from which we obtain

$$v_{ws} = \frac{\beta u_2 + u_1}{1+\beta} \,; \quad \text{with } \beta = \sqrt{\frac{\rho_2}{\rho_1}} \,. \tag{14.9}$$

Therefore, a low β internal working surface travels with the velocity (u_1) of the earlier ejection, and a high β working surface with the velocity (u_2) of the faster, later ejection.

The shock velocities of the two working surface shocks are:

$$v_1 = v_{ws} - u_1 = \frac{\beta(u_2 - u_1)}{1+\beta} \,, \tag{14.10}$$

$$v_2 = u_1 - v_{ws} = \frac{u_2 - u_1}{1+\beta} \,. \tag{14.11}$$

Therefore, in the case in which the two interacting flows have the same density (i.e., $\beta = 1$), the two shocks have a shock velocity of $v_j/2$.

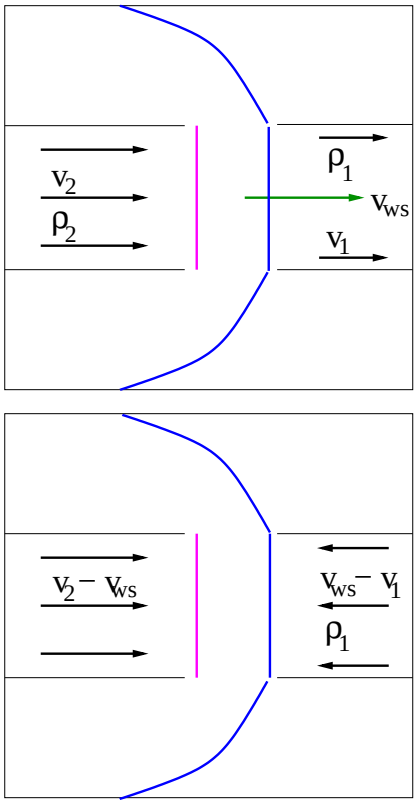

Figure 14.2: Internal working surface formed by the interaction of faster ejecta (of velocity v_2 and density ρ_2) interacting with slower moving material (of velocity u_1 and density ρ_1) ejected earlier. The internal working surface (which moves with a velocity $u_1 < v_{ws} < u_2$) is shown in a reference frame at rest with respect to the outflow source (top) and in a reference frame moving with the working surface (bottom).

14.3 "Catching-up" of fluid parcels

In a hypersonic jet, the pressure gradient force is negligible with respect to the inertia, and therefore (in the absence of other forces, such as an external gravitational force) the fluid parcels have ballistic motions, preserving the velocity with which they were ejected. Let us consider a general ejection velocity variability $u_0(\tau)$, where τ is the time at which the fluid parcels are ejected.

We now consider two fluid parcels, which we number "1" and "2", ejected at (infinitesimally close) times τ and $\tau + \Delta\tau$, respectively. Their velocities therefore are:

$$v_1 = u_0(\tau)\,;$$

$$v_2 = u_0(\tau + \Delta\tau) \approx u_0(\tau) + \Delta\tau\, \dot{u}_0(\tau)\,, \tag{14.12}$$

where $\dot{u}_0(\tau) = du_0/d\tau$. As a function of increasing time t, they then have the trajectories

$$x_1(t) = (t - \tau)\, u_0(\tau)\,;$$

$$x_2(t) = (t - \tau - \Delta\tau)\, u_0(\tau + \Delta\tau) \approx$$

$$(t - \tau)\, u_0(\tau) - \Delta\tau\, u_0(\tau)_(t - \tau)\Delta\tau\, \dot{u}_0(\tau)\,, \tag{14.13}$$

where in the last equality we have kept only the terms up to first order in $\Delta\tau$. From this equation, it is clear that we will have $x_1(t_{col}) = x_2(t_{col})$ at a time

$$t_{col} = \frac{u_0(\tau)}{\dot{u}_0(\tau)} + \tau\,. \tag{14.14}$$

In other words, for $\dot{u}_0(\tau) > 0$, at the time t_{col} (given by equation 14.14), the faster fluid parcel ejected at $\tau + \Delta\tau$ catches up with the slower parcel ejected immediately before (at time τ), leading to the formation of a two-shock working surface. For $\dot{u}_0(\tau) \leq 0$, this catching up does not take place.

The two parcels catch up with each other at a distance

$$x_{col} = (t_{col} - \tau)\, u_0(\tau) = \frac{u_0^2(\tau)}{\dot{u}_0(\tau)} \tag{14.15}$$

from the source.

This catching-up of fluid parcels to form a working surface of course only takes place if the parcels do not collide before with a previously existing working surface. This possibility is explored in the following sections.

14.4 Free-streaming flow and the formation of working surfaces

14.4.1 General considerations

Let us consider the equation for a 1D flow in the form of Newton's second law:

$$\frac{\partial u}{\partial t} + u\frac{\partial u}{\partial x} + \frac{1}{\rho}\frac{\partial P}{\partial x} = 0\,, \tag{14.16}$$

where u is the x-velocity, ρ the density and P the pressure. It is clear that if the variations of u and P have similar characteristic spatial scales, the ratio between the second and third terms of this equation scales as $\sim \gamma M^2$, where γ is the specific heat ratio and $M^2 = \rho u^2/(\gamma P)$ is the Mach number of the flow. Therefore, in the continuous segments of a hypersonic jet (with $M \gg 1$), the second term of equation (14.16) dominates over the third term, and therefore the equation of motion reduces to

$$\frac{\partial u}{\partial t} + u\frac{\partial u}{\partial x} = 0\,. \tag{14.17}$$

This is Riemann's equation (also known as the "inviscid Burgers's equation", which actually corresponds to the limit of viscosity going to zero of an equivalent equation with a "volume viscosity" term). Riemann's equation has the free-streaming solution:

$$u(x,t) = \frac{x}{t-\tau} = u_0(\tau)\,, \tag{14.18}$$

where $u_0(\tau)$ is the ejection velocity at the time τ at which the parcel at (x,t) was ejected. One can show that this is indeed a solution by inserting it in equation (14.17).

It is a straightforward exercise to consider the 1D Lagrangean continuity equation for a jet of slowly varying cross section $\sigma(x)$, in the form:

$$\frac{d}{dt}\ln\sigma\rho + \frac{\partial u}{\partial x} = 0, \tag{14.19}$$

and to combine it with equation (14.18) to obtain the time and position-dependent density. From (14.18), $x = (t-\tau)\,u_0(\tau)$, so that at constant t we have:

$$dx = -\left[u_0 + (t-\tau)\dot{u}_0\right] d\tau\,, \tag{14.20}$$

where $\dot{u}_0 = du_0/d\tau$. This can be inserted into (14.19) to obtain:

$$\frac{d}{dt} \ln \sigma\rho = \frac{\dot{u}_0}{u_0 - (t-\tau)u_0} \,. \tag{14.21}$$

This equation has the integral:

$$\sigma\rho = \frac{\sigma_0 \rho_0 u_0}{u_0 - (t-\tau)\dot{u}_0} \,, \tag{14.22}$$

where σ_0 and $\rho_0(\tau)$ are the injection cross section and density, respectively.

Clearly, if u_0 is a growing function of τ, the fluid parcels ejected at later times will eventually catch up with slower parcels ejected earlier. The catching up of two parcels occurs at the points in which the travelling wave resulting from the $u_0(\tau)$ ejection steepens to a vertical: i.e., attains values $\partial u/\partial x \to -\infty$.

From equation (14.18) one can easily calculate:

$$\frac{\partial u}{\partial x} = \frac{\dot{u}_0(\tau)}{(t-\tau)\dot{u}_0(\tau) - u_0(\tau)} \,, \tag{14.23}$$

where $\dot{u}_0 = du_0/d\tau$. As the ejection velocity is positive ($u_0 > 0$), it is clear that $\partial u/\partial x$ can diverge only if $\dot{u}_0 > 0$. Therefore, two parcels ejected infinitesimally close to time τ will catch up with each other at the time t_{col} that annuls the denominator of equation (14.23),

$$t_{col} = \frac{u_0}{\dot{u}_0} + \tau \,. \tag{14.24}$$

However, this catching up will not necessarily occur because the flow parcels ejected at time τ might enter an already developed working surface before their catching-up time.

The first working surface along the jet will be formed by the fluid parcels ejected at a time τ_c, which corresponds to the minimum value of t_{col}. In other words, τ_c is the root of the equation

$$\frac{dt_{col}}{d\tau} = \frac{d}{d\tau}\left(\frac{u_0}{\dot{u}_0}\right) + 1 = 0 \,. \tag{14.25}$$

Through simple manipulations, this equation can be written as

$$u_0(\tau_c)\, \ddot{u}_0(\tau_c) = 2\, \dot{u}_0^2(\tau_c) \,, \tag{14.26}$$

where $\ddot{u}_0 = d^2u_0/d\tau^2$.

For a given functional form of the ejection velocity $u_0(\tau)$ we can find the ejection time (or times) τ_c which lead to the formation of a working surface. Once we have obtained these values, we can then calculate (from equation 14.24) the time t_c:

$$t_c = \frac{u_0(\tau_c)}{\dot{u}_0(\tau_c)} + \tau_c \tag{14.27}$$

at which it is formed, and (from equation 14.18) its initial distance

$$x_c = (t_c - \tau_c)\, u_0(\tau_c)\,. \tag{14.28}$$

An alternative criterion for determining the time and position at which working surfaces are formed is to calculate the catching-up distance between parcels:

$$x_{col} = \frac{u_0^2(\tau)}{\dot{u}_0(\tau)}\,, \tag{14.29}$$

and then compute the values of τ_c from the minima of $x_{col}(\tau)$. The condition of minimal x_{col} can be straightforwardly shown to be equivalent to equation (14.26).

14.4.2 The case of a sinusoidal ejection variability

Let us consider an ejection velocity of the form

$$u_0(\tau) = v_0 + v_a \sin(\omega\tau)\,, \tag{14.30}$$

with constant v_0, v_a and ω.

Inserting equation (14.30) into (14.26), one obtains:

$$\sin^2\omega\tau_c - \frac{v_0}{v_a}\sin\omega\tau - 2 = 0\,, \tag{14.31}$$

which has the solution

$$\sin\omega\tau_c = \frac{1}{2}\left(1 - \sqrt{1 + 8\frac{v_a^2}{v_0^2}}\right) \approx -2\frac{v_a}{v_0}\,, \tag{14.32}$$

where the second equality is valid for the $v_a/v_0 \ll 1$ limit. The root with a positive sign for the discriminant (see equation 14.32) gives an unphysical solution with $\sin\omega\tau_c > 1$.

Now, with the value obtained for τ_c (from equation 14.32), we can calculate the time t_c (from equation 14.27) and the position x_c (equation 14.28) at which the successive working surfaces are formed. In the $v_a/v_0 \ll 1$ limit, we obtain:

$$t_c - \tau_c = \frac{v_0}{\omega v_a}\,, \quad x_c = \frac{v_0^2}{\omega v_a}\,. \tag{14.33}$$

14.4.3 Ejection variability with two sinusoidal modes

We now consider an ejection time-variability of the form

$$u_0(\tau) = v_0 + v_1\sin(\omega_1\tau + \phi_1) + v_2\sin(\omega_2\tau)\,, \tag{14.34}$$

with constant v_0, v_1, v_2, ω_1, ω_2 and ϕ_1. The mean velocity and the velocity amplitudes have to satisfy the $v_0 \geq v_1 + v_2$ condition so that unphysical, negative outflow velocities do not occur.

Inserting equation (14.34) into (14.26), one straightforwardly obtains:

$$\begin{aligned} v_1\omega_1^2\big[v_0\sin(\omega_1\tau+\phi_1) + v_1\sin^2(\omega_1\tau+\phi_1) + \\ 2v_1\cos^2(\omega_1\tau+\phi_1)\big] + \\ v_2\omega_2^2\big[v_0\sin(\omega_2\tau) + v_2\sin^2(\omega_2\tau) + \\ 2v_2\cos^2(\omega_2\tau)\big] = \\ -v_1v_2\big[(\omega_1^2+\omega_2^2)\sin(\omega_1\tau+\phi_1)\sin(\omega_2\tau) \\ +4\omega_1\omega_2\cos(\omega_1\tau+\phi_1)\cos(\omega_2\tau)\big]\,. \end{aligned} \tag{14.35}$$

This equation can in principle be solved numerically in order to obtain the values τ_c of the ejection times which lead to the formation of working surfaces.

In order to proceed analytically, we consider the case in which ω_1 and ω_2 correspond to a "slow" and a "fast mode", which satisfy the conditions:

$$\omega_2 \gg \omega_1\,;\;\; v_2\omega_2^2 \gg v_1\omega_1^2\,. \tag{14.36}$$

Under this assumption, equation (14.35) takes the simpler form:

$$\left(1+\frac{v_1}{v_0}\sin\phi\right)\sin\omega_2\tau+\frac{v_2}{v_0}\left(2-\sin^2\omega_2\tau\right)=0\,. \tag{14.37}$$

In this equation, $\phi=\omega_1\tau_c+\phi_1$.

Equation (14.37) has the solution

$$\sin\omega_2\tau_c=\frac{v_0+v_1\sin\phi}{2v_2}\left[1-\sqrt{1+\frac{8v_2^2}{(v_0+v_1\sin\phi)^2}}\right]\,. \tag{14.38}$$

The τ_c corresponding to the solution with lowest modulus of the arcsine can then be inserted in equations (14.34), (14.27) and (14.28) to obtain the time and position of the working surface.

It is possible to derive simpler expressions in the case for which the "fast" mode has a small amplitude, i.e.

$$v_2\ll v_0,\,v_1\,. \tag{14.39}$$

Clearly, the chosen values of v_2 cannot be too small, because if not condition (14.36), on which our solution is based, will not be satisfied. In this limit of small v_2, equation (14.38) simplifies to

$$\sin\omega_2\tau_c=-\frac{2v_2}{v_0+v_1\sin\phi}\,, \tag{14.40}$$

which can be used together with equations (14.34) and (14.28) to obtain:

$$x_c=\frac{(v_0+v_1\sin\phi)^2}{\omega_1 v_1\cos\phi+\omega_2 v_2}\,, \tag{14.41}$$

valid in the $v_2\ll v_1$ limit.

It is clear that for

$$\omega_1 v_1>\omega_2 v_2\,, \tag{14.42}$$

equation (14.41) does not give positive values of x_c for all possible values of the phase ϕ of the "slow" mode. The negative values of x_c correspond to a suppression of the working surfaces of the (ω_2,v_2) mode due to the presence

of the slow, (ω_1, v_1) mode. When condition (14.42) is met, the suppression of the "fast" (ω_2, v_2) mode occurs for phases ϕ such that $\phi_a < \phi < \phi_b$, where

$$\phi_a = \cos^{-1}\left(-\frac{\omega_2 v_2}{\omega_1 v_1}\right) \; ; \quad \phi_b = 2\pi - \phi_a \, , \tag{14.43}$$

where ϕ_a corresponds to the first positive value of the arccosine.

Figure 14.3 shows examples for a two-sine variability (see equation 14.34) with $v_0 = 1$, $\omega_1 = 0.1$, $\omega_2 = 1$ and $\phi_1 = 0$, and three choices for the amplitudes of the two modes: $(v_1, v_2) = (0.4, 0.4)$, (0.6,0.2) and (0.8,0.05). The three choices of parameters satisfy the conditions of equation (14.36), and the two latter choices satisfy condition (14.39), at least in a marginal way. Also, the last choice of parameters satisfies condition (14.42), so that it develops a gap in the formation of "fast mode" working surfaces.

Figure 14.3 shows the three chosen time variabilities (left column) and the resulting working surface formation. The right column shows the value of the catching-up distance (equation 14.29), which has minima at the $\tau = \tau_c$ values. In these graphs, we also show the results obtained for x_c from equations (14.38) and (14.29) (dotted line) and from equation (14.41) (dashed line), calculated by setting the phase to $\phi = \omega_1 \tau$.

We see that for all parameters the catching-up distance (see equation 14.29 and Figure 14.3) has positive and negative (unphysical) branches. The minima of the positive branches coincides with the values of x_c derived from equations (14.38) and (14.28) for all of the chosen parameters. The simpler solution of equation (14.41) does not work well for the $(v_1, v_2) = (0.4, 0.4)$ (top frames), but is basically indistinguishable from the more accurate solution (obtained from equations 14.38 and 14.29) in the other two cases (which do satisfy condition 14.39).

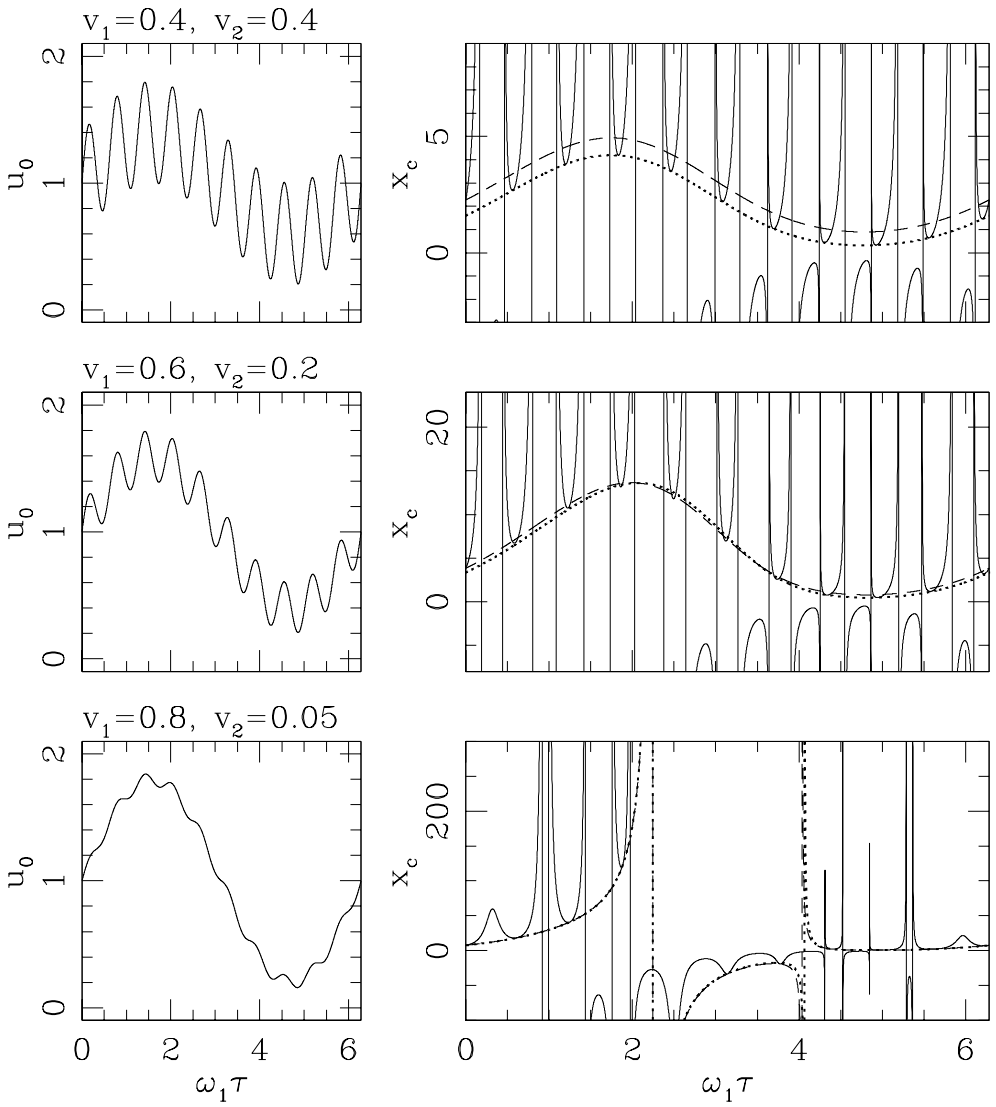

Figure 14.3: Three forms of the ejection variability (see equation 14.34), all sharing the parameters $v_0 = 1$, $\omega_1 = 0.1$, $\omega_2 = 1$ and $\phi_1 = 0$, and with $(v_1, v_2) = (0.4, 0.4)$ (top), (0.6,0.2) (centre) and (0.8,0.05) bottom) are shown in the left column. The right column shows the catching up distances x_{col} as a function of time (equation 14.29) resulting from these three variabilities (solid lines) and the distances of working surface formation x_c calculated from equations (14.38,14.29) (dashed lines) and from equation (14.41) (dotted lines). It is clear that the minima of x_{col} are well reproduced (except in the model displayed on the top row for the case of the results of equation 14.41) by the analytically obtained values of x_c.

Chapter 15

The centre of mass equation of motion

15.1 General considerations

If we want to solve for the motion of an internal working surface, we have to consider the free-streaming solution (equations 14.18 and 14.22) and an equation of motion for the working surface itself. A possibility is to use the ram-pressure balance condition (equation 14.4), which is appropriate for a variable velocity working surface provided that the working surface efficiently ejects matter sideways, so that the inertia of the material within it is negligible.

It is also possible to consider the opposite limit, in which most of the shocked material remains within the working surface. This case is clearly the appropriate one for a spherically symmetric flow, and also for a jet working surface in an appropriate regime. The position of a mass conserving working surface is equal to the position of the centre of mass of all of the fluid parcels which have piled up at the working surface:

$$x_{cm} = \frac{\int x\, dm}{\int dm}\,, \tag{15.1}$$

where for a variable outflow $dm = \sigma_0 \rho_0 u_0 d\tau$, with σ_0 the ejection cross section, and $\rho_0(\tau)$ and $u_0(\tau)$ the variable ejection density and velocity, and

$$x = (t - \tau)\, u_0(\tau) \tag{15.2}$$

is the position x along the jet that the fluid parcels (ejected at time τ) would have had (at time t) if they had not merged with the working surface. For such a variable ejection, the integration limits are τ_1 and τ_2, the ejection times for the fluid parcels that are now entering the working surface from the downstream and upstream directions (respectively). These can be obtained by finding appropriate roots of the free-streaming flow equation:

$$x_{cm} = (t - \tau)\, u_0(\tau)\,. \tag{15.3}$$

For a working surface moving into a stationary environment, the environmental contribution to the integrals in equation (15.1) are obtained setting $dm = \sigma(x)\rho_a(x)dx$ and using appropriate spatial limits. Here, $\sigma(x)$ is the cross section of the jet, and $\rho_a(x)$ is the (in principle, position-dependent) environmental density.

This "centre of mass formalism" has the practical advantage that it gives the time-dependent position of the working surfaces (see equation 15.1) as a function of time (or position) integrals of combinations of τ, $u_0(\tau)$ and $\rho_0(\tau)$ (or possibly also $\rho_a(x)$, see above). If the functions within the integrals are integrable analytically, one then obtains a system of algebraic equations that give the time-dependent position of the working surface. These functions are quite complicated, and many times x_{cm} has to be obtained through a numerical inversion of the system of equations (composed of equations 15.1 and 15.3).

This has to be compared with the "ram-pressure balance" formalism (see equation 14.4) which gives an expression for $dx_{ws}/dt = v_{ws}$, which has then to be integrated to obtain the solution. Only in very particular cases can this equation be integrated analytically, and the solutions are generally computed numerically.

15.2 Asymptotic regime of large distances from the outflow source

Let us now consider an arbitrary, periodic variation $u_0(\tau)$, $\rho_0(\tau)$ of the ejection velocity and density. This periodic ejection variability produces a chain of

internal working surfaces, and we consider the time-dependent position

$$x_{cm} = \frac{\int_{\tau_1}^{\tau_2} x(\tau)\rho_0(\tau)u_0(\tau)d\tau}{\int_{\tau_1}^{\tau_2} \rho_0(\tau)u_0(\tau)d\tau}\,, \tag{15.4}$$

of the centre of mass of the material within one of the working surfaces, where τ_1 and τ_2 are two successive roots of equation (15.3):

$$x_{cm} = (t - \tau_{1,2})\, u_0(\tau_{1,2})\,, \tag{15.5}$$

and $x(\tau)$ (in equation 15.4) is given by equation (15.2).

For large distances from the source, most of the ejected material has already entered the working surfaces, so that the ejection time-interval of the material entering the working surface from the upstream and downstream directions becomes $\tau_2 - \tau_1 \approx \tau_p$, where τ_p is the period of the ejection variability. In this regime, the $\tau_1 \to \tau_2$ interval of the integrals can therefore be replaced by the $-\tau_p/2 \to \tau_p/2$ interval. Equation (15.4) then becomes:

$$x_{cm} = (t - \tau_a)v_a\,, \tag{15.6}$$

where

$$v_a = \frac{\int_{-\tau_p/2}^{\tau_p/2} \rho_0(\tau)u_0^2(\tau)d\tau}{\int_{-\tau_p/2}^{\tau_p/2} \rho_0(\tau)u_0(\tau)d\tau}\,, \tag{15.7}$$

is the (constant) asymptotic velocity of the working surface and

$$\tau_a = \frac{\int_{-\tau_p/2}^{\tau_p/2} \tau\rho_0(\tau)u_0^2(\tau)d\tau}{v_a \int_{-\tau_p/2}^{\tau_p/2} \rho_0(\tau)u_0(\tau)d\tau}\,, \tag{15.8}$$

is an average ejection time of the material that is within a given internal working surface. Clearly, by choosing to carry out the integrals over the $-\tau_p/2 \to \tau_p/2$ range, we are choosing the internal working surface formed by the material ejected in this ejection time interval.

Therefore, regardless of the form of the periodic ejection velocity and density variability, at large distances from the source the working surfaces travel at a constant velocity, which is given by equation (15.7). It is also possible to obtain the shock velocities of the working surface shocks in the following way.

At large distances from the source, the material in the continuous segments of the jet corresponds to a small range of ejection times around τ_n, where the index n numbers the successive continuous segments. The ejection time τ_n is determined by the condition $u_0(\tau_n) = v_a$ (where v_a is given by equation 15.7). Clearly,

$$\tau_{n+1} = \tau_n + \tau_p \,, \tag{15.9}$$

and the free-streaming flow on the two sides of the working surface have linear velocity vs. position relationships, giving velocities

$$u_1 = \frac{x_{cm}}{t - \tau_n} \,, \quad u_2 = \frac{x_{cm}}{t - \tau_{n+1}} \,, \tag{15.10}$$

immediately down- and up-stream of the working surface.

Using equation (15.9), we have

$$t - \tau_{n+1} = (t - \tau_n)\,(1 - \epsilon) \;, \;\; \text{with } \epsilon = \frac{\tau_p}{t - \tau_n} \,, \tag{15.11}$$

with $\epsilon \ll 1$ in the asymptotic regime.

We can then use equations (15.6), (15.10) and (15.11) to calculate the velocity jump accross the working surface:

$$\Delta v = u_2 - u_1 = \frac{v_a^2 \tau_p}{x_{cm}} \,, \tag{15.12}$$

where we have carried out a first order expansion in ϵ (see equation 15.11).

Also, the free-streaming flow density integral (14.22), when evaluated in τ_n gives:

$$\rho_{1,2} \approx \frac{\rho_0(\tau_n)\sigma_0}{\sigma(x_{cm})\left[1 - (t - \tau_n)\frac{d\ln u_0}{d\tau}(\tau_n)\right]} \,, \tag{15.13}$$

where we can calculate both upstream and downstream densities using τ_n given that in the asymptotic regime we have $\epsilon \ll 1$ (see equation 15.11). In this equation, σ_0 is the ejection cross section and $\sigma(x_{cm})$ the cross section at the position of the working surface. Equation (15.13) can be further simplified by noting that

$$-(t - \tau_n)\frac{d\ln u_0}{d\tau}(\tau_n) \sim \frac{t - \tau_n}{\tau_p} = \epsilon^{-1} \,, \tag{15.14}$$

and therefore, in the asymptotic, $\epsilon \ll 1$ regime the first term in the denominator of equation (15.13) can be neglected. In this way, we obtain

$$\rho_{1,2} \approx -\frac{\rho_0(\tau_n)\sigma_0 u_0(\tau_n)}{\sigma(x_{cm})\dot{u}_0(\tau_n)(t-\tau_n)}\,, \tag{15.15}$$

with equal densities on both sides of the internal working surface. The fact that the densities on both sides of the working surface asymptotically approach each other, and that the velocity of the working surface becomes constant implies that the shock velocities of the two working surface shocks also have the same value. Therefore, the velocity jump Δu across the working surface (see equation 15.12) is divided into two shocks of velocities $\Delta u/2$. In this way, we see that as the working surface travels away from the outflow source at the asymptotic velocity v_a, the shocks have velocities that decrease as $1/x_{cm}$ (see equation 15.12).

Combining equations (15.7) and (15.15) we obtain:

$$\rho_{1,2} = -\frac{\rho_0(\tau_n)\sigma_0}{\sigma(x_{cm})}\frac{1}{\frac{d\ln u_0}{d\tau}(\tau_n)}\frac{1}{x_{cm}}\,. \tag{15.16}$$

For a cylindrical jet, σ_0 and $\sigma(x_{cm})$ have the same value and cancel out. $\rho_0(\tau_n)$ and $d\ln u_0/d\tau(\tau_n)$ are calculated at the time at which the material of the asymptotic continuous jet beam segments were ejected, which is given by the condition $u_0(\tau_n) = v_a$ (see above). For a given variability they are constants, and the densities on both sides of the internal working surface have a dependency

$$\rho_{1,2} \propto \frac{1}{x_{cm}}\,. \tag{15.17}$$

Finally, if we consider the fit to the emission of plane shock models given in equation (14.6), using equations (15.12) and (15.17) we obtain the result that the intensity of an emission line emitted by a working surface scales as:

$$L_{line} \propto x_{cm}^{-(\alpha+1)}\,, \tag{15.18}$$

which for Hα ($\alpha \approx 3$) gives a steep decline of the emission as distance to the source to a power -4. This decrease is satisfied by a single working surface which as a function of time travels away from the source, and also by successive working surfaces formed by a periodic ejection variability. Both effects (the

decrease in intensity of a single, evolving working surface, and the intensity decrease between successive working surfaces along a jet) are observed in some Herbig-Haro jets.

Chapter 16

The uniformly accelerating jet in a homogeneous environment

16.1 Defining the problem

In this chapter, we present an example of a simple ejection velocity and density variability, and how to obtain solutions with the ram-pressure balance and centre of mass formalisms for the head of the jet.

We consider a jet with an ejection velocity of the form

$$u_0(\tau) = 0 \,\text{for}\, \tau < 0 \quad u_0(\tau) = a\tau \,\text{for}\, \tau \geq 0\,, \tag{16.1}$$

with constant "acceleration" a. We will assume that the jet is cylindrical (i.e., with a position-independent cross section σ_0) and that it moves into a uniform environment of density ρ_a.

It is easy to show that a working surface is formed at $t = 0$ at a position $x = 0$. In order to follow the time evolution of this "jet head", we will use both the "center of mass" and the "ram pressure balance" formalisms. In order to do this, we also have to specify the time dependence of the ejection density $\rho_0(\tau)$. Let us analyze two possibilities:

1. a constant mass loss rate $\dot{m} = \rho_0(\tau)u_0(\tau)$, so that the ejection density is given by $\rho_0(\tau) = \dot{m}/u_0(\tau)$ (where $\dot{m}$ is the mass loss rate at the jet source per unit area of the jet beam),

2. a time-independent ejection density ρ_0.

16.2 Centre of mass equation of motion

16.2.1 The equation for the position of the jet head

From equation (15.1) we have:

$$x_{cm}\left[\int_0^{\tau}\rho_0 u_0 d\tau' + \int_0^{x_{cm}}\rho_a dx\right] = \int_0^{\tau} x_j \rho_0 u_0 d\tau' + \int_0^{x_{cm}} x\rho_a dx\,, \qquad (16.2)$$

where ρ_a is the (position-independent) environment density, ρ_0 and u_0 are the time-dependent ejection density and velocity. x_j is given as a function of the ejection time τ' and the present time t by:

$$x_j = (t-\tau')u_0(\tau') = (t-\tau')a\tau'\,, \qquad (16.3)$$

and τ (the ejection time of the material which is now entering the jet head) is the root of equation

$$x_{cm} = (t-\tau)u_0(\tau) = (t-\tau)a\tau\,. \qquad (16.4)$$

The second equalities in equations (16.3-16.4) correspond to our choice of ejection velocity (equation 16.1). From equation (16.4), we can find τ as a function of t and x_{cm}:

$$\tau = \frac{1}{2}\left(1+\sqrt{t^2-4x_{cm}/a}\right)\,. \qquad (16.5)$$

Combining equations (16.2-16.4) we have:

$$x_{cm}\left[\int_0^{\tau}\rho_0 a\tau' d\tau' + \rho_a x_{cm}\right] = \int_0^{\tau}(t-\tau')a\tau'\rho_0 a\tau' d\tau' + \frac{\rho_a x_{cm}^2}{2}\,. \qquad (16.6)$$

In order to proceed, we have to specify our choice for the ejection density $\rho_0(\tau')$.

16.2.2 The case of constant $\dot{m}$

Setting $\rho_0(\tau') = \dot{m}/u_0(\tau') = \dot{m}/(a\tau')$, equation 16.6 becomes:

$$x_{cm}\left(\dot{m}\tau + \rho_a x_{cm}\right) = \dot{m}a\tau^2\left(\frac{t}{2} - \frac{\tau}{3}\right) + \frac{\rho_a x_{cm}^2}{2}\,. \tag{16.7}$$

From equation (16.4), we find the relation

$$t = \frac{x_{cm}}{a\tau} + \tau\,, \tag{16.8}$$

which we substitute in (16.7) to finally obtain:

$$\frac{\rho_a}{\dot{m}}\tau x_{cm}^2 + x_{cm} - \frac{a\tau^3}{3} = 0\,, \tag{16.9}$$

with positive solution

$$x_{cm}(\tau) = \frac{\dot{m}\tau}{2\rho_a}\left[-1 + \sqrt{1 + \frac{4a\rho_a\tau}{2\dot{m}}}\right]\,. \tag{16.10}$$

We can then generate the full solution to the problem of a uniformly accelerating jet in a parametric form by generating $x_{cm}(\tau)$ (equation 16.10) and $t(x_{cm}, \tau)$ (equation 16.8) in order to plot x_{cm} as a function of evolutionary time t.

Let us note that in the $\rho_a \to 0$ limit, the solution to the problem takes the simpler form:

$$x_{cm} = \frac{a}{3}\tau^2\,. \tag{16.11}$$

We can also obtain x_{cm} as an explicit function of t by combining equations (16.5) and (16.7), giving:

$$x_{cm} = \frac{8}{9}x_c\left[\left(1 + \frac{3}{4}\frac{t}{t_c}\right)^{3/2} - \left(1 + \frac{9}{8}\frac{t}{t_c}\right)\right]\,, \tag{16.12}$$

with

$$t_c \equiv \frac{\dot{m}}{a\rho_a}\,,\ \text{ and } x_c \equiv \frac{\dot{m}^2}{a\rho_a^2} = \frac{\dot{m}}{\rho_a}t_c\,. \tag{16.13}$$

In the $t \ll t_c$ limit, this equation becomes:

$$x_{cm} \approx \frac{3}{16}at^2\,, \tag{16.14}$$

16.2.3 The case of constant ρ_0

Setting $\rho_0 = const.$ in equation (16.6) and following the steps of the previous subsection, we obtain the quadratic equation:

$$\frac{3\rho_a}{\rho_0 a\tau^2} x_{cm}^2 + x_{cm} - \frac{a\tau^2}{2} = 0\,, \tag{16.15}$$

with positive solution

$$x_{cm} = \frac{\rho_a a\tau^2}{6\rho_a}\left[-1 + \sqrt{1 + \frac{6\rho_a}{\rho_0}}\right]\,. \tag{16.16}$$

In order to plot x_{cm} as a function of evolutionary time t, one has to generate $t(\tau)$ using equation (16.8).

In the $\rho_a \to 0$ limit, equation (16.16) takes the form

$$x_{cm} = \frac{a}{2}\tau^2\,. \tag{16.17}$$

We also obtain x_{cm} explicitly as a function of evolutionary time t combining equations (16.5) and (16.15), giving:

$$x_{cm} = \frac{a}{9}\beta_0\left[\frac{\beta_0(\beta_0^2 - 18) + (\beta_0^2 + 6)^{3/2}}{(\beta_0^2 - 2)^2}\right] t^2\,, \tag{16.18}$$

where $\beta_0 = \sqrt{\rho_0/\rho_a}$. Therefore, the jet head travels with a constant acceleration (which is twice the factor multiplying t^2 on the right hand side of equation 16.18).

16.3 Ram-pressure balance equation of motion

16.3.1 The equation for the position of the jet head

From equation (14.4) we have:

$$\left(1 + \sqrt{\frac{\rho_a}{\rho}}\right)\frac{dx_{ws}}{dt} = u_0(\tau)\,, \tag{16.19}$$

where we have set $v_{ws} = dx_{ws}/d\tau$, $u_0(\tau)$ is the ejection velocity, ρ_a is the ambient density and ρ is the density of the jet beam just upstream of the working surface. The ejection time τ of the material entering the working surface is obtained from the free-streaming relation:

$$x_{ws} = (t - \tau)u_0(\tau)\,. \tag{16.20}$$

Now, from equation (16.20) we have

$$t = \tau + \frac{x_{ws}}{u_0(\tau)}. \tag{16.21}$$

and differentiating both sides we obtain

$$dt = \left(1 + \frac{1}{u_0}\frac{dx_{ws}}{d\tau} - \frac{x_w}{u_0^2}\frac{du_0}{d\tau}\right)d\tau\,. \tag{16.22}$$

Using this relation, we now convert equation (16.19) into the differential equation

$$\frac{dx_{ws}}{d\tau}\sqrt{\frac{\rho_a}{\rho}} = u_0 - x_{ws}\frac{d\ln u_0}{d\tau}\,, \tag{16.23}$$

where ρ is given by the free-streaming flow density solution (equation 14.22).

For our chosen form $u_0(\tau) = a\tau$ for the ejection velocity, we use equations (16.1) and (14.22) to obtain the equation of motion:

$$\frac{dx_{ws}}{d\tau} = \sqrt{\frac{\rho_0(\tau)}{\rho_a}}a\tau\sqrt{1 - \frac{x_{ws}}{a\tau^2}}\,. \tag{16.24}$$

In order to proceed, we have to specify our choice for the ejection density $\rho_0(\tau)$.

16.3.2 The case of constant $\dot{m}$

Setting $\rho_0(\tau) = \dot{m}/u_0(\tau) = \dot{m}/(a\tau)$, equation (16.24) becomes:

$$\frac{dx_{ws}}{d\tau} = \sqrt{\frac{\dot{m}}{\rho_a}}\sqrt{a\tau - x_{ws}/\tau}\,. \tag{16.25}$$

This equation has two regimes with analytical integrals. It is clear that in the $\rho_a \to 0$ or the $\tau \to 0$ limits, equation (16.25) has the "near" solution

$$x_{ws}^{(n)} = a\tau^2 \,. \tag{16.26}$$

The large τ, the "far" solution:

$$x_{ws}^{(f)} = \frac{2}{3}\sqrt{\frac{a\dot{m}}{\rho_a}}\tau^{3/2} \,, \tag{16.27}$$

is obtained by assuming a working surface with substantial slowing down, so that $x_{ws} \ll a\tau^2$.

It is also possible to obtain a "small ρ_a" series solution in the following way. We write equation (16.25) in the form:

$$x_{ws} = \tau\left[a\tau - \frac{\rho_a}{\dot{m}}\left(\frac{dx_{ws}}{d\tau}\right)^2\right] \,, \tag{16.28}$$

and use it to generate an iteration chain of approximations to x_{ws}. As a first approximation, we use $x_{ws}^{(0)} = x_{ws}^{(n)} = a\tau^2$, and insert it in the right-hand side of equation (16.28) to obtain:

$$x_{ws}^{(1)} = a\tau^2\left(1 - \frac{4\rho_a a\tau}{\dot{m}}\right) \,. \tag{16.29}$$

We can now differentiate $x_{ws}^{(1)}$ with respect to τ, and insert the result in the right-hand-side of equation (16.28) to obtain the next iteration:

$$x_{ws}^{(2)} = a\tau^2\left[1 - 4\frac{\rho_a a\tau}{\dot{m}}\left(1 - 6\frac{\rho_a a\tau}{\dot{m}}\right)^2\right] \,. \tag{16.30}$$

It is straigthforward to show numerically that this series of successive approximations diverges from the full solution of equation (16.25) when τ approaches $\dot{m}/(\rho_a a)$.

In order to proceed, we first write an adimensional version of equation (16.25), and then integrate it numerically. In terms of the dimensionless variables

$$\eta = \frac{a\rho_a^2}{\dot{m}^2}x_{ws} \,; \quad y = \frac{a\rho_a}{\dot{m}}\tau \,, \tag{16.31}$$

equation (16.25) takes the form:

$$\frac{d\eta}{dy} = \sqrt{y - \eta/y}\,, \tag{16.32}$$

and by integrating it numerically we obtain the $\eta(y)$ dependence shown in Figure 16.1.

In this Figure, we also show the "near" and "far" field solutions:

$$\eta^{(n)}(y) = y^2\,; \quad \eta^{(f)}(y) = \frac{2}{3}y^{3/2}, \tag{16.33}$$

corresponding to the dimensional equations (16.26-16.27).

We compute a non-linear average of the near and far approximations of the form

$$\eta^{(a)} = \left(\eta_n^{-5/4} + \eta_f^{-5/4}\right)^{-4/5}\,. \tag{16.34}$$

which has a relative error $\epsilon_{rel} = \eta^{(a)}/\eta - 1 < 0.04$ with respect to "exact" (i.e., numerical) solution $\eta(y)$, and is therefore a reasonable analytic approximation of the solution. The dependence of ϵ_{rel} on y is shown in the bottom panel of Figure (16.1).

The average between the "near" and "far" solutions of equation (16.34) can also be done with the dimensional near and far solutions (equations 16.26-16.27), to obtain an analytic approximation to the full (numerical), dimensional solution.

Another approximation to the numerical $\eta(y)$ solution is:

$$\eta^{(b)} = \frac{2y}{9}\left(-1 + \sqrt{1 + 9y}\right)\,, \tag{16.35}$$

which coincides with the full solution in the $y \to 0$ and $y \to \infty$ limits, and has a maximum relative deviation of ~ 0.09. This interpolation has a functional form similar to the centre of mass, constant $\dot{m}$ solution (see equation 16.10).

16.3.3 The case of constant ρ_0

Setting $\rho_0 = const.$ in (16.6) and taking the square of the equation, we obtain:

$$\frac{\rho_a}{\rho_0 a}\left(\frac{dx_{ws}}{d\tau}\right)^2 + x_{ws} = a\tau^2 = 0\,. \tag{16.36}$$

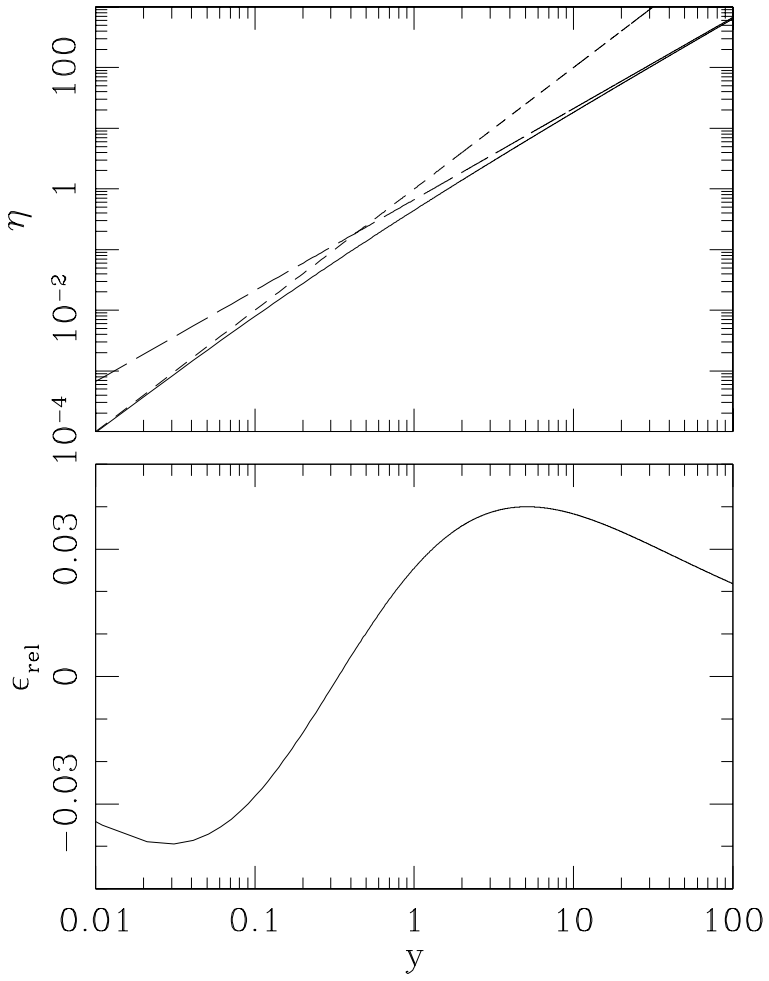

Figure 16.1: Top panel: the solid line shows the dimensionless solution $\eta(y)$ for the time-dependent position of the jet head, and the two analytic approximations, $\eta^{(n)}$ (short dashes) and $\eta^{(f)}$ (long dashes). Bottom panel: the relative deviation between the full analytic approximation $\eta^{(a)}$ (see equation 16.34) and the "exact" (i.e., numerical) solution.

Proposing a power law solution, one straightforwardly finds:

$$x_{ws} = \frac{\rho_a a \tau^2}{8\rho_a} \left[-1 + \sqrt{1 + \frac{16\rho_a}{\rho_0}} \right] . \tag{16.37}$$

In order to plot x_{cm} as a function of evolutionary time t, one has to generate $t(\tau)$ using equation (16.8).

In the $\rho_a \to 0$ limit, equation (16.37) takes the form

$$x_{ws} = a\tau^2 . \tag{16.38}$$

Finally, we obtain the explicit dependence of the position x_{ws} of the jet head as a function of evolutionary time t combining equations (16.5) and (16.37), giving:

$$x_{ws} = \frac{8a\left(-1 + \sqrt{1 + \frac{16\rho_a}{\rho_0}}\right)}{[\frac{8\rho_a}{\rho_0} - 1 + \sqrt{1 + \frac{16\rho_a}{\rho_0}}]^2} t^2 . \tag{16.39}$$

In the limits of a high and low density jet, this expression simplifies to:

$$x_{ws} \approx \frac{at^2}{4} \text{ for } \rho_0 \gg \rho_a ; \quad x_{ws} \approx \frac{a}{2}\sqrt{\frac{\rho_0}{\rho_a}} t^2 \text{ for } \rho_0 \ll \rho_a . \tag{16.40}$$

16.4 The head of an accelerating Herbig-Haro jet

We now consider an example appropriate for a jet from a young star. For the "acceleration parameter" a, we consider an ejection velocity with an increment of 100 km s^{-1} per millennium: $a = 100$ km s^{-1}/1000 yr$= 3.17 \times 10^{-4}$ s^{-2}. For the models of constant mass loss rate, we choose $\dot{M}_j = 10^{-8}$ M$_\odot$yr^{-1} and a $r_j = 50$ AU radius, giving $\dot{m} = \dot{M}_j/(\pi r_j^2) = 3.359 \times 10^{-13}$ g cm^{-2} s^{-1}. For the constant density case, we choose a density $\rho_j = 3.60 \times 10^{-20}$ g cm^{-3} (i.e., an atom+ion number density $n_j = 1.666 \times 10^4$ cm^{-3} for a gas with 90% H and 10% He), which gives $\dot{M}_j = 10^{-8}$ M$_\odot$yr^{-1} for a velocity of 100 km s^{-1}. For the environment, we choose two number densities: $n_a = 5000$ and 100 cm^{-3}.

Figure 16.2 shows the positions of the jet head as a function of evolutionary time t (calculated as a function of ejection time τ using, e.g., equation

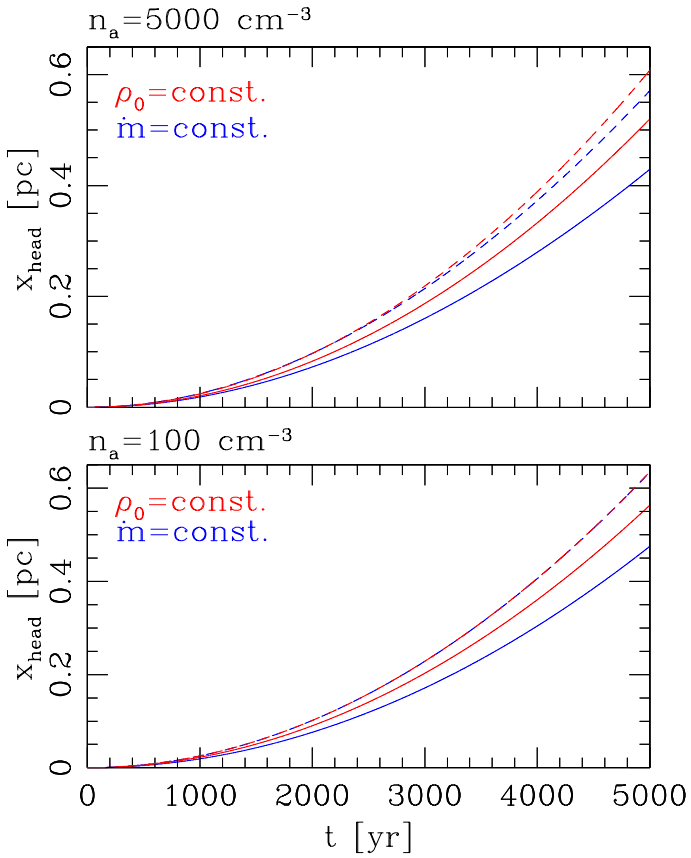

Figure 16.2: Models of jet heads moving into an environment with density $n_a = 10^4$ cm^{-3} (top) and 10^3 cm^{-3} (bottom), with the remaining model parameters being discussed in the text. The curves in red correspond to a time-independent ejection density, and the blue curves to models with a time-independent ejection mass loss rate. The solid curves are obtained from the "centre of mass" and the dashed lines from the "ram-pressure balance" formalisms.

16.21) for the four jet models (constant $\dot{m}$ and constant ρ_0, with the centre of mass and the ram-pressure balance formalisms), for an environment with $n_a = 5000$ cm^{-3} (top) and $n_a = 100$ cm^{-3} (bottom frame). It is clear that the ram-pressure balance formalism gives higher velocities for the jet head, resulting in larger distances from the outflow source. In the $n_a = 100$ cm^{-3} models, the ram-pressure balance solutions are in the "small ρ_a limit", and therefore the constant $\dot{m}$ and constant ρ_0 models coincide (see equations 16.26 and 16.38).

Chapter 17

Time-dependent ejection direction

17.1 General comments

Many astrophysical jets show evidence for a time-dependence in the ejection direction. Many times this evidence is a locus on the plane of the sky that can be interpreted as the projection of a spiral. This has been interpreted as the result of a precession of the outflow axis.

Another possibility is that the outflow source is part of a binary, and that the motion of the source in an orbit produces an additional, time-varying component in the ejection velocity of the outflow. If the orbit is approximately circular, and with an orbital axis parallel to the outflow axis, the resulting jet has a locus that quite closely resembles a precession spiral.

A "precession spiral" and an "orbital spiral" clearly have a quite dramatic difference: while the first one produces jet/counterjet pairs with a "point symmetric" structure, the latter one produces a "mirror symmetric" jet/counterjet pair. It appears that both kinds of structures are observed in astrophysical jets.

17.2 Precession

A ballistic jet with a constant ejection velocity modulus v_j, and with an ejection direction that precesses with a period τ_p around the z-axis with an angle α, at time t has a beam with the locus:

$$x(t,\tau) = (t-\tau)v_j \sin\alpha \cos\omega\tau \,, \tag{17.1}$$

$$y(t,\tau) = (t-\tau)v_j \sin\alpha \sin\omega\tau \,, \tag{17.2}$$

$$z(t,\tau) = (t-\tau)v_j \cos\alpha \,, \tag{17.3}$$

where $\omega = 2\pi/\tau_p$ is the precession frequency, and it has been assumed that at an ejection time $\tau = 0$ the jet lies on the xz-plane.

Equations (17.1-17.3) can be combined to obtain the 3D shape of the locus of the jet at time t:

$$x = z\tan\beta\cos\left[\omega(t - z/v_j\cos\alpha)\right] \,, \tag{17.4}$$

$$y = z\tan\beta\sin\left[\omega(t - z/v_j\cos\alpha)\right] \,. \tag{17.5}$$

17.3 Circular orbital motion

We now consider a ballistic jet ejected with a constant velocity modulus v_j, parallel to the axis of a circular orbital motion of the outflow source. At a time t, the locus of the jet is:

$$x(t,\tau) = r_o\cos\Omega\tau - (t-\tau)r_o\Omega\sin\Omega\tau \,, \tag{17.6}$$

$$y(t,\tau) = r_o\sin\Omega\tau - (t-\tau)r_o\Omega\cos\Omega\tau \,, \tag{17.7}$$

$$z(t,\tau) = (t-\tau)v_j \,, \tag{17.8}$$

where z is the orbital axis, and we have assumed that at an ejection time $\tau = 0$ the source lies on the y axis, and rotates towards the x-axis. In these equations, r_o is the radius and $\Omega = 2\pi/\tau_o$ the frequency of the circular orbit.

It is straightforward to combine equations (17.6-17.8) to obtain:

$$x = \kappa z\,\sin\left(\frac{\kappa z}{r_o} - \Omega t\right) + r_o\cos\left(\frac{\kappa z}{r_o} - \Omega t\right) \,, \tag{17.9}$$

$$y = \kappa z \cos\left(\frac{\kappa z}{r_o} - \Omega t\right) - r_o \sin\left(\frac{\kappa z}{r_o} - \Omega t\right) , \tag{17.10}$$

where $\kappa = v_o/v_j$, and we have used the relation $\Omega = 2\pi/\tau_o = v_o/r_o$, where τ_o is the orbital period.

The separation between the jet beam and the orbital axis is:

$$r(z) = r_o \sqrt{1 + \kappa^2 \left(\frac{z}{r_o}\right)^2} , \tag{17.11}$$

where we have used equations (17.9-17.10). Therefore, for small z/r_o the radius grows quadratically with z, and at large z/r_o, the separation r with respect to the orbital axis grows linearly with z. Therefore, at large z/r_o, the locus joins a precession spiral of opening angle β that satisfies the relation

$$\kappa = \tan\beta . \tag{17.12}$$

At scales much larger than the orbital radius of the source, the effect of a circular orbital motion is to produce a precession-like signature in the observed locus of the jet. If a counterjet is also detected, this "orbital jet" flow can easily be distinguished from a precessing flow because it shows a "mirror symmetry" with respect to the orbital plane, with the jet and the counterjet having mirror symmetric excursion from the mean outflow axis (instead of the point-symmetric "jet to one side-counterjet to the other side" excursions of a precessing flow).

Interestingly, in the case of an "orbital motion spiral", the opening angle α directly gives the ratio $\kappa = v_o/v_j = \tan\beta$ (see equation 17.12) between the orbital and the outflow velocities. Also, the spatial pass of the spiral is

$$\Delta z = \frac{2\pi r_o}{\kappa} . \tag{17.13}$$

Using equations (17.12-17.13) one can then use the observed shape of locus of the jet beam, together with a separate measure of the jet velocity v_j, to deduce the orbital radius and velocity of the outflow source.

Therefore, under the assumptions of a circular orbit and an ejection parallel to the orbital radius, it is possible to derive an estimate of the mass of the companion of the outflow source. If this estimated mass has a reasonable (i.e., stellar or planetary) mass, the explanation of the observed jet/counterjet shape in terms of an orbital motion is likely to be correct.

17.4 Precession+orbital motion

We now assume that we have a jet from a source in a circular orbit of radius r_o and frequency Ω, with position:

$$x_s(\tau) = r_o \cos\Omega\tau\,; \quad y_s = r_o \sin\Omega\tau\,, \tag{17.14}$$

with a constant velocity v_j along the direction of the outflow, measured in a reference system moving with the source. If the jet also has a precession with an angle α, and a frequency ω, the velocity in an inertial system attached to the centre of the circular orbit is:

$$v_x = v_j \sin\alpha \cos\omega\tau - v_o \sin\Omega\tau\,, \tag{17.15}$$

$$v_y = -v_j \sin\alpha \sin\omega\tau + v_o \cos\Omega\tau\,, \tag{17.16}$$

$$v_z = -v_j \cos\alpha,\,, \tag{17.17}$$

where Ω and r_o are the frequency and radius of the orbit (respectively), and τ is the ejection time. The ballistic equation of motion for parcels ejected at a time τ then is:

$$(x, y, z) = (t - \tau)\,[v_x(\tau), v_y(\tau), v_z] + [x_s(\tau), y_s(\tau), z_s(\tau)]\ , \tag{17.18}$$

where t is the present time. We now set $t = 0$ ("now") and combine equations (17.15-17.18) to obtain:

$$x' = \frac{z'}{\cos\alpha}\left[\sin\alpha\cos\left(\frac{z'}{\cos\alpha}\right) + \frac{v_o}{v_j}\sin\left(\frac{\Omega}{\omega}\frac{z'}{\cos\alpha}\right)\right]\ , \tag{17.19}$$

$$y' = \frac{|z|'}{\cos\alpha}\left[\sin\alpha\sin\left(\frac{z'}{\cos\alpha}\right) + \frac{v_o}{v_j}\cos\left(\frac{\Omega}{\omega}\frac{z'}{\cos\alpha}\right)\right]\ , \tag{17.20}$$

where

$$(x', y', z') = (x, y, z)/D\,; \quad D = v_j\omega\,. \tag{17.21}$$

and we have neglected terms of order r_o/D (i.e., assuming that the orbital radius is much smaller than the length scales observed along the jet).

As we expect the precession period to be substantially longer than the orbital period, we expect to see a "short pass", mirror symmetric spiral due to the orbital motion superimposed on a "long pass", point symmetric spiral due to the precession. A numerical example of this kind of structure is shown in Figure 17.1.

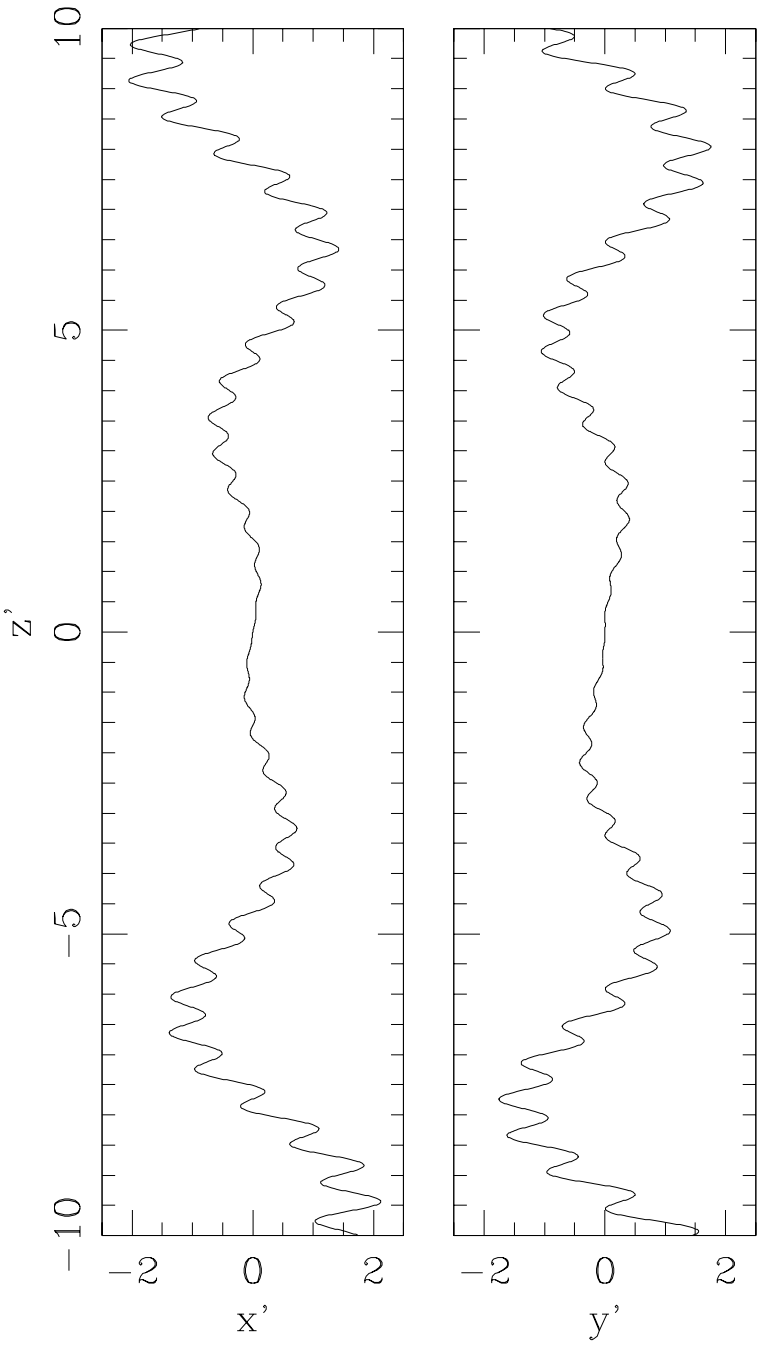

Figure 17.1: Example of the locus of a jet/counterjet system, obtained froom equations (17.19-17.20) setting $v_o/v_j = 0.05$, $\Omega/\omega = 10$ and $\alpha = 10°$. The "fast", mirror symmetric "orbital spiral" and the "slow", point-symmetric precession spiral are seen.

Chapter 18

Steady jet in a sidewind

18.1 The problem

In a jet source at the centre of an active galaxy, one would expect the jet source not to have a peculiar motion with respect to the surrounding environment. In jets ejected by stars or by stellar mass compact objects, however, we would expect the jet source to have a motion relative to the surrounding, undisturbed environment. In a frame of reference attached to the outflow source, this motion is seen as a "sidewind" arriving from an arbitrary direction.

For the case of an isothermal jet, there exists a complete analytic solution giving the shape of the cross section of the jet and the curved locus of the jet/counterjet system. This solution is applicable of course to the case of HH jets, and is described in the following section. It is also possible to construct a similar model for the non-radiative case, but the resulting differential equation has to be integrated numerically (see Cantó & Raga[8]), and is not discussed in this chapter.

18.2 The isothermal model

Let us consider a source that ejects a jet/counterjet system, embedded in a hypersonic sidewind along the z-axis of density ρ_a and velocity v_a. The jet/counterjet system lies on the yz-plane, and is ejected at an angle β with

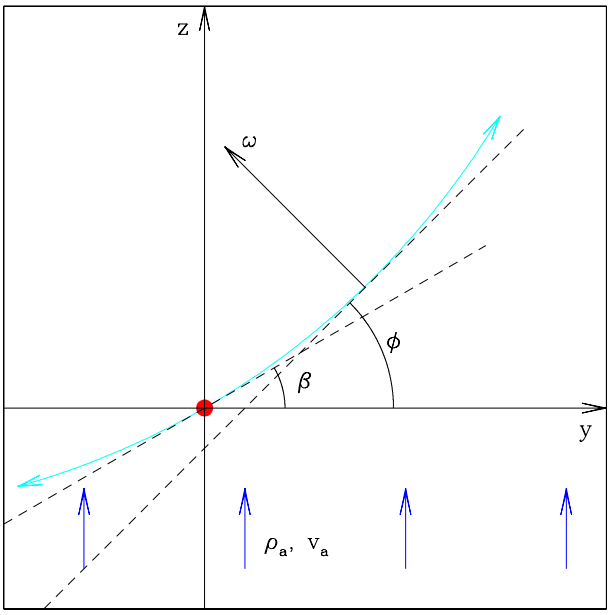

Figure 18.1: Schematic diagram of a jet/counterjet system (in cyan) ejected from a source (red star) immersed,in a sidewind.

respect to the y-axis, as shown in the schematic diagram of Figure 1. The ω axis lies on the xz-plane, and is locally normal to the locus of the jet beam.

As the material in the jet flows along the curved jet path, it feels an effective acceleration a perpendicular to the $z(y)$ trajectory of the jet. This acceleration is given by:

$$a = \kappa v_j^2 \,, \tag{18.1}$$

where v_j is the jet velocity (assumed to be time- and position-independent), and

$$\kappa = \frac{d^2z/dy^2}{[1 + (dz/dy)^2]^{3/2}} \tag{18.2}$$

is the curvature of the jet path, i.e., the inverse of the local radius of curvature of the $z(y)$ curve.

The material within the cross section of the jet feels this acceleration, and therefore develops a stratified pressure. The cross section is shown schematically in Figure 18.2.

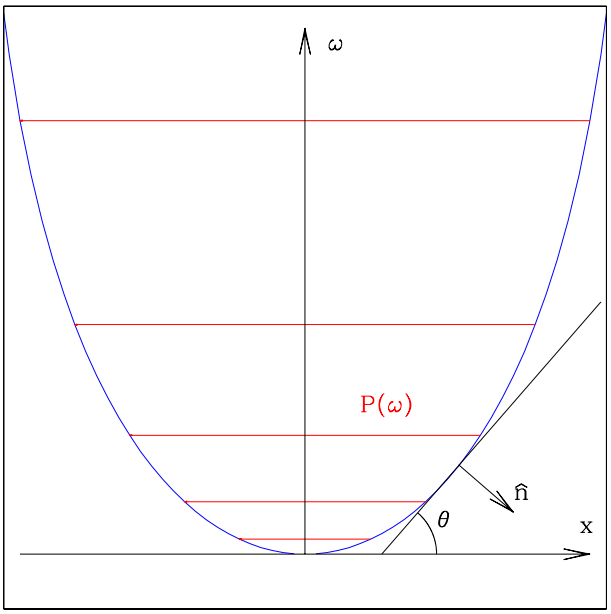

Figure 18.2: Stratified pressure in a cross section of the jet. The ω axis is directed perpendicular to the curved locus of the jet (see figure 18.1).

Assuming that the cross section adjusts to a hydrostatic distribution along the ω direction (see Figures 18.1 and 18.2), we then have

$$\frac{dP}{d\omega} = -a\rho\,, \tag{18.3}$$

which can be integrated to obtain

$$P(\omega) = P_0 e^{\omega/\omega_0}\,, \tag{18.4}$$

where P_0 is the gas pressure at the tip ($\omega = 0$) of the cross section, $P(\omega)$ is the stratified pressure, $\rho(\omega) = P/c_0^2$ the density (with c_0 being the isothermal sound speed of the gas) and $\omega_0 = c_0^2/a$ is the scale height.

Let $\hat{n}$ be the unit vector normal to the surface of the jet:

$$\hat{n} = \sin\theta\hat{e}_x + \sin\phi\cos\theta\hat{e}_y - \cos\theta\cos\phi\hat{e}_z\,, \tag{18.5}$$

where ϕ and θ are defined in Figures 18.1-18.2.

The form of the cross-section of the jet is determined by the balance between the internal gas pressure and the normal ram pressure exerted by the impinging sidewind. Therefore:

$$P(\omega) = \rho_a \left(\overline{v}_a.\hat{n}\right)^2 = \rho_a v_a^2 \cos^2\phi\,, \tag{18.6}$$

where

$$\cos\theta = \left[1 + (d\omega/dx)^2\right]^{-1/2}\,. \tag{18.7}$$

Equations (18.4) and (18.6-18.7) can be combined to obtain

$$P_0 = \rho_a v_a^2 \cos^2\phi\,, \tag{18.8}$$

and

$$\frac{d\omega}{dx} = \sqrt{e^{\omega/\omega_0} - 1}\,, \tag{18.9}$$

which can be integrated to give the shape of the cross section:

$$w = -2\omega_0 \ln\left[\cos(x/2\omega_0)\right]\,. \tag{18.10}$$

This is the "plasmon" solution (shown in Figure 18.2) first found by De Young & Axford[12]. The maximum extent of the plasmon in the x-direction is $x_m = \pi\omega_0$.

In order to find the $z(y)$ path of the jet by integrating equation (18.8), one has to relate the pressure P_0 to the mass-loss rate of the jet:

$$\dot{M}_j = 2\int_0^{x_m}\int_{\omega(x)}^{\infty} \rho(x,\omega) v_j d\omega dx = \pi\omega_0^2 \frac{P_0}{c_0^2} v_j\,, \tag{18.11}$$

where we have used equations (18.4) and (18.10).

From equations (18.1), (18.4) and (18.11), we have:

$$P_0 = \frac{\dot{M}_j v_j^3}{\pi c_0^2}\kappa^2\,, \tag{18.12}$$

and, using equations (18.2), (18.8) and (18.12) we finally obtain

$$\lambda\frac{d^2z}{dy^2} = 1 + \left(\frac{dz}{dy}\right)^2\,, \tag{18.13}$$

where

$$\lambda \equiv \sqrt{\frac{\dot{M}_j v_j^3}{\pi c_0^3 \rho_a v_a^2}} \tag{18.14}$$

is a characteristic length of the model.

Equation (18.13) can be integrated with the boundary conditions $z = 0$ and $dz/dy = \tan\beta$ at $y = 0$ to obtain

$$z = \lambda \ln\left[\frac{\cos\beta}{\cos\left(y/\lambda + \beta\right)}\right] . \tag{18.15}$$

This solution gives the locus of the jet for $y > 0$ and for the counterjet for $y < 0$. Substituting into the appropriate relations, we also obtain:

$$\kappa = \frac{1}{\lambda}\cos(y/\lambda + \beta) , \tag{18.16}$$

$$a = \frac{v_j^3}{\lambda}\cos(y/\lambda + \beta) , \tag{18.17}$$

and

$$P_0 = \rho_a v_a^2 \cos^2(y/\lambda + \beta) . \tag{18.18}$$

It is clear from equation (18.18) that the maximum pressure in the jet/counterjet system is formed in the "stagnation point"

$$y_s = -\lambda\beta ; \quad z_s = \lambda \ln(\cos\beta) , \tag{18.19}$$

where the wind velocity is perpendicular to the jet path. From equation (18.16) we then see that λ is the radius of curvature of the jet trajectory at the stagnation point.

Needless to say, the fact that the jet cross section (equation 18.10) and locus (18.15) have the same functional form is an unexpected result of the jet/sidewind jet model.

Chapter 19

Bullets

19.1 Why bullets?

The general problem of a jet with a general velocity (modulus) + direction variability has been repeatedly modeled numerically, but its complexity has defied a general analytic approach. A situation which appears to be relevant for many astrophysical jets is as follows:

- a velocity variability (i.e., of the modulus of the ejection velocity) produces internal working surfaces which capture most of the ejected mass,
- because of an ejection direction variability with a longer timescale, these internal working surfaces travel in different directions, and interact directly with the surrounding, undisturbed environment.

With such an ejection time-variability, at large enough distances from the outflow source the jet becomes a chain of gaseous "bullets" travelling in different directions, and gradually slowing down due to their interaction with the surrounding environment.

Such a scenario is justified by observations of HH jets, which close to the source show chains of aligned knots, and at larger distances (of the order of parsecs) sometimes show disconnected "heads" with lower velocities at larger distances.

19.2 The plasmon model

We will assume that we have an isothermal bullet of mass M and (isothermal) sound speed c_0, travelling hypersonically at a velocity v within a homogeneous environment of density ρ_a. The interaction with the environment will produce a deceleration a which will result in a stratified pressure within the bullet. With the same arguments as the ones of the previous chapter (see Figure 18.2), the condition of balance between the post-bow shock pressure and the thermal pressure within the bullet produces a pressure stratification

$$P(z) = P_0 e^{-z/z_0}\,, \tag{19.1}$$

a density stratification $\rho(z) = P(z)/c_0^2$ and a bullet of shape

$$z(r) = -2z_0\,\ln\left[\cos\left(\frac{r}{2z_0}\right)\right]\,, \tag{19.2}$$

where z is the distance along the symmetry axis from the tip of the plasmon, and r its cylindrical radius (see equations 18.4 and 18.10, and Figure 18.2). The pressure scale-height is

$$z_0 \equiv \frac{c_0^2}{a}\,, \tag{19.3}$$

where c_0 is the isothermal sound speed and a the deceleration of the plasmon. From equation (19.2), one can see that the plasmon shape has a maximum cylindrical radius

$$r_m = \pi z_0\,, \tag{19.4}$$

obtained for $z \to \infty$.

Now, the mass of the clump can be calculated as:

$$M = \int_0^{r_m}\left[\int_{z(r)}^{\infty}\rho(z)dz\right]2\pi r dr = \xi\rho_0 z_0^3\,, \tag{19.5}$$

where

$$\xi = 2\pi\left(\frac{\pi^2}{4} - 1\right)\,. \tag{19.6}$$

The second equality of equation (19.5) is obtained using the $\rho(z)$ and $z(r)$ relations of equations (19.1) and (19.2).

The model is completed with the ram/gas pressure balance relation

$$P_0 = \rho_0 c_0^2 = \rho_a v^2 \tag{19.7}$$

for the tip of the plasmon. Combining this relation with equation (19.5) we then obtain:

$$a = -\frac{dv}{dt} = -\left(\frac{\xi \rho_a c_0^4}{M}\right)^{1/3} v^{2/3}\,, \tag{19.8}$$

which, by setting $dv/dt = vdv/dx$ (with x being the position of the tip of the plasmon), can be integrated to obtain

$$v(x) = v_0 \left(1 - \frac{x}{x_0}\right)^3\,, \tag{19.9}$$

where v_0 is the initial velocity of the clump, and

$$x_0 \equiv \frac{3 v_0^{4/3}}{4} \left(\frac{M}{\xi \rho_a c_0^4}\right)^{1/3}\,. \tag{19.10}$$

Integrating equation (19.9) with respect to time, we then obtain:

$$x(t) = x_0 \left[1 - \left(1 - \frac{t}{t_0}\right)^4\right]\,, \tag{19.11}$$

where

$$t_0 \equiv \frac{4 x_0}{v_0}\,. \tag{19.12}$$

It is clear that the bullet decelerates, reaching a zero velocity at a position x_0 and time t_0 (see equations 19.9 and 19.12).

This model has to be considered as qualitative, since a clump-like flow braking down through an interaction with the surrounding environment has a tendency to break down into smaller structures. This is seen in numerical simulations of bullet flows, and also in astrophysical bullet-type flows, which many times have a lot of substructure. The plasmon model described here has been used to model working surfaces scattered by a time-dependent ejection direction, and also for working surfaces ejected by a source moving with respect to the surrounding environment.

Bibliography

[1] Abramowitz, M., Stegun, I. A. 1965, Handbook of Mathematical Functions (New York: Dover)

[2] Aldrovandi, S. M. V., Péquignot, D. 1973, A&A, 25, 137

[3] Aldrovandi, S. M. V., Péquignot, D. 1976, A&A, 47, 321

[4] Aller, L. H. 1984, Physics of Thermal Gaseous Nebulae (Dordrecht: Reidel)

[5] Bonnor, W. B. 1956, MNRAS, 116, 351

[6] Brocklehurst, M. 1971, MNRAS, 153, 471

[7] Brown, R. L., Mathews, W. 1970, ApJ, 160, 939

[8] Cantó, J., Raga, A. C. 1995, MNRAS, 277, 1120

[9] Capriotti, E. R., Kozminski, J. F. 2001, PASP, 113, 677

[10] Carral, P., Kurtz, S.E., Rodríguez, L. F., Menten, K., Cantó, J., & Arceo, R. 2002, AJ, 123, 2574

[11] Chevalier, R. A. 1999, ApJ, 511, 798

[12] De Young, D. S., Axford, W. I. 1967, Nature, 216, 129

[13] Dyson, J. E., Williams, D. A. 1997, "Physics of the Interstellar Medium" (Oxford: IoP Publishing)

[14] Hartigan, P., Raymond, J. C., Hartmann, L. W. 1987, ApJ, 316, 323

[15] Huggins, W. 1871, RSPS, 20, 379

[16] Hunter, C. 2001, MNRAS, 328, 839

[17] Marcolino, W. L. F., Bouret, J.-C., Martins, F., Hillier, D. J., Lanz, T., & Escolano, C. 2009, A&A, 498, 837

[18] Osterbrock, D. E. 1989, "Astrophysics of gaseous nebulae and active galactic nuclei" (Mill Valley: Univ. Sci. Books)

[19] Pengelly, R. M., Seaton, M. J. 1964, MNRAS, 127, 165

[20] Pradhan, A., Nahar, S. 2015, "Atomic astrophysics and spectroscopy" (Cambridge: Cambridge Univ. Press)

[21] Raga, A. C., Noriega-Crespo, A., Cantó, J., Steffen, W., Van Buren, D., Mellema, G., Lundqvist, P. 1997, RMxAA, 33, 73

[22] Raga, A. C., Cantó, J., Rodríguez, L. F. 2012, RMxAA, 48, 149

[23] Raga, A. C., Cantó, J., Rodríguez, L. F. 2012, MNRAS, 419, L39

[24] Raga, A. C., Cantó, J., Rodríguez, L. F. 2012, RMxAA, 48, 149

[25] Rasiwala, M. 1969, A&A, 431, 441

[26] Raymond, J. C., Hartigan, P., Hartmann, L. W. 1988, ApJ, 326, 323

[27] Seaton, M. J. 1955, PPSA, 68, 457

[28] Seaton, M. J. 1959, MNRAS, 119, 81

[29] Seaton, M. J. 1960, Rept. Prog. Phys., 23, 313

[30] Shull, J. M., McKee, C. F. 1979, ApJ, 227, 131

[31] Shore, S. N. 2007, "An introduction to astrophysical hydrodynamics" (New York: Wiley)

[32] Sternberg, A., Hoffman, T. L., Pauldrach, A. W. A. 2003, ApJ, 599, 1333

[33] Tang, S., Wang, Q. D. 2005, ApJ, 628, 205

[34] Zel'dovich, I. A., Raizer, Y. P. 1967, "Physics of shock waves and high-temperature hydrodynamic phenomena", Academic Press, New York

Index